Noname manuscript No.
(will be inserted by the editor)

Topology Optimization of General Structures with Anisotropic Fatigue Constraints

Asbjørn Olesen · Sebastian Hermansen

Received: date / Accepted: date

Abstract Additively manufactured metals are special in that they behave close to isotropic in elasticity and monotonic strength, however their fatigue behavior is anisotropic and the fatigue strength is degraded. Designs generated by topology optimization have commonly been used as inspiration rather than realizing the actual design, primarily due to restrictions of the manufacturing methods. However, with additive manufacturing, it is possible to manufacture the highly complex designs common in topology optimization. An increased focus is therefore placed on design for manufacture, and for this purpose a novel smoothing approach is developed. Assuming isotropic stiffness and monotonic strength, the topology optimization is formulated as an extension to existing fatigue constraint functions using density-based topology optimization. An improved formulation for the fatigue damage is proposed to achieve a good combination of accuracy and computational efficiency, which has caused problems in previously published literature. These approaches and methods are demonstrated by solving both 2D and 3D problems, and the designs are subsequently verified using commercial finite element software.

Keywords Topology Optimization · Anisotropic Fatigue · Manufacturing Constraints · Additive Manufacturing

A. Olesen
E-mail: amol15@student.aau.dk

S. Hermansen
E-mail: sherma15@student.aau.dk

Department of Materials and Production, Aalborg University
Fibigerstraede 16, DK-9220 Aalborg East, Denmark

1 Introduction

Best use of material for load-carrying structures is a long-standing objective in engineering and several mathematical optimization methods have been developed to achieve this (Christensen and Klarbring, 2009). As computational power has increased, the preferable approach has become optimization in a Finite Element (FE) formulation (Lund, 1994). The earliest approach taken was sizing optimization, which concerns structures parameterized by common dimensions (typically thickness or cross sectional area). To be able to treat more complex problems and achieve better designs, shape optimization was developed, which allows finer control in generation of design, e.g. the shape of a curve (Haftka and Grandhi, 1986). Although the design freedom has increased with the introduction of shape optimization, the resulting geometry is however still restricted by the parameterization, as topological features are persistent - a hole may change shape, but cannot be removed. Topology optimization (TO) is the generalization of this, having no dependence on an input geometry, instead focusing on distributed functions in a fixed domain and optimal layout of material (Bendsøe and Sigmund, 2003). Solving these functions is typically done by FE discretization of the domain and finding an optimal distribution of void and solid elements. This 0-1 problem is however an arduous affair due to the discrete nature of the problem and the number of elements inherent to FE solutions. TO was originally introduced in Bendsøe and Kikuchi (1988), where a homogenization approach is taken to define continuous equivalent material properties of the 0-1 domain. The method is virtually abandoned today as more effective methods have been developed. Many exist (Sigmund and

Maute, 2013), yet the most popular is a density-based approach with stiffness penalization (Bendsøe, 1989; Stolpe and Svanberg, 2001) and level-set approaches (Allaire et al., 2002; Wang et al., 2003; Allaire et al., 2004). In this work the density-based method Solid Isotropic Material with Penalization (SIMP) method is applied due to its simple, yet effective, formulation.

A consistent issue in material layout problems is the illposedness of geometric scale and non-existence of solutions for the continuous problem, leading to mesh dependent designs in FE formulations (Cheng and Olhoff, 1981). Regularization is done to ensure mesh independent convergence, typically by filtering techniques such as sensitivity (Sigmund, 1994) or density filtering (Bruns and Tortorelli, 2001; Bourdin, 2001). Most often, density filtering is adopted as sensitivity filtering heuristically alters the problem sensitivities, whereby the actual descent direction is not correctly represented, which is problematic for line search based optimization algorithms and may prohibit convergence to the optimum (Sigmund, 2007). However, density filtering has a substantial downside in that it introduces a gradient of intermediate density around structural members. Intermediate density is undesirable in the optimized domain, because it does not have an associated physical interpretation. Many regularization schemes have been proposed (Sigmund, 2007), yet the method that seem to garner the most use is projection filtering. First introduced in Guest et al. (2004) as a method to project all intermediate densities to fully solid material using a relaxed version of the Heaviside step function, it has since been reformulated for many purposes. It also deals with the concept of introducing a minimum length scale, i.e. strict control over geometric dimension, which is now definable, however only for the solid phase. Being able to define a minimum length scale is very important considering manufacturability of the design. Sigmund (2007) reformulated the filter such that a minimum length scale can be guaranteed on the void phase instead of the solid. Neither of these filters are volume preserving, which led to the development of the volume preserving projection filter by Xu et al. (2010). This is more generally termed threshold filtering, where a threshold is introduced to define a value around which densities are projected to either void or solid.

To account for uncertainties in the manufacturing process, the robust method was introduced in Sigmund (2009), based on projection methods from Guest et al. (2004) and Sigmund (2007). The robust method makes use of three FE problems defined by projections of densities. The projections are based on image morphology operators erode and dilate, and are used to create an eroded, intermediate, and dilated designs. Ensuring that each design is feasible also imposes minimum length scale on both void and solid material phases. In Wang et al. (2011), the robust method formulation is improved by using the threshold filter to define the three designs, which allows for better defining a desired minimum length scale. Other methods to achieve minimum length scale have also been proposed, in particular noteworthy is the formulation of geometric constraints (Zhou et al., 2015), which imposes an explicit requirement for minimum length scale on the design. Similar to the geometric constraints for minimum length scale, geometric constraints imposing maximum length scale has also been developed (Lazarov and Wang, 2017). Another issue related to minimum length, specifically violation of minimum length at domain edges, stemming from poor definition of filtering boundary conditions, was solved in Clausen and Andreassen (2017), by use of domain extension, such that accurate boundary conditions are achieved in the design domain.

Computation of the density filter may be quite expensive for large models in its discrete form, as it involves determining weighting functions for all elements in the neighborhood defined by a filter radius of each element. Instead the filter can be formulated and solved as a Helmholtz partial differential equation (Lazarov and Sigmund, 2011). Using this formulation of the filter, the extensive search for defining element weight functions is removed, which increases efficiency and reduces the amount of memory required to store the element weighting relations. Further, this formulation allows for better parallelization between the computer cores, such that they all contribute in computing the filter. Including projection filters with this formulation has also been investigated, see Kawamoto et al. (2011). The topic of parallelization has in general been the subject of much attention, such that the TO can be performed as efficiently as possible. Parallelization aspects are discussed in detail in Aage and Lazarov (2013) and a fully parallel framework based on this is provided in Aage et al. (2015). The necessity of parallelization for large problems is highlighted in Aage et al. (2017), where the framework is used to solve an impressively large problem consisting of one billion finite elements.

1.1 Local Constraint Function

In the pursuit of generating optimized designs with adequate structural integrity, commonly occurring failure phenomena have been considered for TO, namely those based on stress. Inclusion of stress criteria in an optimization context is tedious due to its local definition and the appearance of singular optima (Duysinx and Bendsøe, 1998). Early work on stress constrained optimization of truss structures was done in Sved and Ginos (1968), where the problem of singular optima was encountered. Singular optima occur when an optimum belong to a degenerate subspace that is unreachable due to the stress constraints, which prohibit the design variables from reaching the optimum using conventional sensitivity-based optimizers (Kirsch, 1990). The issue translates to TO and is solved by relaxation, typically by either the ε-method (Cheng and Guo, 1997) or qp-method (Bruggi, 2008; Le et al., 2010), whereby the constraints constitute a less strict feasible design domain.

Another issue is that an intractable number of constraint functions is required to capture the local nature of stress, which largely depends on distribution of nearby material. Constraining the maximum stress is desired, but the straightforward implementation is nondifferentiable and thus aggregation functions are introduced to give a continuous approximation of the largest value, such as the P-norm function (Duysinx and Sigmund, 1998; Le et al., 2010). Local control is however lost as the maximum and its function neighborhood cannot be accurately represented by aggregation functions. In Le et al. (2010) two solutions were discussed: (1) regional constraints, where the domain is divided into sections, each with an aggregation function, thus lowering the inaccuracy, and (2) normalized global stress or adaptive constraint scaling, where a scalar factor is determined for each iteration, scaling the aggregation function to the true maximum. More lately, in da Silva et al. (2019) the local constraints are treated in an augmented Lagrange formulation. In this work, manufacturing uncertainties for stress constrained TO are also considered via the robust method, where resultant geometries are analyzed with higher accuracy using a body fitted mesh as a step along the way to manufacturability.

Fatigue is an important consideration in general structural design and stress-based fatigue criteria receive increasing interest in TO. Fatigue TO has all the difficulties of stress optimization, which are exacerbated by the exponential dependence on stress. In Holmberg et al. (2014) a decoupled fatigue analysis determined a maximum stress from a given load spectrum, using SN-curves and Palmgren-Miner linear damage accumulation. Optimization was then performed with a principal stress criterion. Jeong et al. (2015) included fatigue in the optimization for a constant proportional load amplitude and mean, using the signed von Mises measure to account for the multiaxial stress state and a variety of mean stress corrections, specifically Goodman, Gerber and Söderberg criteria. These methods were generalized to an arbitrary proportional load history in Oest and Lund (2017), wherein a logarithmic function is used to reduce the non-linearity of Basquin's approximation of the SN-curve. A method for considering non-proportional loading was presented by Zhang et al. (2019), also introducing a linearization of Basquin's approximation.

1.2 Additive Manufacturing

As the methods of TO have matured, an increased interest is placed on design for manufacture, with Additive Manufacturing (AM) being a prime candidate (Clausen, 2016). AM allows for near-total design freedom as no tool-paths must be considered, which is the main obstacle in conventional subtractive manufacturing due to the complex geometries typical of TO. AM however brings new challenges in design, as fatigue properties of AM metals are degraded as compared to wrought material (Yadollahi and Shamsaei, 2017) and variations are highly dependent on process parameters (Fatemi et al., 2020). Surface quality most obviously depends on process parameters such as material deposition rates and heat input, but also has a geometric aspect, as the orientation during building can lead to inconstant surface roughness (Yadollahi and Shamsaei, 2017). An apparently unavoidable aspect of AM is internal defects, leading to cracks not necessarily initiating at the surface (Fatemi et al., 2020) and a print-direction dependent orientation of these defects, leading to anisotropic fatigue (Yadollahi et al., 2017). Processes to improve fatigue properties include hot isostatic press (HIP) (Leuders et al., 2014) and surface peening (Bag et al., 2020; Hackel et al., 2018), which yield good results, but do not entirely resolve the issue of anisotropic fatigue behavior occurring in AM components (Yadollahi et al., 2017; Fatemi et al., 2020). Further, the results achieved are material dependent, in particular for HIP which, if applied to a material retaining a reasonable amount of ductility after printing, will have the opposite effect and reduce the fatigue strength (Yadollahi and Shamsaei, 2017).

Designing via TO for manufacture presents a range of issues that is often overlooked in purely theoretical approaches. In Langelaar (2016) the problem of overhanging details are treated by introducing a TO filter to exclude unprintable designs, i.e. entirely without support material, whereas Langelaar (2019) presents a formulation for designing the support structure simultaneously with the component in the TO.

The intersection of TO, fatigue, and AM is relatively unexplored, as implementations of fatigue constrained TO assume isotropic behavior, which inevitably converge to a suboptimal design as the lowest fatigue strength must be used to avoid failure. The objective of this work is to develop a continuous anisotropic fatigue criterion from an outset in proportional high cycle fatigue (HCF) of AM metals. The criterion is implemented for both two- and three-dimensional cases. TO designs are commonly used for design inspiration rather the realizing the actual generated design. As such regularization and post-processing is given increased attention to improve manufacturability, specifically by introduction of manufacturing constraints by the robust method and development of a novel framework for smoothing three-dimensional TO models. Examples are presented as both density-based models and as body fitted meshes to illustrate adequate control over local behavior related to stress concentrations for both two- and three-dimensional cases.

The paper is structured as follows. In section 2 general fatigue modeling is presented and the anisotropic fatigue model is developed. Section 3 covers formulation of the TO problem, necessary relaxations and regularization. Analytical expressions of problem sensitivities are derived in section 4, with explicit terms listed in appendix A. Examples using the described methods in two and three dimensions are given in section 5, wherein properties and behavior is also discussed. The 3D example is verified in a commercial FE-program using a post-optimization smoothing scheme described in appendix B. Section 6 gives concluding remarks.

2 Anisotropic Fatigue Analysis

The anisotropic fatigue model, presented in the following, takes offset in elasticity and static strength properties of AM materials behaving close to isotropic (Tolosa et al., 2010; Yadollahi and Shamsaei, 2017), while fatigue does not. For this reason isotropic density-based interpolation schemes, namely SIMP, are not precluded by the introduction of anisotropic fatigue. Consequently, the fatigue model is developed as an extension to the existing density-based approach to TO.

2.1 Classical Stress-based Fatigue Analysis

Estimating fatigue failure is difficult as it is influenced by many parameters - one of which is the loading condition. The present implementation is limited to proportional loading, i.e. when principal directions are constant throughout the load history. Thus, a given time dependent element stress $\boldsymbol{\sigma}^{(e)}(t)$ is determined through a scaling $c(t)$ of the reference stress $\hat{\boldsymbol{\sigma}}^{(e)}$:

$$\boldsymbol{\sigma}^{(e)}(t) = c(t)\,\hat{\boldsymbol{\sigma}}^{(e)} \tag{1}$$

whereby only a single FE problem is solved to find the entire stress history. The scaling constant is then sectioned into amplitude and mean contributions as illustrated in Fig. 1. Combination of amplitude and mean at a time in the discretized load history is termed *load combination*. Nonproportional loading implies a substantial increase in computational effort as a new equilibrium has to be solved for each unique combination of loads in the load history. Given an arbitrary dizcretized load history, a consistent method is needed to determine the combinations of amplitude and mean loads: a popular choice is the Rainflow counting algorithm (Stephens et al., 2001).

Only HCF is considered for this model, thus the stress-life method to fatigue is adequate. For more general application, the strain-life method, which is also able to capture low-cycle fatigue behavior, can be implemented instead. Strain-life models are also better for modeling crack propagation behavior, and should therefore also be adopted if extending the model to include fracture mechanical aspects. In the stress-life method the amplitude and mean stress contributions then have to be converted to an equivalent fully reversed uniaxial stress amplitude such that it is relatable to the material SN curve. Many different criteria have been proposed, which vary in accuracy and computational effort as well as also depend on the load case. A criterion may be classified as either multiaxial or equivalent uniaxial: thorough assessment of these

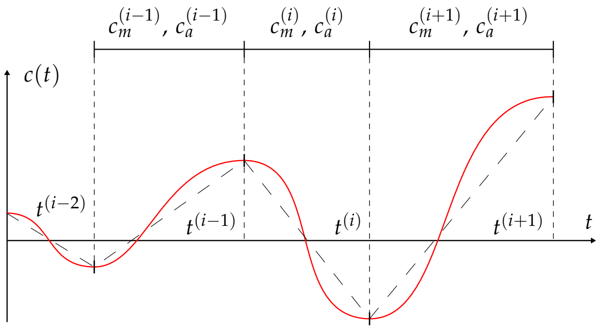

$$c_m^{(i)} = \frac{c(t^{(i-1)} + c(t^{(i)})}{2}, \qquad c_a^{(i)} = \frac{|c(t^{(i-1)} - c(t^{(i)})|}{2}$$

Fig. 1 Discretization of load history into combinations of mean and amplitude factors $c_m^{(i)}$ and $c_a^{(i)}$.

is given in Papuga (2011) and Papuga (2012), respectively. This implementation uses the signed von Mises method with Morrow mean stress correction as basis:

$$\sigma_{Nf}^{(e,i)} = \frac{c_a^{(i)}\,\sigma_{VM}^{(e)}\,\sigma_f}{\sigma_f - \operatorname{sgn}(c_m^{(i)}\,\sigma_h^{(e)})\,c_m^{(i)}\,\sigma_{VM}^{(e)}} \tag{2}$$

where $\sigma_{Nf}^{(e,i)}$ is the element equivalent stress amplitude causing fatigue failure, $\sigma_{VM}^{(e)}$ is the element von Mises stress, $\sigma_h^{(e)}$ is the element hydrostatic stress for element e, σ_f is the fatigue strength of the material, and $c_a^{(i)}$ and $c_m^{(i)}$ are scaling factors for amplitude and mean, respectively, at load combination i. The element von Mises stress is computed in terms of the stress vector components as:

$$\sigma_{VM} = \frac{1}{\sqrt{2}}\sqrt{\begin{array}{r}(\sigma_x-\sigma_y)^2+(\sigma_y-\sigma_z)^2+(\sigma_x-\sigma_z)^2\\ +6(\tau_{xy}^2+\tau_{yz}^2+\tau_{xz}^2)\end{array}} \tag{3}$$

The hydrostatic stress is the mean of the normal stress components:

$$\sigma_h = \frac{\sigma_x+\sigma_y+\sigma_z}{3} \tag{4}$$

The amount of reversals until failure is then determined from the SN-curve, approximated using Basquin's equation:

$$\sigma_{Nf}^{(e,i)} = \sigma_f\left(2N^{(e,i)}\right)^b \tag{5}$$

where $N^{(e,i)}$ is the element life time and b is the Basquin exponent. From this, the element damages $D^{(e)}$ are computed wrt. the imposed number of reversals $n^{(i)}$. To accumulate damage from multiple load combinations, the linear Palmgren-Miner rule is used:

$$D^{(e)} = \sum_{i=1}^{N_{lc}} \frac{n^{(i)}}{N^{(e,i)}} \leq D_{lim} \tag{6}$$

where N_{lc} is the number of load combinations. The damage fraction limit D_{lim} is defined based on the circumstances of the problem, e.g. for a very harsh environment, it should be set conservative. Here it is simply defined as $D_{lim}=1$, commonly used for many steel structures.

2.1.1 Damage Scaling

Solving a fatigue constrained optimization problem is tedious. The convergence is oscillatory due to the nonlinear expressions and the problem is likely to become highly infeasible during the optimization and may diverge as a consequence. To make the problem tractable Zhang et al. (2019) suggests scaling the damage using the Basquin factor b:

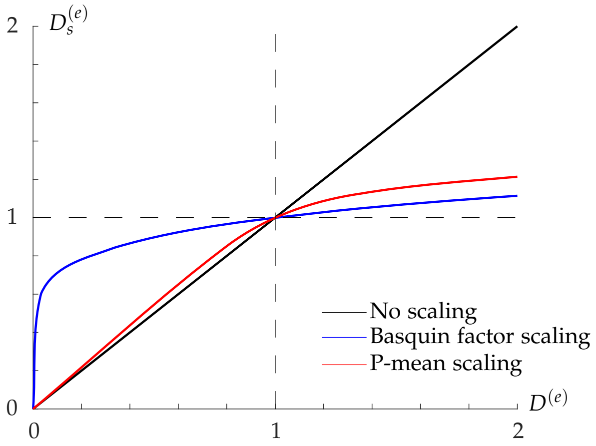

Fig. 2 Damage scaling functions. *No scaling* refers to the unscaled damage computed from the Palmgren-Miner expression of Eq. (6), *Basquin factor scaling* is Eq. (7) and *P-mean scaling* is Eq. (8) i.e. where $c_1=c_2$. The Basquin factor is $b=-0.156$, and $P=8$ is used for aggregation in the P-mean scaling.

$$D_s = \left(D^{(e)}\right)^b \tag{7}$$

However, this essentially changes the damage measure of the model for all element damages not equal to 1, see Fig. 2. The figure also illustrates why the Basquin factor scaling alleviates the nonlinearity in that after the damage becomes infeasible (i.e. >1) the scaled formulation restricts the variation between iterations stabilizing the measure. The Basquin factor scaled measure is conservative, which is good for realizing the design following optimization, however, as the goal is to minimize the volume as much as possible, a more accurate measure is desired. Specifically, it is desired to somehow combine the accuracy of the damage from the unscaled formulation with the stability and speed of the Basquin factor scaled formulation. This is achieved by using the P-norm mean formulation of the weighted sum, to aggregate these two formulations. The P-norm mean is chosen as it exactly represents the intersection of two functions. This implies that the aggregation is exact when the damage is 0 and 1, and increasingly accurate with increasing P elsewhere. The scaled damage is then computed as:

$$D_s^{(e)} = \left(\frac{c_1\left(D^{(e)}\right)^{bP} + c_2\left(D^{(e)}\right)^{-P}}{c_1+c_2}\right)^{-\frac{1}{P}} \tag{8}$$

where c_1 and c_2 are weighting functions. Considering Fig. 2 it is observed that close to the linear behavior is achieved, while also the drop-off at infeasibility is present preventing large variation in the measure.

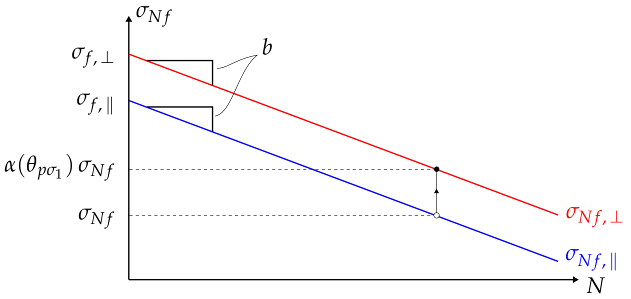

Fig. 3 SN curve interpolation of fatigue strengths varying due to orientation of applied load.

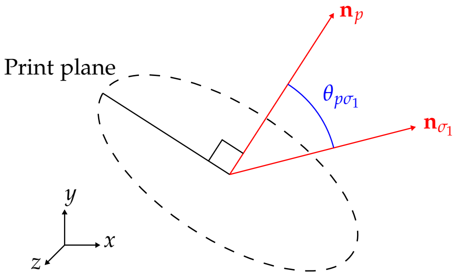

Fig. 4 Angle $\theta_{p\sigma_1}$ between print plane normal $\mathbf{n}_p$ and first principal stress direction $\mathbf{n}_{\sigma_1}$.

2.2 Modeling Anisotropy

The AM metals behavior will depend on the print orientation, as it governs the orientation of the imposed defects. In Basquin's approximation, if the exponent b can be assumed constant for all orientations of loading wrt. print orientation (which mostly agrees with published experimental data (Yadollahi et al., 2017)), the stress level will be proportional for all N:

$$\sigma_{Nf,\perp} \propto \sigma_{Nf,\parallel} \tag{9}$$

Here, $\perp$ indicates perpendicularity between a print plane normal and the load direction, and $\parallel$ indicates parallelity. With these proportional SN-curves, see Fig. 3, an interpolation is made for angles between $\perp$ and $\parallel$. If only the fatigue strength is affected by the orientation on the print plane, the proportionality is uniquely given by a factor α:

$$\sigma_{Nf,\perp} = \sigma_{f,\perp}(2N)^b = \alpha\sigma_{Nf,\parallel} = \alpha\sigma_{f,\parallel}(2N)^b$$
$$\Rightarrow \alpha = \frac{\sigma_{f,\perp}}{\sigma_{f,\parallel}} \tag{10}$$

Best utilization of the material is achieved in the direction where it has the highest fatigue strength, this direction should therefore be aligned with the direction of the critical load. The critical load is decided by considering fracture mechanics. Fatigue damage progression is characterized in two phases; crack initiation and crack propagation until complete failure. Defects in AM materials are slit-shaped and mostly small (though for as-built components may be as large as 1mm (Fatemi et al., 2020)), and may therefore be treated as cracks. However, their presence means that the crack initiation is effectively skipped. It is well established that cracks initiate along the plane of maximum shear (Fatemi et al., 2019; Stephens et al., 2001), but grows as a mode I crack normal to the maximum principal stress direction. By considering the mechanics of a mode I crack, if the component is oriented such that the major-axis of the slit-shaped defects is perpendicular to the principal direction, the effective stress on the crack is minimized. This is accomplished in the model by taking the print plane orientation (specifically the orientation of its normal) into account, by which an associated angle is defined, see Fig. 4. The strength interpolation variable α may therefore be expressed as:

$$\alpha(\theta_{p\sigma_1}) = 1 + \beta_p\,\frac{1+\cos 2\theta_{p\sigma_1}}{2}, \tag{11}$$
$$\text{where} \quad \beta_p = \frac{\sigma_{f,\perp}}{\sigma_{f,\parallel}} - 1$$

The expression of β_p is used as its value gives an intuitive measure for the degree of anisotropy, in particular $\beta_p = 0$ for isotropy. The angle $\theta_{p\sigma_1}$ is found from the dot product:

$$\theta_{p\sigma_1} = \cos^{-1}\frac{\mathbf{n}_p \cdot \mathbf{n}_{\sigma_1}}{|\mathbf{n}_p||\mathbf{n}_{\sigma_1}|} \tag{12}$$

where $\mathbf{n}_p$ is the print plane normal and $\mathbf{n}_{\sigma_1}$ is the principal direction of the maximum principal stress. The vectors are assumed normalized, such that their lengths are unity, and the expression is inserted into Eq. (11), where it is further rewritten using the equality:

$$\cos\left(2\cos^{-1}(\mathbf{n}_p \cdot \mathbf{n}_{\sigma_1})\right) = 2(\mathbf{n}_p \cdot \mathbf{n}_{\sigma_1})^2 - 1 \tag{13}$$

Reinserting results in the simple expression:

$$\alpha = 1 + \beta_p\,(\mathbf{n}_p \cdot \mathbf{n}_{\sigma_1})^2 \tag{14}$$

where the print plane normal $\mathbf{n}_p$ is defined for two dimensions as:

$$\mathbf{n}_p(\theta) = \begin{bmatrix}\cos\theta\\ \sin\theta\end{bmatrix} \tag{15}$$

For three dimensions it is defined using rotation matrices. In this case, the normal is assumed to be placed in the z-direction, whereby Bryan z-y-x transformation is effectively used as the initial z-rotation

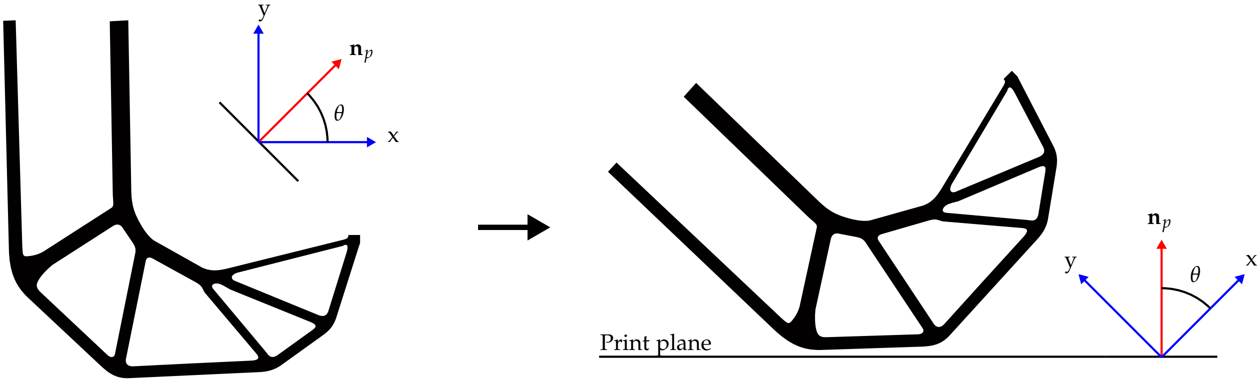

Fig. 5 Relation between orientations of the TO coordinate system (left) and the printing process (right). Printing starts with a horizontal slice of the lowest part of the geometry on the right and proceeds with slices in the direction of $\mathbf{n}_p$. Support structure is neglected here. The illustrated geometry is an optimized L-beam, see Section 5.

may be disregarded as it corresponds to a drilling rotation not affecting the placement of the plane:

$$\mathbf{n}_p(\boldsymbol{\theta}) = R_y\ (R_x\ \mathbf{z}) = \begin{bmatrix} \cos\theta_x \sin\theta_y \\ -\sin\theta_x \\ \cos\theta_x \cos\theta_y \end{bmatrix} \tag{16}$$

The angle(s) θ describing the print plane orientation may be defined before optimization, if the intent is to orient the component in a predetermined way, or they can be included in the optimization as design variables to find an optimized print plane orientation. The print plane normal is related to the geometry coordinate system and actual manufacturing print plane as illustrated in Figure 5.

2.3 Criterion Formulation

Having established that the defects propagate in the maximum tensile direction and by assuming that compressive stress does not contribute to the fatigue damage, the equivalent stress is computed from the maximum principal stress. Contributions from amplitude and mean stress are included through the Morrow correction expression as:

$$\sigma_{Nf} = \alpha\ \frac{c_a\ \sigma_1\ \sigma_{f,\perp}}{\sigma_{f,\perp} - c_m\ \sigma_1} \tag{17}$$

Including the anisotropy variable α in this expression increases the damaging stress proportional to the decrease in fatigue strength. For realizing a design optimized with this measure a stress constraint is required in the optimization as static failure due to compressive stress is not accounted for in criterion.

3 Topology Optimization Approach

The density-based approach to TO has been successfully applied for performing optimization of many different structural problems and is also used to solve the presented fatigue problem. For this reason, modeling is restricted to FE simulation of linear elasticity and static structures, and structural problems are discretized using linear quadrilateral or hexahedral elements. The governing state equation for this problem is:

$$\mathbf{K}(\boldsymbol{\rho})\mathbf{U} = \mathbf{F} \tag{18}$$

Here $\mathbf{K}$ is the global stiffness matrix, $\boldsymbol{\rho}$ is a vector of design variables, $\mathbf{U}$ is the global displacement vector and $\mathbf{F}$ is the load vector. The load is assumed independent of the design variables however this is not always the case, see e.g. Chen and Kikuchi (2001). The stiffness design variable dependence enters through the SIMP method used for density interpolation with stiffness penalization, performed here by the modified SIMP expression (Sigmund, 2007):

$$\bar{E} = E_{min} + \rho^p(E - E_{min}) \tag{19}$$

where $\bar{E}$ is the penalized material stiffness, E is the material stiffness, E_{min} is a small number introduced to prevent numerical issues when solving the FE problem, ρ is the density variable and p is the penalization factor. Stress relaxation is performed using the qp-approach (Bruggi, 2008) as:

$$\bar{\boldsymbol{\sigma}}^{(e)} = \left(\rho^{(e)}\right)^q\ \mathbf{E}^{(e)}\mathbf{B}^{(e)}\mathbf{u}^{(e)} \tag{20}$$

Here $\bar{\boldsymbol{\sigma}}^{(e)}$ is the relaxed element stress measure, $\mathbf{E}^{(e)}$ is the unpenalized material constitutive matrix, $\mathbf{B}^{(e)}$ is

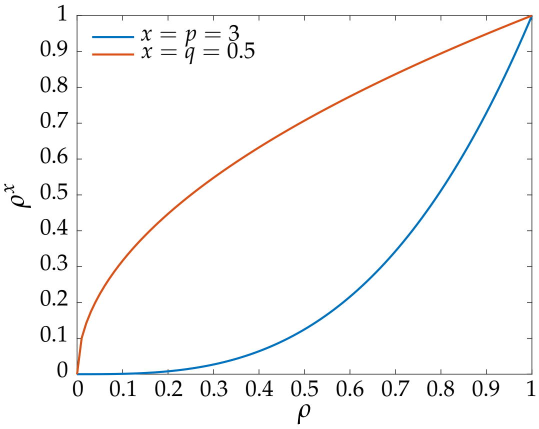

Fig. 6 Penalization and relaxation with commonly used exponents for stiffness and stress calculations.

the element strain-displacement matrix, $\mathbf{u}^{(e)}$ is the element displacement vector and q is the relaxation factor. Stress is always computed in the superconvergent Gauss integration point in the element center.

How the SIMP model penalizes and relaxes is illustrated in Fig. 6. The purpose is make intermediate density uneconomical, such that either void or solid density is favorable. In Bendsøe and Sigmund (1999) the micromechanical implications of SIMP stiffness penalization are investigated. Whereas the method beforehand was labeled as ”fictitious material interpolation”, the paper clarified that in many cases it actually falls within the framework of microstructurally-based models. In particular for materials with a Poisson’s ratio of $\nu = 0.3$ it was shown that $p \geq 3$ is appropriate for penalization of intermediate density stiffness as it falls within the Hashin-Strikmann bounds. The stress relaxation factor q is defined slightly differently to the introductory paper of the qp-method (Bruggi, 2008). It follows the definition in Oest and Lund (2017), such that the bounds are defined as $0 < q \leq 1$. In Bruggi (2008), the same measure is defined as $p - q$. Choosing $q < 1$ allows for further penalization of intermediate density, which makes the qp-method favored over the ε-method of Cheng and Guo (1997).

3.1 Regularization

Density filtering is used to regularize the illposed TO problem, with a two-fold purpose when using linear finite elements. Because of the inability of linear elements to model bending deformation correctly, the density in the optimized solution will be distributed in a checkerboard pattern (Díaz and Sigmund, 1995). This represents nonconvergence of the FE problem and is therefore not an optimized solution. Regularization may also be achieved by sensitivity filtering, where problem sensitivities are heuristically altered. Consistency between expressions before and after filtering is however lost, whereas the density filter is applied directly to the design variables and therefore included in all expressions. Sensitivity filtering is thus not considered further.

The density filter defines the filtered density $\tilde{\rho}$ as a weighted mean of surrounding densities:

$$\tilde{\rho}^{(j)} = \frac{\sum_{e=1}^{N_{elem}} H^{(j,e)}\, v^{(e)}\, \rho^{(e)}}{\sum_{e=1}^{N_{elem}} H^{(j,e)}\, v^{(e)}} \tag{21}$$

where $v^{(e)}$ are element volumes and $H^{(j,e)}$ is a linear weighting function defined as:

$$H^{(j,e)} = \max(0,\, R - |\mathbf{c}^{(j)} - \mathbf{c}^{(e)}|) \tag{22}$$

Here, R is a filter radius defining the set of elements included for averaging and $\mathbf{c}$ is the position of j^{th} and e^{th} element centers. The use of total number of elements N_{elem} implies looping over all elements in the model to check if they are within the filter radius of each filtered element. A more efficient formulation is to consider only elements in the neighborhood of the filtered element, though this requires an efficient identification scheme. The filtered density variables $\tilde{\rho}$ should replace the design variables ρ when solving the structural problem, computing sensitivities and visualization as these represent the physical structure with the design variables being restricted to optimization variables only (Sigmund, 2007).

For defining a minimum length scale the robust method as formulated by Wang et al. (2011) is implemented. As this formulation uses threshold projection of densities, increased discreteness of the design can also be attained. A continuous formulation of the threshold projection is presented by Wang et al. (2011) as:

$$\bar{\tilde{\rho}} = \frac{\tanh(\beta\eta) + \tanh(\beta(\tilde{\rho} - \eta))}{\tanh(\beta\eta) + \tanh(\beta(1 - \eta))} \tag{23}$$

where $\bar{\tilde{\rho}}$ is the threshold filtered density, η is the threshold value and β controls the sharpness of projection. Although the expression is not strictly equivalent to the original expression by Xu et al. (2010), a similar projection is attained and as $\beta \rightarrow \infty$ both expressions converge to the Heaviside step function. The robust designs are formulated by using the threshold filter for three different threshold values, i.e. $[\eta_e, \eta_i, \eta_d]$ which define eroded, intermediate and dilated designs, respectively. A FE problem is then solved and constraints are formulated for each design. Optimization may then be performed by considering only the worst case design. A minimum length scale is then guaranteed on the intermediate design, if the three designs have equivalent topology. In Qian and Sigmund (2013) an analytical expression for the imposed minimum length scale is derived from the erode threshold η_e:

$$\frac{l_e}{R} = \begin{cases} 2 - 2\sqrt{1-\eta_e}, & \eta_e \in [0.75, 1] \\ 2\sqrt{\eta_e - 1/2}, & \eta_e \in [0.5, 0.75] \end{cases} \tag{24}$$

where l_e is the minimum length scale.

Ideally, a projection filter should always be appended to the linear density filtered variables to remove intermediate densities, introduced as part of the density gradient resulting from the linear filter formulation, which do not have a physical interpretation. However, increasing the discreteness introduces a new problem in relation to stress-based optimization, namely stress singularities in jagged mesh boundaries. Because the optimized mesh layout is likely to contain stair-case like jagged edges, the sharp corners between elements will erroneously increase the stress of the structure. Solutions to the problem available in literature are stress extrapolation (Svärd, 2015) or allowing some gradient of density (da Silva et al., 2019). The latter is determined based on a simple expression for choosing the appropriate amount of discreteness in the filter. It is defined as:

$$\beta_{lim} = \frac{2R}{L^{(e)}} \tag{25}$$

This should be used together with numerical studies of relaxed stress behavior to ensure that the limit is low enough to avoid singularities. da Silva et al. (2019) developed the measure for use with the ε-method and suggest redoing the numerical study if implementation is made for the qp-method; similar results are therefore not expected here. Yet it provides a simple first estimate for the allowed discreteness, and implementations are therefore based on this measure.

A solution to poor surface definition (and often a required step for design verification with body-fitted mesh) is to apply some form of surface extraction and smoothing post-optimization. A method focusing on accurate treatment of density is presented here. The method revolves around interpolation of a surface at the element level based on information about nodal density values and design domain boundaries, such that boundary geometry is preserved. The method is described in detail in Appendix B, where Fig. 14 can be consulted for an overview.

3.2 Problem Formulation

The optimization problem is performed exclusively as volume V minimization subject to structural constraints $\mathbf{g}$. In standard formulation, the problem solved is:

$$\begin{aligned} \underset{(\boldsymbol{\rho})}{\text{minimize}} \quad & V(\boldsymbol{\rho}) \\ \text{subject to} \quad & \frac{g(\boldsymbol{\rho})}{g_{lim}} - 1 \leq 0 \\ & \boldsymbol{\rho} \in [\rho_{min}, 1] \end{aligned} \tag{26}$$

Here g is a constraint function and g_{lim} an associated limit. Multiple constraint function may be included in the case of the robust method or if including a stress constraint to ensure static structural integrity. A minimum of density ρ_{min} is necessary to avoid singular terms in the sensitivities as a consequence of the stiffness interpolation derivative (see Appendix A for the explicit expression). Formulation is done using the nested analysis and design (NAND) approach such that state equations of Eq. (18) are implicitly included in the structural constraint functions. Normally when the state variables are independent of the design variables the state equation has to be included as a constraint in the optimization problem, thereby solving the optimization problem and state problem simultaneously. However, as the state variables (in this case the displacements) are unique defined from a set of design variables, the two may be decoupled such that solution to the state equations is obtained before optimization - this is the NAND approach (Christensen and Klarbring, 2009).

The volume objective function is formulated as a sum of all element volumes v:

$$V = \sum_{e=1}^{N_{elem}} \rho^{(e)} v^{(e)} \tag{27}$$

To formulate the problem constraints, the local measures are aggregated using the P-norm scalarization function:

$$g_{\Psi} = \left(\sum_{e=1}^{N_{elem}} \left(g^{(e)} \right)^{P} \right)^{\frac{1}{P}} \tag{28}$$

Here g_{Ψ} represents the aggregated measure and P is an exponent governing how accurately the aggregation approximates the maximum function value. If using the P-norm expression alone a high value of P is required for accurate representation, increasing the nonlinearity of an already highly nonlinear problem, and thus increases the difficulty of achieving a solution. To solve this problem, the adaptive constraint scaling method is used (Le et al., 2010), where a factor c, computed based on iteration history data, is multiplied the aggregated measure. For damage, the factor is defined as:

$$c^{(k)} = \frac{\max\left(\boldsymbol{D}^{(k)}\right)}{g_{\Psi}^{(k)}} \tag{29}$$

for iterations $k = 1, 2$. For subsequent iterations, it is updated as:

$$c^{(k)} = \alpha^{(k)} \frac{\max\left(\boldsymbol{D}^{(k-1)}\right)}{g_{\Psi}^{(k-1)}} + (1 - \alpha^{(k)})\, c^{(k-1)} \tag{30}$$

Here, α is a damping parameter preventing the scaling factor from oscillating, $\boldsymbol{D}$ is a vector of all element damages and index k refers to iteration number. The use of the max operator in the expression implies the function becomes nondifferentiable. However, as the problem converges, the measure becomes better distributed in the design, and thus the maximum is better approximated by the P-norm function alone. The factor therefore converges along with the problem reducing the nondifferentiability. For implementational aspects, see Le et al. (2010). This implementation uses the same values for α as defined in Oest and Lund (2017).

Two fatigue constraints are defined: the anisotropic and an isotropic, using signed von Mises (Eq. (2)) for comparison. The isotropic fatigue constraint function is defined as:

$$g_D(\boldsymbol{\rho}) = c^{(k)}\, g_{\Psi}\left(\mathbf{D}_s\left(\boldsymbol{\sigma}_{Nf}(\boldsymbol{\rho})\right)\right) \tag{31}$$

where $\mathbf{D}_s$ is all element damages scaled according to P-mean scaling of Eq. (8) and $\boldsymbol{\sigma}_{Nf}$ is all signed von Mises equivalent stresses from Eq. (2). The signed von Mises is used despite it poorly capturing mean stress effects (Papuga, 2012), as it is simple and computationally efficient. Another criteria may be substituted for better accuracy.

The anisotropic fatigue constraint, including print plane orientation variables $\boldsymbol{\theta}$, becomes:

$$g_{D\alpha}(\boldsymbol{\rho}, \boldsymbol{\theta}) = c^{(k)}\, g_{\Psi}\left(\mathbf{D}_s\left(\boldsymbol{\sigma}_{Nf}(\boldsymbol{\alpha}(\boldsymbol{\rho}, \boldsymbol{\theta}), \boldsymbol{\rho})\right)\right) \tag{32}$$

where $\boldsymbol{\alpha}$ refers to all element fatigue strength interpolations from Eq. (14) and $\boldsymbol{\sigma}_{Nf}$ is equivalent stresses from Eq. (17).

Additionally, a constraint related to von Mises stress is introduced, primarily to restrict compressive stress. The constraint is defined by:

$$g_{\sigma}(\boldsymbol{\rho}) = c^{(k)}\, g_{\Psi}\left(\boldsymbol{\sigma}_{VM}(\boldsymbol{\rho})\right) \tag{33}$$

where $\boldsymbol{\sigma}_{VM}$ refers to Eq. (3). The adaptive constraint scaling factor $c^{(k)}$ is calculated for maximum stress here, rather than damage.

4 Design Sensitivity Analysis

The TO problem is efficiently solved using sensitivity-based optimization algorithms, presuming the sensitivities can be computed efficiently. This is achieved by analytical derivative expressions of the optimization functions. The individual explicit partial derivative terms that compose the sensitivity expression are derived in Appendix A.

4.1 Volume Function

The derivative of the volume function is the element volume multiplied the physical density derivative:

$$\frac{\mathrm{d}V}{\mathrm{d}\rho^{(j)}} = v^{(e)} \frac{\partial \bar{\rho}^{(e)}}{\partial \rho^{(j)}} \tag{34}$$

4.2 Fatigue Function

The sensitivity of the fatigue function is composed of the following derivatives:

$$\frac{\mathrm{d}D_{\Psi}}{\mathrm{d}\rho^{(e)}} = \frac{\partial D_{\Psi}}{\partial D^{(e)}} \frac{\partial D^{(e)}}{\partial \bar{\boldsymbol{\sigma}}^{(e)}} \frac{\partial \bar{\boldsymbol{\sigma}}^{(e)}}{\partial \rho^{(e)}} \tag{35}$$

Within this equation term are multiple function dependencies resulting in many partial derivatives. Furthermore, as the constraint is formulated using the NAND approach, the total derivative will contain derivatives of the state equation:

$$D = D(\boldsymbol{\rho}, \mathbf{U}(\boldsymbol{\rho})) \tag{36}$$

Direct differentiation of these will require solving an equation per design variable in the optimization. Due to the application of aggregation functions to scalarize the many local constraints, the adjoint method is the preferable choice for computing these derivatives as it involves solving an equation per constraint. The adjoint method entails defining an adjoint vector to be able to easily obtain a solution for derivatives of the state equation of Eq. (18). The state equation derivatives $\frac{\partial \mathbf{u}^{(e)}}{\partial \rho^{(e)}}$ enter through the stress partial derivative, which is:

$$\begin{aligned} \frac{\partial \bar{\boldsymbol{\sigma}}^{(e)}}{\partial \rho^{(e)}} &= q \left(\rho^{(e)}\right)^{q-1} \mathbf{E}\mathbf{B}^{(e)} \mathbf{u}^{(e)} \\ &\qquad - \left(\rho^{(e)}\right)^{q} \mathbf{E}\mathbf{B}^{(e)} \frac{\partial \mathbf{u}^{(e)}}{\partial \rho^{(e)}} \end{aligned} \tag{37}$$

The global version of the term, i.e. $\frac{\partial \mathbf{U}}{\partial \rho^{(e)}}$, is determined by differentiating the governing equation:

$$\mathbf{K}\frac{\partial \mathbf{U}}{\partial \rho^{(e)}} + \frac{\partial \mathbf{K}}{\partial \rho^{(e)}}\mathbf{U} = \frac{\partial \mathbf{F}}{\partial \rho^{(e)}} \tag{38}$$

In case of the load being design independent, the load vector derivative is zero, and the displacement derivative is thereby isolated as:

$$\frac{\partial \mathbf{U}}{\partial \rho^{(e)}} = \mathbf{K}^{-1}\left(-\frac{\partial \mathbf{K}}{\partial \rho^{(e)}}\mathbf{U}\right) \tag{39}$$

which is inserted into Eq. (37). The adjoint vector is then defined as:

$$\boldsymbol{\lambda}^T = \left(\frac{\partial g}{\partial \mathbf{U}}\right)\mathbf{K}^{-1} \tag{40}$$

where g is the considered function. The stiffness matrix is symmetric and as such Eq. (40) is transformed to the linear system:

$$\mathbf{K}\boldsymbol{\lambda} = \left(\frac{\partial g}{\partial \mathbf{U}}\right)^T \tag{41}$$

from which solutions can efficiently obtained for each function. Inserted into Eq. (35) yields:

$$\begin{aligned}\frac{\mathrm{d}D_\Psi}{\mathrm{d}\rho^{(e)}} = \frac{\partial D_\Psi}{\partial D^{(e)}}\frac{\partial D^{(e)}}{\partial \bar{\boldsymbol{\sigma}}^{(e)}} q\left(\rho^{(e)}\right)^{q-1}\mathbf{E}\mathbf{B}^{(e)}\mathbf{u}^{(e)} \\ - \boldsymbol{\lambda}_D^T\frac{\partial \mathbf{K}}{\partial \rho^{(e)}}\mathbf{U}\end{aligned} \tag{42}$$

Denoting $\boldsymbol{\lambda}_D$ as the adjoint vector of the damage function, which is computed by solving a set of linear equations (corresponding to Eq. (41)), with the following right hand side:

$$\begin{aligned}\mathbf{K}\boldsymbol{\lambda}_D = \left(\frac{\partial g_D}{\partial \mathbf{U}}\right)^T = \\ \left(\sum_{e=1}^{N_{elem}}\frac{\partial D_\Psi}{\partial D^{(e)}}\frac{\partial D^{(e)}}{\partial \bar{\boldsymbol{\sigma}}^{(e)}}\left(\rho^{(e)}\right)^q\mathbf{E}\mathbf{B}^{(e)}\mathbf{L}^{(e)}\right)^T\end{aligned} \tag{43}$$

where $\mathbf{L}^{(e)}$ is a bookkeeping matrix handling local-to-global transformation of the element strain-displacement matrices $\mathbf{B}^{(e)}$.

Considering the angle design variable, the expanded total derivative is:

$$\frac{\mathrm{d}D_\Psi}{\mathrm{d}\boldsymbol{\theta}} = \sum_{e=1}^{N_{elem}}\frac{\partial D_\Psi}{\partial D^{(e)}}\left(\sum_{i=1}^{N_{RF}}\frac{\partial D^{(e,i)}}{\partial N^{(e,i)}}\frac{\partial N^{(e,i)}}{\partial \bar{\sigma}_{Nf}^{(e,i)}}\frac{\partial \bar{\sigma}_{Nf}^{(e,i)}}{\partial \alpha}\frac{\partial \alpha}{\partial \mathbf{n}_p}\frac{\partial \mathbf{n}_p}{\partial \boldsymbol{\theta}}\right) \tag{44}$$

The computation of this is more straightforward as there is no implicit dependence of the state equations.

4.3 Stress Function

The sensitivity of the stress function is derived similarly to the fatigue function. It is composed of the following derivatives:

$$\frac{\mathrm{d}\bar{\sigma}_\Psi}{\mathrm{d}\rho^{(e)}} = \frac{\partial \bar{\sigma}_\Psi}{\partial \bar{\boldsymbol{\sigma}}^{(e)}}\frac{\partial \bar{\boldsymbol{\sigma}}^{(e)}}{\partial \rho^{(e)}} \tag{45}$$

The $\frac{\partial \bar{\boldsymbol{\sigma}}^{(e)}}{\partial \rho^{(e)}}$ term is the same as used in the fatigue expression, see Eq. (37). As a consequence the same steps are taken in defining the adjoint vector, which expression become:

$$\begin{aligned}\mathbf{K}\boldsymbol{\lambda}_\sigma = \left(\frac{\partial g_\sigma}{\partial \mathbf{U}}\right)^T = \\ \left(\sum_{e=1}^{N_{elem}}\frac{\partial \bar{\sigma}_\Psi}{\partial \bar{\boldsymbol{\sigma}}^{(e)}}\frac{\partial \bar{\boldsymbol{\sigma}}^{(e)}}{\partial \rho^{(e)}}\left(\rho^{(e)}\right)^q\mathbf{E}\mathbf{B}^{(e)}\mathbf{L}^{(e)}\right)^T\end{aligned} \tag{46}$$

Inserted, the stress sensitivity is:

$$\begin{aligned}\frac{\mathrm{d}\bar{\sigma}_\Psi}{\mathrm{d}\rho^{(e)}} = \frac{\partial \bar{\sigma}_\Psi}{\partial \bar{\boldsymbol{\sigma}}^{(e)}} q\left(\rho^{(e)}\right)^{q-1}\mathbf{E}\mathbf{B}^{(e)}\mathbf{u}^{(e)} \\ - \boldsymbol{\lambda}_\sigma^T\left(\frac{\partial \mathbf{K}}{\partial \rho^{(e)}}\mathbf{U}\right)\end{aligned} \tag{47}$$

5 Numerical Examples

This section presents implementation aspects regarding the presented problem. Examples are then demonstrated, which illustrate the implications of the developed models. Three optimization problems are defined for this purpose; $\mathbb{P}_1$: volume minimization subject to a fatigue constraint formulated using regular signed von Mises, $\mathbb{P}_2$: volume minimization subject to an anisotropic fatigue constraint and $\mathbb{P}_3$: volume minimization subject to an anisotropic fatigue constraint and a von Mises stress constraint. These are defined as:

$$\mathbb{P}_1 = \begin{cases}\min\limits_{(\boldsymbol{\rho})} & V(\boldsymbol{\rho}) \\ \text{s.t.} & g_D(\boldsymbol{\rho}) - 1 \leq 0 \\ & \boldsymbol{\rho} \in [\rho_{min}, 1]\end{cases} \tag{48}$$

$$\mathbb{P}_2 = \begin{cases}\min\limits_{(\boldsymbol{\rho})} & V(\boldsymbol{\rho}) \\ \text{s.t.} & g_{D\alpha}(\boldsymbol{\rho}, \boldsymbol{\theta}) - 1 \leq 0 \\ & \boldsymbol{\rho} \in [\rho_{min}, 1]\end{cases} \tag{49}$$

$$\mathbb{P}_3 = \begin{cases} \min\limits_{(\boldsymbol{\rho})} & V(\boldsymbol{\rho}) \\ \text{s.t.} & g_{D\alpha}(\boldsymbol{\rho},\boldsymbol{\theta}) - 1 \leq 0 \\ & \dfrac{g_\sigma(\boldsymbol{\rho})}{\sigma_{lim}} - 1 \leq 0 \\ & \boldsymbol{\rho} \in [\rho_{min}, 1] \end{cases} \tag{50}$$

5.1 Implementation

The optimization problems are solved using the Method of Moving Asymptotes (MMA) (Svanberg, 1987, 2007). In order to increase stability of the optimization, a small change is made to the settings for how the moving asymptotes are updated. The default increase and decrease factors are reduced to 1.05 and 0.65, respectively, as also done in Oest and Lund (2017). Besides the moving asymptotes, external move limits of 5% are applied to the design variables as well to further ensure stability.

The continuous density-based formulation of the optimization problem is non-convex, which when using sensitivity-based methods is likely to converge to a local optimum (Lund, 2018). Using initial high factors in the SIMP method enforces this, as the constraints increasingly restrict the design domain. This is especially evident in case of the stress relaxation, where the singular optima may be closed-off entirely by the constraints. To be able to find a good optimum continuation can be applied to the SIMP exponents by starting off with a small amount of penalization, such that the design space is more open in the beginning of the optimization and then gradually closed by increasing the exponents. This approach was used to be able to solve the large-scale problem in Aage et al. (2017), where the stiffness penalty factor is slowly increased from 1 to 3. An increase in solution time however follows by using continuation, as essentially the problem formulation is changed for each continuation step whereby convergence to a new optimum is required.

In this work, no continuation is applied to the stiffness and stress exponents, which are kept constant at $p = 3$ and $q = 0.75$ for all presented examples. Instead, application is made to β of the threshold filter, and to the scaling factors c_1 and c_2 of Eq. (8). The specific continuation strategy applied to the examples are described in detail for each problem.

The reason for applying continuation on β is not directly related to achieving a strong optimum. Threshold filtering should only increase discreteness of the design - not alter the topology. However, the discrete formulation is nonlinear and immediate application using large values of β is likely to result in divergence. Preemptive application may also cause unintentional convergence to a local minimum. The optimization is therefore much more stable if keeping β low until a good minimum has been found, where after it can be increased by continuation. This however implies further increase on the solution time, especially if continuation is applied to the stiffness or stress exponents beforehand. To alleviate this Guest et al. (2011) proposes adjusting the initial MMA asymptote variables, initially setting them quite conservative. Although the concepts of the method seems promising, it is not adopted for this work, mainly since it does not work well with the robust method, as it forces the eroded and dilated designs to fully void and solid (depending on the starting density) immediately, where they may get stuck.

All designs assume all element densities are $\rho^{(0)} = 0.5$ as the starting guess. To measure the degree of black- and whiteness in the design a measure of nondiscreteness (Sigmund, 2007) is defined as:

$$M_{nd} = \frac{\sum\limits_{e=1}^{N_{elem}} 4\tilde{\rho}^{(e)}(1-\tilde{\rho}^{(e)})}{N_{elem}} \times 100\% \tag{51}$$

where $\tilde{\rho}$ is the physical density obtained by either linear density or projection filtering. The measure of nondiscreteness is defined to be 0% at a density value of 0 or 1 and 100% at a density value of 0.5, i.e. the most intermediate density possible.

5.2 L-beam Problem and Settings

The L-beam example is a commonly used benchmark problem for TO problems involving stress. Its reentrant sharp corner, see Fig. 7, is a notorious stress concentration site, which should be alleviated when exposed to an optimization with stress-based criteria. To avoid issues with violation of minimum length scale near the boundaries, the domain extension approach (Clausen and Andreassen, 2017) is applied, extending the domain in all directions (except at boundary condition locations). This method solves issues with filtering boundary conditions, where unmodified boundaries act as Neumann conditions, imposing an assumed symmetry in the filter. This in turn means that the minimum length scale would be halved at the boundaries.

A simple repeated load case is used to illustrate effects of fatigue, such that a reference load $P = 50$ kN is repeated for $n = 2 \times 10^6$ reversals at a single

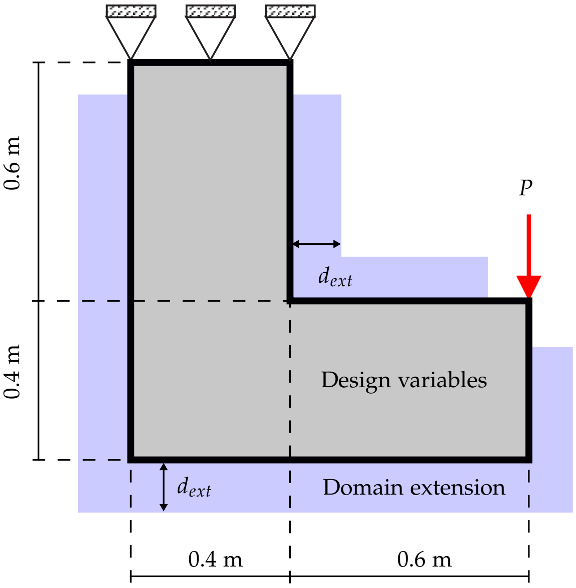

Fig. 7 Plane stress L-beam problem with domain extension. Plate thickness is 20 mm.

load combination of $c_m = c_a = 0.5$, corresponding to zero-based load history.

Material used is AISI 1020, i.e. characteristic values are $E = 203$ GPa and $\nu = 0.3$. Regarding fatigue behavior, the Basquin factor is $b = -0.156$ and best case fatigue strength is $\sigma_{f\perp} = 1384$ MPa. The anisotropic fatigue factor is assumed to be $\beta_p = 1$, such that fatigue strength is halved in the $\sigma_{f\|}$-case.

Filtering is restricted to a linear density filter of radius $R = 0.025$ m. This value is also used for domain extension, i.e. $d_{ext} = R$. The domain is discretized using 57,600 elements with design variables and 15,525 elements for domain extension.

5.3 Effects of Damage Scaling

To illustrate the importance of proper damage scaling in terms of accuracy and computational time required to converge, two examples are solved, using $\mathbb{P}_1$ and best case fatigue strength $\sigma_{f\perp}$. First, pure Basquin factor scaling (Eq. (7)) is used. This is then compared to results from a continuation approach to P-mean scaling (Eq. (8)), where c_1 is initially 1 and reduced by 0.2 every 50 iterations, starting at the 400th iteration, and $c_2 = 1 - c_1$. Results are illustrated in Fig. 8.

The pure Basquin factor scaling has fast and stable convergence, achieving 0.2174, but fails to use all available fatigue strength. Applying the P-mean scaling, convergence is equivalent until iteration 400, where the Basquin factor scaling is gradually changed to an unscaled formulation. This allows more accurate representation of damage and thus better distribution and lower volume fraction (0.2035).

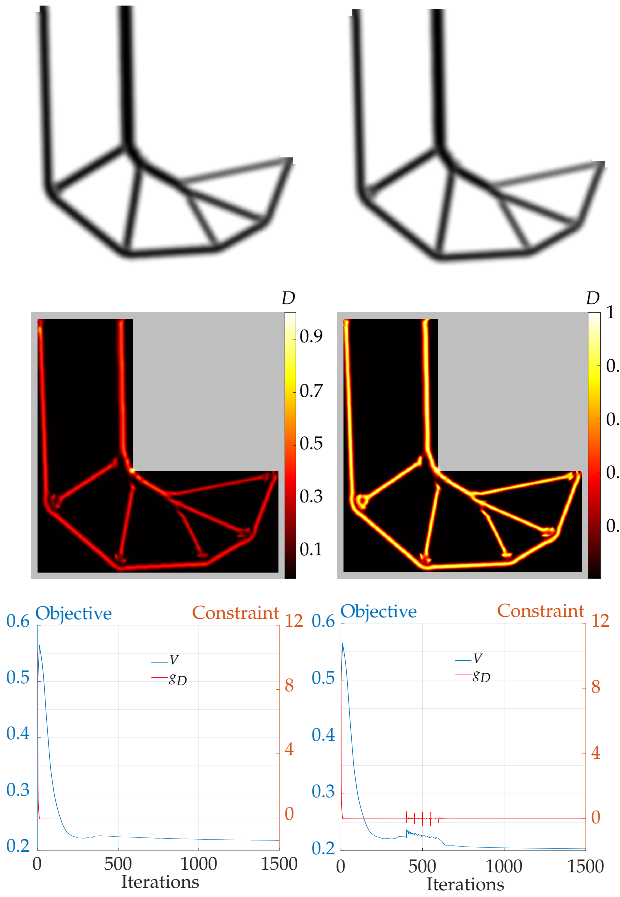

Fig. 8 Fatigue optimized designs of $\mathbb{P}_1$ achieved by Basquin factor scaling (left) and P-mean scaling (right). The continuation approach is observed in the convergence plot when the constraint function oscillates. Resultant volume fractions are 0.2174 (top) and 0.2035 (bottom).

5.4 Anisotropic Fatigue Optimization

Problem $\mathbb{P}_3$ is solved, setting $\sigma_{lim} = 262$ MPa. With the introduction of anisotropic fatigue, continuation of c_1 and $c_2 = 1 - c_1$ is delayed to start at the 550th iteration for stability. The starting guess for the angle design variable is $\theta^{(0)} = \pi/2$. Results are presented in Fig. 9.

The anisotropic fatigue criterion only considers the first principal stress and the damage distribution reflects this. Considering the geometry as a truss structure, where only uniaxial stress may be transferred in a structural member, the fully damaged section corresponds to first principal stress (tension) aligning with the axis of the local geometry and the second principal disappearing. For the undamaged section corre-

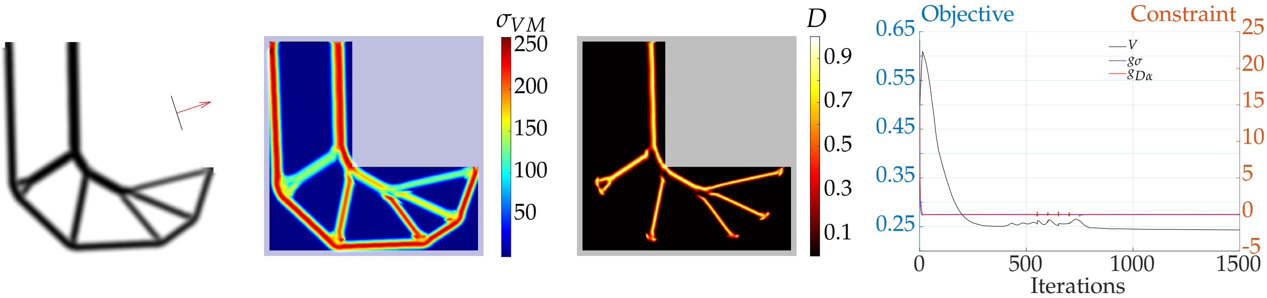

Fig. 9 Fatigue optimized designs of $\mathbb{P}_3$, with resultant volume fraction 0.2433 and optimized print plane normal angle $\theta = 0.3160$. The orientation is illustrated next to the design (left most figure).

sponds to the opposite, being primarily in compression.

The distribution of σ_{VM} illustrates the effect of the α parameter. Geometry aligning with the print plane normal are stressed the least, as expected, since the fatigue strength here should be close to $\sigma_{f\parallel}$. Similarly, geometry not aligning have higher stress, as the fatigue strength approaches $\sigma_{f\perp}$. A constant stress distribution is observed for the compressed section, since only the stress constraint is active here.

With the anisotropic fatigue model a volume fraction of 0.2433 is obtained. Had the anisotropic model not been available and an isotropic model (e.g. Eq. (2)) was used instead, worst case fatigue strength $\sigma_{f\parallel}$ should be used to ensure the design would not fail in fatigue, which would lead to higher volume.

5.5 3D L-Beam Problem

For the general 3D case, the geometry and loads of the L-beam are updated, see Fig. 10. The loads are defined as $P_y = P_z = 1350$ kN. Linear density filtering is used with at filter radius of 0.045 m, which size corresponds to a 3x3x3 filter. The considered problem $\mathbb{P}_2$ is solved using robust method for minimum length scale control. This is required for the surface interpolation, as it performs poorly for low density, single element thickness geometry. The threshold variables are defined as $[\eta_e, \eta_i, \eta_d] = [0.25, 0.5, 0.75]$ for the eroded, intermediate and dilated designs respectively. A continuation approach is applied to the discreteness variable β, starting at 1, and then at 400 iterations it doubles for each 150 iteration, ending with $\beta_{lim} = 16$ at 850 iterations. Starting guess for both angle design variables is $\boldsymbol{\theta} = -\pi/10$ q is kept constant at 0.75 for the first 100 iterations, then decreased to 0.5 to help further penalize intermediate density. The resulting intermediate design is illustrated with the optimized orientation of the print plane and convergence in Fig. 11.

A quite significant reduction in volume is achieved for every design due to the geometry being hollow.

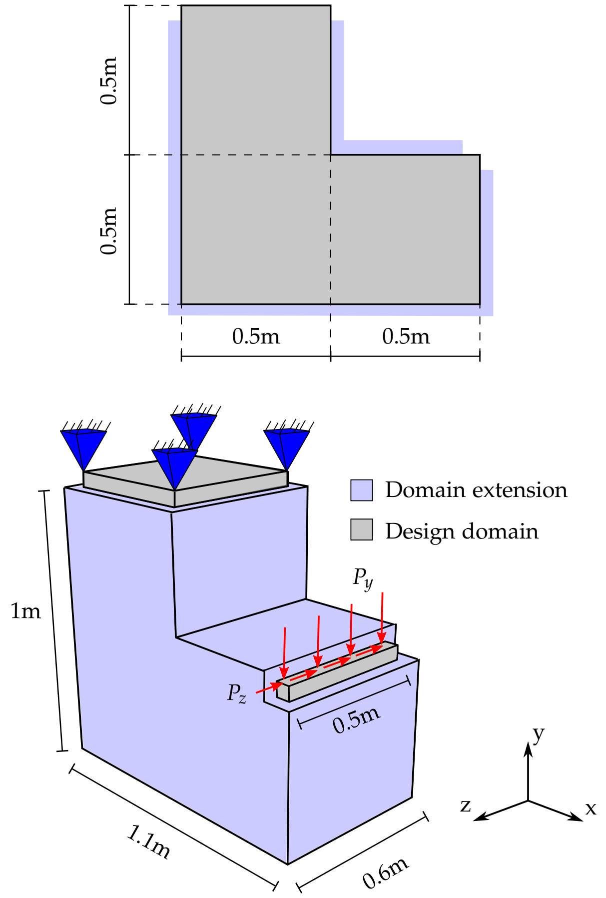

Fig. 10 Domain dimensions and boundary conditions for the three dimensional problem.

The resulting volume fraction is 0.286. This very well illustrates the potential of TO for these three-dimensional design, where placement of material is not at all intuitive. The design is highly discrete as a result of the penalization and threshold filtering through the robust method with $M_{nd} = 6.111\%$.

The damage distribution of each design is illustrated in Fig. 12. Only the erode design achieves a good distribution of damage. This is due to the increase in thickness of the solid phase of the interme-

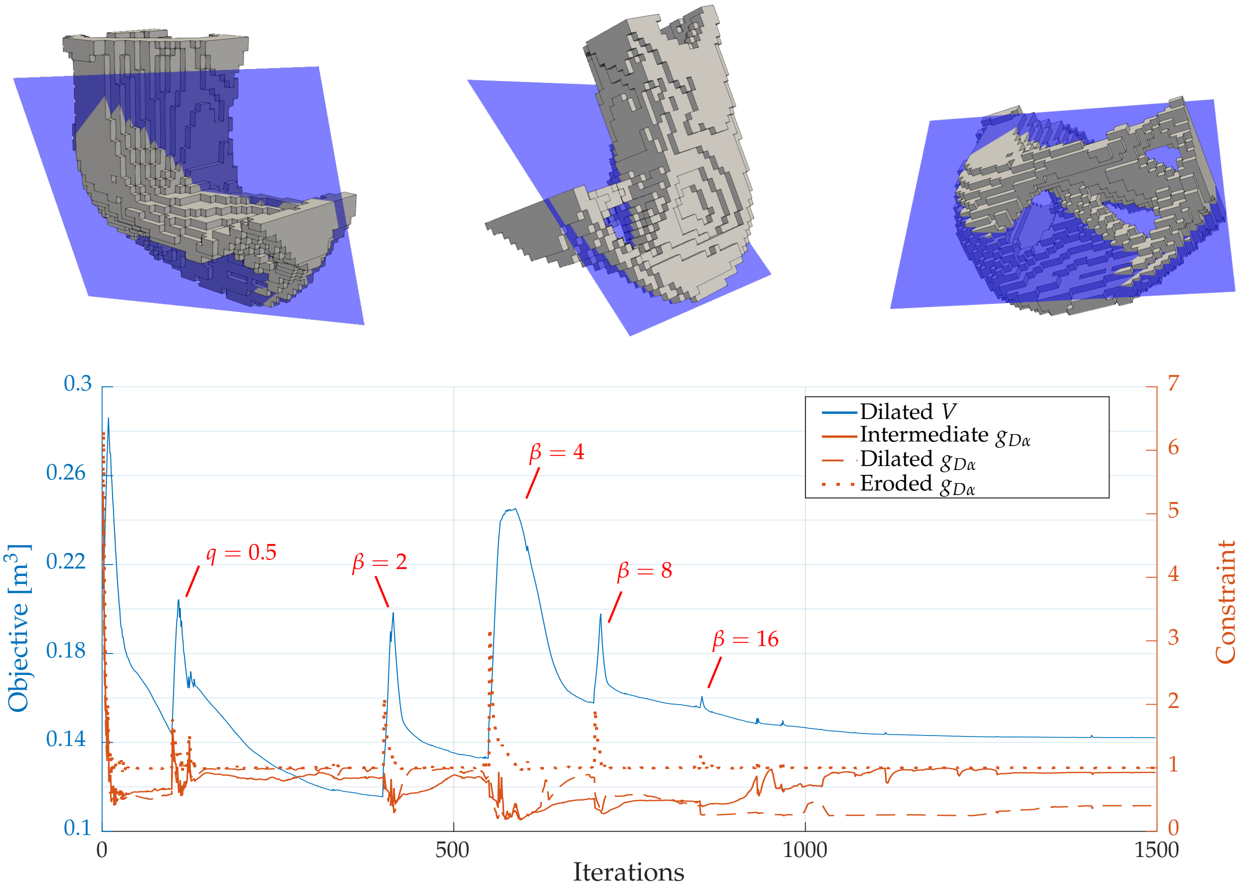

Fig. 11 Intermediate design, plotted for a cutoff density of $\tilde{\rho} = 0.5$, with illustration of the print plane orientation (top) and convergence plot (bottom). The optimized orientation of the print plane normal is found (in radians) as $[\theta_x, \theta_y]$ = [0.3313, 0.2935].

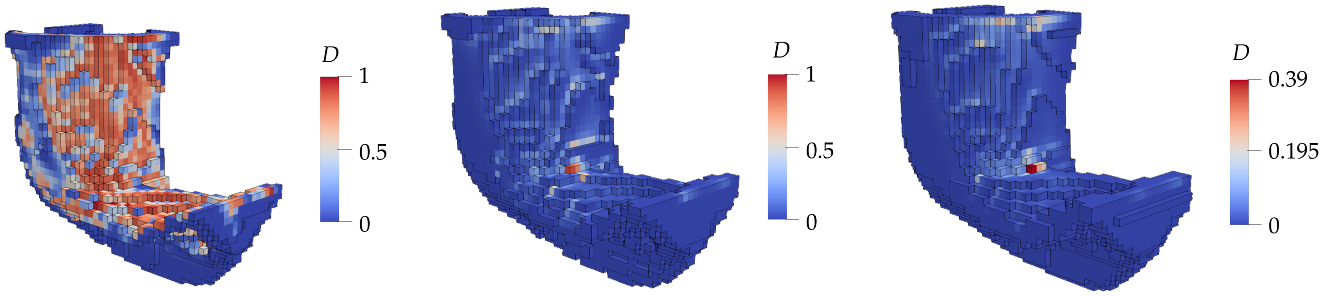

Fig. 12 Damage distribution in the erode (left), intermediate (middle) and dilate (right) designs. The highest damaged element in each design is 0.9999, 0.9011, and 0.3875, respectively.

diate and dilate designs. Damage depends exponentially on the stress, such that even small changes results in drastically different damage distribution. The highest damage of the intermediate and dilate designs is observed to appear very locally in the stress concentration area. This is caused by the discreteness imposed by the threshold filter, such that no density gradient remains around these elements, creating stress singularities. Due to the use of only maximum principal stress in the fatigue criterion formulation no damage is predicted in the part of the structure that is stressed in compression, see Fig. 13 for the stress plots.

Using the surface interpolation method described in Appendix B, a solid geometry is extracted for a cutoff value $\rho_{cut} = 0.5$. This geometry is then used to define a body fitted mesh with smoother surface representation and evaluated in ANSYS using 26,927 quadratic tetrahedral elements, with an average aspect ratio of 2.8785. Distribution of σ_1 and σ_3 for this

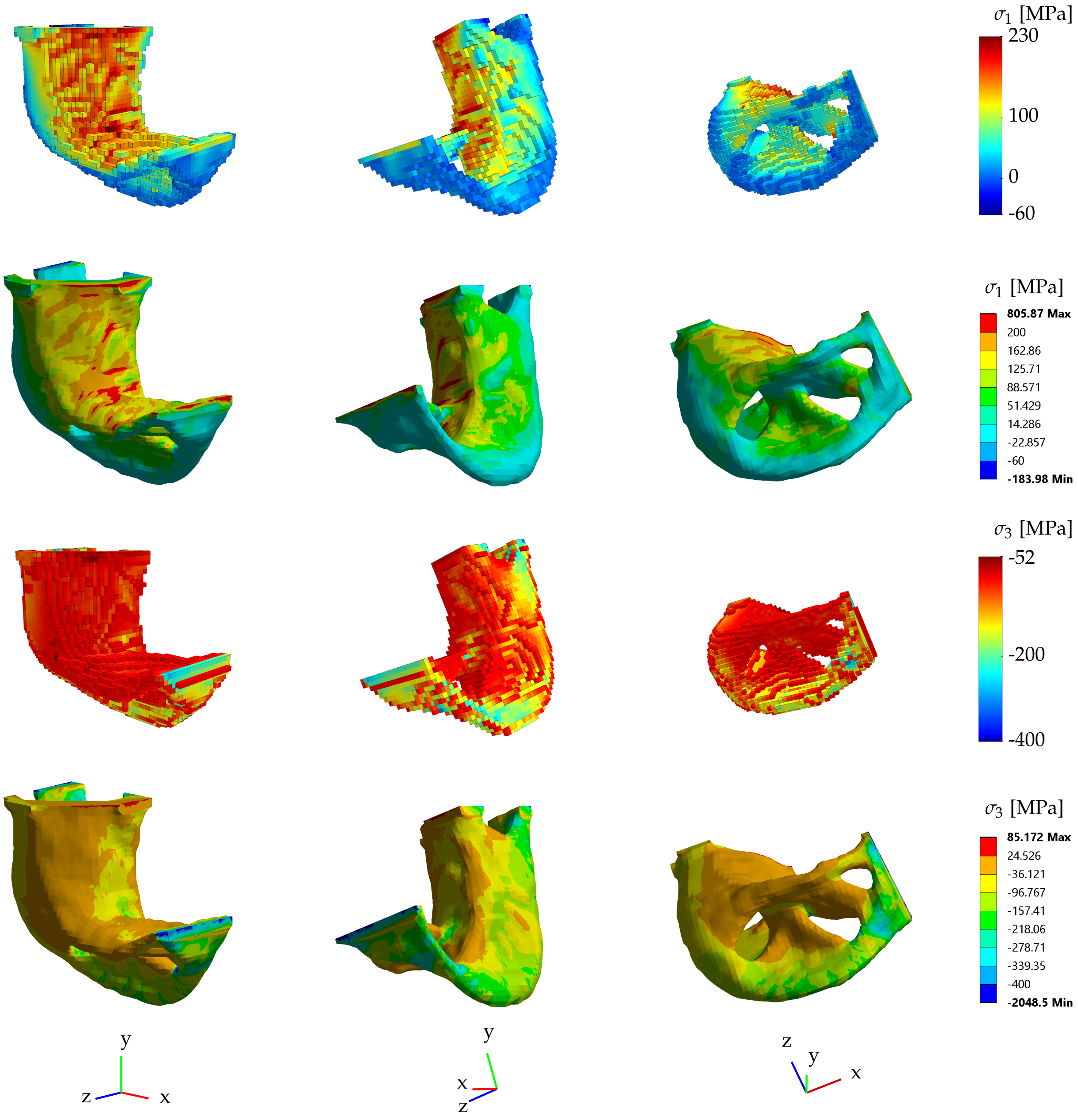

Fig. 13 Stress distribution of $\mathbb{P}_2$ for the intermediate design, illustrating both TO model and ANSYS result using a post processed body fitted mesh.

model are illustrated in Fig. 13 alongside the TO results. Stresses are very similar between the two models, even so far as minor stress concentrations occurring in consistent locations. A difference in the models is the accuracy of stress calculation leading to very high stresses around the fixed ANSYS geometry, which are not seen in the TO models.

6 Conclusion

In this work, a continuous anisotropic fatigue criterion focusing on additively manufactured (AM) metals has been formulated, which can be applied with the widely used density-based approach to solve fatigue topology optimization (TO) problems. The criterion assumes that the considered metals behave close to isotropic in stiffness and monotonic strength, such that anisotropy only occurs in fatigue strength, and is derived via an interpolation of SN-curves relating AM printing direction to directional fatigue strength. Analytic expressions of sensitivities are derived from the nested analysis and design problem, using the adjoint method.

Previous published works on fatigue constrained TO have struggled with achieving both fast and accurate convergence of the fatigue problem due to its inherent nonlinearity. In this work a scaling method is developed, which by the use of continuation is able to ensure efficient convergence, initially using a scaled measure and subsequently recovering the original damage formulation once convergence has been achieved.

For achieving manufacturing-ready designs from the TO, the state-of-the-art regularization methods have been considered, in particular the robust TO method, to impose a minimum length scale on the design. To make a non voxel-based 3D model, a novel smoothing method is presented which uses only existing information from the finite element density mesh.

Examples are finally shown, demonstrating the capabilities and implications of the presented methods. The generated designs have a good distribution of damage throughout the geometry and stable convergence as a result of the new scaling method. The 3D design is verified using commercial finite element software and shows good agreement with stress distributions in TO models.

A Sensitivity Terms

This appendix contains the partial derivatives used for computing the optimization function sensitivities.

First the damage sensitivity is considered. For reference, the full sensitivity is found in Eq. (35). By expansion of the aggregation damage term by the chain rule the following is achieved:

$$\frac{\partial g_\Psi}{\partial D^{(e)}} = \frac{\partial g_\Psi}{\partial D_s^{(e)}} \frac{\partial D_s^{(e)}}{\partial D^{(e)}} \tag{52}$$

The derivative of the P-norm function of Eq. (28) is:

$$\frac{\partial g_\Psi}{\partial g^{(e)}} = \left(\sum_{l=1}^{N_{elem}} \left(g^{(l)} \right)^P \right)^{\frac{1}{P}-1} \left(g^{(e)} \right)^{P-1} \tag{53}$$

where $g^{(e)} = D_s^{(e)}$ when using damage scaling. If Basquin factor scaling of Equation (7) is used, the derivative wrt. damage is found as:

$$\frac{\partial D_s^{(e)}}{\partial D^{(e)}} = -b \left(D^{(e)} \right)^{-b-1} \tag{54}$$

For the P-mean scaling, see Equation (8), the derivative is computed as:

$$\frac{\partial D_s^{(e)}}{\partial D^{(e)}} = \left(\frac{1}{c_1 + c_2} \right)^{-\frac{1}{P}} \times \frac{-b \left(c_1\, D^{(e)} \right)^{bP-1} + \left(c_2\, D^{(e)} \right)^{-P-1}}{\left(\left(c_1\, D^{(e)} \right)^{bP} + \left(c_2\, D^{(e)} \right)^{-P} \right)^{\frac{1}{P}+1}} \tag{55}$$

The element damage partial derivative term is expanded as follows:

$$\frac{\partial D^{(e)}}{\partial \bar{\boldsymbol{\sigma}}^{(e)}} = \sum_{i=1}^{N_{lc}} \frac{\partial D^{(e,i)}}{\partial N^{(e,i)}} \frac{\partial N^{(e,i)}}{\partial \bar{\sigma}_{Nf}^{(e,i)}} \frac{\partial \bar{\sigma}_{Nf}^{(e,i)}}{\partial \bar{\boldsymbol{\sigma}}^{(e)}} \tag{56}$$

The damage fraction of Eq. (6) differentiated wrt. number of reversals is:

$$\frac{\partial D^{(e,i)}}{\partial N^{(e,i)}} = -\frac{n^{(i)}}{\left(N^{(e,i)} \right)^2} \tag{57}$$

Number of reversals, computed through Basquin's approximation of Eq. (5), differentiated wrt. equivalent stress is:

$$\frac{\partial N^{(e,i)}}{\partial \bar{\sigma}_{Nf}^{(e,i)}} = \frac{1}{2\sigma_f\, b} \left(\frac{\bar{\sigma}_{Nf}^{(e,i)}}{\sigma_f} \right)^{\frac{1}{b}-1} \tag{58}$$

The stress derivative term of Eq. (56) is further expanded. For the anisotropic criterion of Eq. (17), it takes the form:

$$\frac{\partial \bar{\sigma}_{Nf}^{(e,i)}}{\partial \bar{\boldsymbol{\sigma}}^{(e)}} = \frac{\partial \sigma_{Nf}}{\partial \bar{\boldsymbol{\sigma}}} = \frac{\partial \sigma_{Nf}}{\partial \sigma_1} \frac{\partial \sigma_1}{\partial \bar{\boldsymbol{\sigma}}} + \frac{\partial \sigma_{Nf}}{\partial \alpha} \frac{\partial \alpha}{\partial \mathbf{n}_{\sigma_1}} \frac{\partial \mathbf{n}_{\sigma_1}}{\partial \bar{\boldsymbol{\sigma}}} \tag{59}$$

Here, the derivative of equivalent stress wrt. principal stress is:

$$\frac{\partial \sigma_{Nf}}{\partial \sigma_1} = \frac{c_a\ \alpha}{(1 - \frac{c_m}{S_f} \sigma_1)^2} \tag{60}$$

The derivative of the equivalent stress wrt. α is simply the Morrow correction:

$$\frac{\partial \sigma_{Nf}}{\partial \alpha} = \frac{c_a\ \sigma_1}{1 - \frac{c_m}{S_f} \sigma_1} \tag{61}$$

and the derivative of α wrt. the principal direction is:

$$\frac{\partial \alpha}{\partial \mathbf{n}_{\sigma_1}} = 2\beta_p \left(\mathbf{n}_p \cdot \mathbf{n}_{\sigma_1} \right) \mathbf{n}_p^T \tag{62}$$

Deriving the sensitivity terms of the anisotropic criterion involves finding analytical expressions of the stress eigenvalue and -vector derivatives. This is a nontrivial task and for completeness it is presented here. Following Nelson (1976) and further assuming that a stress matrix $\boldsymbol{\sigma}$ is real and symmetric, such its right and left eigenvectors are equal, the eigensystem is described as:

$$\boldsymbol{\sigma}\mathbf{n}_{\sigma} = \mathbf{n}_{\sigma}\boldsymbol{\lambda} \tag{63}$$

where $\mathbf{n}_{\sigma}$ is the eigenvector matrix and $\boldsymbol{\lambda}$ is a diagonal matrix containing the eigenvalues. Performing differentiation of the system of equations wrt. an entry of matrix $\boldsymbol{\sigma}$ and rewriting yields a system $\mathbf{F}_m$:

$$\mathbf{F}_m = (\boldsymbol{\sigma} - \lambda_m \boldsymbol{I})\,\frac{\partial \mathbf{n}_{\sigma_m}}{\partial \sigma_{pq}} = -\left(\frac{\partial \boldsymbol{\sigma}}{\partial \sigma_{pq}} - \frac{\partial \lambda_m}{\partial \sigma_{pq}}\boldsymbol{I}\right)\mathbf{n}_{\sigma_m} \tag{64}$$

where $\boldsymbol{I}$ is the identity matrix with size equal to $\boldsymbol{\sigma}$. The sensitivity of the eigenvalue is found by premultiplying the above expression with $\mathbf{n}^T_{\sigma_m}$. By considering Eq. (63) for a single eigenvalue and -vector:

$$\mathbf{n}^T_{\sigma_m}(\boldsymbol{\sigma} - \lambda_m \boldsymbol{I}) = \mathbf{0}^T \tag{65}$$

the left hand side of Eq. (64) become zero as $\mathbf{n}^T_{\sigma_m}\mathbf{n}_{\sigma_m}$ is the Kronecker delta, see Eq. (69). It then reduces to:

$$\frac{\partial \sigma^{(e)}_m}{\partial \sigma^{(e)}_{pq}} = \frac{\partial \lambda_m}{\partial \sigma_{pq}} = \mathbf{n}^T_{\sigma_m}\,\frac{\partial \boldsymbol{\sigma}}{\partial \sigma_{pq}}\,\mathbf{n}_{\sigma_m} \tag{66}$$

which is the eigenvalue sensitivity.

Assuming there are no repeated eigenvalues, it is observed from Eq. (64) that the sensitivity for each eigenvector may be uniquely determined as a linear combination of all eigenvectors as the eigenvectors form a linearly independent orthogonal basis:

$$\frac{\partial \mathbf{n}_{\sigma_m}}{\partial \sigma_{pq}} = \sum_{n \neq m} c_{mn}\,\mathbf{n}_{\sigma_n} \tag{67}$$

By substituting Eq. (67) into Eq. (64) and by premultiplying $\mathbf{x}^T_n$ an expression for the constants c_{mn} is determined:

$$c_{mn} = \frac{\mathbf{F}_m \cdot \mathbf{n}_{\sigma_n}}{\lambda_n - \lambda_m}, \qquad n \neq m \tag{68}$$

The equation in the presented formulation is simplified such that $\mathbf{x}_n$ is no longer transposed. As the eigenvectors form an orthonormal basis, the dot product yields:

$$\mathbf{n}_{\sigma_m} \cdot \mathbf{n}_{\sigma_n} = \begin{cases} 0, & m \neq n \\ 1, & m = n \end{cases} \tag{69}$$

which cancels out the eigenvalue derivative terms of Eq. (64). By insertion of the remainder of Eq. (64), the expression of c_{mn} is:

$$c_{mn} = \frac{\left(\frac{\partial \boldsymbol{\sigma}}{\partial \sigma_{pq}}\,\mathbf{n}_{\sigma_m}\right) \cdot \mathbf{n}_{\sigma_n}}{\lambda_m - \lambda_n}, \qquad n \neq m \tag{70}$$

Insertion into Eq. (67) yields the eigenvector sensitivity:

$$\frac{\partial \mathbf{n}^{(e)}_{\sigma_m}}{\partial \bar{\sigma}^{(e)}_{pq}} = \frac{\partial \mathbf{n}_{\sigma_m}}{\partial \bar{\sigma}_{pq}} = \sum_{n \neq m} \frac{\left(\frac{\partial \boldsymbol{\sigma}}{\partial \sigma_{pq}}\,\mathbf{n}_{\sigma_m}\right) \cdot \mathbf{n}_{\sigma_n}}{\sigma_m - \sigma_n}\,\mathbf{n}_{\sigma_n} \tag{71}$$

Thus, Eqs. (66) and (71) are used in Eq. (59).

For formulating the element stress measure, von Mises stress is used exclusively in this work. Expanding the stress derivative of Eq. (37) in terms of von Mises yields:

$$\frac{\mathrm{d}\bar{\sigma}_{\Psi}}{\mathrm{d}\rho^{(e)}} = \frac{\partial \bar{\sigma}_{\Psi}}{\partial \bar{\sigma}^{(e)}_{VM}}\,\frac{\partial \bar{\sigma}^{(e)}_{VM}}{\partial \bar{\boldsymbol{\sigma}}^{(e)}}\,\frac{\partial \bar{\boldsymbol{\sigma}}^{(e)}}{\partial \rho^{(e)}} \tag{72}$$

The derivatives of the von Mises stress of Eq. (3) wrt. the stress components are:

$$\frac{\partial \bar{\sigma}^{(e)}_{VM}}{\partial \bar{\sigma}^{(e)}_x} = \frac{1}{2\bar{\sigma}^{(e)}_{VM}}(2\,\bar{\sigma}^{(e)}_x - \bar{\sigma}^{(e)}_y - \bar{\sigma}^{(e)}_z) \tag{73}$$

$$\frac{\partial \bar{\sigma}^{(e)}_{VM}}{\partial \bar{\sigma}^{(e)}_y} = \frac{1}{2\bar{\sigma}^{(e)}_{VM}}(2\bar{\sigma}^{(e)}_y - \bar{\sigma}^{(e)}_x - \bar{\sigma}^{(e)}_z) \tag{74}$$

$$\frac{\partial \bar{\sigma}^{(e)}_{VM}}{\partial \bar{\sigma}^{(e)}_z} = \frac{1}{2\bar{\sigma}^{(e)}_{VM}}(2\bar{\sigma}^{(e)}_z - \bar{\sigma}^{(e)}_x - \bar{\sigma}^{(e)}_y) \tag{75}$$

$$\frac{\partial \bar{\sigma}^{(e)}_{VM}}{\partial \bar{\tau}^{(e)}_{xz}} = \frac{3}{\bar{\sigma}^{(e)}_{VM}}\bar{\tau}^{(e)}_{xz} \tag{76}$$

$$\frac{\partial \bar{\sigma}^{(e)}_{VM}}{\partial \bar{\tau}^{(e)}_{yz}} = \frac{3}{\bar{\sigma}^{(e)}_{VM}}\bar{\tau}^{(e)}_{yz} \tag{77}$$

$$\frac{\partial \bar{\sigma}^{(e)}_{VM}}{\partial \bar{\tau}^{(e)}_{xy}} = \frac{3}{\bar{\sigma}^{(e)}_{VM}}\bar{\tau}^{(e)}_{xy} \tag{78}$$

The partial derivative of the density filtered variable of Eq. (21) wrt. the design variable is:

$$\frac{\partial \tilde{\rho}^{(e)}}{\partial \rho^{(j)}} = \frac{H^{(j,e)}}{\sum\limits_{l=1}^{N_j} H^{(j,l)}} \tag{79}$$

where N_j is the set of elements enclosed by the filter. This derivative expression is independent of the design variables and does therefore not change through the optimization. It is therefore precomputed before starting the optimization. As sensitivities from all elements in N_j contribute to the filter sensitivity, computation of sensitivities which are not included in the optimization itself, in the case of using domain extension, is required.

Introducing a projection filter results in another term being added to the function derivative by the chain rule:

$$\frac{\partial f}{\partial \rho^{(j)}} = \sum_{e=1}^{N_j} \frac{\partial f}{\partial \bar{\tilde{\rho}}^{(e)}} \frac{\partial \bar{\tilde{\rho}}^{(e)}}{\partial \tilde{\rho}^{(e)}} \frac{\partial \tilde{\rho}^{(e)}}{\partial \rho^{(j)}} \tag{80}$$

Using the continuous approximation of the threshold filter, i.e. Equation (23), the intermediate derivative term is found as:

$$\frac{\partial \bar{\tilde{\rho}}^{(e)}}{\partial \tilde{\rho}^{(e)}} = \frac{\beta \operatorname{sech}^2(\beta(\tilde{\rho}^{(e)} - \eta))}{\tanh(\beta\eta) + \tanh(\beta(1-\eta))} \tag{81}$$

The derivative of the stiffness matrix is:

$$\frac{\partial \mathbf{k}^{(e)}}{\partial \rho^{(e)}} = \frac{\partial \bar{E}}{\partial \rho^{(e)}} \mathbf{k}_0^{(e)} \tag{82}$$

where $\mathbf{k}_0^{(e)}$ is the unit stiffness matrix. The partial derivative of the SIMP expression, appearing in the above equation, is:

$$\frac{\partial \bar{E}}{\partial \rho^{(e)}} = p \left(\tilde{\rho}^{(e)}\right)^{p-1} (E - E_{min}) \tag{83}$$

Note that the minimum stiffness term is removed leading to the minimum density requirement in order to avoid singularity problems when solving the state equation. Note that most partial derivatives from the expression have already been derived in the previous.

The partial derivative terms regarding the print plane orientation angle are now presented. For reference, the full derivative is given in Eq. (44). The derivative of α wrt. the normal vector is:

$$\frac{\partial \alpha}{\partial \mathbf{n}_p} = 2\beta_p \left(\mathbf{n}_p \cdot \mathbf{n}_{\sigma_1}\right) \mathbf{n}_{\sigma_1}^T \tag{84}$$

The direction vectors are then differentiated wrt. the angle design variable. For the two and three dimensional cases, the derivatives are respectively:

$$\frac{\partial \mathbf{n}_p}{\partial \theta} = \begin{bmatrix} -\sin\theta \\ \cos\theta \end{bmatrix} \tag{85}$$

and

$$\frac{\partial \mathbf{n}_p}{\partial \boldsymbol{\theta}} = \begin{bmatrix} -\sin\theta_x \sin\theta_y & \cos\theta_x \cos\theta_y \\ -\cos\theta_x & 0 \\ -\sin\theta_x \cos\theta_y & -\cos\theta_x \sin\theta_y \end{bmatrix} \tag{86}$$

B Post-optimization Density Interpolation

The interpolation scheme revolves around finding the surface of the entire structure on a per-element basis and is split into three steps:

1. **Global operations**
   Data of neighboring elements is collected, such that computations with a single element also considers surrounding element data - specifically this is finding nodal density values and element faces that lie on the outside of the design domain (these would be the outermost faces visible, including domain extension).
2. **Element interpolation**
   Using the above data, the density is interpolated and points are found which will eventually describe the surface. A density gradient vector is also determined. Isoparametric finite element expressions used are inspired by Cook et al. (2002).
3. **Surface description**
   Using the density gradient as an approximate surface normal, the points are sorted and used to generate a surface.

An illustrated overview of element interpolation and surface description is presented in Fig. 14.

Nodal density is found by simple nodal averaging:

$$\rho_n^{(n)} = \frac{1}{N^{(n)}} \sum_{e \in S^{(n)}} \rho^{(e)} \tag{87}$$

where $\rho_n^{(n)}$ and $\rho^{(e)}$ are nodal and element densities, respectively, $N^{(n)}$ is the total number of elements connected to node n and $S^{(n)}$ is the set of elements connected to the node. Note that no calculations for the density interpolation use element density.

Outer faces of the domain are found by comparison of global node numbers - if faces of different elements share all nodes, then neither is an outer face. In explicit terms, this is done by a series of loops, see the pseudo code of Algorithm 1.

Once nodal densities and outer element faces are found, individual elements are considered. Three things must be found to determine a surface:

- points $\mathbf{v}_i$ along element edges
- a center point $\mathbf{v}_0$
- an approximate normal $\mathbf{n}$ to the surface, pointing away from the inferred solid

A surface constructed from these is illustrated in Fig. 15. The element is considered in its natural coordinates, rather than global Cartesian coordinates, such that a point $\mathbf{v}$ is given by:

$$\mathbf{v} = \left[\xi \ \eta \ \zeta\right] \qquad \text{where} \qquad -1 \leq \{\xi,\ \eta,\ \zeta\} \leq 1 \tag{88}$$

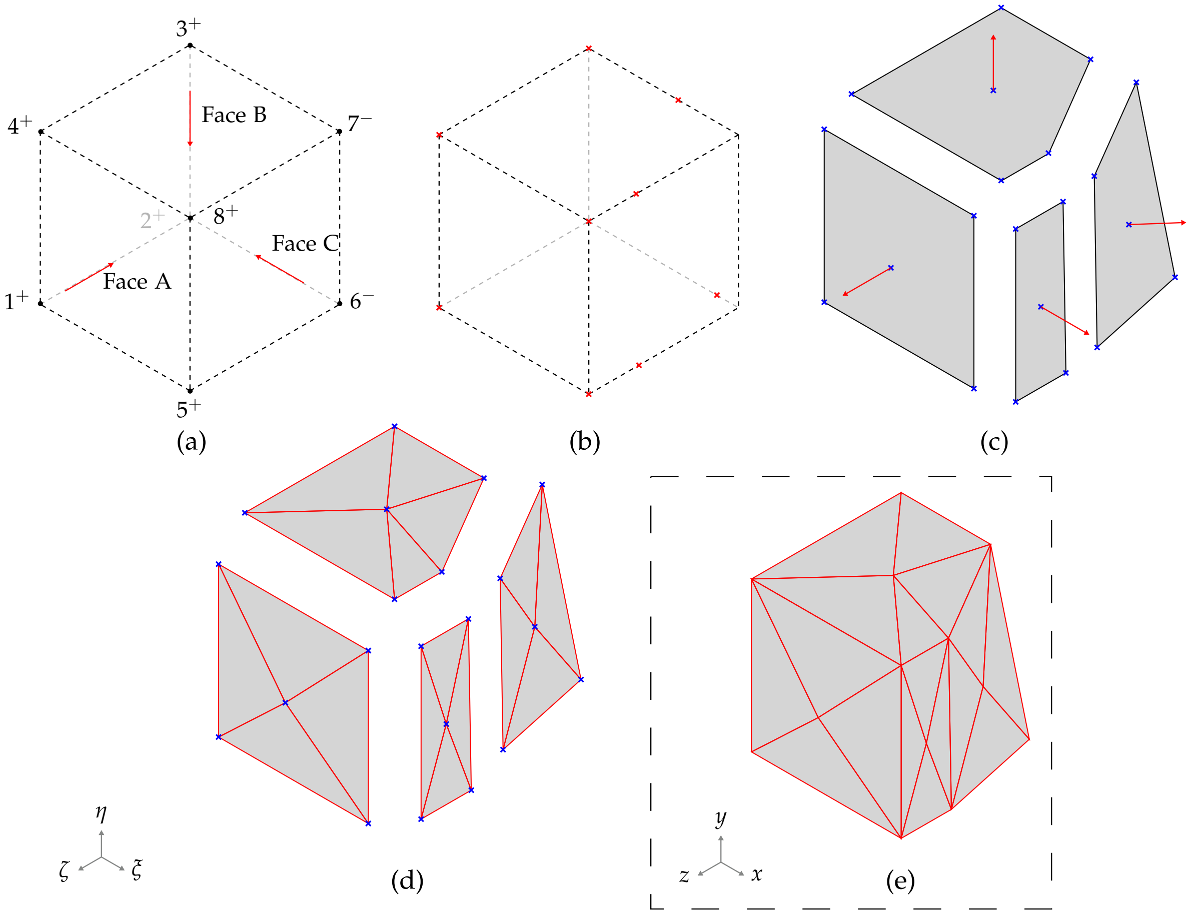

Fig. 14 Overview of element interpolation and surface description. (a): For an element it is found that all nodal densities are above the cutoff value except 6 and 7, and that faces A (nodes 1,5,8,4), B (nodes 3,4,8,7) and C (nodes 5,6,7,8) are outside faces. (b): It is determined that the surface consists of nodes 1,3,4,5,8 and interpolated points on edges between nodes (3,7), (6,8), (7,8), and (5,6). (c): Individual faces and the element intersection are considered; center points and approximate normals are calculated. (d): Using the center point and normals, non-overlapping triangular facets are found. (e): The facets are transformed from natural to Cartesian coordinates, normals are recalculated and the data is written to an .STL file. Process is repeated for all elements.

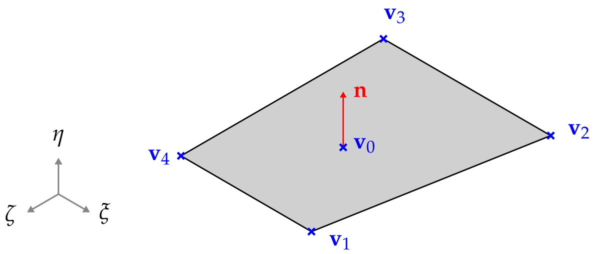

Fig. 15 Information required to describe a surface: center point $\mathbf{v}_0$, corner points $\mathbf{v}_i$, and a surface normal $\mathbf{n}$.

By doing this, elements can be considered as voxels and then generalized to an arbitrary distortion - or even collapsed into a tetrahedral element, if some additional bookkeeping is done. This means that the method is general for any linear solid element mesh.

The interpolated surface is found by locating points corresponding to a cutoff density value. To simplify consistency with neighbouring elements, corner points $\mathbf{v}_i$ are found exclusively along the edges of an element, such that only the nodal densities which are shared between elements are needed. The points that do not coincide with an element node are found by interpolating along the element edge:

$$\mathbf{v}_i = \begin{bmatrix} \frac{\rho_{nb}-\rho_{cut}}{\rho_{nb}-\rho_{na}} & \frac{\rho_{cut}-\rho_{na}}{\rho_{nb}-\rho_{na}} \end{bmatrix} \begin{bmatrix} \mathbf{c}_a \\ \mathbf{c}_b \end{bmatrix}, \quad \rho_{na} < \rho_{cut} < \rho_{nb} \tag{89}$$

where ρ_{na} and ρ_{nb} are nodal densities and $\mathbf{c}_a$ and $\mathbf{c}_b$ are nodal coordinates, with subscripts a and b indicating the node at either end of the edge. The center point is found as a mean coordinate of $\mathbf{v}_i$:

$$\mathbf{v}_0 = \frac{1}{N_v} \sum_{i=1}^{N_v} \mathbf{v}_i \tag{90}$$

where N_v is the number of corner points.

The entire element is not considered at once, but as element faces first, followed by the element interior.

Algorithm 1: Determination of outer faces.

```
Data: Nodal numbers $n$, element numbers $e$, local node
      numbers belonging to face $f$
Result: Boolean matrix $\mathbf{O}$ containing state of all
        element faces, with True for outer faces, False
        for inner.
Initialization;
$\mathbf{O} = False$;
for $e_1 \leftarrow 1$ to $N_{elem}$ do
    for $e_2 \leftarrow 1$ to $N_{elem}$ do
        if $e_1 \neq e_2$ then
            for $f \in e_1$ do
                if $n(f) \notin n(e_2)$ then
                    $\mathbf{O}(e_1, f) = True$
                end if
            end for
        end if
    end for
end for
```

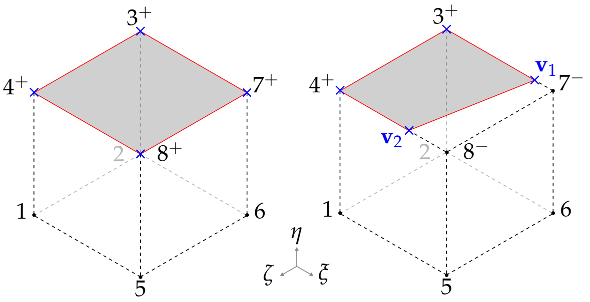

Fig. 16 An element where an outer face contains node numbers $\{3;4;7;8\}$. If all relevant nodal densities are above a cutoff, a full surface is generated (left). If only some are above cutoff, a partial surface is generated (right). Blue crosses indicate corners of the surface, which are the points that must determined. The superscript sign indicates whether the node density is above the cutoff (+) or below (-).

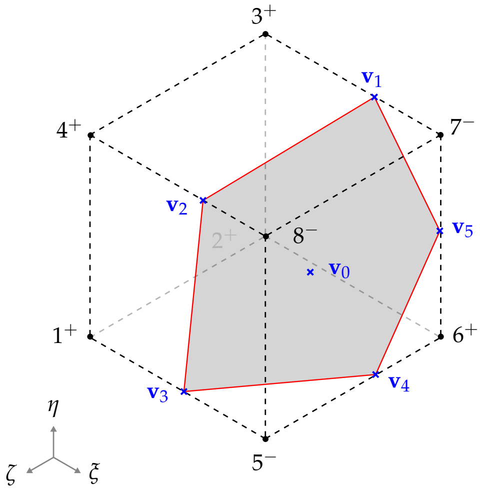

Fig. 17 Isoparametric element intersection.

Program-wise, this means considering 7 potential surfaces: 6 element faces and an interior intersection. By treating the element faces separately, it is possible to describe flat surfaces as required near boundary conditions, one of the things lost by naive smoothing. This also involves differences in computation of $\mathbf{v}_i$ and $\mathbf{n}$, elaborated in the following.

A surface must be generated on the element face, if two conditions are fulfilled: it is an outer face and at least one node has a nodal density $\rho_n^{(n)}$ higher than or equal to a chosen cutoff value ρ_{cut}. The number of nodes where $\rho_n^{(n)} \geq \rho_{cut}$ decides how the surface is made. If all nodes making up the given face are above the cutoff, the full face is the surface - otherwise, it is a partial surface, see Fig. 16.

Given that the isoparametric element is axis parallel in natural coordinates, the normal vector can be described as a positive or negative basis vector, e.g. for the surface in Fig. 16 the normal would be:

$$\mathbf{n} = \hat{\boldsymbol{\eta}} = \begin{bmatrix} 0 & 1 & 0 \end{bmatrix}^T \tag{91}$$

where $\hat{\boldsymbol{\eta}}$ is a coordinate basis vector.

The element interior is then considered. The element is intersected if nodal densities are to both sides of the cutoff value, i.e. if

$$\rho_{cut} \begin{cases} < \rho_n^{(n_1)} \\ > \rho_n^{(n_2)} \end{cases}, \qquad n_1 \cup n_2 = n \tag{92}$$

where n is the set of node numbers. Again, corner points are only found on element edges according to Eq. (89), however they are not restricted to a single element face, see Fig. 17.

The approximate normal is taken as the negative density gradient, such that the normal points away from the solid, as required:

$$\mathbf{n} = -\nabla\rho = -\mathbf{B}\ \boldsymbol{\rho}_n \tag{93}$$

where $\nabla\rho$ is the linear gradient vector, $\mathbf{B}$ is the first derivative of shape functions evaluated at the element center, and $\boldsymbol{\rho}_n$ is a vector containing all nodal densities.

The end result of the interpolation scheme is an .STL file, which provides a convenient way of describing a surface geometry. The surface is described as a set of triangular facets, each consisting of three vertices and a normal vector, see Fig. 18. The description of the individual facet must follow certain conventions:

- The normal must point outwards, away from the model.
- The normal must be unit length.
- All vertex coordinates must be positive.

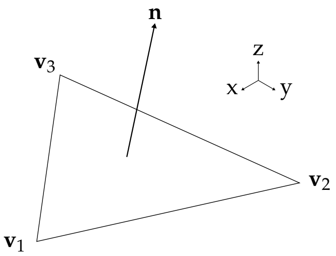

Fig. 18 Components of a single .STL facet.

- Vertex numbering must follow right hand rotation wrt. the normal.

The information needed for the .STL file is determined from that found in the previous section. Specifically, a group of points must be found to describe a surface of facets, with no overlaps. The local point coordinates are then transformed to global Cartesian coordinates and an exact normal is determined for each facet.

The grouping of points is done by considering the surface as a set of triangles/facets, all connected at the center point, see Fig. 19. The points needed to make each facet is found by a sorting algorithm, using the angles between vectors from $\mathbf{v}_0$ to $\mathbf{v}_i$.

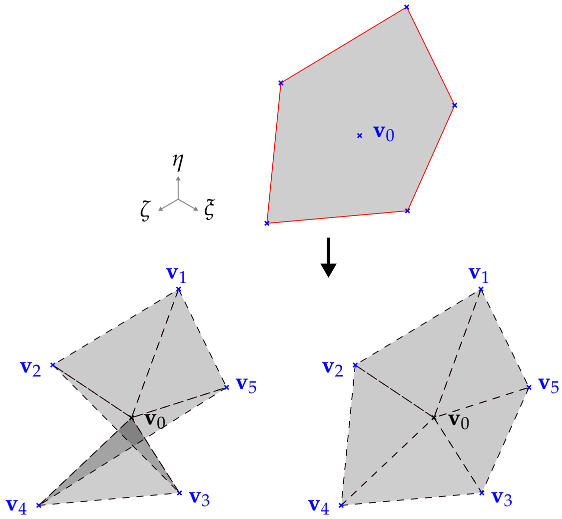

{1;2;3;4;5} {1;2;4;3;5}

Fig. 19 Order of corner points must be correct for facets to represent the surface completely and with no overlaps.

Because the points are rarely perfectly in a common plane, inconsistencies can occur in the angle calculation. The angle calculation and sorting are therefore done wrt. the approximate normal $\mathbf{n}$. First, vectors $\mathbf{r}_i$, lying in the plane to which $\mathbf{n}$ is normal, are found as the rejection from $\mathbf{n}$. The rejection vector is the complement to the vector $(\mathbf{v}_i - \mathbf{v}_0)$ projected onto $\mathbf{n}$, see Fig. 20, and is found as vector subtracted by projection:

$$\mathbf{r}_i = (\mathbf{v}_i - \mathbf{v}_0) - \frac{(\mathbf{v}_i - \mathbf{v}_0) \cdot \mathbf{n}}{\mathbf{n} \cdot \mathbf{n}} \mathbf{n} \tag{94}$$

As $\mathbf{r}_i$ are all in the same plane, the sum of angles between vectors is exactly 2π for a non-overlapping surface. A right-hand convention is then introduced when calculating the angles, see Fig. 20.

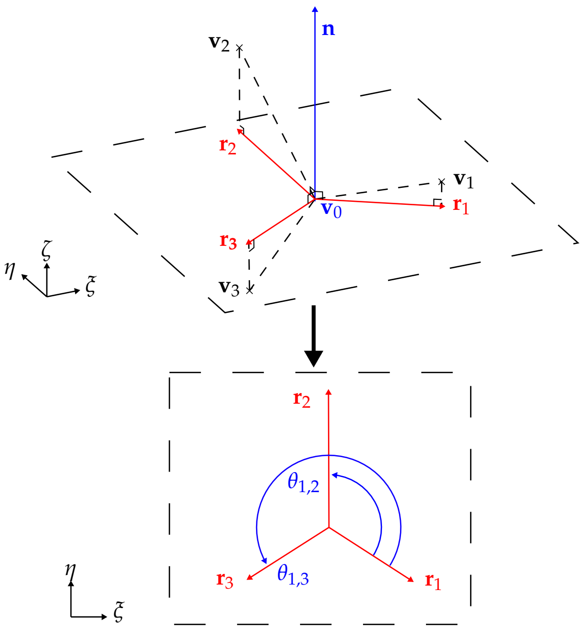

Fig. 20 *Top*: rejection vectors $\mathbf{r}_i$ all lie in a plane normal to $\mathbf{n}$. *Bottom*: Angles between vectors are calculated by right-hand rule wrt. $\mathbf{n}$, which is pointing outwards here.

The sorting is then done as follows:

- Select a vector $\mathbf{r}_i$.
- Calculate angle $\theta_{i,k} = \mathbf{r}_i \angle \mathbf{r}_k$ to all other $\mathbf{r}_k$.
- Select the vector that satisfies $(\mathbf{r}_i \times \mathbf{r}_k) \angle \mathbf{n} = 0$ and minimizes $\theta_{i,k}$
- Save the index k in a list and add angle $\theta_{k,i}$ and restart from vector $\mathbf{r}_k$, unless $\sum \theta = 2\pi$, then stop

When the sorting is complete, the list of indices is used to select and group the original points $\mathbf{v}_i$, such that a facet is always made up of vertices $\mathbf{v}_0$, $\mathbf{v}_{I(k)}$, and $\mathbf{v}_{I(k+1)}$, in that order as required by the .STL format.

The points are converted to Cartesian coordinates as:

$$\begin{bmatrix} x \; y \; z \end{bmatrix} = \mathbf{N}_{\mathbf{v}_i} \begin{bmatrix} \mathbf{x} \; \mathbf{y} \; \mathbf{z} \end{bmatrix} - \begin{bmatrix} x_{min} \; y_{min} \; z_{min} \end{bmatrix} \tag{95}$$

The vector of minimum values is subtracted to ensure that all coordinates are positive, again required in the STL format. Finally, the actual unit normal vector is found for each facet:

$$\mathbf{n} = \frac{\mathbf{v}_{I(k)} \times \mathbf{v}_{I(k+1)}}{\left|\mathbf{v}_{I(k)} \times \mathbf{v}_{I(k+1)}\right|} \tag{96}$$

Note that due to the sorting using a strict right-hand rule, the direction of the normal is preserved, i.e. it points away from the solid material.

References

Aage N, Lazarov BS (2013) Parallel framework for topology optimization using the method of moving asymptotes. Structural and Multidisciplinary Optimization 47:493–505

Aage N, Andreassen E, Lazarov BS (2015) Topology optimization using PETSc: An easy-to-use, fully parallel, open source topology optimization framework. Structural and Multidisciplinary Optimization 51:565–572

Aage N, Andreassen E, Lazarov BS, Sigmund O (2017) Giga-voxel computational morphogenesis for structural design. Nature 550:84–94

Allaire G, Jouve F, Toader AM (2002) A level-set method for shape optimization. Numerical Analysis 334:1125–1130

Allaire G, Jouve F, Toader AM (2004) Structural optimization using sensitivity analysis and a level-set method. Journal of Computational Physics 194:363–393

Bag A, Delbergue D, Ajaja J, Bocher P, Lévesque M, Brochu M (2020) Effect of different shot peening conditions on the fatigue life of 300 M steel submitted to high stress amplitudes. International Journal of Fatigue 130

Bendsøe M, Sigmund O (2003) Topology Optimization - Theory, Methods and Applications. Springer

Bendsøe MP (1989) Optimal shape design as a material distribution problem. Structural Optimization 1:193–202

Bendsøe MP, Kikuchi N (1988) Generating Optimal Topologies in Structural Design Using a Homogenization Method. Computer Methods in Applied Mechanics and Engineering 71:197–224

Bendsøe MP, Sigmund O (1999) Material interpolation schemes in topology optimization. Archive of Applied Mechanics 69:635–654

Bourdin B (2001) Filters in topology optimization. International Journal for Numerical Methods in Engineering 50:2143–2158

Bruggi M (2008) On an alternative approach to stress constraints relaxation in topology optimization. Structural and Multidisciplinary Optimization 36:125–141

Bruns TE, Tortorelli DA (2001) Topology optimization of non-linear elastic structures and compliant mechanisms. Computer Methods in Applied Mechanics and Engineering 191:3443–3459

Chen BC, Kikuchi N (2001) Topology optimization with design-dependent loads. Finite Elements in Analysis and Design 37:57–70

Cheng GD, Guo X (1997) ε-relaxed approach in structural topology optimization. Structural Optimization 13:258–266

Cheng KT, Olhoff N (1981) An investigation concerning optimal design of solid elastic plates. International Journal of Solids and Structures 17(3):305–323

Christensen PW, Klarbring A (2009) An Introduction to Structural Optimization. ISBN 978-1-4020-8665-6, Springer

Clausen A (2016) Topology Optimization for Additive Manufacturing. Ph.d. Thesis

Clausen A, Andreassen E (2017) On filter boundary conditions in topology optimization. Structural and Multidisciplinary Optimization 56:1147–1155

Cook RD, Malkus DS, Plesha ME, Witt RJ (2002) Concepts and Applications of Finite Element Analysis, 4th edn. ISBN: 978-0-471-35605-9, John Wiley & Sons

Duysinx P, Bendsøe MP (1998) Topology Optimization of Continuum Structures with Local Stress Constraints. International Journal for Numerical Methods in Engineering 43:1453–1478

Duysinx P, Sigmund O (1998) New developments in handling stress constraints in optimal material distribution. American Institute of Aeronautics and Astronautics 98(4906):1–9

Díaz A, Sigmund O (1995) Checkerboard patterns in layout optimization. Structural Optimization 10:40–45

Fatemi A, Molaei R, Phan N (2019) Multiaxial Fatigue of Additive Manufactured Metals. MATEC Web of Conferences 300, DOI 10.1051/matecconf/201930001003

Fatemi A, Molaei R, Phan N (2020) Multiaxial fatigue of additive manufactured metals: Performance, analysis, and applications. International Journal of Fatigue 134:1911–1919

Guest JK, Prévost JH, Belytschko T (2004) Achieving minimum length scale in topology optimization using nodal design variables and projection functions. International Journal for Numerical Methods in Engineering 61:238–254

Guest JK, Asadpoure A, Ha SH (2011) Eliminating beta-continuation from heaviside projection and density filter algorithms. Structural and Multidisciplinary Optimization 44:443–453

Hackel L, Rankin JR, Rubenchik A, King WE, Matthews M (2018) Laser peening: A tool for additive manufacturing post-processing. Additive Manufacturing 24:67–75

Haftka RT, Grandhi RV (1986) Structural shape optimization - a survey. Computer Methods in Applied Mechanics and Engineering 57:91–106

Holmberg E, Torstenfelt B, Klarbring A (2014) Fatigue constrained topology optimization. Structural and Multidisciplinary Optimization 50:207–219

Jeong SH, Choi DH, Yoon GH (2015) Fatigue and static failure considerations using a topology optimization method. Applied Mathematical Modelling 39:1137–1162

Kawamoto A, Matsumori T, Yamasaki S, Nomura T, Kondoh T, Nishiwaki S (2011) Heaviside projection based topology optimization by a pde-filtered scalar function. Structural and Multidisciplinary Optimization 44:19–24

Kirsch U (1990) On singular topologies in optimum structural design. Structural Optimization 2:133–142

Langelaar M (2016) Topology optimization of 3D self-supporting structures for additive manufacturing. Additive Manufacturing 12:60–70

Langelaar M (2019) Integrated component-support topology optimization for additive manufacturing with post-machining. Rapid Prototyping Journal 25(2):255–265

Lazarov BS, Sigmund O (2011) Filters in topology optimization based on Helmholtz-type differential equations. Computer Methods in Applied Mechanics and Engineering 86:765–781

Lazarov BS, Wang F (2017) Maximum length scale in density based topology optimization. Computer Methods in Applied Mechanics and Engineering 318:826–844

Le C, Norato J, Bruns T, Ha C, Tortorelli D (2010) Stress-based topology optimization for continua. Structural and Multidisciplinary Optimization 41:605–620

Leuders S, Lieneke T, Lammers S, Tröster T, Niendorf T (2014) On the fatigue properties of metals manufactured by selective laser melting – the role of ductility. Journal of Materials Research 29(17):1911–1919

Lund E (1994) Finite Element Based Design Sensitivity Analysis and Optimization. Ph.d. Dissertation

Lund E (2018) Discrete Material and Thickness Optimization of laminated composite structures including failure criteria. Structural and Multidisciplinary Optimization 57:2357–2375

Nelson RB (1976) Simplified Calculation of Eigenvector Derivatives. AIAA Journal 14(9):1201–1205

Oest J, Lund E (2017) Topology optimization with finite-life fatigue constraints. Structural and Multidisciplinary Optimization 56(5):1045–1059

Papuga J (2011) A survey on evaluating the fatigue limit under multiaxial loading. International Journal of Fatigue 33:153–165

Papuga J (2012) Evaluation of uniaxial fatigue criteria applied to multiaxially loaded unnotched samples. Engineering Mechanics 19:99–111

Qian X, Sigmund O (2013) Topological design of electromechanical actuators with robustness toward over- and under-etching. Computer Methods in Applied Mechanics and Engineering 253:237–251

Sigmund O (1994) Design of Material Structures using Topology Optimization. Ph.d. Thesis

Sigmund O (2007) Morphology-based black and white filters for topology optimization. Structural and Multidisciplinary Optimization 33:401–424

Sigmund O (2009) Manufacturing tolerant topology optimization. Acta Mechanica Sinica 25:227–239

Sigmund O, Maute K (2013) Topology Optimization Approaches. Structural and Multidisciplinary Optimization 48:1031–1055

da Silva GA, Beck AT, Sigmund O (2019) Stress-constrained topology optimization considering uniform manufacturing uncertainties. Computer Methods in Applied Mechanics and Engineering 344:512–537

Stephens RI, Fatemi A, Stephens RR, Fuchs HO (2001) Metal Fatigue in Engineering, 2nd edn. Wiley Interscience

Stolpe M, Svanberg K (2001) An alternative interpolation scheme for minimum compliance topology optimization. Structural and Multidisciplinary Optimization 22:116–124

Svanberg K (1987) The Method of Moving Asymptotes - A New Method for Structural Optimization. International Journal for Numerical Methods in Engineering 24:359–373

Svanberg K (2007) MMA and GCMMA, versions September 2007. Technical Report

Sved G, Ginos Z (1968) Structural Optimization Under Multiple Loading. International Journal of Mechanical Sciences 10:803–805

Svärd H (2015) Interior value extrapolation: a new method for stress evaluation during topology optimization. Structural and Multidisciplinary Optimization 51:613–629

Tolosa I, Garciandía F, Zubiri F, Zapirain F, Esnaola A (2010) Study of mechanical properties of AISI 316 stainless steel processed by "selective laser melting", following different manufacturing strategies. The International Journal of Advanced Manufacturing Technology 51:639–647

Wang F, Lazarov BS, Sigmund O (2011) On projection methods, convergence and robust formulations in topology optimization. Structural and Multidisciplinary Optimization 43:767–784

Wang MY, Wang X, Guo D (2003) A level set method for structural topology optimization. Computer Methods in Applied Mechanics and Engineering 192:227–246

Xu S, Cai Y, Cheng G (2010) Volume preserving nonlinear density filter based on heaviside functions. Structural and Multidisciplinary Optimization 41:495–505

Yadollahi A, Shamsaei N (2017) Additive manufacturing of fatigue resistant materials: Challenges and opportunities. International Journal of Fatigue 98:14–31

Yadollahi A, Shamsaei N, Thompson SM, Elwany A, Bian L (2017) Effects of building orientation and heat treatment on fatigue behavior of selective laser melted 17-4 PH stainless steel. International Journal of Fatigue 94:218–235

Zhang S, Le C, Gain AL, Norato JA (2019) Fatigue-based topology optimization with non-proportional loads. Comput Methods Appl Mech Engrg 345:805–825

Zhou M, Lazarov BS, Wang F, Sigmund O (2015) Minimum length scale in topology optimization by geometric constraints. International Journal for Numerical Methods in Engineering 293:266–282

Topology Optimization of General Structures with Anisotropic Fatigue Constraints

Master's Thesis

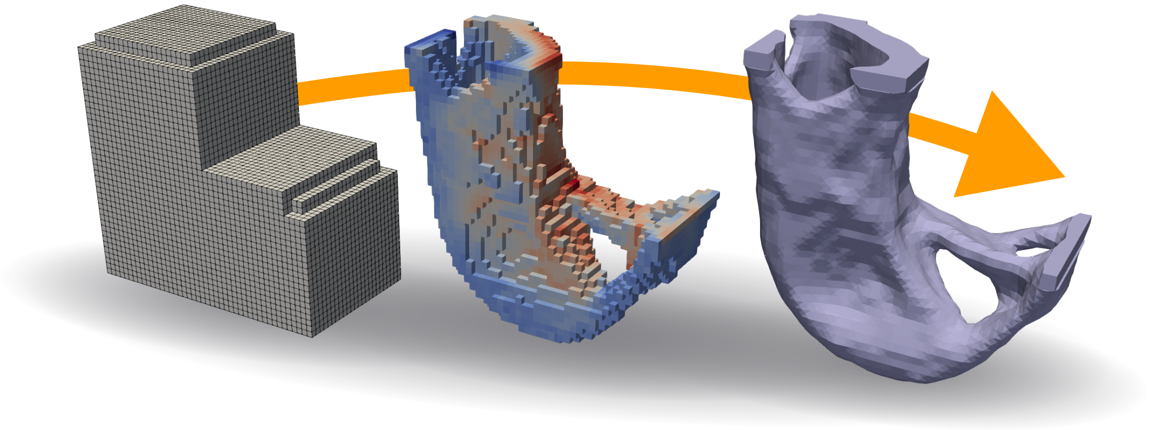

Group Fib14/23c
Design of Mechanical Systems
Aalborg University
June 3rd, 2020

AALBORG UNIVERSITY
STUDENT REPORT

Department of
Materials and Production
Design of Mechanical Systems
4^{th} semester
Fibigerstræde 16
9220 Aalborg East, Denmark
`https://www.mp.aau.dk`

Title:

Topology Optimization of General Structures with Anisotropic Fatigue Constraints

Theme:

Topology optimization

Project period:

February 3^{rd} - June 3^{rd} 2020

Participants:

Asbjørn Malte Olesen
Sebastian Hermansen

Supervisor:

Erik Lund
Professor, Aalborg University

Company supervisor:

Martin Bang Kristensen
Senior development engineer, Grundfos

Examiner:

Mathias Stolpe
Professor, DTU Wind Energy

Page numbers: 97
Appendix enclosures: 1
Date of completion: June 3^{rd}, 2020

Abstract:

Additively manufactured metals are special in that they behave close to isotropic in elasticity and monotonic strength, however their fatigue behavior is anisotropic and the fatigue strength is degraded. Designs generated by topology optimization have commonly been used as inspiration rather than realizing the actual design, primarily due to restrictions of the manufacturing methods. However, with additive manufacturing, it is possible to manufacture the highly complex designs common in topology optimization. An increased focus is therefore placed on design for manufacture, and for this purpose a novel smoothing approach is developed. Assuming isotropic stiffness and monotonic strength, the topology optimization is formulated as an extension to existing fatigue constraint functions using density-based topology optimization. An improved formulation for the fatigue damage is proposed to achieve a good combination of accuracy and computational efficiency, which has caused problems in previously published literature. These approaches and methods are demonstrated by solving both 2D and 3D problems, and the designs are subsequently verified using commercial finite element software.

Resume

Denne kandidatafhandling omhandler udvikling og implementering af topologioptimeringsmetoder til optimering af generelle 3D-printede metalkonstruktioner. Der gøres brug af en densitetsbaseret formulering, som sammenkobles med en lineær elastisk, statisk elementmetodemodel til analyse. Løsninger til topologioptimeringsproblemer i densitetsformulering er ikke veldefinerede og skal gøres geometrisk konsistente. Til dette formål benyttes filtrering, en metode oprindeligt brugt til signalbehandling. Typisk benyttes et sensitivitetsfilter eller et densitetsfilter - i den givne implementering foretrækkes densitetsfilteret. Filtermetoden udbygges ved brug af projektionsfiltre, der skal sikre en højere grad af diskretisering i designet. Disse anvendes efterfølgende til implementering af en metode til robust topologioptimering, som anvendes til at påtvinge produktionsbibetingelser i form af en veldefineret mindstestørrelse af de strukturelle detaljer. Ydermere forlænges elementdomænet for at tage højde for randbetingelsernes ukorrekte effekter på filtrering og mindstestørrelse.

Optimeringskoncepter relaterende til spændingsanalyse diskuteres med særlig fokus på de medfølgende problemer; spændingers lokale definitioner og forekomsten af singulære optimum. Som løsning på disse problemer præsenteres henholdsvis aggregatfunktioner til at definere et globalt spændingsmål, som efterfølgende normaliseres med adaptiv skalering af bibetingelsen for at opnå højere nøjagtighed, og relaksering af spændingerne ved qp-metoden. Singulariteter kan fejlagtigt opstå i geometrien grundet skarpe kanter mellem elementerne, og løsningsmetoder hertil diskuteres.

Formålet med at gennemgå spændingsaspekter er, at de skal bruges til at formulere en udmattelsesbetingelse til optimeringen. Generelle udmattelsesmodellering og -aspekter præsenteres. Udmattelses-optimeringsproblemer er komplicerede at løse grundet den ulineære formulering, og hertil præsenteres en effektiv skaleringsmetode, der sikrer høj nøjagtighed of hurtig optimering. Dette efterfølges af et grundigt studie af udmattelsesegenskaber for 3D-printede metaller, hvor det viser sig, at disse er væsentlig forringet sammenlignet med et tranditionelt fremstillet metal. Derudover forekommer der også anisotropisk opførsel i udmattelse som en bivirkning af processen. Dette benyttes til at udvikle en kontinuert funktion, der tager højde for den anisotropiske opførsel af det 3D-printede metal.

Til at løse problemet benyttes førsteordens sensitivitetsbaserede metoder, hvilket anses som en effektiv løsning til disse komplekse optimeringsproblemer. Sensitiviteterne findes ved brug af adjoint design-sensitivitetsanalyse, hvilket er fordelagtigt når der er få bibetingelser - dette opnås ved brug af aggregatfunktioner.

Efter præsentation af disse metoder løses flere eksempler, i både to og tre dimensioner, for at vise implikationerne ved brug og kombination af de forskellige metoder.

Preface

This Master's thesis has been submitted in partial fulfillment of the requirement for the degree of Master of Science. The work has been carried out at the Department of Materials and Production at Aalborg University over a period of four months in the spring of 2020. The thesis succeeds a 9^{th} semester report titled *"Structural Topology Optimization with Fatigue Constraints"* submitted by the authors in the winter of 2019. For newcomers to the field of topology optimization, the authors recommends to study this work first as it provides a more in-depth description of the basics.

Reading guide:
The report is written using American English spelling. Source referencing uses the Harvard method. The complete list of literature can be found at the end of the report, before appendices.

Headlines are given a number according to what type of headline it is. This number can be up to three numbers in the format of (x.y.z), where x is the chapter, y is the section and z it the subsection numbers. Figures, equations and tables presented in the report are enumerated accordingly in the format of (x.y), where x represents the chapter number wherein the figure/equation/table is placed and y represents the order of these in the given chapter, e.g. Figure 3.1 would be the first figure in the third chapter. The appendices are designated alphabetically and the sections are enumerated like in the main report, e.g. Section C.1 is the first section in the third appendix.

Throughout the report, boldface notation is used to indicate matrices and vectors. Consistent index definitions are load combination i and iteration k. Indices e and j are used for element and design variable, respectively. Indices are written as superscript in parentheses, e.g. $\mathbf{x}^{(e)}$ is some vector or matrix $\mathbf{x}$ related to element e. Function dependencies are written explicitly only when the function is defined, e.g. a function defined as $f(x)$ is later always referred to as simply f.

In this report, *gradient* refers to the smooth change of some function quantity over a dimension, while *sensitivity* strictly refers to the mathematical notion of function derivative in the context of optimization objective and constraint functions. All other derivative quantities, e.g. stress and strain, will be referred to as *derivative*.

Signatures

Asbjørn Olesen

Sebastian Hermansen

Table of contents

1 Introduction

Achieving optimal use of material for load carrying structures is a long-standing goal in engineering. This has spiked an ever-increasing interest in using mathematical optimization methods to design complex and high performing solutions at low cost. Around its introduction, the application of mathematical optimization to solve complex problems was limited by the lack of computational power available, as it involves solving problems iteratively by use of a programming algorithm. As computational power improved substantially during the late 20^{th} century, these solution schemes were made viable and the preferable approach has since become optimization in a Finite Element (FE) formulation [Lund, 1994].

The first approach taken was sizing optimization, which concerns structures parameterized by common dimensions such as thickness or cross sectional area. To be able to treat more complex problems, shape optimization was developed, which allows finer control in generation of design, e.g. the shape of a curve [Haftka and Grandhi, 1986]. In Bendsøe and Kikuchi [1988] shape optimization was generalized to what is now known as topology optimization (TO). TO is concerned with material layout in a fixed domain and unlike shape optimization, is able to change the occurrence of structural details, such as holes, providing almost total freedom within the design space, resulting in synthesis of highly complex designs, near impossible to derive based on intuition.

During the 1990's the field gained much academic attention and evolved at a high pace as a consequence. A compact MATLAB implementation was provided in Sigmund [2001] to educate engineers in TO, which further allowed the field to develop in many directions. The method has since been applied to solve many different challenging problems [Eschenauer and Olhoff, 2001][Bendsøe et al., 2005]. An impressive example of TO is the optimization of an entire airplane wing by Aage et al. [2017], which meant solving an very large-scale problem consisting of one billion finite elements. Being able to solve such complex problems have also caused an increasing interest from industry to be able to incorporate TO to improve their products. This project is a good example of this, as it is conducted with pump manufacturer Grundfos as an industrial partner. The industrial relevance has also lead to implementation in many commercially available FE programs such as ABAQUS, ANSYS, and COMSOL, making TO available to a broad audience outside of academia.

Despite the academic and industrial attention problems persist, preventing application to attractive areas. In relation to the theme of this thesis is in particular the combination of additive manufacturing (AM) and TO. Beforehand, a major limiting factor to realizing TO designs was the capability of the manufacturing methods available. As AM builds components from the bottom up it does not suffer from accessibility constraints, which is the significant restriction of conventional subtractive manufacturing methods. Some factors must be taken into account regarding the AM-process and works have been published regarding including this in TO, see Clausen [2016], Langelaar [2016] and [Langelaar, 2019]. However, ensuring structural integrity of metal AM components against common failure criteria has not been given too much attention. Being able to take fatigue damage into account for dynamically loaded AM components is in particular important. Studies indicate that the fatigue strength of AM metals is degraded as a result of the process, whereas in comparison the static strength is in general comparative or in some cases better than a wrought counterpart [Yadollahi and Shamsaei, 2017]. How much the strength is degraded differs for each considered material. The effectiveness of applying post-treatment to recover some of the fatigue strength is also material dependent, and may actually for some materials reduce the fatigue strength even further. Furthermore, because the direction in which the component is built induces anisotropy in the fatigue formulation, accurate modeling is non-trivial.

1.1 State of the Art of Topology Optimization

Although the method of TO was introduced in Bendsøe and Kikuchi [1988], the homogenization approach used to define material properties of the solid-void structure herein is all but abandoned today. Instead either a density-based method with stiffness penalization [Bendsøe, 1989][Stolpe and Svanberg, 2001a] or a level set method [Allaire et al., 2002][Wang et al., 2003][Allaire et al., 2004] is used. Especially the Solid Isotropic Material with Penalization (SIMP) approach to penalize stiffness has been widely used due to its simplicity and effectiveness. For an overview of less used methods and discussion of their uses see Sigmund and Maute [2013].

Efficient solution of optimization problems is typically achieved by first order sensitivity-based programming. These involve computing sensitivities through a Design Sensitivity Analysis (DSA). Analytical sensitivities are preferable as these are computed most efficiently using either the direct differentiation or an adjoint formulation. The most popular method for solving TO problems is the Method of Moving Asymtotes (MMA) by Svanberg [1987].

A consistent issue in material layout problems is the illposedness of geometric scale and non-existence of solutions for the continuous problem, leading to mesh dependent designs in FE formulations. Regularization is done to ensure mesh independent convergence, typically by filtering techniques such as sensitivity [Sigmund, 1994] or density filtering [Bruns and Tortorelli, 2001][Bourdin, 2001]. Linear density filtering is the most popular choice since the sensitivity filter alters the problem sensitivities such that they are inconsistent with the other expressions in the optimization, which causes problems for line search based optimization algorithms such that convergence to the optimum may be prohibited [Sigmund, 2007].

However, the linear density filter leaves a gradient of intermediate density around structural members. Intermediate densities in the optimized domain are undesirable as there is no physical interpretation associated with them. Although effort has been placed on formulating a nonlinear density filter, e.g. by replacing the linear expression with a Gaussian probability function [Bruns and Tortorelli, 2003] to achieve a more crisp transition between solid and void, no advantage of using this formulation has been observed [Sigmund, 2007].

In Guest et al. [2004] an alternative solution to the problem was proposed, entailing appending a projection filter to the linear density filter. The proposed projection filter would force all intermediate densities to fully solid material. Besides being able to increase the discreteness of the design, the method is also able to introduce a minimum length scale on the structural members, albeit only on the solid phase. The concept of minimum length scale, i.e. strict control over geometric dimension, has for a while been in focus due to considerations of manufacturing constraints. Sigmund [2007] reversed the presented projection filter formulation to be able to introduce a minimum length scale on the void phase instead, yet a scheme for defining minimum length scale on both phases simultaneously is desirable. Such control has been achieved by using multiple projections of density as in the robust method [Sigmund, 2009][Wang et al., 2011] or by inclusion of geometric constraints [Zhou et al., 2015]. Similar geometric constraints may be introduced for defining a maximum length scale in the optimized design [Lazarov and Wang, 2017].

Another issue related to minimum length, specifically violation of minimum length at domain edges, stemming from poor definition of filtering boundary conditions, was solved in Clausen and Andreassen [2017], by use of domain extension, such that accurate boundary condition are achieved in the design domain.

Computation of the linear density filter is time consuming especially for larger models. Parallelization is desirable, as it allows for distributing the computational burden to multiple cores for faster computation, however the standard formulation of the density filter is not suitable for this purpose. Instead, the filter may be defined implicitly as a solution of a Helmholtz partial differential equation [Lazarov and Sigmund, 2011][Kawamoto et al., 2011], which is better suited for parallelization. A framework was presented in Aage and Lazarov [2013] and a PETSc implementation in Aage et al. [2015], focusing on parallelization of the Helmholz filter and MMA routines, which is what allowed the solution of the large-scale problem in Aage et al. [2017].

Early work on structural TO is primarily restricted to global criteria such as volume, compliance or eigenfrequency [Bendsøe and Sigmund, 2003]. Within the last decade, the focus has shifted to more commonly occurring failure criteria, in particular stress and fatigue. These are notoriously difficult to handle as they inherent complex issues, namely their local definition and singular optima [Duysinx and Bendsøe, 1998]. The former is typically solved by aggregation using a scalarization function [Duysinx and Sigmund, 1998] with normalization by the adaptive constraint scaling method [Le et al., 2010]. More lately, the problem has also been solved by reformulating the problem using an augmented Lagrangian formulation [da Silva et al., 2019]. The singular optima problem is treated by relaxation techniques, usually either the ε-approach [Cheng and Guo, 1997] or the qp-approach [Bruggi, 2008] is adopted. Implementation of these procedures has been successfully done for stress-constraint TO in many published studies, e.g. Le et al. [2010], Holmberg et al. [2013] and da Silva et al. [2019]. However, the inclusion of fatigue functions is quite more tedious. Fatigue is dependent on multiple factors and its behavior is highly nonlinear making the combination of high accuracy and efficiency in the modeling difficult to achieve. Oest and Lund [2017] provided a framework for including finite-life fatigue constraints for variable amplitude loading in the optimization for the proportional load case. The model was extended to nonpropotional loading in Zhang et al. [2019], where also a scaling method to reduce the nonlinearity of the fatigue damage measure is introduced.

A different problem, present for both stress and fatigue, is the handling of artificial stress singularities emanating from jagged edges of highly discrete designs. Using a linear density filter to smooth these removes the singularities, however the stress measure is not coherently defined in intermediate densities leading to an erroneous measure, worsened by the nonlinear dependence in fatigue problems. Solutions include stress extrapolation [Svärd, 2015b] or leaving a small density gradient for reducing the impact of jagged edges [da Silva et al., 2019].

1.2 Objectives

This work concerns development of methods for performing TO on AM metal components. AM metals are substantially affected by the process, which degrades their fatigue properties. Anisotropic fatigue behavior appears and the degree hereof varies for each material and process method, making modeling quite challenging. To be able to accomplish this optimization, a continuous function describing the fatigue damage as a function of the fatigue strength reduction from the induced anisotropy is required. Complex TO problems, such as fatigue, are in general difficult and time consuming to solve. Efficiency is therefore an important consideration, when choosing the approach for solving the problem. For this purpose, sensitivity-based methods with analytically derived sensitivities are essential, but they are only applicable if continuous and differentiable expression can be obtained.

The design resulting from an optimization should be at the limit of the material's capacity. If the design is altered post-optimization, there is no guarantee that the structural integrity is maintained - at least not wrt. the model used. TO geometry have therefore commonly been used as inspiration for a final design instead of realizing the actual geometry. Because of the high capabilities of AM the complex geometries are now manufacturable, which makes it even more relevant to be able to directly manufacture a generated TO design.

The motivation from the industrial partner Grundfos is to be able to achieve better designs for AM by using TO. It is therefore further desired to extend the methods presented to general three-dimensional cases for use in generating designs for industrial products.

In conclusion, the following objectives are specified:

- Develop a continuous anisotropic fatigue model for performing TO of AM metals.
- Develop a TO scheme capable of generating designs ready for AM with minimal post-processing.
- Develop an effective method to generate solid material models from density distributions.
- Implement all presented routines for solving general three-dimensional problems.

2 | Topology Optimization

The following chapter will present the density-based approach to topology optimization of finite element problems. Benchmark problems are established, which are used to illustrate the effect of the implemented methods throughout the report. Filtering is introduced as a regularization technique. Several methods of filtering are discussed and used to define a robust topology optimization scheme. The effects associated with filtering are discussed and solutions are presented.

2.1 Problem Setting

Analysis of general structures (i.e. structures of any shape and size) is most commonly done using the Finite Element (FE) method. FE is a numerical method based on discretizing the governing partial differential state equations to a set of linear algebraic equations. For the linear elastic static structural case, the discretized governing equation is:

$$\mathbf{KU} = \mathbf{F} \tag{2.1}$$

where **K** is the global stiffness matrix, **U** is the global displacement vector and **F** is the load vector. The structure is usually discretized into a mesh of many finite elements to increase accuracy of the analysis. Many element formulations are available [Cook et al., 2002] and the choice hereof depends on the problem considered, the desired accuracy and efficiency.

Topology optimization (TO) of general structures takes outset in the FE formulation and the standard optimization problem is stated as:

$$\begin{aligned} \underset{(\boldsymbol{\rho})}{\text{minimize}} \quad & f(\boldsymbol{\rho}) \\ \text{subject to} \quad & g(\boldsymbol{\rho}) \leq 0 \\ & \boldsymbol{\rho} \in [\rho_{min}, 1] \end{aligned} \tag{2.2}$$

where f is the objective function, g is a constraint function, $\boldsymbol{\rho}$ is a vector of design variables and ρ_{min} is a small number introduced to avoid numerical issues in solving the FE problem. The simplest definition of a TO problem in a FE form is by assigning elements a design variable with one of two values, deciding whether a given element should contain material or not. Alternatively, design variables could be assigned to nodes, as done in Guest et al. [2004], however the element approach is sufficient for this implementation and is adopted for this work.

The governing equation in Equation (2.1) becomes dependent on the design variables in the optimization, where the global stiffness matrix **K** becomes dependent of the contribution from each element. The load vector **F** is assumed constant and design-independent, although this may not always be the case, see e.g. Chen and Kikuchi [2001]. If the state variables are independent of the design variables, the governing equation has to be included as a constraint function in Equation (2.2), such that the governing equation is solved simultaneously with the TO problem - this is termed the simultaneous formulation. However, in the case of static structural problems, the state variables $\mathbf{U}$ are uniquely defined for a given set of design variables. The FE problem may therefore be solved a priori, as the state variables are implicitly included in the optimization functions (e.g. $f(\boldsymbol{\rho}, \mathbf{U}(\boldsymbol{\rho}))$) - this is termed the nested formulation [Christensen and Klarbring, 2009].

2.2 Density-based Approach

The FE formulation implies solving an integer optimization problem, using an indicator function to determine whether a given element should be assigned material (i.e. non-zero element stiffness) or not. This is usually designated by 0 for no material and 1 for material, or simply void and solid, respectively. Solutions are then the 0-1 distribution of the indicator function in the FE domain. The discrete formulation is however cumbersome, as solving an integer programming problem becomes exponentially more expensive as the amount of design variables in the model increase using the solution methods available at present, e.g. branch-and-bound methods or genetic algorithms [Sigmund, 2011].

To improve efficiency of the solution, the problem is relaxed by making design variables continuous and allowing element stiffness to take intermediate values. Continuity is desirable as it allows for computation of sensitivities (typically first order derivatives) and thus much more efficient optimization (given that sensitivities can be computed efficiently). The continuous design variables, henceforth called density variables, are an artificial measure in that it is inconsistent with physics and therefore it needs to be removed during the optimization. This motivated the development of the Solid Isotropic Material with Penalization (SIMP) method by Bendsøe [1989]. The SIMP method was initially branded as a "fictitious" method, favoring efficient and simple implementation at the cost of accuracy, with many studies preferring the homogenization method of Bendsøe and Kikuchi [1988] around its introduction. However, studies by Bendsøe and Sigmund [1999] on the SIMP method's micromechanical implications demonstrated that the method satisfies the Hashin-Shtrikman bounds, whereby the SIMP method is a valid and physically meaningful method for density interpolation.

The SIMP method introduces penalization of intermediate stiffness with respect to the density measure through a power law:

$$\bar{E} = \rho^p E \tag{2.3}$$

where $\bar{E}$ is the penalized elastic modulus of the material, p is the penalization factor, ρ is the density variable, and E is the unmodified elastic modulus. For higher penalization factor p, the stiffness becomes more costly for elements with intermediate density, graphically represented in Figure 2.1, such that density is forced towards fully void or solid.

A modified version of the SIMP method [Sigmund, 2007] is expressed as:

$$\bar{E} = E_{min} + \rho^p (E - E_{min}) \tag{2.4}$$

where E_{min} indicates a minimum stiffness term to avoid a singular stiffness matrix. This formulation is preferable for regularization purposes [Sigmund, 2007][Andreassen et al., 2011], see Section 2.4.

Another stiffness penalization method was presented in Stolpe and Svanberg [2001a] termed the Rational Approximation of Material Properties (RAMP):

$$\bar{E} = E_{min} + \frac{\rho}{1 + p(1-\rho)}(E - E_{min}) \tag{2.5}$$

This method similarly includes a penalization factor p, however the degree of penalization differs from the SIMP method, see Figure 2.1. The method was introduced in order to alleviate the non-concavity of the SIMP function and thus ensure convergence for compliance problems [Stolpe and Svanberg, 2001b]. RAMP has a finite, non-zero derivative at zero density, which is an advantage over SIMP, and the RAMP method therefore sees much use in TO areas such as the discrete material optimization method for laminated composites, see e.g. Lund [2018]. The RAMP method does however not achieve the same degree of penalization as the SIMP model for highly nonlinear problems, leading to slower convergence [Olesen and Hermansen, 2019].

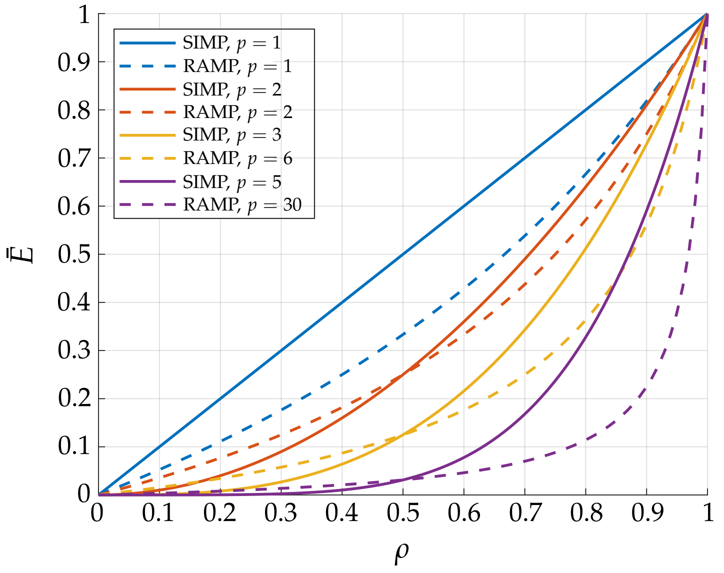

Figure 2.1. Effect of penalization for SIMP and RAMP interpolation methods.

2.3 Benchmark Problems

Two structural problems are defined for use in this work. Both are commonly used in TO literature to benchmark developed methods. The material will be AISI 1020 HR steel for all examples with properties as defined in Table 2.1.

The first problem is the MBB-beam, see Figure 2.2. The MBB-beam is equivalent to a three point bending setup. Symmetry conditions are applied at the center of the beam to reduce problem size.

Young's modulus	E	203	GPa
Poisson's ratio	ν	0.3	
Yield strength	S_y	262	MPa
Ultimate tensile strength	S_{Ut}	441	MPa
Fatigue strength	σ_f	1384	MPa
Basquin's parameter	b	-0.156	

Table 2.1. Material data for AISI 1020 HR steel [Stephens et al., 2001].

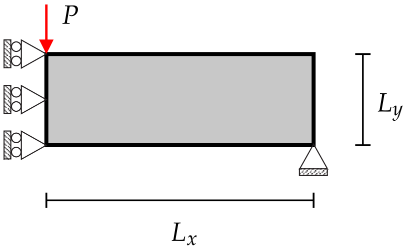

P = 50 kN
L_x = 1 m
$L_y = L_x/3$
t = 20 mm

Figure 2.2. MBB-beam definition and default values. t is thickness.

The second problem is the L-beam, see Figure 2.3. The L-beam has a reentrant corner, creating a large stress concentration, whereby stress effects become more pronounced than in the MBB-beam and thus stress-based designs become more distinct from those not considering stress.

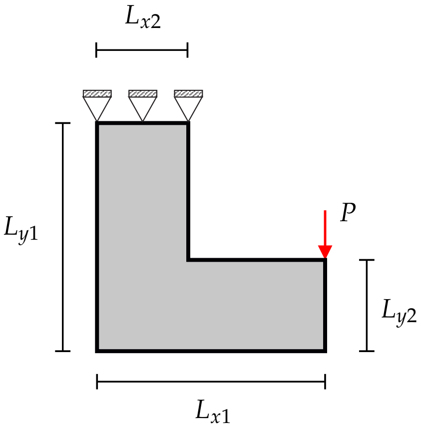

P = 50 kN
L_{x1} = 1 m
L_{x2} = 0.4 m
L_{y1} = 1 m
L_{y2} = 0.4 m
t = 20 mm

Figure 2.3. L-beam definition and default values.

Volume and structural compliance are used as objective and constraint functions for illustrations in this chapter. Volume V is defined:

$$V = \sum_{e=1}^{N_{elem}} \rho^{(e)} v^{(e)} \tag{2.6}$$

where e is the element index, N_{elem} is the total amount of elements in the design domain and $v^{(e)}$ are reference element volumes. Note that $\rho^{(e)}$ refers to the density variable used for the physical design, as density is changed via regularization (explained in Section 2.4). Compliance C is defined as:

$$C = \mathbf{U}^T\mathbf{F} = \mathbf{U}^T\mathbf{K}\mathbf{U} \tag{2.7}$$

The general implementation of the compliance problem follows Andreassen et al. [2011]. The geometry is represented by a pixel-based mesh of regular linear Q4 elements. Regularity of the elements makes the isoparametric formulation unnecessary, and as such the element stiffness matrix is found analytically in Cartensian coordinates. For solving the problems, the optimality criteria method used in Andreassen et al. [2011] is replaced with a sensitivity-based method termed the Method of Moving Asymptotes. This is done as optimality criteria can not be defined for more complex problems such as stress and fatigue, which are treated later in this paper. The Method of Moving Asymptotes is discussed further in Chapter 5.

General nomenclature of geometric components used throughout the report is illustrated on a compliance optimized MBB-beam in Figure 2.4.

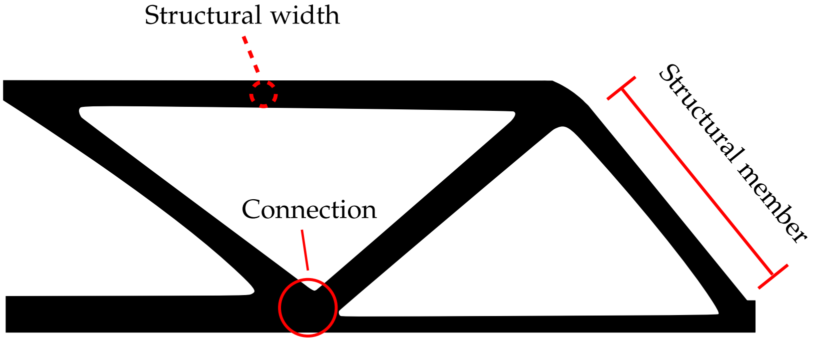

Figure 2.4. Nomenclature used highlighted on an optimized MBB beam. "Structural members" refer to the members that compose the structure, "structural width" their width, and where they connect are termed "connections".

2.4 Regularization

Structural TO problems are in general ill-posed, as solving the same problem with an increasing resolution of the FE mesh will result in solutions with increasingly fine detail of the structural members within the design domain [Cheng and Olhoff, 1981][Sigmund, 1994], see Figure 2.5. Refinement of the mesh should only result in more accurate modeling, not changes to geometry, and as many elements are usually required to properly capture derivative field quantities such as stress, the resulting optimized solution may contain unmanufacturable details. In order to achieve manufacturing-ready designs the problem must be regularized by removing the mesh dependency and introducing a minimum length scale on the structural details.

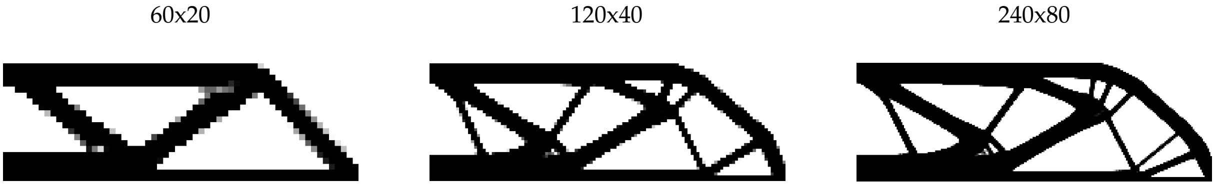

Figure 2.5. Ill-posedness of the TO problem (MBB-beam). Increasing the amount of elements in the FE model (indicated by the numbers above as elements in horizontal and vertical directions) without changing the problem leads to new geometry.

Another problem arises when using linear FE, as is often done for computational efficiency. It is observed that the optimized density variables will alternate between solid and void, see Figure 2.6. This form of material distribution is termed a checkerboard pattern.

Figure 2.6. Checkerboard pattern formation when solving the MBB problem.

Checkerboard patterns are caused by artificially high stiffness introduced through linear elements' inability to properly capture bending deformation [Díaz and Sigmund, 1995]. Mathematically, the appearance of such a pattern represents non-convergence of the FE problem [Sigmund and Petersson, 1998]. A solution containing a checkerboard pattern does therefore not represent an optimized distribution of material, but instead numerical instability in the computational procedure. It is possible to remove the problem by using elements of higher order, such as quadratic elements, which are not affected by spurious stiffness. However, a regularization scheme is still preferred, as higher order elements do not remove the mesh dependency of the solution. Furthermore, higher order elements increase the computational expense, especially for three-dimensional analysis, which encourages a method to allow for the use of linear elements.

2.4.1 Basic Filtering

Filtering is a common method for regularization and removing checkerboard patterns due to the method's effectiveness and ease of implementation [Sigmund, 2007]. Filtering is a noise-reduction technique adopted from the field of signal processing [Sigmund, 1994], notably used in digital image processing, in which the pixel-based domain is similar to the FE domain used in TO. A structural checkerboard pattern can be interpreted as noise, similar to the noise appearing in digital images. The method used here to filter this noise is based on convolutions, where some appropriate function is used to modify the density function, producing a smoothing of the density distribution. The operation is exemplified in Figure 2.7, where a discrete Heaviside function is convolved with a linear hat function.

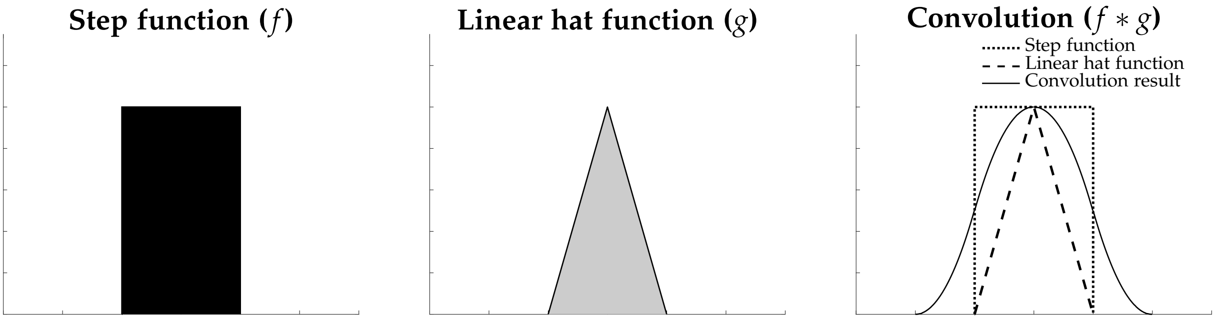

Figure 2.7. Convolution of two functions; a step function (f) and a linear hat function (g). "$*$" is the convolution operator.

In TO, filtering is most commonly applied using one of two methods; sensitivity filtering or density filtering. In this work, only density filtering is considered. Sensitivity filtering heuristically alters the problem sensitivities as a weighted sum of sensitivities from the neighboring elements [Sigmund and Petersson, 1998]. This change makes the sensitivities inconsistent with the problem and may prohibit convergence to the optimum when using line search based optimization algorithms [Sigmund, 2007]. The density filter is applied directly to the design variables and sensitivities are subsequently computed, ensuring consistency between the expressions.

2.4.2 Density Filtering

The density filter was introduced in Bruns and Tortorelli [2001] and convergence to an optimized solution was proven in Bourdin [2001]. The density filter modifies the density of an element as a weighted average of the density of neighboring elements:

$$\tilde{\rho}^{(j)} = \frac{\sum_{e=1}^{N_{elem}} H^{(j,e)} \, v^{(e)} \, \rho^{(e)}}{\sum_{e=1}^{N_{elem}} H^{(j,e)} \, v^{(e)}} \tag{2.8}$$

where $\tilde{\rho}^{(j)}$ is the filtered design variable, $v^{(e)}$ is the element volume and $H^{(j,e)}$ defines the weighting function between design variable j and element e for all N_{elem}. The element volume is included in the expression in order to account for elements having different shapes and sizes in an unstructured FE mesh. The simplest weighting function is linear, which is defined as:

$$H^{(j,e)} = \max(0, R - |\mathbf{c}^{(j)} - \mathbf{c}^{(e)}|) \tag{2.9}$$

where R is the filter radius, $\mathbf{c}^{(e)}$ is the position of the centroid of an element in N_{elem} and $\mathbf{c}^{(j)}$ is the position of the centroid of the element being filtered. Application of this linear operation and the resulting filtered density are equivalent to the example shown in Figure 2.7. An optimized solution with a density filtering is illustrated in Figure 2.8.

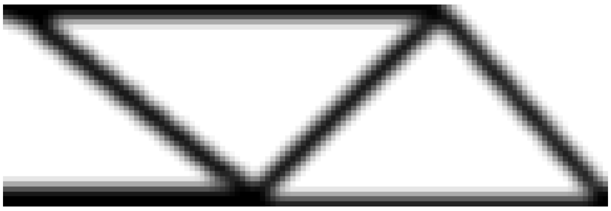

Figure 2.8. Result of a volume minimization of the MBB beam problem subject to a compliance constraint. The problem is regularized using a linear density filter. Three elements are included in the filter radius.

It should be noted, that when using a density filter, the design should be visualized using the filtered density variables $\tilde{\boldsymbol{\rho}}$ and not the original design variables $\boldsymbol{\rho}$, which lose physical meaning when the filter is applied and are only used as intermediate variables for mathematical treatment [Sigmund, 2007]. The filtered variables are therefore termed physical variables.

Using N_{elem} in the formulation implies comparison of all elements. A more efficient formulation is to check the set of elements N only in the neighborhood of the filtered element, i.e.

$$N = \{\, j \mid |\mathbf{c}^{(j)} - \mathbf{c}^{(e)}| \leq R\} \tag{2.10}$$

The amount of elements included in the neighborhood depends on the size of the filter radius. Generating this set may however be even more expensive if no good way of identifying neighbouring elements is available.

To further decrease computational effort, storage required and allow for parallel computation, the filter may be solved using a Helmholtz partial differential equation (PDE) instead of explicitly solving the convolution integral [Lazarov and Sigmund, 2011]. The implementations in this work take offset in the explicit solution to the convolution integral, i.e. Equation (2.8). Implementation of the PDE formulation is left for further work, see the discussion in Chapter 7.

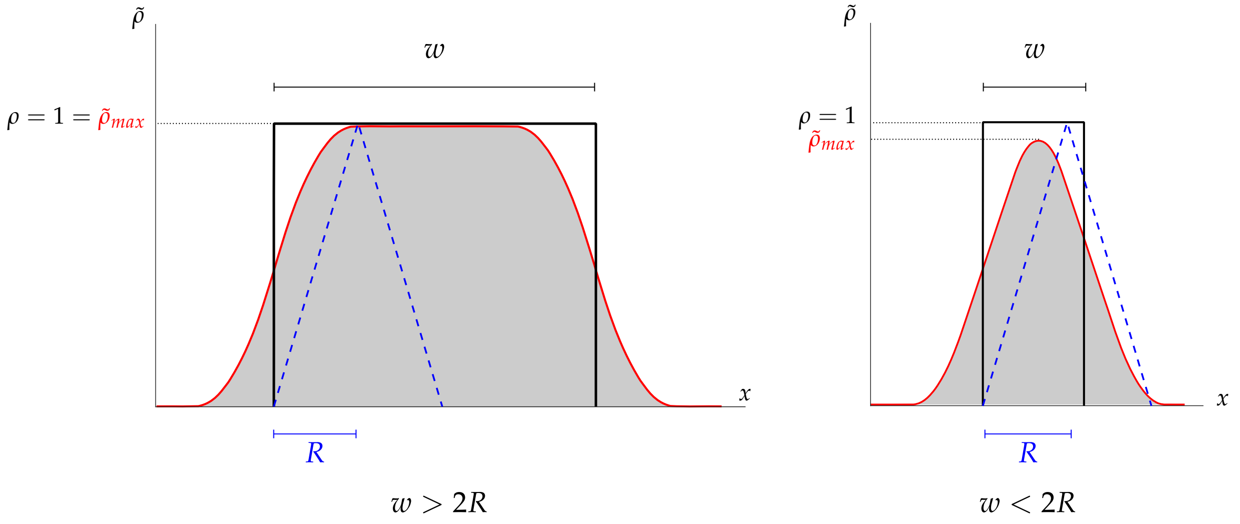

Figure 2.9. Difference in density distribution of features with width larger than the filter diameter (left) and less than filter diameter (right).

The density filter is able to ensure a minimum length scale in the design and prevent checkerboard formation, however solutions will contain gradients of intermediate density around structural members. The size of the gradient around a structural member will decay similarly to a Gaussian distribution function (Figure 2.7, right), and its size will depend on the filter radius. Furthermore, the minimum length scale dictated by the filter can cause areas consisting entirely of artificial intermediate density in cases where the feature width w is lower than the filter diameter $2R$, see Figure 2.9.

To improve the discreteness of the design, Bruns and Tortorelli [2003] suggested replacing the linear weighting function by a more complicated function (in their case a Gaussian bell function) to enforce less density gradient, however Sigmund [2007] observed no advantage of using this formulation of the weighting function.

As intermediate density is a pure mathematical manipulation, the optimized design is usually made manufacturable by removing elements with intermediate density below a cutoff value (often $\tilde{\rho} < 0.5$) from the model and considering the remaining as full density elements. This simple postprocessing strategy however changes the optimized design and introduces jagged geometry, which is undesirable (for further discussion hereof see Subsection 3.1.4).

An improved post-processing for generating smooth surfaces is presented in Appendix A, based on converting to nodal densities and then interpolating a surface on an element level. An overview of the element process is given in Figure A.12 (repeated here).

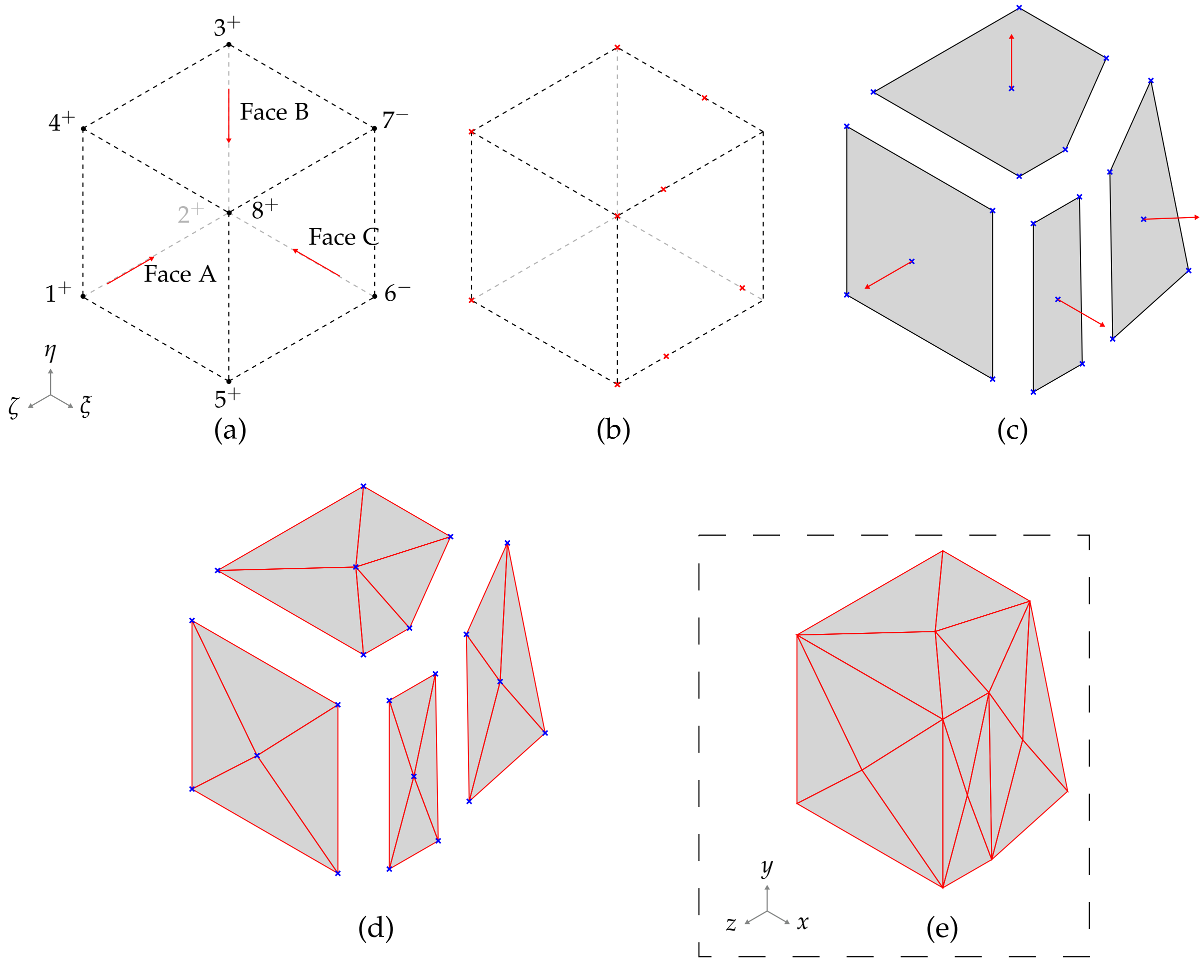

(a) (b) (c) (d) (e)

Figure A.12. Overview of element interpolation and surface description. (a): For an element it is found that all nodal densities are above the cutoff value except 6 and 7, and that faces A (nodes 1,5,8,4), B (nodes 3,4,8,7) and C (nodes 5,6,7,8) are outside faces. (b): It is determined that the surface consists of nodes 1,3,4,5,8 and interpolated points on edges between nodes (3,7), (6,8), (7,8), and (5,6). (c): Individual faces and the element intersection are considered; center points and approximate normals are calculated. (d): Using the center point and normals, non-overlapping triangular facets are found. (e): The facets are transformed from natural to Cartesian coordinates, normals are recalculated and the data is written to an .STL file. Process is repeated for all elements.

2.4.3 Heaviside Projection Filters

In order to achieve more discrete designs, a projection scheme is appended to the linear density filter. The TO problem then becomes a three-field formulation consisting of the design variables $\boldsymbol{\rho}$, the filtered variables $\tilde{\boldsymbol{\rho}}$ and the projected variables $\bar{\tilde{\boldsymbol{\rho}}}$ with the latter becoming the new physical variables. The projection schemes are based on the Heaviside step function to force intermediate densities to 0 or 1. In order to keep the filter differentiable and allow for sensitivity-based optimization methods, the Heaviside filter is usually implemented as a relaxed step function, allowing for a degree of non-discreteness in the design. Guest et al. [2004]

proposed projecting intermediate densities to 1 through the following relaxed formulation of the Heaviside function:

$$\bar{\tilde{\rho}}^{(j)} = 1 - \exp\left(-\beta\tilde{\rho}^{(j)}\right) + \tilde{\rho}^{(j)}\exp(-\beta) \tag{2.11}$$

where β is a tuning parameter for adjusting the degree of relaxation, such that as $\beta \to \infty$, the Heaviside step function is approached. Alternatively, Sigmund [2007] proposed projecting the intermediate densities to 0 through reformulation of Equation (2.11):

$$\bar{\tilde{\rho}}^{(j)} = \exp\left(-\beta[1 - \tilde{\rho}^{(j)}]\right) - [1 - \tilde{\rho}^{(j)}]\exp(-\beta) \tag{2.12}$$

The filters are illustrated in Figure 2.10. Although regularization is ensured and the checkerboard patterns are removed, neither projection filter formulation guarantees minimum length scale of both solid and void phases. The original projection filter of Equation (2.11) will ensure minimum length scale on the solid region and the modified filter of Equation (2.12) on void. Neither of the filters are volume preserving, i.e. volume of the structure is not the same before and after filtering, which is problematic if using a volume constraint. It should be noted that, if the standard SIMP formulation is employed, a lower bound on the physical densities $\bar{\tilde{\rho}}$ is needed to avoid numerical issues. However, if using the modified SIMP, this it not necessary due to the explicitly included minimum stiffness term.

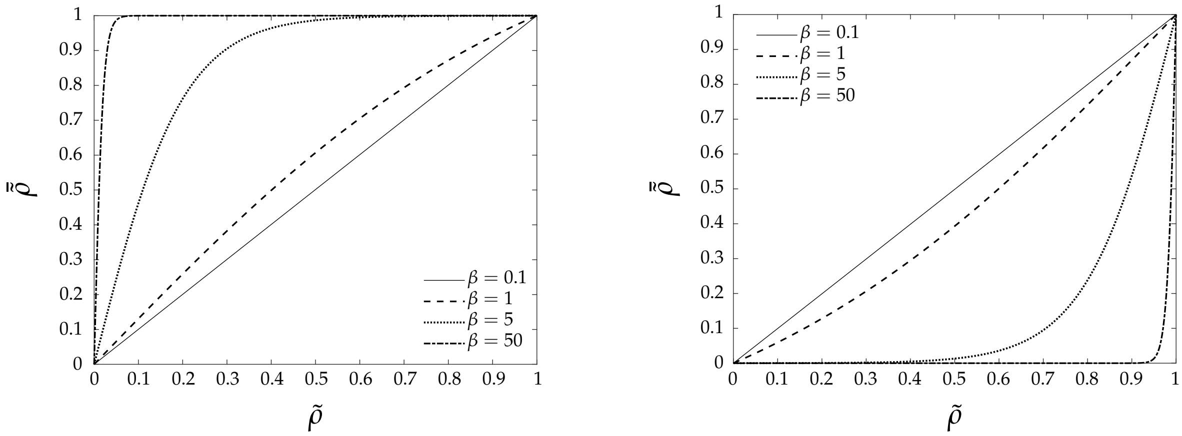

Figure 2.10. Left to right: Original Heaviside projection of Equation (2.11) and modified Heaviside projection of Equation (2.12).

Threshold Projection

A way to preserve volume using the Heaviside filtering method is by reformulating the Heaviside function using a threshold value η. Instead of forcing all densities towards either solid or void, a transition point is defined where densities below are forced toward void and above toward solid. The original formulation given by Xu et al. [2010] is:

$$\bar{\tilde{\rho}} = \begin{cases} \eta[\exp(-\beta\{1-\tilde{\rho}/\eta\}) - (1-\tilde{\rho}/\eta)\exp(-\beta)], & 0 \leq \tilde{\rho} < \eta \\ \eta, & \tilde{\rho} = \eta \\ \begin{array}{c}(1-\eta)[1-\exp(-\beta\{(\tilde{\rho}-\eta)/(1-\eta)\}) \\ +(\tilde{\rho}-1)\exp(-\beta)/(1-\eta)] + \eta,\end{array} & \eta < \tilde{\rho} \leq 1 \end{cases} \tag{2.13}$$

The threshold filter is illustrated in Figure 2.11.

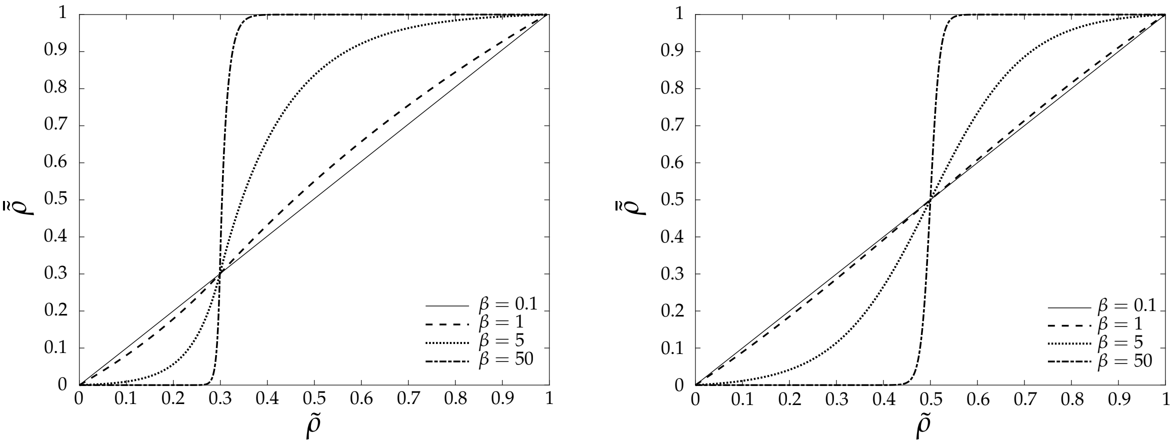

Figure 2.11. Threshold projections using Equation (2.13) with $\eta = 0.3$ (left) and $\eta = 0.5$ (right).

Instead of using exponential terms, Wang et al. [2011] presents a continuous formulation that makes use of the hyperbolic tangent function to achieve a similar smoothing of the Heaviside function:

$$\bar{\tilde{\rho}} = \frac{\tanh(\beta\eta) + \tanh(\beta(\tilde{\rho}-\eta))}{\tanh(\beta\eta) + \tanh(\beta(1-\eta))} \tag{2.14}$$

By removing the exponential functions and by having a continuous expression, computational efficiency is improved. This formulation is not equivalent to the expression of Equation (2.13) and some discrepancy between the projected densities will exist at lower values of β. This is especially obvious when $\eta \neq \{0, 0.5, 1\}$ where projection happens around densities not equal to the threshold value, see Figure 2.12. As $\beta \to \infty$ the two expressions however yield the same result.

The threshold value η is in principle input by the user. Note that if $\eta = 0$ is chosen, the original Heaviside filter of Equation (2.11) is recovered and likewise for the modified Heaviside filter of Equation (2.12) if $\eta = 1$. However, if it is desired to preserve volume, the value of η can not be arbitrarily chosen. Preservation of volume is fulfilled if the volume before and after filtering is unchanged. For the Heaviside filter, this is stated by the following condition:

$$\sum_{e=1}^{N_{elem}} \bar{\tilde{\rho}}^{(e)} v^{(e)} = \sum_{e=1}^{N_{elem}} \tilde{\rho}^{(e)} v^{(e)} \tag{2.15}$$

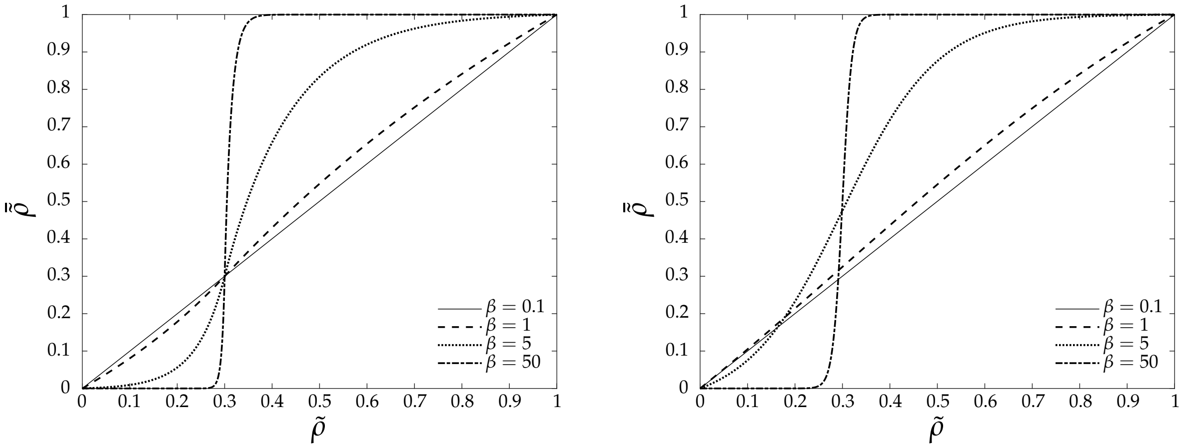

Figure 2.12. Threshold projections using $\eta = 0.3$ of Equation (2.13) (left) and Equation (2.14) (right). With the continuous approximation this threshold value implies that the transition point between projection to solid or void happens elsewhere than $\bar{\tilde{\rho}}$, e.g. for $\beta = 10$ it occurs at approximately $\bar{\tilde{\rho}} = 0.5$. At $\beta = 50$ it is observed, that the projections of the two functions are almost the same.

It is then possible to solve this equation for the value of η. The value of η is found using a one-dimensional search, e.g. Golden Section (see e.g. Arora [2016]), by minimizing the volume residual before and after filtering. It is however observed that *eta* is approximately 0.5 throughout optimization, thus it is reasonable to assume volume is preserved by keeping η constant at 0.5. The change in threshold value is illustrated in Figure 2.13 for the MBB problem with a discreteness parameter gradually increasing to $\beta = 100$.

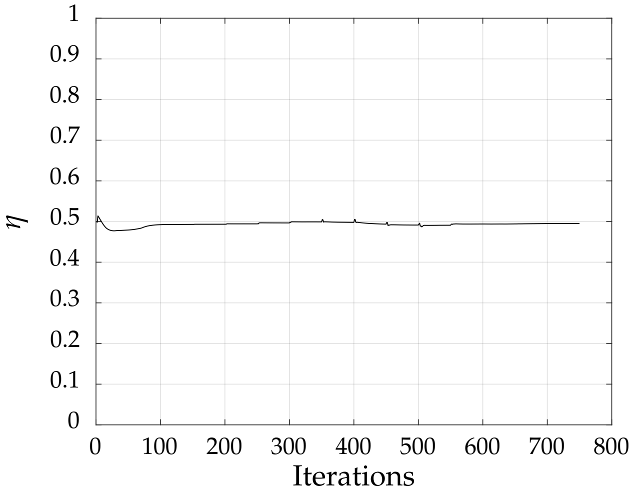

Figure 2.13. Change in threshold value η to ensure volume preservance. The value is found by solving a least squares minimization problem using MATLAB's `fminbnd` optimizer.

Unlike the original Heaviside filter of Equation (2.11) and modified Heaviside filter of Equation (2.12), the threshold filter with intermediate η does not impose a minimum length scale on void nor solid phases.

Minimum Length Scale

The inability of all the presented regularization approaches to impose a minimum length scale on both phases is quite significant for realizing the TO design. If no length scale control is included, the generated designs may contain small solid and void details impossible to manufacture. Assuming regularization has been performed by linear density filtering as defined in Figure 2.9, the inability of imposing a minimum length scale is explained as follows.

If a structural feature of width w is filtered by a linear density filter with filter diameter $2R$, the maximum density in the area or volume of the feature will depend on the ratio between w and R. By filtering the solid phase with a filter diameter $2R \leq w$, it is ensured that the maximum of the filtered density $\tilde{\rho}_{max}$ is equal to the value of the design variable ρ. Opposite, if $2R > w$, the maximum filtered density is less than the design variable density since void is included in the filter, resulting in pure intermediate density of the filtered area. A similar relation exist for the void phase - most importantly if $2R > w$ the minimum of the filtered void phase $\tilde{\rho}_{min}$ is equal or larger than the density of the design variable ρ.

As only densities above the threshold value are projected towards solid, and the remaining densities towards void, it is not possible to define a minimum length scale due to the presence of intermediate densities and due to the distribution hereof differing for each problem. Thus, for a given problem, it is unknown if an arbitrary combination of projection thresholds and filter radii will result in a definite minimum length scale for all solid and void areas and its size is not determinable a priori. The effect is exemplified in Figure 2.14 for a given filter radius and linear density filtered feature.

The relation between maximum filtered density of the solid and void phases and the ratio of width w to filter diameter $2R$ is plotted in Figure 2.15. As illustrated in Figure 2.14, if the projection threshold is greater than the maximum of the solid phase ($\tilde{\rho}_{max}$), the density is projected to void with no associated length scale on this phase. Similarly, if the threshold is less than the maximum of the void phase ($\tilde{\rho}_{min}$), the density is projected to solid also with no length scale. This corresponds to the values above the solid line for the solid phase, and the dashed line for the void phase in Figure 2.15.

2.4.4 Robust Topology Optimization

The robust method to TO is introduced in order to account for manufacturing constraints and to ensure a minimum length scale on the three-field problem [Sigmund, 2009]. This is accomplished by solving three FE problems - defined based on the image morphology operators erosion and dilation. Erosion makes the considered element void if any element in its neighborhood is void. Conversely, dilation makes the considered element solid if any neighboring elements are solid. In discrete form they correspond to min and max operators, respectively (a relaxed implementation is required for sensitivity-based optimization, however). A FE problem is defined and solved for the erosion-based (eroded) design, for an intermediate

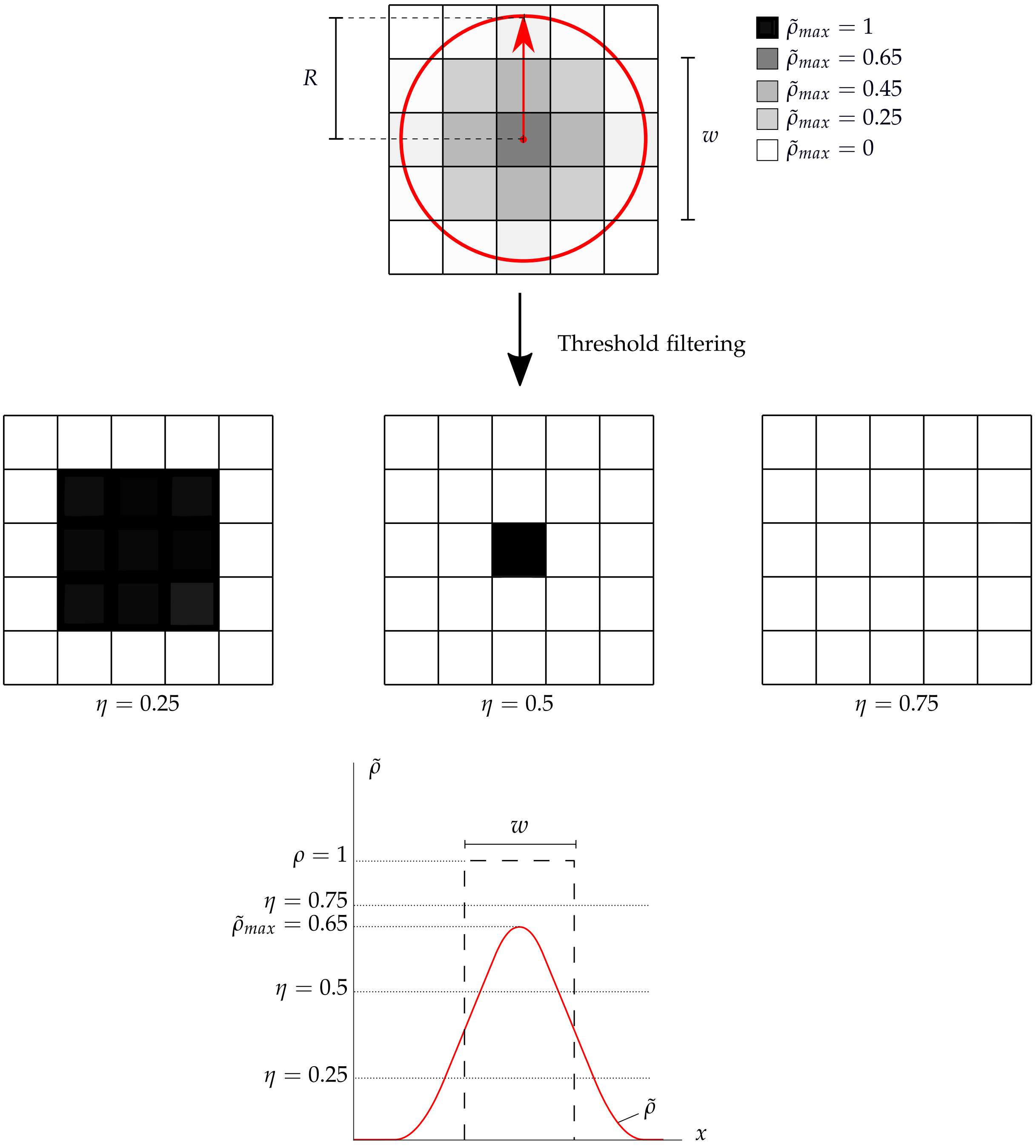

Figure 2.14. Effect of applying threshold projection to an area of intermediate density. The choice of the threshold variable significantly affects the size of the projected structural member's width. The bottom figure illustrates the filtered width and the resulting length scale attained for different values of η. Note that no length is associated with $\eta = 0.75$, since the maximum filtered density is less than the threshold value.

design and for the dilation-based (dilated) design. Optimization is subsequently performed as minimization/maximization of the worst case and subject to constraints for each of these designs. Constraining the problem for all three designs defines allowable tolerances on the blueprint design (i.e. the intermediate design), which ensures that uncertainties of the manufacturing process is taken into account.

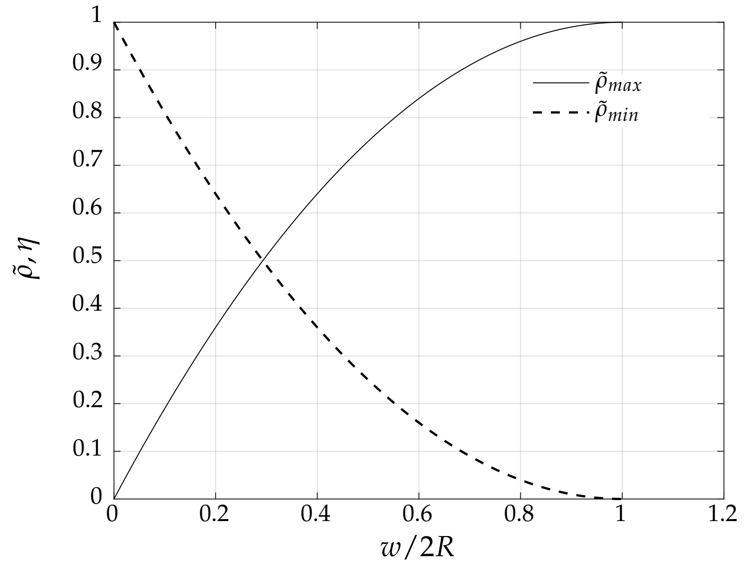

Figure 2.15. Illustration of the boundaries where densities are projected to solid in the case of $\eta > \tilde{\rho}_{max}$ or void if $\eta < \tilde{\rho}_{min}$.

In Sigmund [2009] the robust TO problem is formulated with the intermediate design consisting of the original design variables $\boldsymbol{\rho}$, the dilated design using the original Heaviside filter of Equation (2.11) and the eroded design using the modified Heaviside filter of Equation (2.12). Wang et al. [2011] presented a modified approach, where the threshold filter of Equation (2.14) is used to formulate the designs. The eroded and dilated designs are formulated based on associated threshold values η_e and η_d, respectively. To remove computational instabilities appearing, when using the unfiltered design variables, the intermediate design is reformulated as a three-field formulation, using a threshold value of $\eta_i = 0.5$.

Using this formulation, it is possible to guarantee a definable minimum length scale on the intermediate design if the three designs share the same topology. If this requirement is fulfilled, the solid phase minimum length of the intermediate design is bound by the eroded design and for the void phase it is bound by the dilated design. If a feature is not in the dilated and eroded design, the projection is not controlled in the intermediate design cf. Figure 2.15.

In Qian and Sigmund [2013] an analytical expression for the minimum length scale is derived for use in conjunction with robust TO. The minimum length scale is governed by filter radius R, minimum length l_e and the eroded threshold value η_e:

$$\frac{l_e}{R} = \begin{cases} 2 - 2\sqrt{1-\eta_e}, & \eta_e \in [0.75, 1] \\ 2\sqrt{\eta_e - 1/2}, & \eta_e \in [0.5, 0.75] \end{cases} \tag{2.16}$$

As the robust formulation does not enforce equivalent topology between the designs some parameter tuning on the threshold values and filter radius may be required to ensure a minimum member length. This is required in the case of $\eta_e \geq \tilde{\rho}_{max}$, where the eroded projection will result in a purely void feature, see Figure 2.14. An example of robust TO is solved and the three designs are shown in Figure 2.16.

Figure 2.16. Results of minimizing volume subject to a compliance constraint on the MBB-beam using robust TO. From left: eroded ($\eta = 0.75$), intermediate ($\eta = 0.5$) and dilated ($\eta = 0.25$) designs.

The robust method is inherently computationally expensive as it entails solving the three FE problems - especially for large scale models or in case of using higher order finite elements. If the sole purpose of using the robust method is to enforce a minimum length scale on the problem, geometric constraints [Zhou et al., 2015] may be used as an alternative. The geometric constraints explicitly enforce a minimum length scale, requiring only a solution of a single FE problem. In this work, focus is placed on using the robust method due to the other associated benefits, mainly because the method introduces robustness of the design against changes made in subsequent postprocessing. Implementation of geometric constraints is therefore left for further work, see Chapter 7.

2.4.5 Boundary Effects

Filter boundary effects are often neglected when performing TO and Neumann boundary conditions are implicitly used, perhaps unintentionally. This however imposes undesirable effects leading to poor geometry in the optimized solution. These effects are in Clausen and Andreassen [2017] classified as:

1: Minimum length scale is not satisfied at boundaries.
2: Structural edges are forced to become perpendicular to the domain boundary.
3: The structure tends to "stick" to the domain boundary.

These issues are illustrated in Figure 2.17.

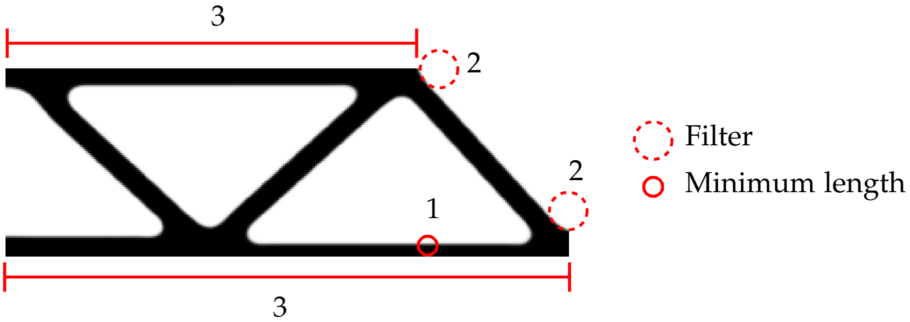

Figure 2.17. Highlight of the effect of the issues presented on a MBB-problem with volume minimization objective and subject to a compliance constraint. Because the Neumann boundary conditions act as symmetry conditions, issue 1 is especially apparent at the bottom structural member, which thickness is only half of the prescribed minimum length scale. At the top right corner of the optimized beam, issue 2 is observed as the geometry is forced to become perpendicular to the domain edges. Issue 3 is observed everywhere the geometry is in contact with the domain boundary, but it is especially obvious at the occurrence of issue 2.

The implicit Neumann condition occurs because only elements in the domain are considered, thus each element in a half circle around a boundary element has double importance in the filter weighting, see Figure 2.18. This is functionally the same as assuming element density symmetry at the boundaries which explains the occurrence of issues 1 and 2. Issue 3 is caused by two factors. The first is issue 2 by which structural edges must be perpendicular to the domain boundaries and thus the geometry cannot smoothly curve away from the edges. The second is that the filter is only applied inside the domain and elements at the structural edges are not filtered with void, whereby no density gradient exists at the boundary and the required quantity of material is achieved with less geometric width.

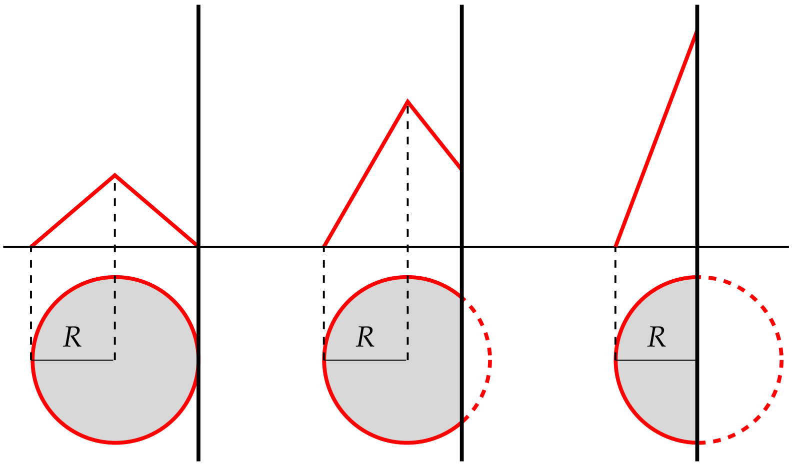

Figure 2.18. As the considered point approaches the domain boundary, the filter effectively changes shape. The relative weightings of the filter, illustrated as the height, increase to maintain consistent averaging in the filter.

Domain Extension Approach

An elegant solution to the three issues is proposed by Clausen and Andreassen [2017] termed the domain extension approach. Here, the FE domain is extended at least one filter radius in all directions by a distance d_{ext}, i.e. $d_{ext} \geq R$. The extension is performed at all boundaries, except where boundary condition are applied to the FE problem, see Fig 2.19. The erroneously defined Neumann boundary conditions are thereby moved to the boundary of the extended domain instead of at the design domain, such that they do not affect the problem. The elements added via the extended domain are used as those in the original domain, with the exception that while the new elements have density, the density variable is not updated in optimization, only through filtering (i.e. the new elements have a density variable but not a design variable). As a consequence, the linear density model will exceed the design domain boundaries if no explicit constraint is formulated. If applying the robust method with projection thresholds larger than zero, the boundary violation will be reduced, as some of the density gradient is projected to void. One way to ensure the no boundary violation is to introduce an upper limit on the density values in the extension region. If the limit chosen is lower than the threshold value, the entire gradient of density will be projected to void by the threshold filter. This approach

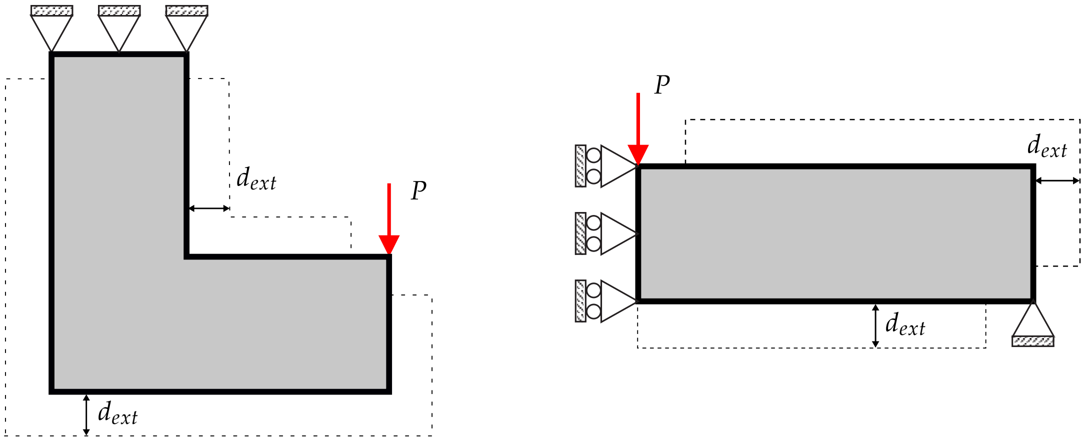

Figure 2.19. The MBB and L-beam problems reformulated with extended FE domains.

is however artificial, and minimum length scale control is lost at the boundaries. Results are illustrated in Figure 2.20, which show a side-by-side comparison of the MBB-beam problem solved as normally and with domain extension.

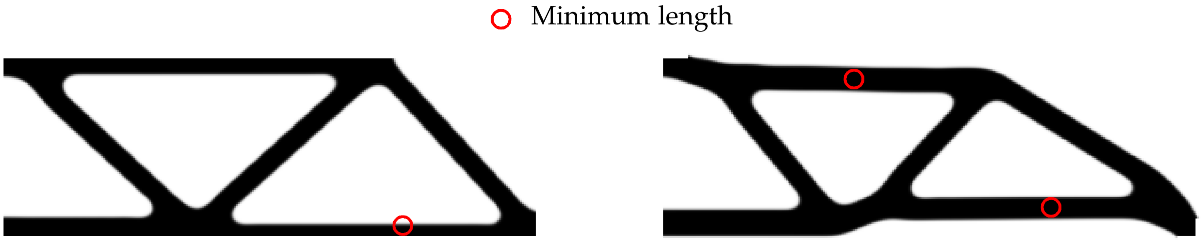

$m = 0.3973$ $m = 0.4779$

Figure 2.20. *Left*: MBB-beam problem solved without domain extension. *Right*: Using domain extension and accounting for boundary effects, the geometry is notably different. The consistent enforcement of minimum length scale via domain extension can incur more material, which causes the difference of volume.

3 | Fatigue Function Formulation

This chapter presents the fatigue modeling used to develop the optimization functions. The concepts of stress-based optimization are revisited as the inherent problems must also be accounted for in fatigue optimization. An isotropic stress-life fatigue model is presented. AM and relevant fatigue characteristics are subsequently presented and discussed with respect to the published literature on the topic. From this an anisotropic fatigue criterion is formulated.

3.1 Concepts of Stress-based Topology Optimization

In developing the fatigue model and criteria based on an equivalent stress measure, stress-based TO has to be considered as its associated problems translate directly to fatigue optimization. Stress-based TO was introduced to achieve designs with structural integrity against common local failure mechanisms, where structural compliance is inadequate. The most obvious example is yielding, particularly wrt. geometric stress concentrations. The area has been the subject of much research and many solutions to its inherent issues have been proposed.

3.1.1 Stress Criteria

In the context of FE analysis, stress is computed on the element level. For the linear elastic case, the penalized stress vector $\bar{\boldsymbol{\sigma}}$ is computed from element displacements using Hooke's constitutive law:

$$\bar{\boldsymbol{\sigma}}^{(e)} = \bar{\mathbf{E}}^{(e)}\mathbf{B}^{(e)}\mathbf{u}^{(e)} \tag{3.1}$$

where $\bar{\mathbf{E}}^{(e)}$ is the penalized constitutive matrix, $\mathbf{B}^{(e)}$ is the strain-displacement matrix and $\mathbf{u}^{(e)}$ is the element displacement vector. The explicit penalization follows the formulation of the standard SIMP formulation:

$$\bar{\boldsymbol{\sigma}}^{(e)} = \left(\tilde{\rho}^{(e)}\right)^{p} \mathbf{E}^{(e)}\mathbf{B}^{(e)}\mathbf{u}^{(e)} \tag{3.2}$$

where $\tilde{\rho}$ indicates the regularized density measure and $\mathbf{E}^{(e)}$ is the unmodified material constitutive matrix. If RAMP is used for stiffness penalization, the RAMP expression is inserted for $\bar{\mathbf{E}}^{(e)}$ instead.

To formulate the stress function for optimization, the stress has to be related to the material strength. For ductile materials the von Mises reference stress measure σ_{VM} can be used:

$$\bar{\sigma}_{VM} = \frac{1}{\sqrt{2}}\sqrt{(\bar{\sigma}_x - \bar{\sigma}_y)^2 + (\bar{\sigma}_y - \bar{\sigma}_z)^2 + (\bar{\sigma}_x - \bar{\sigma}_z)^2 + 6(\bar{\tau}_{xy}^2 + \bar{\tau}_{yz}^2 + \bar{\tau}_{xz}^2)} \tag{3.3}$$

For a brittle material, the first principal stress σ_1 can be used, given here for plane stress:

$$\bar{\sigma}_1 = \frac{\bar{\sigma}_x + \bar{\sigma}_y}{2} + \sqrt{\left(\frac{\bar{\sigma}_x - \bar{\sigma}_y}{2}\right)^2 + \bar{\tau}_{xy}^2} \tag{3.4}$$

If compressive stresses are of interest, the minimum principal plane stress is defined as:

$$\bar{\sigma}_2 = \frac{\bar{\sigma}_x + \bar{\sigma}_y}{2} - \sqrt{\left(\frac{\bar{\sigma}_x - \bar{\sigma}_y}{2}\right)^2 + \bar{\tau}_{xy}^2} \tag{3.5}$$

For the general case the principal stresses may be found either by Mohr's circle equations or as eigenvalues of the stress tensor.

3.1.2 Singular Optima

When solving optimization problems there may exist unreachable optima due to degenerate subspaces or regions of the design domain being closed off by the constraint equations. This problem is known to cause issues in stress-based structural optimization in general and was highlighted in Sved and Ginos [1968], where mass minimization of a three-truss system subject to stress constraints was considered. The optimized solution would contain all three trusses, however the analytical solution to the problem showed that the actual optimal solution is a two-truss system. Investigation of the solution space of the three-truss problem was done in Kirsch [1990], where it was clarified that the problem occurs due to the true optimum being located in a degenerate subspace. This is termed a singular or degenerate optimum. For the truss problem, this corresponds to the inability to remove the redundant truss, because of the presence of the stress constraint associated with this specific truss. Similarly for the general FE problem, the optimizer may converge to a sub-par solution because it is not able to reach singular optima. Illustrative examples of how the design space is affected are shown in Bruggi [2008] and Olesen and Hermansen [2019].

To reach these singular optima, the problem is relaxed. By relaxation it is possible to expand the feasible design domain to include the singular optima. Two methods are primarily used: ε-relaxation and qp-relaxation. Both are developed by considering truss-problems, but are applicable for the general continuum case. In the ε-relaxation [Cheng and Guo, 1997] an adequately small number ε is introduced on the right hand side of the constraint function f, allowing a small violation:

$$\frac{f}{f_{lim}} - 1 \leq \varepsilon \tag{3.6}$$

where f_{lim} is the constraint limit, e.g. the material yield stress S_y. This small value of ε must be chosen such that the design space is opened to include the singular optimum without deteriorating the accuracy of the constraint function. Choosing the ε value is heuristic and finding the adequate value may be rather time consuming, especially for large models. Typically a continuation approach is applied to ε where it is gradually decreased in order to end up in a good optimum. Continuation approaches are described further in Chapter 5.

An alternative relaxation scheme is the qp-relaxation method [Bruggi, 2008]. Here, relaxation is introduced by implementing a relaxation factor q replacing p:

$$\bar{\boldsymbol{\sigma}}^{(e)} = \left(\tilde{\rho}^{(e)}\right)^q \mathbf{E}^{(e)}\mathbf{B}^{(e)}\mathbf{u}^{(e)} \tag{3.7}$$

The benefit of the qp-method is that the stress measure is formulated to further penalize intermediate densities. This is achieved by defining the relaxation factor in the interval $0 < q \leq 1$. Note that this definition of q is different from that of Bruggi [2008], which uses $p - q$ to define the same measure. For elements with intermediate density the stress measure will be higher, thereby making either fully void or solid density the most economical choices for the optimizer, see Figure 3.1. It should be emphasized that relaxation is purely a mathematical manipulation applied in order to be able to solve the problem. As such, stresses for $0 < \tilde{\rho} < 1$ do not have an exact physical interpretation. Ultimately, the sought solution is however a design which does not contain intermediate densities, since these are not physically consistent either. Thus, if intermediate densities are successfully penalized to void and solid states, the stress measure will again be coherent. This increases the attractiveness of using the qp-method, due to the increased penalization of the densities.

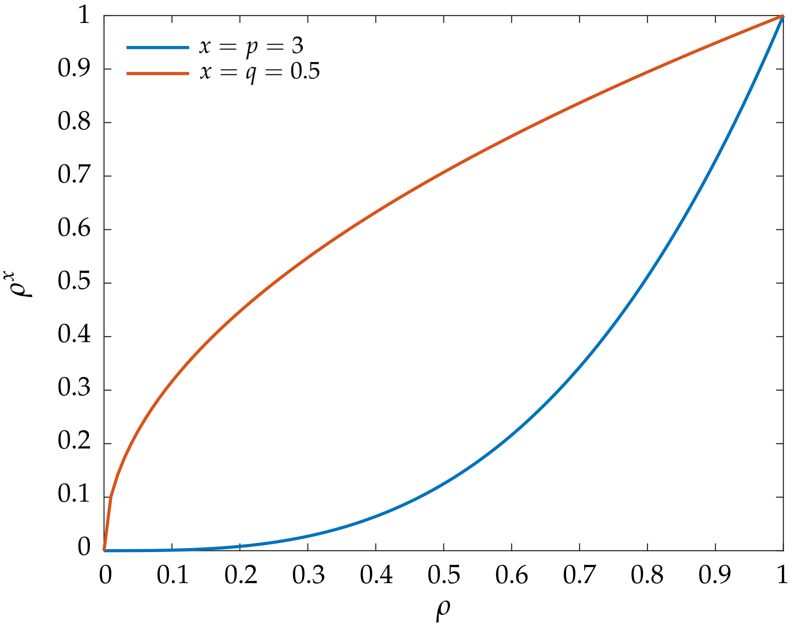

Figure 3.1. Illustration of the relaxation ($q = 0.5$) compared to stiffness penalization ($p = 3$).

3.1.3 Global Aggregation

Using element stresses to define constraints results in N_{elem} functions, which makes the optimization problem inherently large, as many elements are desired for accuracy. In order to efficiently make use of sensitivity-based methods, it is desired to reduce the amount of constraints while still having a continuous and differentiable expression. This is accomplished by using an aggregation function to scalarize the constraints, e.g. by the P-norm [Duysinx and Sigmund, 1998], the P-norm mean (P-mean) or the Kreisselmeier-Steinhauser (KS) functions [Martins and Poon, 2005]. The functions are given in equations (3.8), (3.9) and (3.10).

$$\text{P-norm:} \qquad f_\Psi = \left(\sum_{e=1}^{N_{elem}} \left(f^{(e)} \right)^P \right)^{\frac{1}{P}} \tag{3.8}$$

$$\text{P-mean:} \qquad f_\Psi = \left(\frac{1}{N_{elem}} \sum_{e=1}^{N_{elem}} \left(f^{(e)} \right)^P \right)^{\frac{1}{P}} \tag{3.9}$$

$$\text{KS:} \qquad f_\Psi = \max(\boldsymbol{f}) + \frac{1}{P} \ln \left[\sum_{e=1}^{N_{elem}} \exp\left\{ P \left(f^{(e)} - \max(\boldsymbol{f}) \right) \right\} \right] \tag{3.10}$$

Here, $f^{(e)}$ is the element function value, $\boldsymbol{f}$ is a vector with all function values, f_Ψ is the aggregated measure and P is a factor governing the accuracy of the aggregation. The aggregation functions aims at approximating the maximum value of the functions which is approached as $P \to \infty$. In general a rather large value of P is needed to accurately capture the maximum. Each function aggregates values differently and the resulting function trajectories are therefore different. How aggregation is performed by these functions and the accuracy attained with different values of P are illustrated in Figure 3.2. The aggregation functions are studied in detail in Olesen and Hermansen [2019], where it is concluded that if an adequate P-value is chosen combined with adaptive constraint scaling (presented in the following), all aggregation methods achieve good results. As the P-norm method has the most simple formulation, it will be used exclusively for local constraint aggregation in this work.

Adaptive Constraint Scaling

Adaptive constraint scaling [Le et al., 2010] is introduced in order to achieve higher accuracy from the aggregation functions, when used to define constraints in the optimization problem, allowing for the use of lower values of P thereby decreasing the nonlinearity of the expression. The method is based on defining a scaling factor c by normalizing the aggregated value with the maximum function value from previous iterations. The function is then defined by multiplying the aggregated value with the scaling factor. Computation of the adaptive scaling factor for iteration k is shown in Algorithm 1.

Because of the max-operator used in defining the scaling factor the function becomes discontinuous and thereby non-differentiable. However, as the problem converges, the local measure becomes better distributed in the design, and thus the maximum is more accurately approximated by the P-norm function alone. The factor therefore converges along with the problem reducing the nondifferentiability. The α variable is a damping parameter defined in order to prevent oscillation in the scaling factor. This is necessary due to the scaling factor's discontinuous nature as the maximally stressed element may change between iterations. Algorithm 1 is presented with the same values for reducing and increasing the α-parameter as is used in Oest and Lund [2017], but these can be changed depending on the behavior of the problem.

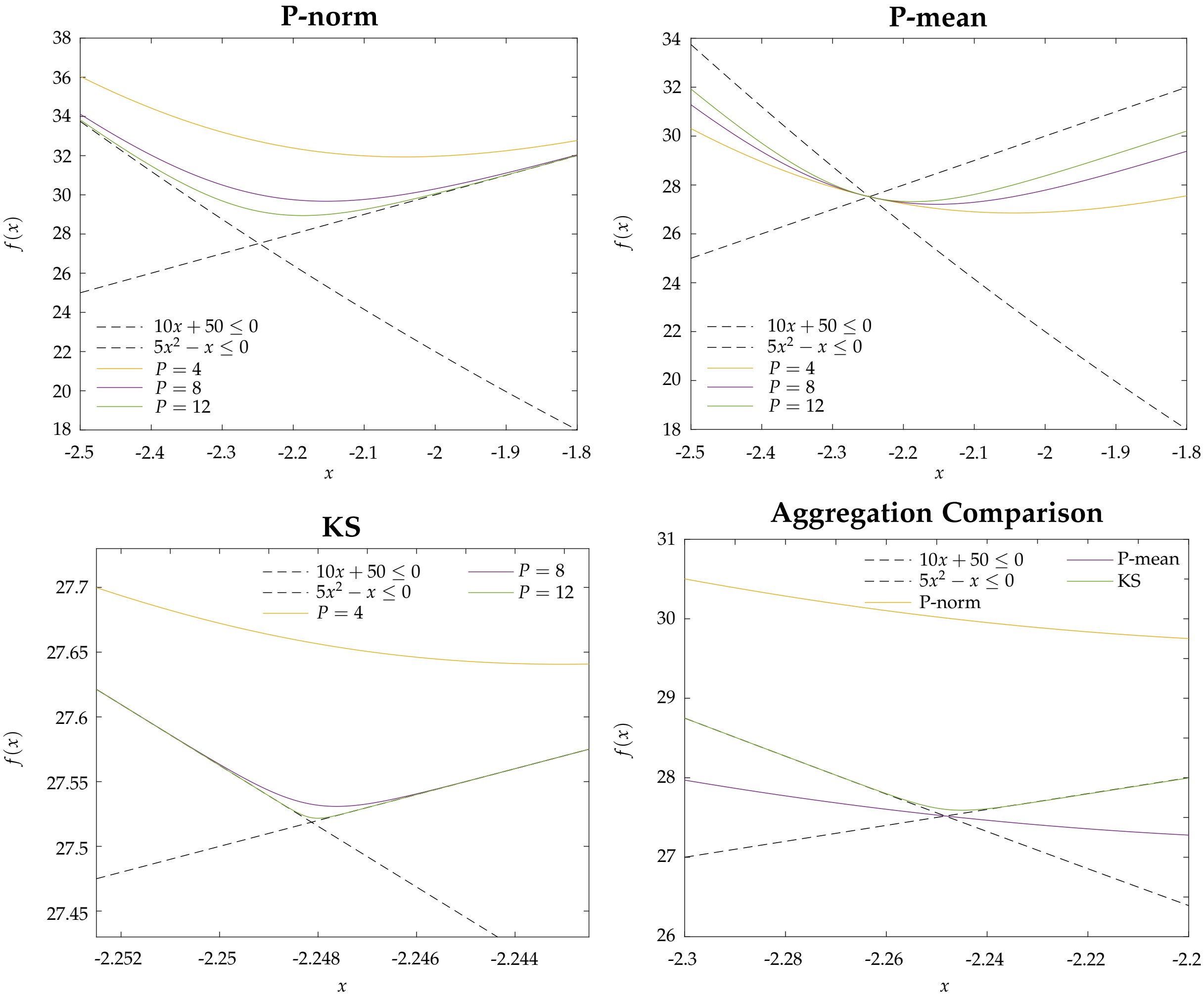

Figure 3.2. Comparison between three aggregation functions. Note the difference in scale between top and bottom. Bottom right aggregation is done at a constant penalty factor $P = 8$. Figure from Olesen and Hermansen [2019].

3.1.4 The Problem of Jagged Edges

In academia, TO is often performed using a pixel- or voxel-based mesh. The high level of discreteness as a result of projection filters, see Subsection 2.4.3, causes a problem when solving FE-problems involving stress. For these formulations, the problem is conspicuous in all non-axis parallel geometry, which will contain jagged geometry. The same effect will occur for a body-fitted mesh, which is used in commercial FE software, particularly from distorted elements, as sharp edges hereof may protrude from the geometry in the optimized layout. If a linear density filter is used, this effect is removed by the density gradient, smoothing the sharp transition of the jagged edges. However if a Heaviside-based filter is applied to increase discreteness, the corners of jagged elements will reappear and will impose stress singularities in the model. These effects are seen in Figure 3.3, where the jagged edges cause an increase of the stress, such that it exceeds the set limit (262 MPa), despite densities primarily being projected toward solid due to the filter formulation applied To compensate for the increase in stress, even more material will be required in this design, resulting in a higher final volume of

Algorithm 1: Calculation of adaptive constraint scaling factor. $k = 0$ initially as three function values are required to determine oscillation.

```
Data: Iteration history.
Result: Computation of $c^{(k)}$.
Initialization;
if iteration $k \leq 2$ then
    $c^{(k)} = \frac{\max\left(\boldsymbol{f}^{(k)}\right)}{f_{\Psi}^{(k)}}$
    $\alpha^{(k)} = 1$
else
    if function oscillates then
        $\alpha^{(k)} = \max(0.5, 0.8\,\alpha^{(k-1)})$
    else
        $\alpha^{(k)} = \min(1, 1.2\,\alpha^{(k-1)})$
    end if
    $c^{(k)} = \alpha^{(k)} \frac{\max\left(\boldsymbol{f}^{(k-1)}\right)}{f_{\Psi}^{(k-1)}} + (1 - \alpha^{(k)})c^{(k-1)}$
end if
```

the optimized structure.

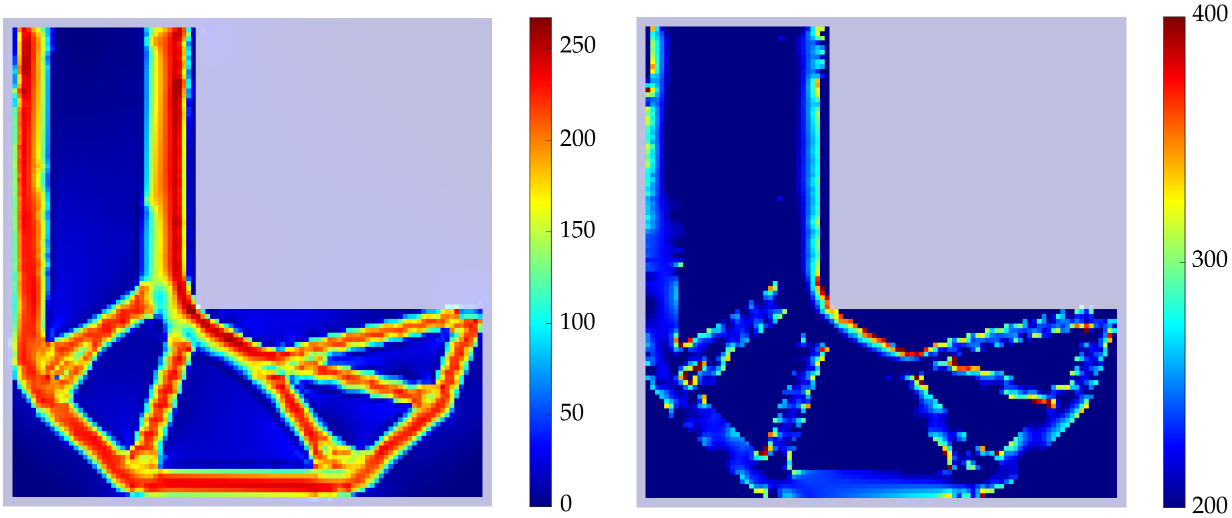

Figure 3.3. Results of a stress-based optimization of the L-beam with plots of the stress for linear density variables (left) and for projected density variables using a threshold filter (right) with $\eta = 0.05$, i.e. similar to the filter of Equation (2.11), yet with a low threshold to avoid projection of very low density elements. The problem is solved with the settings of Section 2.3, except for the load which is increased to 75 kN.

The stress in the interior structure (i.e. in elements that are located away from the structures edges) is of a similar level for the two filters, as it is not affected by the concentration near jagged edges. To remove the stress singularities, Svärd [2015b] proposed a framework for performing an extrapolation of the stress from the interior elements in the mesh to the boundary elements termed Interior Value Extrapolation (IVE). The stress measure is thereby determined in a part of the model, where the stress measure is correct. The concepts of this method are similar to computing improved FE stresses through extrapolation from the superconvergent element Gauss points, see e.g. Cook et al. [2002].

Another approach is to accept a small gradient of intermediate density around the boundary of the structure. The size of this gradient is controlled by the discreteness parameter β of the projection filter. This is utilized in da Silva et al. [2019], which determines the allowable size of the density gradient for a given problem by considering the slope of the threshold filter and numerical studies of the relaxation parameter chosen (in this case the ε-relaxation approach). The analytical expression for the maximum β-value is:

$$\beta_{lim} = \frac{2R}{L^{(e)}} \tag{3.11}$$

where $L^{(e)}$ is the element length size. This should be used together with numerical studies of relaxed stress behavior to ensure that the limit is low enough to avoid singularities. da Silva et al. [2019] developed the measure to be used along with the ε-method and suggests redoing the study if using the qp-method. Similar results as those achieved by the authors of the expression are therefore not expected. Yet, the expression is simple and easy to apply and implementations in this work are therefore based on this method. However, the IVE-method and its associated concepts seem promising and is an interesting topic for further investigation, as it would allow for using larger values of β in the threshold filters resulting in more discrete designs, see Chapter 7 for further discussion.

When transitioning from the FE model to a design the geometry has to be smoothed to remove the jaggedness of the boundaries. For the two-dimensional case, this is performed simply by drawing a contour around the structure using a defined cut off value. In case of the general three-dimensional case this is not a trivial task. The problems are discussed in detail in Appendix A, where a geometric density-interpolation method is developed and presented.

3.2 Fatigue Analysis

This section is based on Stephens et al. [2001].

Fatigue is one of the most important criteria in structural design, as fatigue failure accounts for 50-90% of all mechanical failures in machinery. As compared to more traditional criteria in TO, such as compliance, buckling and stress, fatigue is not an intrinsic result of the linear elastic problem, but relies on additional external factors, e.g. load history, surface quality, geometric size of material and operating temperature.

Specifically, fatigue analysis entails quantifying the lifetime of a component under repeated loading. This is done using one of two approaches; the stress-life (SN) approach or the strain-life (εN) approach. The latter is in general considered the better option, as each point on the stress-strain curve is uniquely defined for a given strain. This is especially beneficial when considering low-cycle fatigue (LCF), which is defined in the interval $1 - 10^3$ cycles, see Figure

3.5, and the primary mechanism of failure is plastic deformation. For high-cycle fatigue (HCF), defined in the interval $10^3 - 10^6$ cycles, the governing failure mechanism is elastic deformation. In this case the SN-approach is sufficient, however the εN-method is just as effective. Only HCF is considered in this work and as stress data is more prevalent in literature, the SN-approach will be used exclusively. In terms of modeling AM materials, see Section 3.4, the εN-approach has some distinct benefits, as considerations of fracture mechanics can be included to model defects. Inclusion of this model is discussed further in Chapter 7.

3.2.1 Characterizing Load History

Repeated loading is separated into two types: proportional and nonproportional. The proportional case occurs when the loading is in-phase, i.e. principal directions are constant everywhere for the entire load history, and nonproportional covers all other cases. The implications of proportional loading are particularly evident in the context of FE, in which a proportional load may be expressed as:

$$\mathbf{F}(t) = c(t)\ \hat{\mathbf{F}} \tag{3.12}$$

where $\mathbf{F}(t)$ is the load vector at some time t in the load history and $c(t)$ is a scalar function describing the load history by scaling a constant reference load vector $\hat{\mathbf{F}}$. For linear elastic problems, the load vector is directly proportional to the stress vector, and thus it can be shown via equations (2.1) and (3.1) that the same scaling applies to element stress, such that:

$$\boldsymbol{\sigma}^{(e)}(t) = c(t)\ \hat{\boldsymbol{\sigma}}^{(e)} \tag{3.13}$$

where $\hat{\boldsymbol{\sigma}}^{(e)}$ is the reference element stress. Because the stress state for the entire history is determined from the reference load, it follows that solving only a single FE problem is required. This scalar relationship does not apply to nonproportional loading, where the stress state must be calculated individually for any point in the load history (i.e. the FE problem must be solved for a new load vector), which immensely increases the computational effort required to solve a problem with a nontrivial load history. In the present work, only proportional loading is considered. For taking non-proportional loading into account in the optimization, see Zhang et al. [2019].

If variable amplitude loading is present, a counting method must be used to consistently count loads. One commonly used is rainflow counting, once the load history has been discretized into peaks and valleys. In the case of proportional loading, application of rainflow counting yields a scaling factor for amplitude and mean stress for each load combination:

$$\boldsymbol{\sigma}_a^{(e,i)} = c_a^{(i)}\ \hat{\boldsymbol{\sigma}}^{(e)} \qquad \text{and} \qquad \boldsymbol{\sigma}_m^{(e,i)} = c_m^{(i)}\ \hat{\boldsymbol{\sigma}}^{(e)} \tag{3.14}$$

where $\boldsymbol{\sigma}_a^{(e,i)}$ is the amplitude stress, $\boldsymbol{\sigma}_m^{(e,i)}$ is the mean stress, $c_a^{(i)}$ and $c_m^{(i)}$ are the scaling factors for amplitude and mean respectively, and $\hat{\boldsymbol{\sigma}}^{(e)}$ is the reference relaxed element stress - as well as having e indicate the element and i indicate the load combination. The load combination refers to the combination of amplitude and mean for a point in the discretized load history,

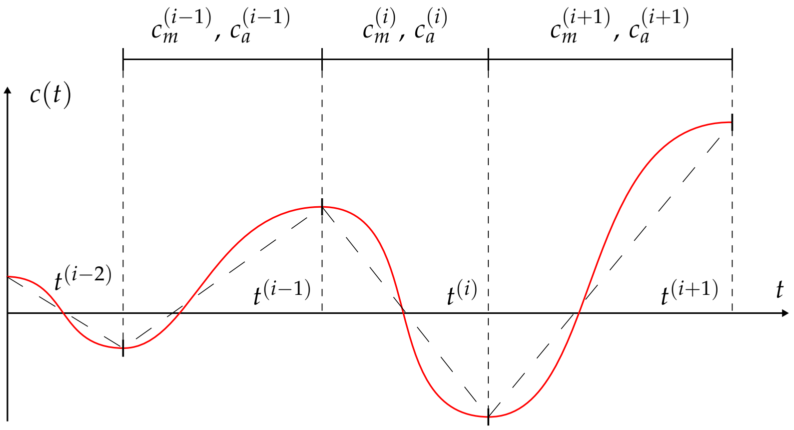

$$c_m^{(i)} = \frac{c(t^{(i-1)} + c(t^{(i)})}{2}$$

$$c_a^{(i)} = \frac{|c(t^{(i-1)} - c(t^{(i)})|}{2}$$

Figure 3.4. Discretization of load history into combinations of mean and amplitude factors $c_m^{(i)}$ and $c_a^{(i)}$.

see Figure 3.4. In some of the published literature considering fatigue TO, a random load history is generated in order to illustrate the use of counting methods in a TO context, see e.g. Oest and Lund [2017] and Zhang et al. [2019]. Here in the present work, only constant amplitude loading is considered, as it makes design interpretation more comprehensible and results replicable, although functions are defined to include an arbitrary set of loads.

3.2.2 The Stress-life Approach for Metals

The SN-approach is based on describing a SN-curve, which describes the cyclic behavior of the material, as illustrated in Figure 3.5 for a generic metal. The SN-curve is generated from

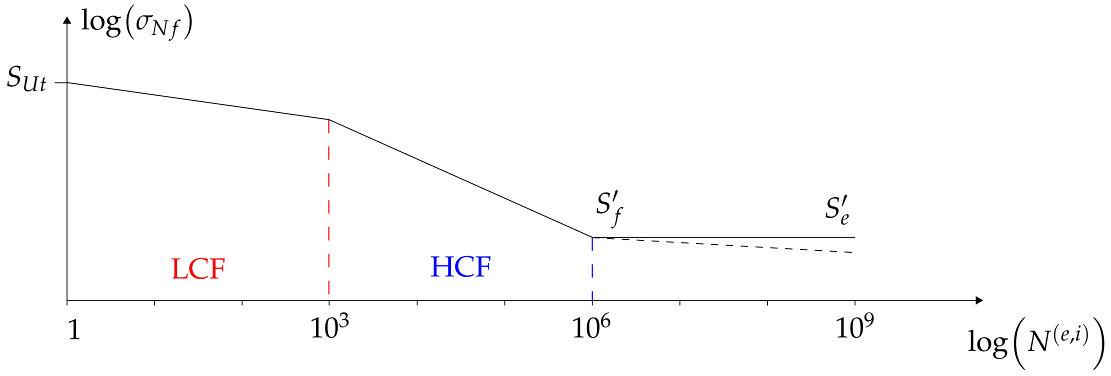

Figure 3.5. Generic SN-curve for a metal with the distinct regions of LCF, HCF and fatigue limit (S'_f) highlighted. This third region on the SN-curve occurs at 10^6 cycles, after which the slope is drastically reduced (dotted line). For steel the area is termed endurance limit (S'_e), and it is assumed that the fatigue strength is not reduced any further during loading.

experiments for a specimen of the considered material loaded in rotational bending, with a diameter $d \leq 8$mm, having smooth surfaces, at ambient temperature and with a reliability (risk of failure) of 50%. For designing for other cases than this, the fatigue limit is adjusted using corrections factors [Norton, 2014]:

$$S_f = C_{load}\, C_{surf}\, C_{size}\, C_{temp}\, C_{reliab}\, S'_f \tag{3.15}$$

where S_f is the corrected fatigue limit strength, S'_f is the uncorrected fatigue limit strength determined from experiments, and the C factors corrects the strength wrt. load, surface quality, size, temperature and reliability.

The HCF area of the SN-curve is approximated using Basquin's equation:

$$\sigma_{Nf}^{(e,i)} = \sigma_f \left(2N^{(e,i)}\right)^b \tag{3.16}$$

where $\sigma_{Nf}^{(e,i)}$ is the equivalent amplitude stress resulting in failure at number of reversals $N^{(e,i)}$, for element e and load combination i. σ_f is the true fracture strength of the metal and b is the exponent or slope of the SN curve, see Figure 3.6. The fatigue limit region is not accounted for during optimization. If it is desired to design components for lifetimes above 10^6 cycles, the optimization will produce overly conservative designs, due to the break in the curve not being accounted for. For steel, Zhang et al. [2019] and Oest and Lund [2017] explain that endurance limit area is problematic when calculating sensitivities, as the curve has no slope and thus these become zero. If it is desired to include this region in the optimization, a small slope has to be added to the curve. Alternatively, Zhang et al. [2019] suggested solving a stress-based TO problem constrained by the endurance limit strength.

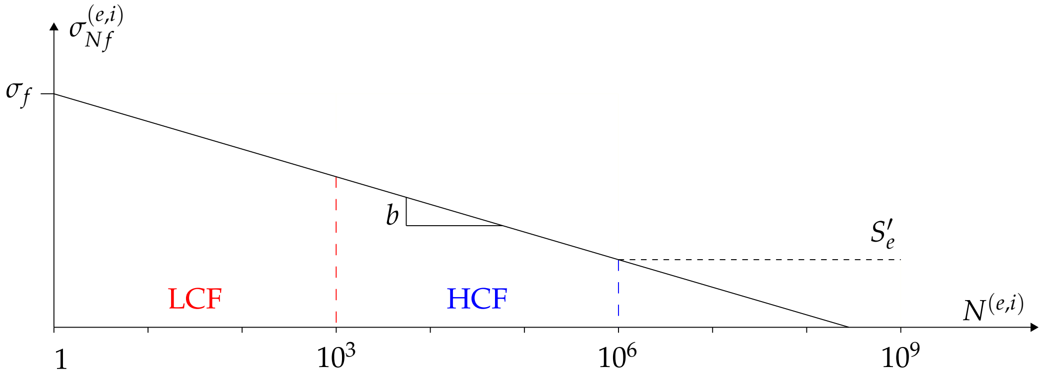

Figure 3.6. Illustration of the curve generated by Basquin approximation.

The SN-curve by itself only takes into account the amplitude stress. This is sufficient for the fully-reversed loading case, but for any other case, a nonzero mean stress is present, which also must be included in the analysis. Methods for mean stress correction include modified Goodman or Morrow corrections, see Figure 3.7. Modified Goodman is the more conservative of the two as it is calculated from the ultimate material tensile strength S_{Ut}:

$$\sigma_{Nf}^{(e,i)} = \sigma_a^{(e,i)} \frac{S_{Ut}}{S_{Ut} - \sigma_m^{(e,i)}} \tag{3.17}$$

The Morrow correction uses the true fracture strength of the material σ_f:

$$\sigma_{Nf}^{(e,i)} = \sigma_a^{(e,i)} \frac{\sigma_f}{\sigma_f - \sigma_m^{(e,i)}} \tag{3.18}$$

The choice of method depends on the desired safety margin. Goodman and Morrow methods are widely used because they are conservative. More complex corrections methods exist, such as Smith-Watson-Topper method [Smith et al., 1970], which provides higher accuracy in evaluation of the mean stress effects [Papuga et al., 2018]. The implementation in this work considers only the linear Goodman and Morrow expressions as they are presented in equations (3.17) and (3.18), i.e. the cut off, as illustrated in Figure 3.7, is not taken into account.

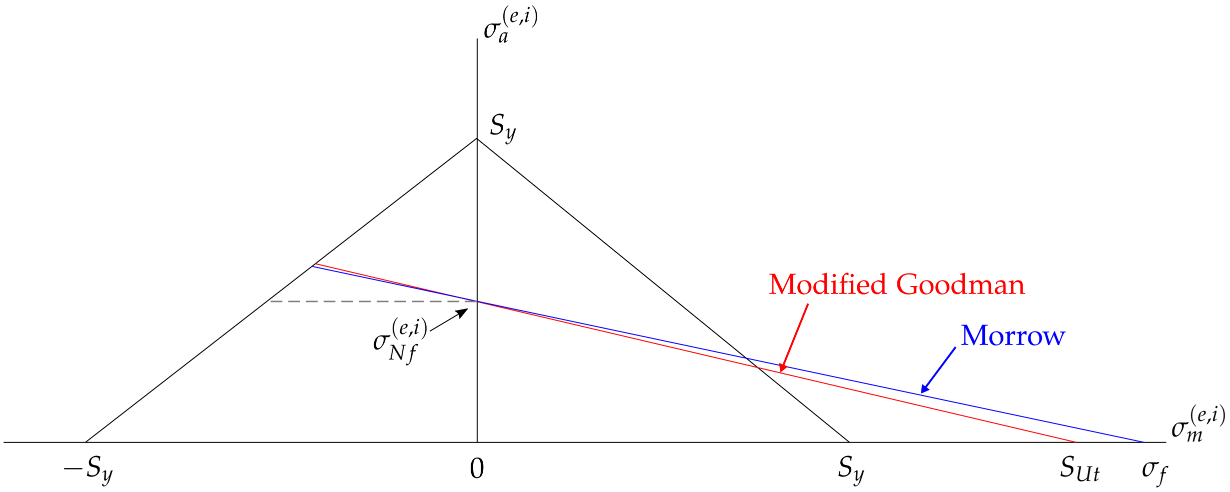

Figure 3.7. Illustration of how the modified Goodman and Morrow correct the equivalent stress. If the methods should account for both yielding and fatigue, a cut off should be made when the lines intersect the yield line ($S_y - S_y$). Compressive mean stress is in general beneficial to fatigue strength, however a conservative estimate is to not account for this and assume that compressive mean stress does not affect fatigue life (the dashed line).

3.2.3 Multiaxial Stress Criteria

As SN-curves and the methods for mean stress correction only apply to uniaxially loaded specimens, a criterion is needed to correlate the multiaxial loads of a general structure to the uniaxial strength data in order to be able to apply them. An option is to use the signed von Mises criterion [Zhang et al., 2019]. Here, the von Mises stress is used for computing both amplitude and mean stresses, where the sign of the hydrostatic stress is used to determine the sign of the mean stress:

$$\sigma_a^{(e,i)} = c_a^{(i)} \sigma_{VM}^{(e)} \tag{3.19}$$

$$\sigma_m^{(e,i)} = \operatorname{sgn}\left(c_m^{(i)} \sigma_h^{(e)}\right) c_m^{(i)} \sigma_{VM}^{(e)} \tag{3.20}$$

where the hydrostatic stress σ_h used for determining the sign is:

$$\sigma_h = \frac{\sigma_x + \sigma_y + \sigma_z}{3} \tag{3.21}$$

The equivalent stress is then computed by insertion into e.g. Morrow, Equation (3.18), or modified Goodman correction, Equation (3.17). Other, more complex, criteria can also be implemented, which will increase the accuracy of the fatigue model. Papuga [2011] provides a comprehensive overview and performance evaluation of many available methods for many different load cases. It is here concluded that critical plane methods (CPM) perform the best in predicting fatigue damage, however its use in an optimization context is limited as analytical sensitivities can not be derived, prohibiting the use of effective methods for sensitivity analysis. CPM is discussed further in Chapter 7.

3.2.4 Palmgren-Miner Linear Damage Accumulation

For all load combinations, Palmgren-Miner's damage accumulation rule is used to sum up the damage contributions:

$$D^{(e)} = \sum_{i=1}^{N_c} \frac{n^{(i)}}{N^{(e,i)}} \leq D_{lim} \tag{3.22}$$

Here, $D^{(e)}$ is the accumulated damage for the element e, $n^{(i)}$ is the number of reversals counted for a given load combination i, N_c is the amount of counted load combinations and D_{lim} is the allowed damage fraction. The rule is such that $D = D_{lim}$ is the expected crack formation, which is typically considered failure in most components. D_{lim} varies depending on the given case and is usually defined with respect to a standard or user experience. This work is not concerned with a single given situation, and therefore $D_{lim} = 1$ is used.

To use Palmgren-Miners rule the load history must be random, which excludes sequences and non-linear effects. The method is simple, however it appears to be as accurate as any other cumulative damage rule regardless of complexity.

To achieve a single expression for the damage, the element damages are aggregated using the P-norm method, i.e. Equation (3.8), and the adaptive constraint scaling method is used to achieve better approximation of the maximum damage in order to avoid using large exponents in the P-norm expression. Algorithm 1 is used to compute the adaptive constraint scaling factor - as was done for the stress function. Explicit constraint functions are given in Section 3.6.

3.3 Fatigue Function Scaling

Due to the high degree of nonlinearity in the formulation of the fatigue function, the problem is notoriously difficult to solve. In particular Basquin's formulation of the SN-curve, Equation (3.16), is highly sensitive to changes in stress level and can lead to very unstable problems.

Regional stress measures were introduced in Le et al. [2010] and París et al. [2010] to reduce the volatility of aggregated local constraints, by sectioning the design domain into several constraint functions, such that aggregation is done where the local measure is of a similar level. This was developed for stress constraints, but would also work for fatigue formulations [Holmberg et al., 2014]. Fatigue specific methods were later introduced to scale the element accumulated damage and reduce the nonlinear dependence of the stress levels, either by a logarithmic function [Oest and Lund, 2017] or a linearization by scaling the damage with the Basquin factor [Zhang et al., 2019]. The Basquin factor scaling is done by:

$$D_s^{(e)} = \left(D^{(e)}\right)^{-b} \tag{3.23}$$

where $D_s^{(e)}$ is the scaled damage, $D^{(e)}$ is the accumulated damage from Palmgren-Miner, and b is the Basquin factor. Studies in the scaling functions in Olesen and Hermansen [2019] concluded that the Basquin factor scaling method is preferable to logarithmic scaling and the latter is therefore not considered any further. It was also concluded that both methods have trouble converging to a fully damaged design, especially the Basquin factor scaling method.

An improved method is therefore proposed in order to have better damage distribution in the final design. It is based on using the P-norm mean function to approximate the minimum of unscaled and Basquin factor scaled damage:

$$D_s^{(e)} = \left(\frac{c_1 \left(D^{(e)}\right)^{b\,P} + c_2 \left(D^{(e)}\right)^{-P}}{c_1 + c_2} \right)^{-\frac{1}{P}} \tag{3.24}$$

where c_1 and c_2 are weighting factors and P is a penalty term similar or equal to that in Equation (3.8). This P-mean scaling is illustrated in comparison to no scaling and Basquin factor scaling in Figure 3.8.

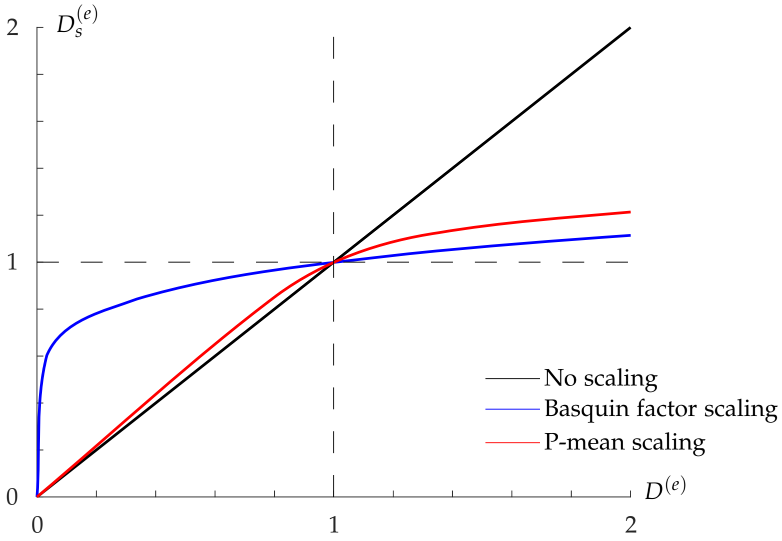

Figure 3.8. Damage scaling functions. *No scaling* refers to the unscaled damage computed from the Palmgren-Miner expression of Equation (3.22), *Basquin factor scaling* is Equation (3.23) and *P-mean scaling* is Equation (3.25) i.e. where $c_1 = c_2$. The Basquin factor is $b = -0.156$, and $P = 8$ is used for aggregation in the P-mean scaling.

From Figure 3.8 it is also evident why Basquin factor scaling is not able to converge to a fully damaged design. No scaling is of course entirely accurate, but the eventual constraint function is very sensitive and may change several orders of magnitude between iterations. Conversely, with Basquin factor scaling, the function will change more or less linearly with stress and convergence is relatively fast. However, any scaling of damage introduces an error in damage calculation and the Basquin factor scaling is inaccurate for damage that is not exactly 0 or 1, severely overestimating otherwise feasible damage (i.e. $D \leq 1$). The new scaling tries to remedy this by instead approximating no scaling for feasible damage, such that $D_s \leq 1$ is accurate while $D_s > 1$ has fast and stable convergence. As Basquin factor scaling is only approximated some penalty to convergence speed incurs, but the P-mean scaling is still much faster and much more stable than no scaling.

Equation (3.25) can be tuned to accommodate a specific behaviour. Using the same P as the aggregation function, i.e. as in the P-norm of Equation (3.8), and $c_1 = c_2$ the function reduces to:

$$D_s^{(e)} = \left(\frac{\left(D^{(e)}\right)^{b\,P} + \left(D^{(e)}\right)^{-P}}{2} \right)^{-\frac{1}{P}} \tag{3.25}$$

Resulting damage distribution when using this formulation of the P-mean scaling examined in-depth in Section 5.3.

3.4 Additive Manufacturing

This section is based on Yadollahi and Shamsaei [2017].

TO allows for a high level of freedom in design exploration unlike any other synthesis method available and is capable of generating designs with many complex features, see e.g. Aage et al. [2017]. Given this, the limiting factor for the final design is often the capability of the manufacturing method. Considering single-operation methods, they can be classified as either subtractive or additive methods. Subtractive methods are based on gradually removing material from a bulk piece to make a desired shape. One of the most common subtractive methods is CNC milling, where the operation is set up using computer programming. The process is in general fast, but as components become more complex the milling tool may be restricted from some areas of the geometry, in particular interior features and voids [Gibson et al., 2016]. Even if it is possible to manufacture the component by subsequent manual treatment or in multiple parts, the implications hereof increase the total lead time of component.

The other option, additive methods, refers to manufacturing components by adding material. This implies less restrictions on the geometric details in the part as the process has no accessibility constraints. It is thereby possible to shape a component in one operation, and although the operation is slower than the CNC milling process, the lead time may be reduced as the need for subsequent operations is reduced. Furthermore, much research is being devoted to improving the AM operation, implying that the technology will become increasingly capable. For metal components, the methods available are Powder Bed Fusion (PBF) methods and Direct Laser Deposition (DLD), see Figure 3.9. For classification of the AM methods and materials for which they should be used, see e.g. Clausen [2016].

When building a component, a support structure must be included if the design includes overhanging details. The reason for this is twofold; accounting for thermal and mechanical effects [Calignano, 2014]. Unfused powder provides higher insulation, so a melt-pool with little connection to surrounding fused material will become too large as the concentration of heat increases, which creates dross and poorly controlled geometry, see Figure 3.10. Further, because solidification happens between layer depositions, a support structure must be present to fix the component to the printing plate to prevent warping from residual thermal stresses. The necessity of this supporting material implies that more material is required to manufacture,

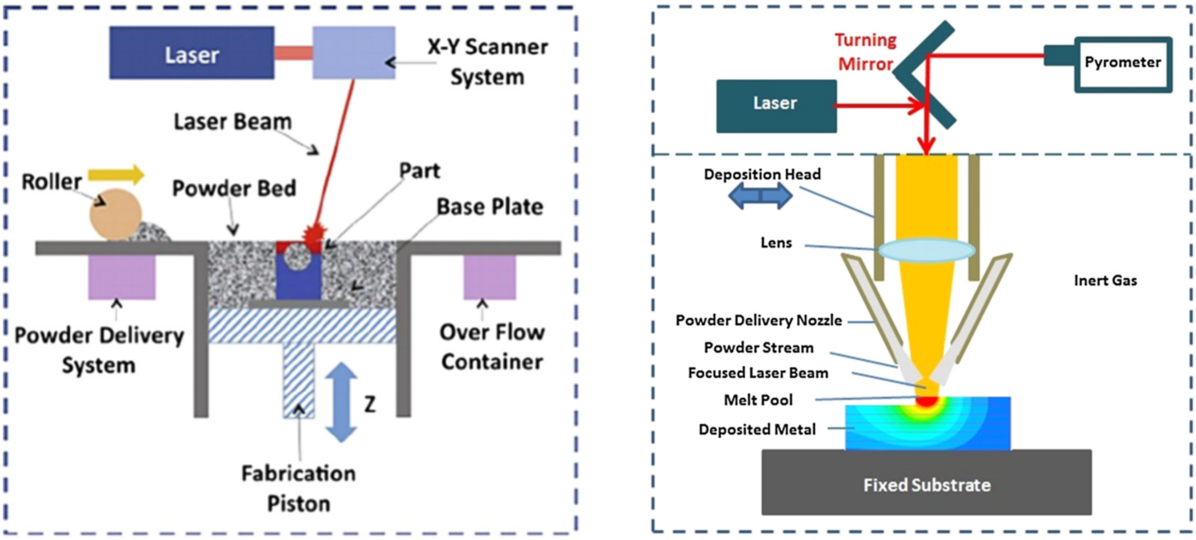

Figure 3.9. The process of Selective Laser Melting (SLM) - a PBF method (left) and DLD (right). Figures from Yadollahi et al. [2017] and Bian et al. [2015] respectively.

which increases build time, and post-treatment is required to remove the support material after printing. Optimization of this support structure to minimize material used is therefore almost given and works have been published on the subject, see e.g. Langelaar [2019].

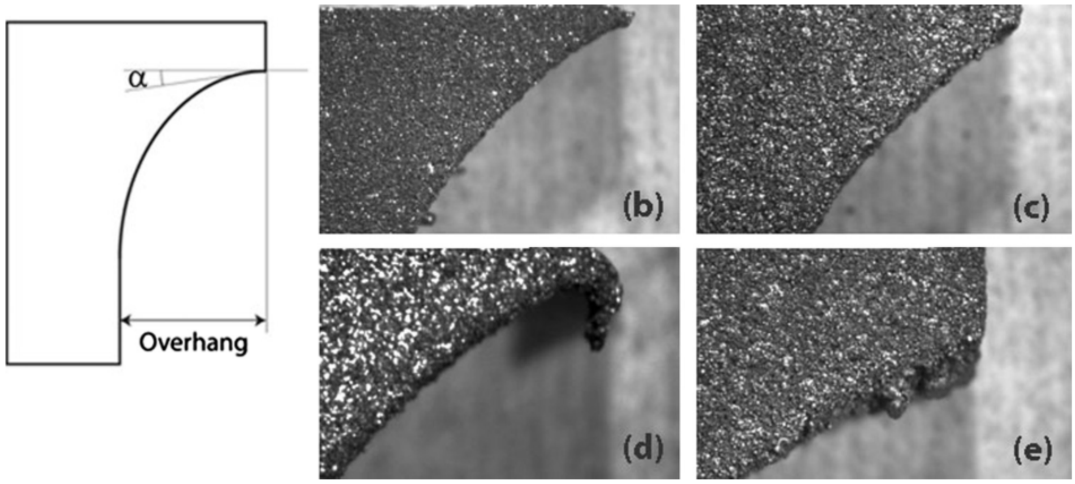

Figure 3.10. Effects of increased overhang; *(b)* and *(c)* illustrate a titanium and aluminum part respectively, with overhang radii of 9 mm. *(d)* and *(e)* illustrate the parts of the same respective materials with the overhang radii increased to 15 mm. Figure from Calignano [2014].

Alternatively, constraints for the degree of overhang can be implemented such that it is possible to print the design generated through TO entirely support-free. In Langelaar [2016] this is enforced by inclusion of a AM density filter, where elements not supported wrt. the printing baseplate are identified and removed during optimization. In the present work, focus is placed on developing models for fatigue optimization using AM materials with support structure optimization left for further work, see Chapter 7.

3.4.1 Additively Manufactured Materials - Properties and Characteristics

Using TO to generate designs for AM therefore seems to be an ideal choice. However, AM material characteristics are highly dependent on its process parameters. To predict the mechanical behavior of an AM component, these parameters must be considered.

In terms of static strength properties, the AM material exhibits comparable, or in some cases even better, properties to the equivalent conventionally manufactured material [Spierings et al., 2011][Bian et al., 2015][Sistiaga et al., 2016]. This is mainly attributed by the high cooling rate of the part during the process, which causes a fine microstructure of the component [Spierings et al., 2013]. The microstructure fineness will however depend on the chosen AM method [Tolosa et al., 2010].

Conversely, many features existing in printed materials are detrimental to the fatigue performance of the part. AM materials are prone to the formation of defects and heterogeneities, leading to anisotropic fatigue [Yadollahi et al., 2017]. The introduced defects will serve as crack initiation sites by acting as stress concentrations in the material, thereby severely lowering the fatigue resistance of the material. The presence of defects is especially important in HCF, where it is assumed that the part spends its entire lifetime in the crack initiation phase of fatigue failure. Furthermore, the defects are typically slit-shaped. Orientation of the defects wrt. the load is therefore important, as the crack simulates a mode I crack opening if load is applied transversely to the defect, see Figure 3.11.

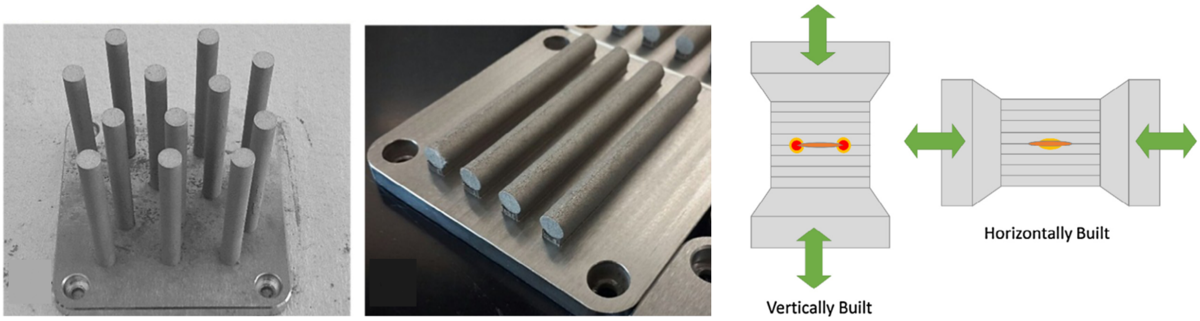

Figure 3.11. Examples of vertically and horizontally built specimens (left) and illustration of how print orientation aligns defects in relation to the applied load (right). Figures from Yadollahi et al. [2017].

Location of defects appears to be more important than shape or size, and surface defects are found to be the most life-limiting. By not accounting for the presence of defects, failure will occur suddenly and at a lower amount of excited load reversals than will be predicted by traditional stress-life analysis, where homogeneity is assumed. Spierings et al. [2013] verified this experimentally, where a reduction of 25% for SS316L and 20% 15-5PH, two stainless steels commonly used in AM, were observed. This study takes offset in cyclic uniaxial tensile loading, which is a more severe loading case as compared to traditional rotating bending. The fatigue strength reduction of a 17-4 PH SS (another stainless steel) with horizontal and vertical print directions is illustrated on the SN-curve in Figure 3.12 along with anisotropy induced by the print direction. Due to changes in print velocity, number of components built at a time, and

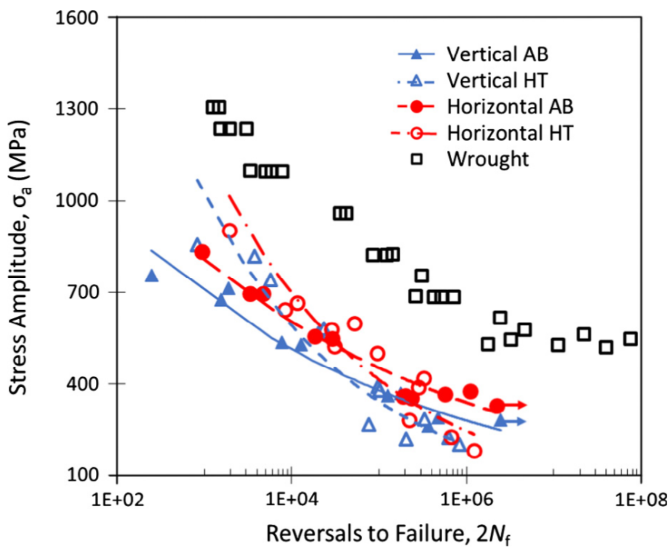

	σ_f [MPa]	b
Vertical AB	2043	-0.15
Horizontal AB	2100	-0.13
Vertical HT	7002	-0.26
Horizontal HT	8622	-0.26

Figure 3.12. SN-curve of 17-4 PH stainless steel for as-built (AB) and heat treated (HT) specimens printed in both vertical and horizontal directions (see Figure 3.11 for illustration of the specimens) compared to wrought specimens. Due to the presence of defects, it is observed that the fatigue strength in general is worse for AM material regardless of the chosen print direction as a result of the presence of defects. Figure and data from Yadollahi et al. [2017].

settings for the printer, such as laser power, scanning strategy, etc., each product is printed differently resulting in each part experiencing a different thermal history. The thermal history affects the quality of the microstructure, i.e. grain size, morphology and orientation, which affect the mechanical properties [Yadollahi et al., 2015].

By optimizing the process parameters, it is possible to reduce the degree of anisotropy of the material by making the microstructure more homogeneous [Clausen, 2016]. However, it is very difficult or even impossible to achieve complete homogeneity for highly complex parts given the current state of the technology and Fatemi et al. [2019] observes that even using same parameters on different machines yields different material characteristics. Yet, it is possible to take into account the defects by considering the orientation of the component in the print plane. By choosing a proper orientation, it is possible to control the orientation of these defects such that they may be aligned in a preferable direction to the imposed load, see Figure 3.11.

In relation to the discussed findings, it should be noted, that some of the current published research on fatigue of AM materials arrive at contradictory conclusions as outlined in Hackel et al. [2018] indicating that AM fatigue behavior is not properly characterized yet. As such, high quality fatigue data is difficult to obtain and to some extent only applies to a specific geometry produced on a specific machine.

Post-print Heat Treatment

Hot Isostatic Pressing (HIP) is a method commonly used on the post-printed component to homogenize the microstructure, relieve stress concentrations, and smooth out potential sharp angles (e.g. from a slit-shaped defect). Although HIP treatment is very beneficial in some cases, resulting in fatigue strength equivalent to that of a wrought material, its effects are not general [Fatemi et al., 2020] and may in some cases result in a lower fatigue strength than that of the as-built material. This is emphasized by Leuders et al. [2014], where TiAl6V4-titanium and SS316L-steel parts are treated by HIP and subsequently tested in a uniaxial fatigue test. The experimental results of the study showed an improvement in fatigue strength for the titanium specimens, but for the steel specimens, the fatigue strength was reduced. This is explained by the ductility of the materials, where a highly ductile material is able to reduce the stress near defects by locally yielding, whereas a material with low ductility would instead fracture. In general, the ductility of an AM material is lower compared to its wrought counterpart, which indicates that post-print annealing would be beneficial. However, although reduced, SS316L still possess a high ductility and thereby high fracture toughness, such that its fatigue strength depends more on the monotonic strength of the material than defects present [Leuders et al., 2014]. HIP treatment of a material reduces its monotonic strength [Sistiaga et al., 2016] and employing it for SS316L is ineffective. Conversely, TiAl6V4 has a lower fracture toughness, whereby its failure mode is dominated by crack growth at defect locations. Alleviating these stress concentration sites therefore results in higher fatigue strength. As such, HIP cannot be assumed to fully homogenize the material or remove anisotropic fatigue behaviour.

Surface Quality

Stress concentration due to surface roughness is a well-known important factor for fatigue strength of metals [Norton, 2014][Stephens et al., 2001]. For AM components it is especially important, as parts often contain high surface roughness similar to a staircase-effect, which happens due to the deposition of discrete layers [Clausen, 2016][Calignano, 2014]. Additionally, the surface roughness of the part may not be uniform and the degree hereof depends on the build orientation, see Figure 3.13.

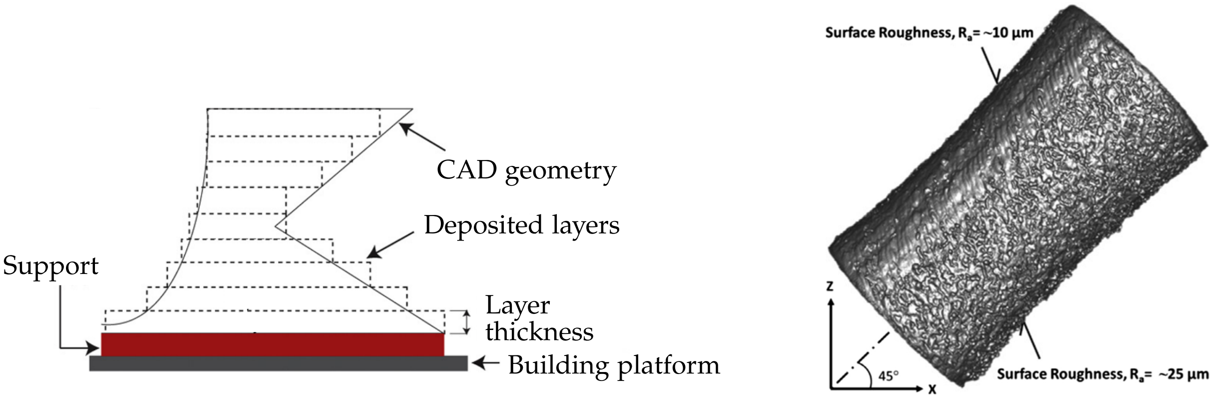

Figure 3.13. The stair case effect as a result of the layer-wise deposition of material (left) and nonuniform surface quality as a consequence of the build orientation (right). Figures from Calignano [2014] (slightly modified) and Yadollahi et al. [2017] respectively.

A common way to remove surface roughness of traditionally manufactured parts is to do a post-polishing of the surfaces. The attractiveness of AM as a method however stems from its ability to directly manufacture highly complex parts. Polishing the parts post-print may therefore be tedious or even impossible and process parameters should therefore be optimized to achieve the lowest surface roughness possible. If a high surface roughness is unavoidable, shot- or laser peening may be an attractive option. The peening methods introduce beneficial compressive residual stresses in the surfaces of the part by plastically deforming them, either by striking with small particles (shot peening) or laser-induced compression (laser peening), which increase the tensile stress required to open and propagate a crack. Current research of the effect of peening AM metals indicates, that the method is able to increase fatigue strength by introducing beneficial compressive residual stress in the surfaces, refine the microstructure and remove defects, similar to effects on wrought metals [Bag et al., 2020][Maamoun et al., 2018][Hackel et al., 2018].

3.5 Anisotropic Fatigue Modeling

The ability to account for existing material anisotropy is essential for optimized designs, to avoid over- or underdimensioning geometry. Accuracy of fatigue model must be balanced with computational effort. This is important when choosing the method for computing fatigue damage, as the criterion must be simple and continuous, whereby sensitivities can be computed efficiently using analytical design sensitivity analysis. A continuous expression is preferable for computational efficiency and an anisotropic model based on interpolating SN-curves is presented here.

It is assumed that the strength varies wrt. to the print plane orientation as observed for CPM, see Figure 3.14 where the Fatemi-Socie failure index is plotted wrt. the load plane. The variation of the damage parameter is clearly cyclical wrt. the angle, inspiring the cosinusoidal simplification developed in the following.

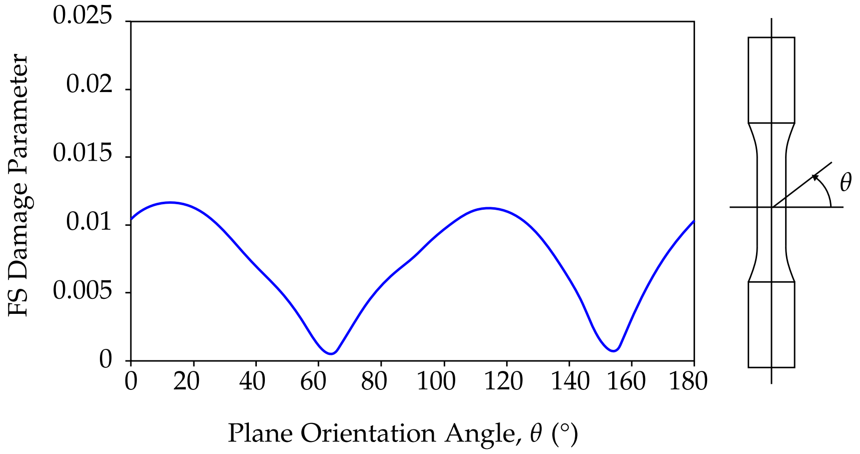

Figure 3.14. Prediction of damage wrt. the orientation of the load plane by the Fatemi-Socie (FS) CPM method [Fatemi and Socie, 1988]. The load case imposed on the test specimen is axial-torsion. The plane orientation angle refers to an analytical plane inserted for CPM to find its most critical orientation, where the loading is most severe. Figure from Yadollahi and Shamsaei [2017].

3.5.1 Anisotropic Equivalent Stress

If all static material characteristics, in particular elasticity and stress, are assumed isotropic, a model for anisotropic fatigue can be developed as an extension to the fatigue models discussed previously. From a micromechanical perspective, this assumption follows from defects being small, such they appear as local stress concentrations but do not appreciably affect a macroscopic cross section. Thus the orientation of defects will affect very locally dependent phenomena, in particular crack initiation and growth, which is expressed by the SN-curve changing depending on a specimen being built vertically or horizontally. In Basquin's approximation, if b can be assumed constant (which mostly agrees with the data of Figure 3.12 from Yadollahi et al. [2017]), the stress level will be proportional for all N:

$$\sigma_{Nf,\perp} \propto \sigma_{Nf,\parallel} \tag{3.26}$$

Here $\perp$ and $\parallel$ refer to load direction being normal and parallel to the print plane normal, respectively. Comparing to Figure 3.11, $\perp$ corresponds to the vertically built specimen and $\parallel$ to the horizontally. If only the fatigue strength is changed, the proportionality is uniquely given by a factor α:

$$\begin{gathered}\sigma_{Nf,\perp} = \sigma_{f,\perp}(2N)^b = \alpha\sigma_{Nf,\parallel} = \alpha\sigma_{f,\parallel}(2N)^b \\ \Rightarrow \alpha = \frac{\sigma_{f,\perp}}{\sigma_{f,\parallel}}\end{gathered} \tag{3.27}$$

This relation however only applies to two orientations and only wrt. a uniaxial force. To be useful in TO, it must be generalized to accept arbitrary orientation and loading condition. Recall that metal fatigue damage is divided into two distinct stages; crack initiation and propagation followed by failure. The crack propagation phase may be further classified as small crack growth (less than 2mm) and long crack growth (larger than 2mm) [Fatemi et al., 2019]. Fatemi et al. [2019] states that for AM materials, first principal stress is governing in crack growth, but not necessarily in initiation. If the defects are considered as existing small cracks, then using the angle between print plane normal and first principal direction, see Figure 3.15, fulfills the required generalizations of arbitrary orientation and loading condition. Thus,

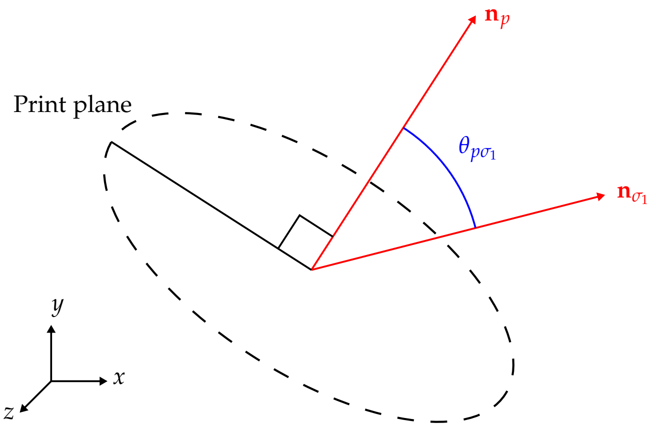

Figure 3.15. Angle $\theta_{p\sigma_1}$ between print plane normal $\mathbf{n}_p$ and first principal stress direction $\mathbf{n}_{\sigma_1}$.

taking the two fatigue strengths into account, α may be expressed by a cosinusoidal function:

$$\alpha(\theta_{p\sigma_1}) = 1 + \beta_p \frac{1 + \cos 2\theta_{p\sigma_1}}{2} \qquad \text{where} \qquad \beta_p = \frac{\sigma_{f,\perp}}{\sigma_{f,\parallel}} - 1 \tag{3.28}$$

The expression of β_p is used as its value gives an intuitive measure for the degree of anisotropy, in particular $\beta_p = 0$ for isotropy, see Figure 3.16. As an example of defining β_p, the results presented in Figure 3.12 for the HT material could be used, yielding:

$$\beta_p = 8622 \text{ MPa}/7002 \text{ MPa} - 1 \approx 0.23 \tag{3.29}$$

The $2\theta_{p\sigma_1}$ term is used to describe that $\mathbf{n}_p$ and $\mathbf{n}_{\sigma_1}$ are axes rather than vectors (e.g. $\mathbf{n}_p$ and $-\mathbf{n}_p$ account for the same behaviour), whereby the largest angle between them is $\frac{\pi}{2}$. A linear interpolation limited to $0 \leq \theta_{p\sigma_1} \leq \frac{\pi}{2}$ might seem sufficient, but loses differentiability at the endpoints.

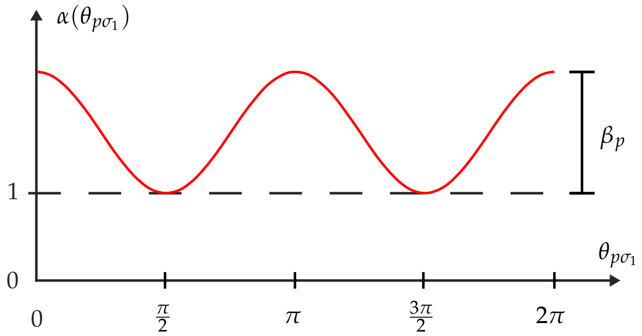

Figure 3.16. Plot of $\alpha(\theta_{p\sigma_1})$, which is used to scale equivalent stress. $\theta_{p\sigma_1} = 0$ corresponds to the $\parallel$-case, where the material is weak and its perceived equivalent stress σ_{Nf} should be higher, and $\theta_{p\sigma_1} = \frac{\pi}{2}$ corresponds to the $\perp$-case, where behaviour is nominal.

The angle between print plane normal and the principal direction is found by the dot product:

$$\theta_{p\sigma_1} = \cos^{-1} \frac{\mathbf{n}_p \cdot \mathbf{n}_{\sigma_1}}{|\mathbf{n}_p||\mathbf{n}_{\sigma_1}|} \tag{3.30}$$

where $\mathbf{n}_p$ is the print plane normal and $\mathbf{n}_{\sigma_1}$ is the principal direction. It is assumed that the vectors are normalized such that:

$$|\mathbf{n}_p| = |\mathbf{n}_{\sigma_1}| = 1 \tag{3.31}$$

After insertion of equations (3.30) and (3.31) into Equation (3.28), the following is obtained:

$$\alpha = 1 + \beta_p \frac{1 + \cos\left(2\cos^{-1}(\mathbf{n}_p \cdot \mathbf{n}_{\sigma_1})\right)}{2} \tag{3.32}$$

The expression is simplified using:

$$\cos\Big(2\cos^{-1}(\mathbf{n}_p \cdot \mathbf{n}_{\sigma_1})\Big) = 2(\mathbf{n}_p \cdot \mathbf{n}_{\sigma_1})^2 - 1 \tag{3.33}$$

which after insertion yields α expressed by the dot product of the vectors:

$$\alpha = 1 + \beta_p \, (\mathbf{n}_p \cdot \mathbf{n}_{\sigma_1})^2 \tag{3.34}$$

The relation between SN-curves and α is illustrated in Figure 3.17.

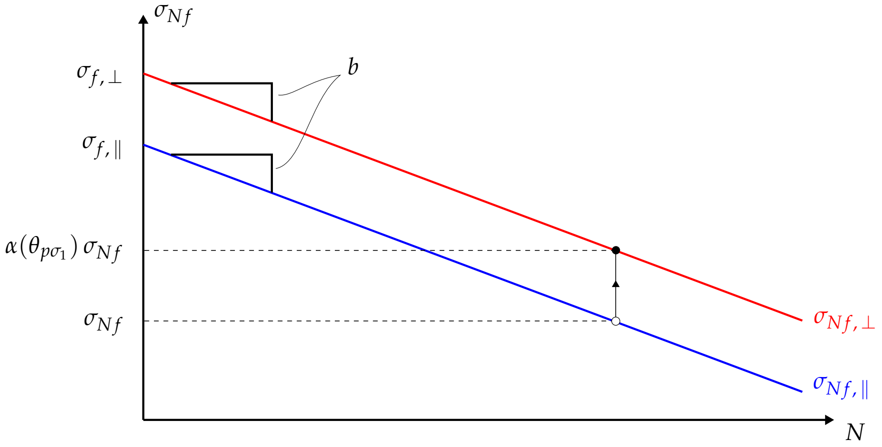

Figure 3.17. Log-log plot of SN-curves for an idealized anisotropic material with constant b. An increase α in stress (up to the $\sigma_{Nf,\perp}$-curve) is equivalent to a decrease in fatigue strength due to anisotropy.

Equation (3.34) is then used in the expressions for the equivalent stress with mean stress correction - in this case Morrow correction. For ductile metals, the signed von Mises stresses, Equations (3.19) and (3.20), are used:

$$\sigma_{Nf} = \alpha \, \frac{c_a \, \sigma_{VM} \, \sigma_{f,\perp}}{\sigma_{f,\perp} - \operatorname{sgn}\left(c_m \sigma_h\right) c_m \, \sigma_{VM}} \tag{3.35}$$

Assuming that only tensile stress creates fatigue damage, a more general expression, covering both brittle and ductile metals, is achieved by using the maximum principal stress:

$$\sigma_{Nf} = \alpha \, \frac{c_a \, \sigma_1 \, \sigma_{f,\perp}}{\sigma_{f,\perp} - c_m \, \sigma_1} \tag{3.36}$$

In this case, the anisotropic fatigue model fails to capture compressive stress, risking static failure. To account for this, a stress constraint is required to enforce a limit on compressive stresses. It should be noted, that although a wrought material is considered ductile, the AM counterpart may not be due to the alteration in microstructure, thermal history, and presence of defects [Fatemi et al., 2019]. The choice of which stress measure is used in the criterion should therefore depend on experimental tests of the given material manufactured on a given AM machine.

The cosine interpolation is an idealization, which has not been experimentally tested. However, if it is demonstrated that the relation is better described by a different function, replacing the cosine function is quite straightforward as the remaining framework developed is still valid wrt. to SN-curves.

3.5.2 Optimization of Print-orientation

To get the best utilization of the used material, it is desired to orient the print plane in the most fatigue tolerant way. This is achieved by including the orientation of $\mathbf{n}_p$ in the optimization. In two dimensions, the orientation is expressed by a single variable angle θ:

$$\mathbf{n}_p(\theta) = \begin{bmatrix} \cos\theta \\ \sin\theta \end{bmatrix} \tag{3.37}$$

The print plane normal is related to the geometry coordinate system and actual manufacturing print plane as illustrated in Figure 3.18.

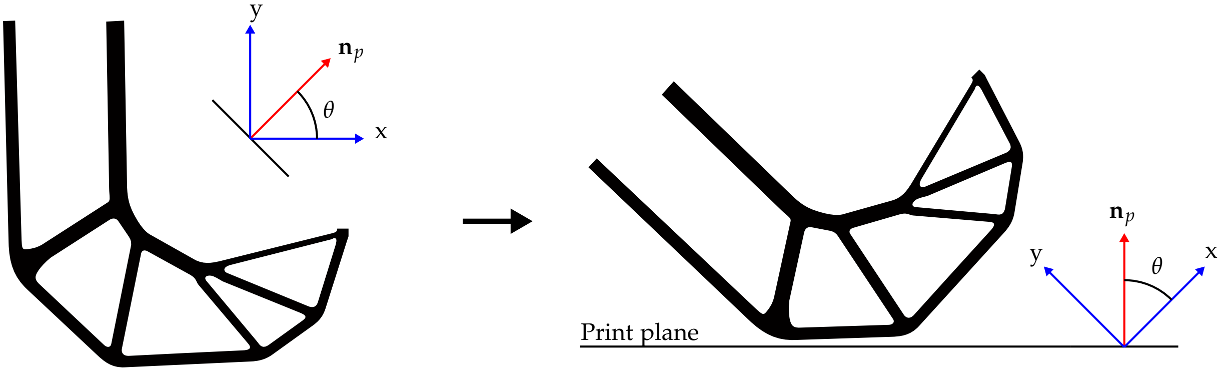

Figure 3.18. Relation between orientations of the TO coordinate system (left) and the printing process (right). Printing starts with a horizontal slice of the lowest part of the geometry on the right and proceeds with slices in the direction of $\mathbf{n}_p$. Support structure is neglected here.

In three dimensions, rotational matrices are used. Assuming the normal is initially placed in the z-direction, rotation around the z-axis is effectively avoided by using z-y-x Bryan angles (rotation around z-axis corresponds to a drilling rotation of the axis, which do not affect placement of the print plane). The expression becomes:

$$\mathbf{n}_p(\boldsymbol{\theta}) = R_y\,(R_x\,\boldsymbol{z}) = \begin{bmatrix} \cos\theta_x \sin\theta_y \\ -\sin\theta_x \\ \cos\theta_x \cos\theta_y \end{bmatrix} \tag{3.38}$$

with $\boldsymbol{\theta} = [\theta_x\ \theta_y]^T$ being the rotations around x- and y-axes respectively, and the rotation matrices defined as:

$$R_x = \begin{bmatrix} 1 & 0 & 0 \\ 0 & \cos\theta_x & -\sin\theta_x \\ 0 & \sin\theta_x & \cos\theta_x \end{bmatrix} \quad \text{and} \quad R_y = \begin{bmatrix} \cos\theta_y & 0 & \sin\theta_y \\ 0 & 1 & 0 \\ -\sin\theta_y & 0 & \cos\theta_y \end{bmatrix} \tag{3.39}$$

Thus, in two dimensions a single additional design variable is included in the optimization and in three dimensions two additional design variables are included.

3.6 Constraint Functions

To give an overview of the several possible problem formulations presented, strict formulations are given here.

The objective in all cases is volume minimization. The volume function given in Equation (2.6) depends solely on the densities included, such that:

$$V(\boldsymbol{\rho}) = \sum_{e=1}^{N_{elem}} \tilde{\rho}^{(e)} v^{(e)} \tag{3.40}$$

Note that the physical densities $\tilde{\rho}$ are used, although the function is still dependent on the design variables.

A single stress constraint based on von Mises stress σ_{VM} is used:

$$g_{\sigma}(\boldsymbol{\rho}) = c^{(k)} f_{\Psi}(\boldsymbol{\sigma}_{VM}) \tag{3.41}$$

where $c^{(k)}$ is the adaptive constraint scaling factor (see Algorithm 1) and $\boldsymbol{\sigma}_{VM}$ is all von Mises stresses, calculated from the relaxed element stresses and implicitly dependent on $\boldsymbol{\rho}$ via Equation (2.1). Other stress measures are possible by replacing σ_{VM} by e.g. σ_1 or σ_3 to obtain strictly lower or upper constraints on stress, respectively.

Three fatigue constraints are used: an isotropic criterion based on signed von Mises and anisotropic criteria with fixed or variable print plane orientation. The isotropic constraint is defined as:

$$g_D(\boldsymbol{\rho}) = c^{(k)} f_{\Psi}(\mathbf{D}_s(\boldsymbol{\sigma}_{Nf})) \tag{3.42}$$

where $\mathbf{D}_s$ is all element damages scaled according to P-mean scaling of Equation (3.25) and $\boldsymbol{\sigma}_{Nf}$ is all signed von Mises equivalent stresses from Equations (3.18), (3.19) and (3.20).

The anisotropic fatigue criterion with variable print plane orientation is given by

$$g_{D\alpha\sigma_1}(\boldsymbol{\rho},\boldsymbol{\theta}) = c^{(k)} f_{\Psi}(\mathbf{D}_s(\boldsymbol{\sigma}_{Nf}(\boldsymbol{\alpha}(\boldsymbol{\rho},\boldsymbol{\theta}),\boldsymbol{\sigma}_1(\boldsymbol{\rho})))) \tag{3.43}$$

if the principal stress formulation of Equation (3.36) is used, or by

$$g_{D\alpha\sigma_{VM}}(\boldsymbol{\rho},\boldsymbol{\theta}) = c^{(k)} f_{\Psi}(\mathbf{D}_s(\boldsymbol{\sigma}_{Nf}(\boldsymbol{\alpha}(\boldsymbol{\rho},\boldsymbol{\theta}),\boldsymbol{\sigma}_{VM}(\boldsymbol{\rho})))) \tag{3.44}$$

if instead Equation (3.35) is used. $\boldsymbol{\alpha}$ refers to all element fatigue strength interpolations from Equation (3.34). For fixed print plane orientation, $\boldsymbol{\theta}$ is no longer a variable and thus the constraint is expressed by

$$g_{D\alpha\sigma_1}(\boldsymbol{\rho}) = c^{(k)} f_{\Psi}(\mathbf{D}_s(\boldsymbol{\sigma}_{Nf}(\boldsymbol{\alpha}(\boldsymbol{\rho}),\boldsymbol{\sigma}_{\mathbf{1}}(\boldsymbol{\rho})))) \tag{3.45}$$

or

$$g_{D\alpha\sigma_{VM}}(\boldsymbol{\rho}) = c^{(k)} f_{\Psi}(\mathbf{D}_s(\boldsymbol{\sigma}_{Nf}(\boldsymbol{\alpha}(\boldsymbol{\rho}),\boldsymbol{\sigma}_{\boldsymbol{VM}}(\boldsymbol{\rho})))). \tag{3.46}$$

4 | Design Sensitivity Analysis

In this chapter the sensitivities for the functions used are derived. The method of analytical adjoint sensitivity analysis is presented and applied to establish efficient sensitivity expression for the formulated structural constraints. Each expression contains terms that are depend on the method used. These individual terms will be derived for the respective methods presented in earlier chapter, and used in the implementation to solve multiple examples, see more in Chapter 5.

4.1 Analytical Design Sensitivity Analysis

This section is based on Christensen and Klarbring [2009].

The process of obtaining problem sensitivities is termed Design Sensitivity Analysis (DSA). Different methods exist for performing DSA and the choice hereof depends on the problem formulation. In this particular work it is inteded to use the Method of Moving Asymptotes (MMA) to solve the optimization problem, see more in Chapter 5. First order sensitivity information of the optimization functions is required for the MMA - higher orders are not considered. They may be obtained by a finite difference scheme, but this quickly becomes prohibitively expensive for anything but the smallest models, as objective and constraint functions must be evaluated at least once per design variable per iteration. Analytical DSA avoid this by only considering optimization functions that are continuous and differentiable, which implies that an analytical sensitivity can be derived, and this allows for efficient computation of sensitivities.

Methods for deriving analytical expressions are the direct differentiation method or the adjoint method. Using the adjoint method is preferable over the direct method when dealing with the particular combination of many design variables and few functions. This becomes evident during derivation of the sensitivity which is done in the following.

4.1.1 The Adjoint Method

Recall that for the nested optimization formulation, the functions are implicitly dependent on the state problem, see Equation (2.2). An optimization function will thus have two dependencies:

$$f = f(\boldsymbol{\rho}, \mathbf{U}(\boldsymbol{\rho})) \tag{4.1}$$

The total derivative of the function is therefore composed of two partial derivative terms due to the chain rule:

$$\frac{\mathrm{d}f}{\mathrm{d}\rho^{(e)}} = \frac{\partial f}{\partial \rho^{(e)}} + \frac{\partial f}{\partial \mathbf{U}} \frac{\partial \mathbf{U}}{\partial \rho^{(e)}} \tag{4.2}$$

Similarly, the derivative of the state equation, see Equation (2.1), is:

$$\mathbf{K}\frac{\partial \mathbf{U}}{\partial \rho^{(e)}} + \frac{\partial \mathbf{K}}{\partial \rho^{(e)}}\mathbf{U} = \frac{\partial \mathbf{F}}{\partial \rho^{(e)}} \tag{4.3}$$

Assuming design independent load, the partial derivative of the load vector is zero. The $\frac{\partial \mathbf{U}}{\partial \rho^{(e)}}$ term is then isolated:

$$\frac{\partial \mathbf{U}}{\partial \rho^{(e)}} = \mathbf{K}^{-1}\left(-\frac{\partial \mathbf{K}}{\partial \rho^{(e)}}\mathbf{U}\right) \tag{4.4}$$

and inserted into Equation (4.2), which yields:

$$\frac{\mathrm{d}f}{\mathrm{d}\rho^{(e)}} = \frac{\partial f}{\partial \rho^{(e)}} + \frac{\partial f}{\partial \mathbf{U}}\mathbf{K}^{-1}\left(-\frac{\partial \mathbf{K}}{\partial \rho^{(e)}}\mathbf{U}\right) \tag{4.5}$$

Solving this expression directly is the direct differentiation method. It entails solving Equation (4.4) for each design variable, which becomes computationally expensive if the problem contains many design variables, which is inherent to TO problems.

Due to the application of aggregation functions there are few functions in the problem formulation. An adjoint vector is therefore defined as:

$$\boldsymbol{\lambda}^T = \frac{\partial f}{\partial \mathbf{U}}\mathbf{K}^{-1} \tag{4.6}$$

As the stiffness matrix is symmetric, the equation is rewritten:

$$\mathbf{K}\boldsymbol{\lambda} = \left(\frac{\partial f}{\partial \mathbf{U}}\right)^T \tag{4.7}$$

This is a linear system of equations which may be solved efficiently for each function, in particular if using a direct solver, since the factored stiffness matrix then can be reused. The adjoint vector is then inserted into Equation (4.5):

$$\frac{\mathrm{d}f}{\mathrm{d}\rho^{(e)}} = \frac{\partial f}{\partial \rho^{(e)}} - \boldsymbol{\lambda}^T\frac{\partial \mathbf{K}}{\partial \rho^{(e)}}\mathbf{U} \tag{4.8}$$

This is the adjoint method and is advantageous as it only requires solution of Equation (4.7) once per function.

4.2 Objective Function Sensitivity

This work will solely consider minimization of volume. The volume of the design depends linearly on physical density, as expressed in Equation (2.6) restated here:

$$V = \sum_{e=1}^{N_{elem}} v^{(e)}\tilde{\rho}^{(e)} \tag{2.6}$$

The volume of a structure is independent of the state equations and no complex method is required to derive the sensitivity. It is simply the element volume multiplied the derivative of the density variable:

$$\frac{\mathrm{d}V}{\mathrm{d}\rho^{(j)}} = v^{(e)}\frac{\partial \tilde{\rho}^{(e)}}{\partial \rho^{(j)}} \tag{4.9}$$

The expression for the density derivative term $\frac{\partial \tilde{\rho}^{(e)}}{\partial \rho^{(j)}}$ depends on which regularization scheme is applied. Derivation hereof is presented in Section 4.4. If print plane orientation angles are included in the problem, these do not affect volume and the sensitivities are of course zero.

4.3 Constraint Function Sensitivity

The considered problems will mainly be subject to fatigue constraints, however the fatigue function is highly associated with the stress function. Furthermore, in some cases a stress constraint is required to limit the compressive stresses of the considered structure to ensure static structural integrity. Both fatigue and stress constraints are therefore derived in the following.

4.3.1 Fatigue

The total derivative of the fatigue function is expanded using the chain rule as:

$$\frac{\mathrm{d}D_{\Psi}}{\mathrm{d}\rho^{(e)}} = \frac{\partial D_{\Psi}}{\partial D^{(e)}} \frac{\partial D^{(e)}}{\partial \bar{\boldsymbol{\sigma}}^{(e)}} \frac{\partial \bar{\boldsymbol{\sigma}}^{(e)}}{\partial \rho^{(e)}} \tag{4.10}$$

where D_{Ψ} refers to the P-norm aggregated damage expression. Within each of these terms there are multiple function dependencies. The derivative of the aggregated damage depends on the aggregation function used. In this work P-norm of Equation (3.8) is exclusively used. Derivative of the P-norm function is given in Section 4.4. The derivative of damage wrt. the stress vector is expanded as:

$$\frac{\partial D^{(e)}}{\partial \bar{\boldsymbol{\sigma}}^{(e)}} = \sum_{i=1}^{N_{lc}} \frac{\partial D^{(e,i)}}{\partial N^{(e,i)}} \frac{\partial N^{(e,i)}}{\partial \bar{\sigma}_{Nf}^{(e,i)}} \frac{\partial \bar{\sigma}_{Nf}^{(e,i)}}{\partial \bar{\boldsymbol{\sigma}}^{(e)}} \tag{4.11}$$

where N_{lc} is the amount of load combinations. The derivative of the stress vector wrt. the density is:

$$\frac{\partial \bar{\boldsymbol{\sigma}}^{(e)}}{\partial \rho^{(e)}} = q \left(\rho^{(e)}\right)^{q-1} \mathbf{E}\mathbf{B}^{(e)}\mathbf{u}^{(e)} - \left(\rho^{(e)}\right)^{q} \mathbf{E}\mathbf{B}^{(e)} \frac{\partial \mathbf{u}^{(e)}}{\partial \rho^{(e)}} \tag{4.12}$$

An adjoint vector is formulated to be able to efficiently solve the right hand side term $\frac{\partial \mathbf{u}^{(e)}}{\partial \rho^{(e)}}$. This term is replaced by Equation (4.4), and then, according to Equation (4.6), the right hand side term is defined as:

$$\frac{\partial D_{\Psi}}{\partial \mathbf{U}} = \sum_{e=1}^{N_{elem}} \frac{\partial D_{\Psi}}{\partial D^{(e)}} \frac{\partial D^{(e)}}{\partial \bar{\boldsymbol{\sigma}}^{(e)}} \left(\rho^{(e)}\right)^{q} \mathbf{E}\mathbf{B}^{(e)}\mathbf{L}^{(e)} \tag{4.13}$$

where $\mathbf{L}^{(e)}$ is a bookkeeping matrix used to bring $\mathbf{B}$ from local to global level - this can also be done programmatically by index manipulation. The right hand term is then inserted into the adjoint equation, i.e. Equation (4.7), yielding:

$$\mathbf{K}\boldsymbol{\lambda}_D = \left(\sum_{e=1}^{N_{elem}} \frac{\partial D_{\Psi}}{\partial D^{(e)}} \frac{\partial D^{(e)}}{\partial \bar{\boldsymbol{\sigma}}^{(e)}} \left(\rho^{(e)}\right)^{q} \mathbf{E}\mathbf{B}^{(e)}\mathbf{L}^{(e)}\right)^{T} \tag{4.14}$$

Inserting the derived terms and the adjoint vector into Equation (4.10) yields the sensitivity:

$$\frac{\mathrm{d}D_{\Psi}}{\mathrm{d}\rho^{(e)}} = \frac{\partial D_{\Psi}}{\partial D^{(e)}} \left(\sum_{i=1}^{N_{lc}} \frac{\partial D^{(e,i)}}{\partial N^{(e,i)}} \frac{\partial N^{(e,i)}}{\partial \bar{\sigma}_{Nf}^{(e,i)}} \frac{\partial \bar{\sigma}_{Nf}^{(e,i)}}{\partial \bar{\boldsymbol{\sigma}}^{(e)}} \right) q \left(\rho^{(e)} \right)^{q-1} \mathbf{E}\mathbf{B}^{(e)} \mathbf{u}^{(e)} - \boldsymbol{\lambda}_D^T \frac{\partial \mathbf{K}}{\partial \rho^{(e)}} \mathbf{U} \tag{4.15}$$

All explicit terms in this expression depend on which method is applied to formulate the term, e.g. σ_{Nf} may be determined by Sines' method [Stephens et al., 2001] instead of the signed von Mises expression. Extending the model in terms of computing new sensitivities through the adjoint method is therefore straightforward, as the derivative terms are simply replaced in the full derivative equation. However, note that the expression is written with SIMP penalization in mind, and if it is desired to use e.g. RAMP instead, the $\left(\rho^{(e)} \right)^{q}$ and $q \left(\rho^{(e)} \right)^{q-1}$ terms should be replaced by the corresponding RAMP formulations, see Olesen and Hermansen [2019]. Although the expression is developed with P-norm in mind, the P-norm function only constitutes a single partial derivative term which is easily replaced by e.g. P-norm mean of Equation (3.9) or Kreisselmeier-Steinhauser (3.10) [Olesen and Hermansen, 2019].

Considering the angle design variable, the expanded total derivative is:

$$\frac{\mathrm{d}D_{\Psi}}{\mathrm{d}\boldsymbol{\theta}} = \sum_{e=1}^{N_{elem}} \frac{\partial D_{\Psi}}{\partial D^{(e)}} \left(\sum_{i=1}^{N_{RF}} \frac{\partial D^{(e,i)}}{\partial N^{(e,i)}} \frac{\partial N^{(e,i)}}{\partial \bar{\sigma}_{Nf}^{(e,i)}} \frac{\partial \bar{\sigma}_{Nf}^{(e,i)}}{\partial \alpha} \frac{\partial \alpha}{\partial \mathbf{n}_p} \frac{\partial \mathbf{n}_p}{\partial \boldsymbol{\theta}} \right) \tag{4.16}$$

The computation of this is more straightforward as there is no implicit dependence of the state equations.

The non-differentiable adaptive constraint scaling factor c is multiplied the sensitivity to adjust for the change is constraint measure, yielding the final damage constraint sensitivities:

$$\frac{\mathrm{d}g_D}{\mathrm{d}\rho^{(e)}} = c \frac{\mathrm{d}D_{\Psi}}{\mathrm{d}\rho^{(e)}} \quad \text{and} \quad \frac{\mathrm{d}g_D}{\mathrm{d}\boldsymbol{\theta}^{(e)}} = c \frac{\mathrm{d}D_{\Psi}}{\mathrm{d}\boldsymbol{\theta}^{(e)}} \tag{4.17}$$

4.3.2 Stress

The stress sensitivity is derived like the fatigue sensitivity, however its derivation is more comprehensible due to less implicit function dependencies. The total derivative of the stress aggregation σ_{Ψ} measure is:

$$\frac{\mathrm{d}\bar{\sigma}_{\Psi}}{\mathrm{d}\rho^{(e)}} = \frac{\partial \bar{\sigma}_{\Psi}}{\partial \bar{\boldsymbol{\sigma}}^{(e)}} \frac{\partial \bar{\boldsymbol{\sigma}}^{(e)}}{\partial \rho^{(e)}} \tag{4.18}$$

The stress terms in the equation depend on which measure is used. In this case, they are wrt. to either von Mises or a principal stress, derived in Section 4.4. The $\frac{\partial \bar{\boldsymbol{\sigma}}^{(e)}}{\partial \rho^{(e)}}$ term is exactly Equation (4.12) for which the adjoint vector is defined. Equivalent to for the fatigue function the right hand side is defined using Equation (4.6):

$$\frac{\partial \sigma_{\Psi}}{\partial \mathbf{U}} = \sum_{e=1}^{N_{elem}} \frac{\partial \bar{\sigma}_{\Psi}}{\partial \bar{\boldsymbol{\sigma}}^{(e)}} \frac{\partial \bar{\boldsymbol{\sigma}}^{(e)}}{\partial \rho^{(e)}} \left(\rho^{(e)} \right)^{q} \mathbf{E}\mathbf{B}^{(e)} \mathbf{L}^{(e)} \tag{4.19}$$

which is used to formulate the adjoint equation from Equation (4.7):

$$\mathbf{K}\boldsymbol{\lambda}_{\sigma} = \left(\sum_{e=1}^{N_{elem}} \frac{\partial \bar{\sigma}_{\Psi}}{\partial \bar{\boldsymbol{\sigma}}^{(e)}} \frac{\partial \bar{\boldsymbol{\sigma}}^{(e)}}{\partial \rho^{(e)}} \left(\rho^{(e)}\right)^{q} \mathbf{E}\mathbf{B}^{(e)}\mathbf{L}^{(e)} \right)^{T} \tag{4.20}$$

Insertion of Equation (4.12) and the adjoint vector into Equation (4.18) yields the sensitivity:

$$\frac{\mathrm{d}\bar{\sigma}_{\Psi}}{\mathrm{d}\rho^{(e)}} = \frac{\partial \bar{\sigma}_{\Psi}}{\partial \bar{\boldsymbol{\sigma}}^{(e)}} q \left(\rho^{(e)}\right)^{q-1} \mathbf{E}\mathbf{B}^{(e)}\mathbf{u}^{(e)} - \boldsymbol{\lambda}_{\sigma}^{T} \left(\frac{\partial \mathbf{K}}{\partial \rho^{(e)}} \mathbf{U} \right) \tag{4.21}$$

which is then multiplied by the adaptive constraint scaling factor, resulting in the final stress constraint sensitivity:

$$\frac{\mathrm{d}g_{\sigma}}{\mathrm{d}\rho^{(e)}} = c \frac{\mathrm{d}\bar{\sigma}_{\Psi}}{\mathrm{d}\rho^{(e)}} \tag{4.22}$$

4.4 Explicit Sensitivity Terms

The relevant individual terms, i.e. those used in the present implementation, for the defined sensitivities are derived in the following.

4.4.1 P-norm Function

The derivative of the used aggregation function, i.e. the P-norm function of Equation (3.8), is:

$$\frac{\partial f_{\Psi}}{\partial f^{(e)}} = \left(\sum_{l=1}^{N_{elem}} \left(f^{(l)} \right)^{P} \right)^{\frac{1}{P}-1} \left(f^{(e)} \right)^{P-1} \tag{4.23}$$

Note that this derivative is used for both the stress and damage derivative terms in equations (4.10) and (4.18), as the element damages and stresses can be inserted without affecting the expression.

4.4.2 Density Filter

An additional term is added to the derivative of the density design variable, due to the introduction of filtered variables. The total function derivative is found by application of the chain rule:

$$\frac{\partial f}{\partial \rho^{(j)}} = \sum_{e=1}^{N_j} \frac{\partial f}{\partial \tilde{\rho}^{(e)}} \frac{\partial \tilde{\rho}^{(e)}}{\partial \rho^{(j)}} \tag{4.24}$$

where N_j is the set of elements enclosed by the filter. The derivative of the filtered variable $\tilde{\rho}$, defined in Equation (2.8), wrt. the design variable is:

$$\frac{\partial \tilde{\rho}^{(e)}}{\partial \rho^{(j)}} = \frac{H^{(j,e)}}{\sum\limits_{l=1}^{N_j} H^{(j,l)}} \tag{4.25}$$

Note that this expression is independent of the design variables, thus it does not change through the optimization and may therefore be precomputed. As sensitivities from all elements in N_j contribute to the filter sensitivity, computation of sensitivities of elements which are not included in the optimization itself, in the case of using domain extension, is required.

Threshold Filter

Introducing a projection filter results in another term being added to the function derivative by the chain rule:

$$\frac{\partial f}{\partial \rho^{(j)}} = \sum_{e=1}^{N_j} \frac{\partial f}{\partial \bar{\tilde{\rho}}^{(e)}} \frac{\partial \bar{\tilde{\rho}}^{(e)}}{\partial \tilde{\rho}^{(e)}} \frac{\partial \tilde{\rho}^{(e)}}{\partial \rho^{(j)}} \tag{4.26}$$

Using the continuous approximation of the threshold filter, i.e. Equation (2.14), the intermediate derivative term is found as:

$$\frac{\partial \bar{\tilde{\rho}}^{(e)}}{\partial \tilde{\rho}^{(e)}} = \frac{\beta \operatorname{sech}^2(\beta(\tilde{\rho}^{(e)} - \eta))}{\tanh(\beta\eta) + \tanh(\beta(1-\eta))} \tag{4.27}$$

4.4.3 Stiffness

As the element stiffness matrices and element densities are uniquely associated, the derivative of global stiffness wrt. the densities may be assembled from a single element:

$$\frac{\partial \mathbf{k}^{(e)}}{\partial \rho^{(e)}} = \frac{\partial \bar{E}^{(e)}}{\partial \rho^{(e)}} \mathbf{k}_0^{(e)} \;\Rightarrow\; \frac{\partial \mathbf{K}}{\partial \rho^{(e)}} \tag{4.28}$$

where $\mathbf{k}_0^{(e)}$ is the unit stiffness matrix. The derivative of the modified SIMP expression of Equation (2.4) is:

$$\frac{\partial \bar{E}}{\partial \rho^{(e)}} = p \left(\tilde{\rho}^{(e)}\right)^{p-1} (E - E_{min}) \tag{4.29}$$

where $\tilde{\rho}^{(e)}$ is used to indicate the physical variable, i.e. it may represent the density filtered by any operation.

4.4.4 Stress

Expansion of the derivative of the stress aggregation function $\bar{\sigma}_\Psi$ yields:

$$\frac{\mathrm{d}\bar{\sigma}_\Psi}{\mathrm{d}\rho^{(e)}} = \frac{\partial \bar{\sigma}_\Psi}{\partial \bar{\sigma}_*^{(e)}} \frac{\partial \bar{\sigma}_*^{(e)}}{\partial \bar{\boldsymbol{\sigma}}^{(e)}} \frac{\partial \bar{\boldsymbol{\sigma}}^{(e)}}{\partial \rho^{(e)}} \tag{4.30}$$

where $\bar{\sigma}_*^{(e)}$ refers to a scalar reference stress of the multiaxial stress state, either von Mises $\bar{\sigma}_{VM}^{(e)}$ or a principal stress (e.g. $\bar{\sigma}_1^{(e)}$ or $\bar{\sigma}_3^{(e)}$ for 3D).

von Mises

The derivative of the von Mises expression, see Equation (3.3), is found for each element wrt. the stress components:

$$\frac{\partial \bar{\sigma}_{VM}^{(e)}}{\partial \bar{\sigma}_{x}^{(e)}} = \frac{1}{2\bar{\sigma}_{VM}^{(e)}}(2\,\bar{\sigma}_{x}^{(e)} - \bar{\sigma}_{y}^{(e)} - \bar{\sigma}_{z}^{(e)}) \tag{4.31}$$

$$\frac{\partial \bar{\sigma}_{VM}^{(e)}}{\partial \bar{\sigma}_{y}^{(e)}} = \frac{1}{2\bar{\sigma}_{VM}^{(e)}}(2\bar{\sigma}_{y}^{(e)} - \bar{\sigma}_{x}^{(e)} - \bar{\sigma}_{z}^{(e)}) \tag{4.32}$$

$$\frac{\partial \bar{\sigma}_{VM}^{(e)}}{\partial \bar{\sigma}_{z}^{(e)}} = \frac{1}{2\bar{\sigma}_{VM}^{(e)}}(2\bar{\sigma}_{z}^{(e)} - \bar{\sigma}_{x}^{(e)} - \bar{\sigma}_{y}^{(e)}) \tag{4.33}$$

$$\frac{\partial \bar{\sigma}_{VM}^{(e)}}{\partial \bar{\tau}_{xz}^{(e)}} = \frac{3}{\bar{\sigma}_{VM}^{(e)}}\bar{\tau}_{xz}^{(e)} \tag{4.34}$$

$$\frac{\partial \bar{\sigma}_{VM}^{(e)}}{\partial \bar{\tau}_{yz}^{(e)}} = \frac{3}{\bar{\sigma}_{VM}^{(e)}}\bar{\tau}_{yz}^{(e)} \tag{4.35}$$

$$\frac{\partial \bar{\sigma}_{VM}^{(e)}}{\partial \bar{\tau}_{xy}^{(e)}} = \frac{3}{\bar{\sigma}_{VM}^{(e)}}\bar{\tau}_{xy}^{(e)} \tag{4.36}$$

Principal Stresses and Vectors

Principal stress sensitivities are found as sensitivities to an eigenvalue problem. While analytical derivation can be made from the equations of Mohr's circle, sensitivities based on Nelson [1976] are used here, as the formulation applies to both 2D and 3D problems, and is more robust for near-axis-parallel principal directions. The derivation is presented in general terms first and the resulting expressions are then subsequently used to formulate the derivatives for stress.

For abbreviated notation, the derivative of a matrix wrt. its entries is defined as:

$$\delta \mathbf{A}_{pq} \equiv \frac{\partial \mathbf{A}}{\partial A_{pq}} \tag{4.37}$$

where $\mathbf{A}$ represents a matrix and pq are indices of a given entry. Assuming $\mathbf{A}$ is real and symmetric, its right and left eigenvectors are equal. The eigensystem of the matrix is therefore given in the form:

$$\mathbf{A}\mathbf{x} = \mathbf{x}\boldsymbol{\lambda} \tag{4.38}$$

where $\mathbf{x}$ is the eigenvector matrix and $\boldsymbol{\lambda}$ is a diagonal matrix containing the eigenvalues. Performing differentiation of the system of equations wrt. an entry of matrix $\mathbf{A}$ and rewriting yields the system $\mathbf{F}_m$:

$$\mathbf{F}_m = (\mathbf{A} - \lambda_m \boldsymbol{I})\frac{\partial \mathbf{x}_m}{\partial A_{pq}} = -\left(\delta \mathbf{A}_{pq} - \frac{\partial \lambda_m}{\partial A_{pq}}\boldsymbol{I}\right)\mathbf{x}_m \tag{4.39}$$

where $\boldsymbol{I}$ is the identity matrix with size equal to $\mathbf{A}$. The sensitivity of the eigenvalue is found by premultiplying the above expression with $\mathbf{x}_m^T$. This is found by considering Equation (4.38) for a single eigenvalue and -vector:

$$\mathbf{x}_m^T(\mathbf{A} - \lambda_m \boldsymbol{I}) = \mathbf{0}^T \tag{4.40}$$

thus, the left hand side of Equation (4.39) is zero due to the appearance of the Kronecker delta i.e. $\mathbf{x}^T\mathbf{x} = \delta_{ij}$, see Equation (4.44). The equation thereby reduces to:

$$\frac{\partial \lambda_m}{\partial A_{pq}} = \mathbf{x}_m^T \, \delta\mathbf{A}_{pq} \, \mathbf{x}_m \tag{4.41}$$

If it is assumed that there are no repeated eigenvalues, then from Equation (4.39) it is observed that the sensitivity for each eigenvector may be uniquely determined as a linear combination of all eigenvectors as the eigenvectors form a linearly independent orthogonal basis:

$$\frac{\partial \mathbf{x}_m}{\partial A_{pq}} = \sum_{n \neq m} c_{mn} \, \mathbf{x}_n \tag{4.42}$$

By substituting Equation (4.42) into Equation (4.39) and by premultiplying $\mathbf{x}_n^T$ an expression for the constants c_{mn} is determined:

$$c_{mn} = \frac{\mathbf{F}_m \cdot \mathbf{x}_n}{\lambda_n - \lambda_m}, \qquad n \neq m \tag{4.43}$$

The equation in the presented formulation is simplified such that $\mathbf{x}_n$ is no longer transposed. As the eigenvectors form an orthonormal basis, the dot product yields:

$$\mathbf{x}_m \cdot \mathbf{x}_n = \begin{cases} 0, & m \neq n \\ 1, & m = n \end{cases} \tag{4.44}$$

which cancels out the eigenvalue derivative terms of Equation (4.39). By insertion of the remainder of Equation (4.39), the expression of c_{mn} is:

$$c_{mn} = \frac{\left(\delta\mathbf{A}_{pq} \, \mathbf{x}_m\right) \cdot \mathbf{x}_n}{\lambda_m - \lambda_n}, \qquad n \neq m \tag{4.45}$$

Insertion into Equation (4.42) yields the eigenvector sensitivity:

$$\frac{\partial \mathbf{x}_m}{\partial A_{pq}} = \sum_{n \neq m} \frac{\left(\delta\mathbf{A}_{pq} \, \mathbf{x}_m\right) \cdot \mathbf{x}_n}{\lambda_m - \lambda_n} \mathbf{x}_n \tag{4.46}$$

Expressed in terms of stress, Equations (4.41) and (4.46) become

$$\frac{\partial \sigma_m^{(e)}}{\partial \bar{\sigma}_{pq}^{(e)}} = \left(\mathbf{n}_{\sigma_m}^{(e)}\right)^T \delta\bar{\boldsymbol{\sigma}}_{pq}^{(e)} \, \mathbf{n}_{\sigma_m}^{(e)} \tag{4.47}$$

and

$$\frac{\partial \mathbf{n}_{\sigma_m}^{(e)}}{\partial \bar{\sigma}_{pq}^{(e)}} = \sum_{n \neq m} \frac{\left(\delta\bar{\boldsymbol{\sigma}}_{pq}^{(e)} \, \mathbf{n}_{\sigma_m}^{(e)}\right) \cdot \mathbf{n}_{\sigma_n}^{(e)}}{\sigma_m^{(e)} - \sigma_n^{(e)}} \mathbf{n}_{\sigma_n}^{(e)} \tag{4.48}$$

where

$$\delta \bar{\boldsymbol{\sigma}}^{(e)}_{pq} = \frac{\partial \bar{\boldsymbol{\sigma}}^{(e)}}{\partial \bar{\sigma}^{(e)}_{pq}} \tag{4.49}$$

Note that the tensor form of $\bar{\boldsymbol{\sigma}}^{(e)}$ is used here, i.e. Equation (4.49) is a symmetric matrix of ones and zeros and is exactly equal to Equation (4.37).

4.4.5 Fatigue

By expansion of the aggregation damage term by the chain rule the following is achieved:

$$\frac{\partial D_{\Psi}}{\partial D^{(e)}} = \frac{\partial D_{\Psi}}{\partial D_s^{(e)}} \frac{\partial D_s^{(e)}}{\partial D^{(e)}} \tag{4.50}$$

The derivative of the damage wrt. reversals until failure N is found by differentiating the Palmgren-Miner expression of Equation (3.22):

$$\frac{\partial D^{(e,i)}}{\partial N^{(e,i)}} = -\frac{n^{(i)}}{\left(N^{(e,i)}\right)^2} \tag{4.51}$$

The derivative Basquin expression of Equation (3.16) wrt. equivalent stress yields:

$$\frac{\partial N^{(e,i)}}{\partial \bar{\sigma}^{(e,i)}_{Nf}} = \frac{1}{2\sigma_f\, b} \left(\frac{\bar{\sigma}^{(e,i)}_{Nf}}{\sigma_f}\right)^{\frac{1}{b}-1} \tag{4.52}$$

Scaled Damage

The derivative of the Basquin factor scaled damage of Equation (3.23) is found as:

$$\frac{\partial D_s^{(e)}}{\partial D^{(e)}} = -b \left(D^{(e)}\right)^{-b-1} \tag{4.53}$$

For the P-mean scaling, see Equation (3.24), the derivative is computed as:

$$\frac{\partial D_s^{(e)}}{\partial D^{(e)}} = \left(\frac{1}{c_1 + c_2}\right)^{-\frac{1}{P}} \frac{-b\left(c_1\, D^{(e)}\right)^{bP-1} + \left(c_2\, D^{(e)}\right)^{-P-1}}{\left(\left(c_1\, D^{(e)}\right)^{bP} + \left(c_2\, D^{(e)}\right)^{-P}\right)^{\frac{1}{P}+1}} \tag{4.54}$$

Signed von Mises

The derivative of the signed von Mises expression includes derivative of the Morrow expression of Equation (3.18) and then subsequently the derivative of amplitude and mean stress terms, i.e. equations (3.19) and (3.20). The expanded expression is:

$$\frac{\partial \bar{\sigma}^{(j,i)}_{Nf}}{\partial \bar{\boldsymbol{\sigma}}^{(j)}} = \left(\frac{\partial \bar{\sigma}^{(j,i)}_{Nf}}{\partial \bar{\sigma}^{(j,i)}_{a}} \frac{\partial \bar{\sigma}^{(j,i)}_{a}}{\partial \bar{\sigma}^{(j)}_{VM}} + \frac{\partial \bar{\sigma}^{(j,i)}_{Nf}}{\partial \bar{\sigma}^{(j,i)}_{m}} \frac{\partial \bar{\sigma}^{(j,i)}_{m}}{\partial \bar{\sigma}^{(j)}_{VM}}\right) \frac{\partial \bar{\sigma}^{(j)}_{VM}}{\partial \bar{\boldsymbol{\sigma}}^{(j)}} \tag{4.55}$$

The derivative terms related to amplitude stress are:

$$\frac{\partial \bar{\sigma}_{Nf}^{(j,i)}}{\partial \bar{\sigma}_{a}^{(j,i)}} = \frac{\sigma_f}{\sigma_f - \bar{\sigma}_m^{(j,i)}} = \frac{\sigma_f}{\sigma_f - \operatorname{sgn}\left(c_m^{(i)} \bar{\sigma}_h^{(j)}\right) c_m^{(i)} \bar{\sigma}_{VM}^{(j)}} \tag{4.56}$$

and

$$\frac{\partial \bar{\sigma}_{a}^{(j,i)}}{\partial \bar{\sigma}_{VM}^{(j)}} = c_a^{(i)} \tag{4.57}$$

The terms related to mean stress are:

$$\frac{\partial \bar{\sigma}_{Nf}^{(j,i)}}{\partial \bar{\sigma}_{m}^{(j,i)}} = \bar{\sigma}_a^{(j,i)} \frac{\sigma_f}{(\sigma_f - \bar{\sigma}_m^{(j,i)})^2} = c_a^{(i)} \bar{\sigma}_{VM}^{(j)} \frac{\sigma_f}{\left(\sigma_f - \operatorname{sgn}\left(c_m^{(i)} \bar{\sigma}_h^{(j)}\right) c_m^{(i)} \bar{\sigma}_{VM}^{(j)}\right)^2} \tag{4.58}$$

and

$$\frac{\partial \bar{\sigma}_{m}^{(j,i)}}{\partial \bar{\sigma}_{VM}^{(j)}} = \operatorname{sgn}\left(c_m^{(i)} \bar{\sigma}_h^{(j)}\right) c_m^{(i)} \tag{4.59}$$

The von Mises derivatives in Equation (4.55) are shown in Equations (4.31)-(4.36).

4.4.6 Anisotropic Fatigue

For the anisotropic fatigue criteria of Equations (3.35) and (3.36), sensitivities must be found for both the density design variables and the angle design variables $\boldsymbol{\theta}$ introduced in Section 3.5 to determine the print plane orientation. The stress is dependent of the density design variables, and an expression of the criterion derivative wrt. stress components is thus derived as:

$$\frac{\partial \sigma_{Nf}}{\partial \bar{\boldsymbol{\sigma}}} = \frac{\partial \sigma_{Nf}}{\partial \sigma_1} \frac{\partial \sigma_1}{\partial \bar{\boldsymbol{\sigma}}} + \frac{\partial \sigma_{Nf}}{\partial \alpha} \frac{\partial \alpha}{\partial \mathbf{n}_{\sigma_1}} \frac{\partial \mathbf{n}_{\sigma_1}}{\partial \bar{\boldsymbol{\sigma}}} \tag{4.60}$$

Using the maximum principal stress as the stress measure:

$$\frac{\partial \sigma_{Nf}}{\partial \sigma_1} = \frac{c_a\ \alpha}{(1 - \frac{c_m}{S_f}\sigma_1)^2} \tag{4.61}$$

If using the signed von Mises, this derivative is equivalent to that derived in the above multiplied by α. The derivative of the equivalent stress wrt. α is simply the Morrow correction. Using the maximum principal stress the derivative is:

$$\frac{\partial \sigma_{Nf}}{\partial \alpha} = \frac{c_a\ \sigma_1}{1 - \frac{c_m}{S_f}\sigma_1} \tag{4.62}$$

The derivative of α wrt. the principal direction is:

$$\frac{\partial \alpha}{\partial \mathbf{n}_{\sigma_1}} = 2\beta_p \left(\mathbf{n}_p \cdot \mathbf{n}_{\sigma_1}\right) \mathbf{n}_p^T \tag{4.63}$$

The derivative expression for the principal direction vector wrt. the stress components were derived in Equation (4.48).

In relation to the full derivative of damage wrt. the print plane angle of Equation (4.16) two additional terms need to be derived. The derivative of α wrt. the normal vector is:

$$\frac{\partial \alpha}{\partial \mathbf{n}_p} = 2\beta_p \left(\mathbf{n}_p \cdot \mathbf{n}_{\sigma_1}\right) \mathbf{n}_{\sigma_1}^T \tag{4.64}$$

The direction vectors are then differentiated wrt. the angle design variable. For the two- and three-dimensional cases, the derivatives are respectively:

$$\frac{\partial \mathbf{n}_p}{\partial \theta} = \begin{bmatrix} -\sin\theta \\ \cos\theta \end{bmatrix} \quad \text{or} \quad \frac{\partial \mathbf{n}_p}{\partial \boldsymbol{\theta}} = \begin{bmatrix} -\sin\theta_x \sin\theta_y & \cos\theta_x \cos\theta_y \\ -\cos\theta_x & 0 \\ -\sin\theta_x \cos\theta_y & -\cos\theta_x \sin\theta_y \end{bmatrix} \tag{4.65}$$

By the adjoint method, efficient computation of the sensitivities is now possible. These derived expression are then implemented and used to solve multiple problems in Chapter 5.

5 | Numerical Examples

This chapter concerns implementation of the proposed methods. General aspects regarding implementations will be discussed. The method of continuation used to achieve better designs is presented and strategies implemented are discussed. Numerical examples are then presented, emphasizing the implemented methods in a fatigue context. Verification of the implemented methods are performed on both 2D and 3D designs in the commercial FE program ANSYS.

5.1 Implementation

Two implementations of the TO routines presented have been made. The first one is a MATLAB implementation, developed to solve plane stress benchmark problems in order to test and verify the methods presented. Most calculations in MATLAB are performed as vectorized operations rather than loops, leading to fast solution times. The L-beam examples in the following in general have a per iteration time of 3.0-3.5 seconds for a 330 by 330 mesh of elements (including elements from domain extension) on a 3.8 GHz Intel i7-7700HQ CPU. For comparison, a problem of similar size solved with the `top88`-code of Andreassen et al. [2011] has an iteration time of 1.8-2.1 seconds on the same CPU, despite only considering compliance.

The second implementation is a TO module for the Fortran95 program MUltidisciplinary Synthesis Tool (MUST) developed at the Department of Materials and Production, Aalborg University. Many FE procedures are implemented as part of the MUST library and the program is therefore used for solving three-dimensional problems.

Settings presented in Table 5.1 are used in all examples, unless otherwise noted for the specific examples.

All examples solved are discretized with linear elements. The elements used are the bilinear Q4 elements for two-dimensional plane stress analysis and the linear hexahedral elements for three-dimensional. The focus of the examples will be on fatigue designs. The signed von Mises is applied for the examples without anisotropy, despite it poorly capturing mean stress effects [Papuga, 2012], as it is simple and computationally efficient. Focus is on TO formulations rather than representation of the physical system, whereby the criterion is deemed sufficient. Passive elements and domain extension are illustrated in Figure 5.1. Passive elements are used to simplify bookkeeping, particularly wrt. defining new problems, but are excluded from filter and DSA computations.

To measure the discreteness of a design, a measure of nondiscreteness M_{nd} [Sigmund, 2007] is defined:

$$M_{nd} = \frac{\sum_{e=1}^{N_{elem}} 4\tilde{\rho}^{(e)}(1-\tilde{\rho}^{(e)})}{N_{elem}} \times 100\% \tag{5.1}$$

Initial density	$\boldsymbol{\rho}^{(0)}$	0.5
Active design variables	N_{DV}	57 600
Total elements	N_{elem}	108 900
Load combinations	N_{RF}	1
Mean scaling factor	c_m	0.5
Amplitude scaling factor	c_a	0.5
Reversals	n	2×10^6
Aggregation factor	P	16
Stiffness relaxation factor	p	3
Stress relaxation factor	q	0.75
Damage scaling method	D_s	P-mean
Move limits	$\Delta\rho$	0.05
Filter radius	R	0.025 m
Max. no. of iterations		1500

$$\begin{aligned} \underset{(\boldsymbol{\rho})}{\text{minimize}} \quad & V(\boldsymbol{\rho}) \\ \text{subject to} \quad & \mathbf{g}(\boldsymbol{\rho}) - 1 \leq 0 \\ & \boldsymbol{\rho} \in [\rho_{min}, 1] \end{aligned}$$

Table 5.1. General settings for the implementation (left) and the optimization problem (right). Note that **g** is presented as a vector as multiple constraints may be included in the optimization, e.g. from the robust method, which defines three of the same type, or an accompanying stress constraint to ensure static structural integrity.

where $\tilde{\rho}$ is the physical density computed by either linear density or projection filtering. The measure of nondiscreteness is defined to be 0% at a density value of 0 or 1 and 100% at a density value of 0.5, i.e. the most intermediate density possible.

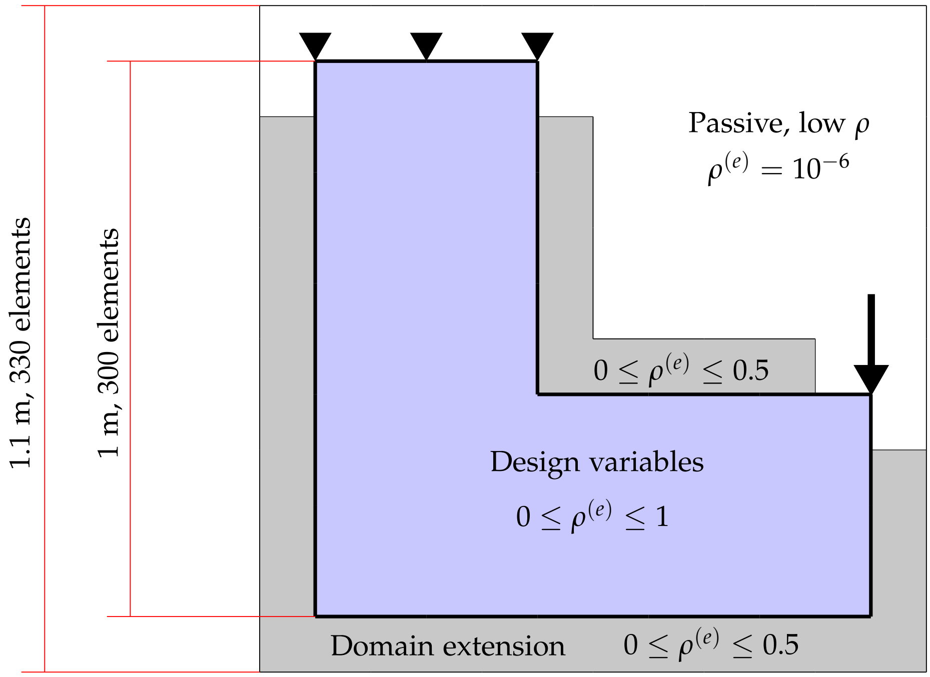

Figure 5.1. Sectioning of domain into various element types: 57 600 design variables, 15 525 domain extension elements, 35 775 passive elements. The large area with passive elements is due to the way domains are specified in matrix-form in MATLAB, to simplify bookkeeping and specification of new domains.

5.1.1 Method of Moving Asymptotes

The Method of Moving Asymptotes (MMA) [Svanberg, 1987] is used to solve the optimization problem. MMA is developed with structural optimization in mind, and it has been used successfully to solve many different TO problems. For an in-detail description of the method and implementation, reference is made to Svanberg [2007]. In short, the method is based on rewriting the original problem into an approximating convex subproblem, which is easier to solve. Formulation of these subproblems is based on sensitivity information of the current iteration and variables termed "moving asymptotes". These moving asymptotes are in particular important because they act as adaptive move limits and thereby control the behavior of the convergence. For iterations $k = 1$ and $k = 2$, they are computed as:

$$l^{(j,k)} = \rho^{(j,k)} - \gamma^{(j,k)} \left(\rho_{max}^{(j)} - \rho_{min}^{(j)} \right) \tag{5.2}$$

$$u^{(j,k)} = \rho^{(j,k)} + \gamma^{(j,k)} \left(\rho_{max}^{(j)} - \rho_{min}^{(j)} \right) \tag{5.3}$$

where $l^{(j,k)}$ is the lower asymptote, $u^{(j,k)}$ is the upper asymptote, $\rho_{max}^{(j)}$ is the upper bound, $\rho_{min}^{(j)}$ is the lower bound for the jth design variable of iteration k and $\gamma^{(j,k)}$ is a value used to control the asymptotes. For these first iterations, $\gamma^{(j,1)} = \gamma^{(j,2)} = 0.5$. When $k \leq 3$, the asymptotes are updated as:

$$l^{(j,k)} = \rho^{(j,k)} - \gamma^{(j,k)} \left(\rho^{(j,(k-1))} - l^{(j,(k-1))} \right) \tag{5.4}$$

$$u^{(j,k)} = \rho^{(j,k)} + \gamma^{(j,k)} \left(u^{(j,(k-1))} - \rho^{(j,(k-1))} \right) \tag{5.5}$$

Svanberg [2007] assigns the following values for these $\gamma^{(j,k)}$:

$$\gamma^{(j,k)} = \begin{cases} 0.7 & \text{if } \left(\rho^{(j,k)} - \rho^{(j,(k-1))} \right) \left(\rho^{(j,(k-1))} - \rho^{(j,(k-2))} \right) < 0 \\ 1.2 & \text{if } \left(\rho^{(j,k)} - \rho^{(j,(k-1))} \right) \left(\rho^{(j,(k-1))} - \rho^{(j,(k-2))} \right) > 0 \\ 1 & \text{if } \left(\rho^{(j,k)} - \rho^{(j,(k-1))} \right) \left(\rho^{(j,(k-1))} - \rho^{(j,(k-2))} \right) = 0 \end{cases} \tag{5.6}$$

However, they may be adjusted depending on the behavior of the problem. Oest and Lund [2017] suggests reducing the increase and decrease of γ to 1.05 and 0.65 respectively to cope with the nonlinearity in fatigue. This reduction is also used for this implementation.

External Move Limits

When using highly nonlinear problems, the moving asymptotes usually needs to be strict to prevent divergence. Another way is to use external move limits on the design variables. Here, implementation is made using a constant move limit strategy:

$$\rho^{(j,k)} - \Delta\rho \;\leq\; \rho^{(j,k)} \;\leq\; \rho^{(j,k)} + \Delta\rho \tag{5.7}$$

where $\Delta\rho$ is the chosen move limit. Alternatively, one may use adaptive move limits, where the move limits are adjusted depending on how well the problem is converging. This process is similar to how the moving asymptotes operate.

5.1.2 Continuation Strategies

The continuous density-based formulation of the optimization problem is non-convex, which when using sensitivity-based methods is likely to converge to a local optimum [Lund, 2018]. Using initial high factors in the SIMP method enforces this, as the constraints increasingly restrict the design domain. This is especially evident in case of the stress relaxation, where the singular optima may be closed-off entirely by the constraints as was discussed in Chapter 3.

Continuation increases the required time to solve the problem, as the problem formulation changes and a new optimum must be found every time a variable is changed. Additionally, if continuation is included in the constraints convergence will be slow in the case that continuation is done in small steps every iteration; every time a continuation variable is updated, the design (with active constraints) may become infeasible, and thus optimization tends to favor feasibility over convergence. The continuation strategy applied (i.e. how, how much, and when a variable is changed) should therefore be chosen based on a balance between computational efficiency and desired accuracy as well as studies of the stability of the problem in order to avoid divergence. Application of continuation on multiple variables should be done with care though, as simultaneously altering the variables may cause the problem to become unstable or diverge entirely.

Penalization and Relaxation Continuation

To achieve a good local optimum using the density-based approach, continuation can be applied to the SIMP method by gradually increasing the penalization (p) and relaxation (q) variables. The basic idea is that by keeping penalization and relaxation low, the feasible design space will be larger allowing the search method to more easily find a good minimum. Penalization and relaxation are then increased, gradually tightening the design domain. This also promotes more distinctly black/white designs. Starting the optimization with a higher degree of penalization the optimizer may converge to an unacceptably poor minimum. Using continuation, the optimizer is able to find a good minimum and subsequently increase discreteness of the design.

In the present implementation, stiffness penalization is kept constant as the designs generated are deemed sufficient with this penalization. If further penalization is needed, continuation is applied through relaxation by decreasing the q-variable. When the examples are presented in the following sections, the accompanying continuation strategy will be described for the given example. Common for all examples is that the increase is done in constant intervals, e.g. q is decreased for each 100 iterations.

Projection Filter Discreteness Continuation

Continuation is usually necessary when using a Heaviside-based filter, however its purpose is slightly different from continuation of penalization and relaxation. The Heaviside-filter ensures more discrete designs with interpretations coherent with developed models. The optimization problem should therefore be solved with the linear density filter for regularizing the problem, followed subsequently by application of the Heaviside projection to increase discreteness. Continuation is therefore applied primarily to keep the convergence stable and prevent divergence. Preemptive application may also cause unintentional convergence to a local minimum, which is undesirable.

As the projection filtering should not impact the problem, removal of continuation for the β-variable is desirable to achieve a higher convergence speed. Guest et al. [2011] proposes a method for eliminating the continuation, by adjusting the moving asymptotes through $\gamma^{(j,k)}$ for iteration $k = 1, 2$, defining them as:

$$\gamma^{(j,1)} = \gamma^{(j,2)} = \frac{0.5}{\beta + 1} \tag{5.8}$$

Although it removes the continuation, the generated design will, in general, not be equal to the one generated by applying continuation, see Figure 5.2. The optimization is highly unstable in the beginning, resulting in increased computational effort needed by MMA to solve the problem per iteration. The total amount of iterations is however reduced as a benefit of avoiding continuation.

Figure 5.2. Left: a volume minimization MBB-problem subject to a compliance constraint solved with regular continuation of the β-variable. The resulting volume fraction is 0.340 and measure of nondiscreteness $M_{nd} = 0.004$. Right: the same problem solved with adjusted MMA asymptotes and no continuation. Resulting volume fraction is 0.406 and $M_{nd} = 0.01$. The eventual discreteness parameter is $\beta_{lim} = 256$ in both cases, and the volume preserving threshold filter is used with $\eta = 0.5$.

The same degree of volume minimization is not achieved using the method for this example (volume fraction of 0.406 compared to 0.340 when not applying continuation), most likely due to the optimizer being stuck in a local minimum. This is a general tendency observed in multiple examples tested with higher levels of discreteness. Increasing discreteness makes the problem more difficult to solve. Continuation of the penalization or relaxation variables may guide the optimizer to a better optimum, however this further increases computational effort.

An interesting observation is made regarding stress-based problems. Performing continuation of β results in more instability of the optimization, due to the negative impact of sharp jagged edges, gradually increasing the stress as β is increased. If the problem is solved with a high β, the jagged edges are accounted for in the optimization from the beginning. Using the adjusted asymptotes therefore may cause faster convergence and result in a better end design, see Figure 5.3. Note that this observation is only valid for designs adhering to around the limit

β_{lim} defined by Equation (3.11). If a larger level of discreteness is used, the singularities will dominate the problem and will cause divergence.

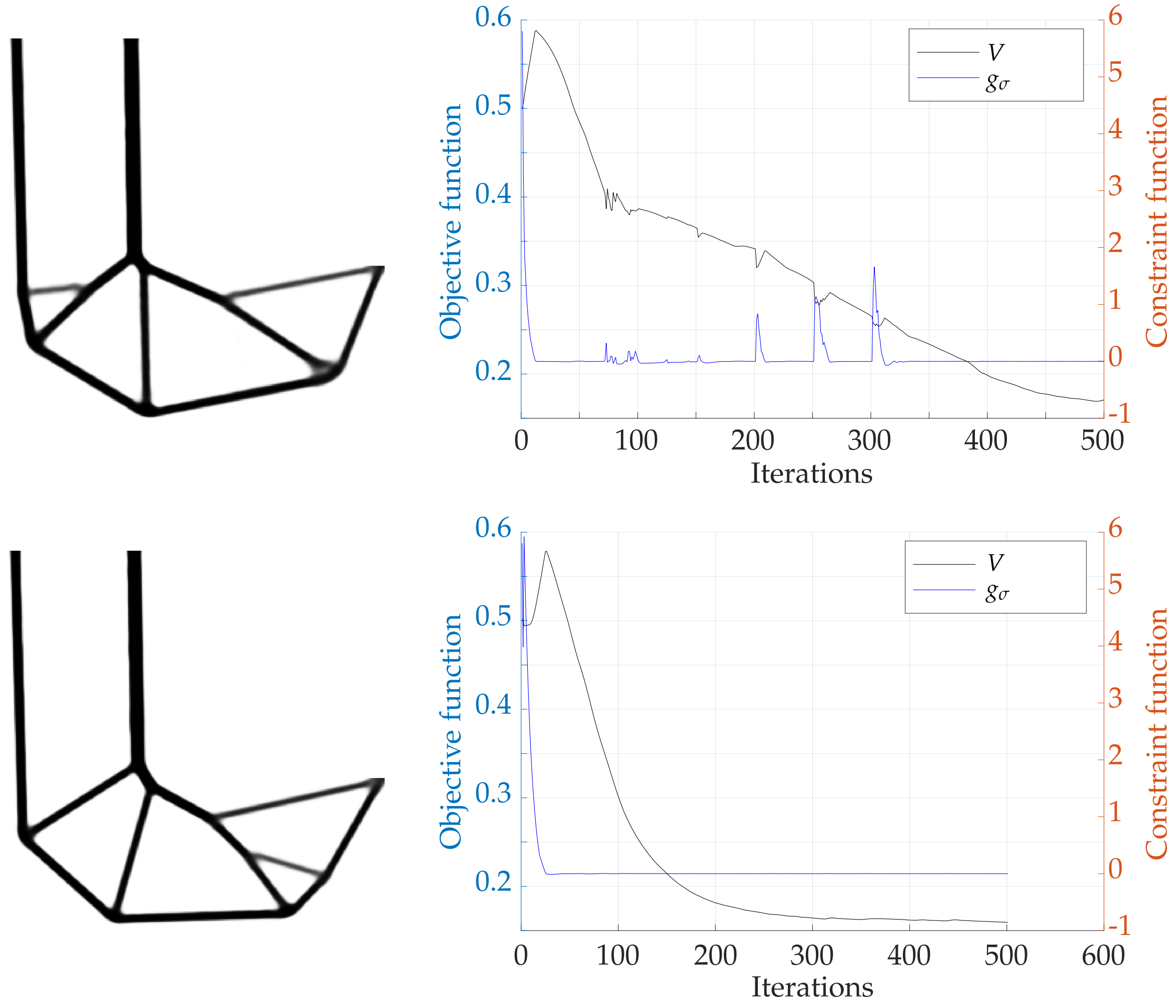

Figure 5.3. Stress constrained problem solved with continuation (top) and with the adjusted asymptote value (bottom). The volume fractions are 0.1708 and 0.1593 respectively and M_{nd} is 0.08 and 0.07 respectively. The discreteness variable limit is $\beta_{lim} = 15$ and the volume preserving threshold filter is used with $\eta = 0.5$.

The method is developed with the approximately volume preserving threshold filter in mind (i.e. $\eta = 0.5$). If using another value of η, such as in the robust method where three different values are used, the eroded and dilated design will have their densities forced to fully void and fully solid respectively, and may take unacceptably long to converge or become stuck entirely. Adjustment of the method may make it useful for this case, but this is left for further work, see Chapter 7.

5.2 General Distribution of Principal Stress

For the stress and fatigue based criteria used in this work a general tendency of principal stress aligning with geometry is observed, with the remaining component disappearing, see Figure 5.4. Additionally, bending stresses are small in the optimized design, meaning that the geometry has similarities to a truss structure. This distribution should be expected, as stress transverse to a structural member does not contribute to load carrying capacity and is thus not part of an optimal design. This directional preference is beneficial, as fatigue properties relating to uniaxial load are usable, even though they are non-conservative for the general case of stress.

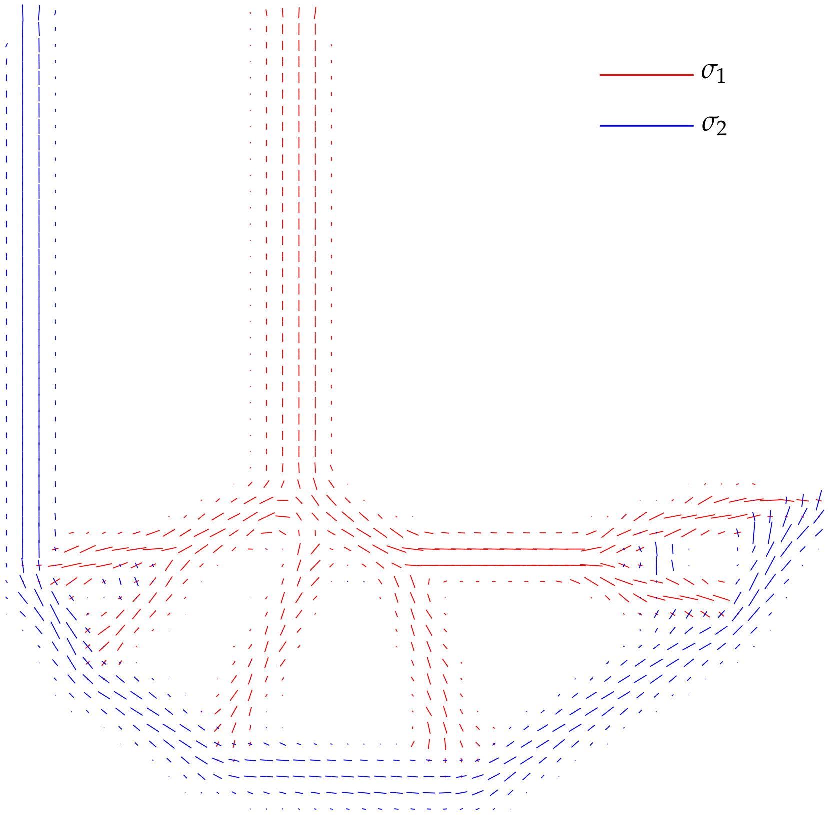

Figure 5.4. Orientation of principal stresses for a fatigue constrained problem, using isotropic signed von Mises equivalent stress.

5.3 Effects of Damage Scaling

From the studies done by Olesen and Hermansen [2019] it is evident that using Basquin factor scaling of Equation (3.23) is not able to generate a fully damaged design. To investigate the effect of the new P-mean scaling of Equation (3.25), the L-beam problem is solved with each scaling method, and the density distributions and convergence of the problems are presented in Figure 5.5. Effects of stress singularities at jagged edges are avoided by using the linear density filter.

The designs are similar, yet there are some quite significant differences. Firstly, considering convergence, despite the fine discretization and high nonlinearity of the problem, rapid convergence is achieved for the Basquin factor scaling method, approximately converging at 400 iterations. Conversely, the P-mean scaling did not converge without continuation of the relaxation variable, changing q from 1 to 0.5 over 800 iterations (this causes the sharp spikes in the damage constraint in the convergence plot). Even with continuation the design did not manage to fully remove intermediate densities around the connections between structural members, which is also reflected in the larger final volume and measure of nondiscreteness of the design. The convergence when using exclusively P-mean with equal weighting seems to worsen as the amount of elements in the problem increase. However, a much better damage distribution is achieved for P-mean scaling, see Figure 5.6, as Basquin factor scaling does not achieve a fully damaged design, but suffers from an apparent stress concentration. Similar distributions occur for many different cases and settings tested. The implications of each method are therefore as follows. Scaling the damages with the Basquin factor provides efficiency and stability for the optimization, but because element damages cannot be 0 or 1 everywhere (which is required for Basquin factor scaling to be accurate, see Figure 3.8), a sub-par design is achieved. P-mean scaling with equal weighting of the functions yields an even damage distribution, but convergence is slow.

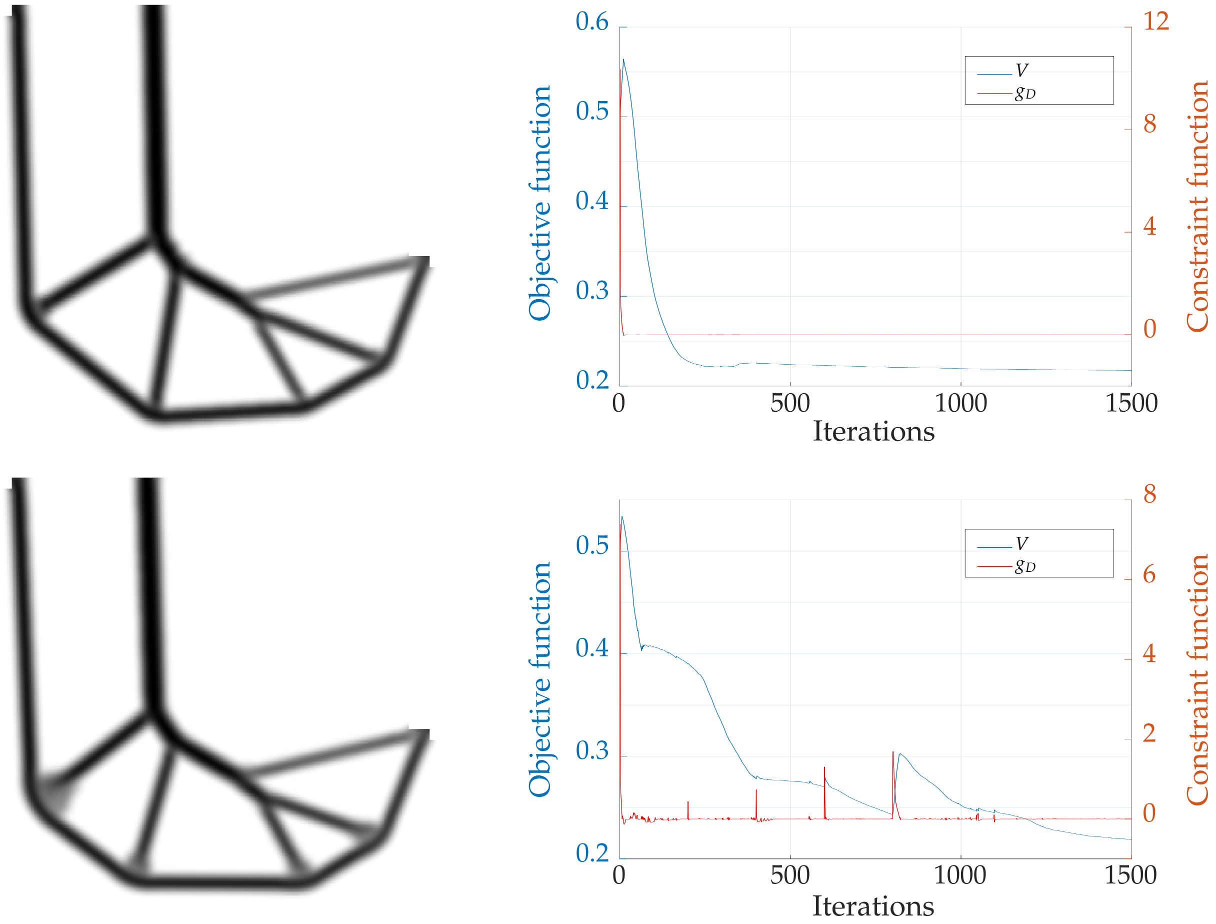

Figure 5.5. Results generated using Basquin factor scaling (top) and P-mean scaling (bottom) formulations. Volume fractions are 0.2174 and 0.2186 respectively, and measure of nondiscreteness are 29% and 30% respectively.

A continuation approach is applied to the weights of Equation (3.24), such that the optimization starts with the Basquin formulation and then changes to the unscaled formulation after adequate convergence has been achieved. Specifically, the weighing factors are set at iterations

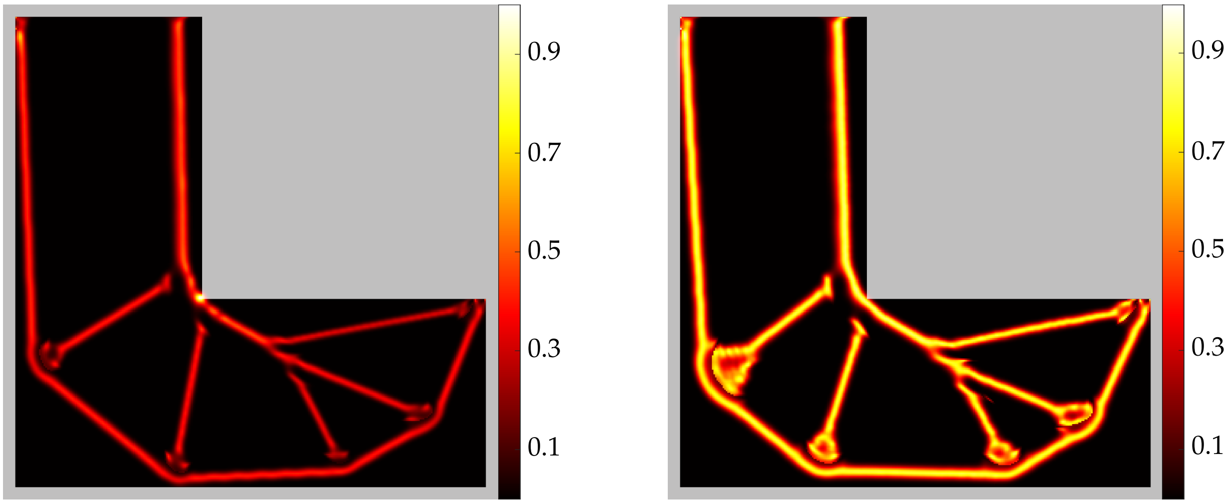

Figure 5.6. Damage distribution using Basquin factor scaling (left) and P-mean scaling (right). Highest element damages are 1.000 and 0.9974 respectively.

{0, 400, 450, 500, 550, 600} to c_1 ={1, 0.8, 0.6, 0.4, 0.2, 0} and c_2 ={0, 0.2, 0.4, 0.6, 0.8, 1}. The problem is solved using the standard settings defined in Table 5.1. The resulting density, damage and convergence are shown in Figure 5.7. Regarding convergence, the volume function has fast descent initially and once it stabilizes, the scaling factor is gradually updated. An added benefit is that this lowers the volume compared to pure Basquin factor scaling, as the element damage capacity is better utilized. Convergence is achieved without continuation of q, the inclusion of which could improve discreteness of the design.

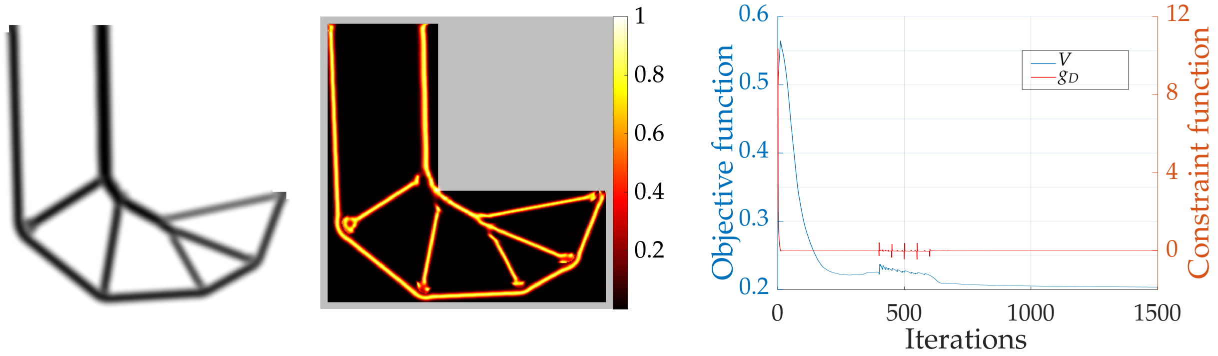

Figure 5.7. Design, damage and convergence generated using continuation on the P-mean scaling formulation. Volume fraction is 0.2035, discreteness is 29% and highest element damage is 1.0001.

5.4 Robust Optimization

To test the implications of the robust TO method on a fatigue constrained design, the L-beam problem is solved using the general settings of Table 5.1, using signed von Mises as the multiaxial criterion (Equation (3.42)). The eroded, intermediate and dilated designs are defined using threshold-variables of $[\eta_e, \eta_i, \eta_d] = [0.75, 0.5, 0.25]$. Continuation is applied according to Table 5.2. The resulting density distributions are illustrated for each design in Figure 5.8.

Iteration	0	100	200	300	400	500	550	600	650	700	800	1000
β	1							2			4	8
q	1	0.875	0.75	0.625	0.5							
c_1	1					0.8	0.6	0.4	0.2	0		
c_2	0					0.2	0.4	0.6	0.8	1		

Table 5.2. Continuation of parameters used in the robust optimization example. The limit $\beta_{lim} = 8$ is a bit lower than the maximum predicted by Equation (3.11), to reduce the influence of jagged edges.

As observed from the figure, high discreteness is achieved by applying the threshold filter ($M_{nd} = 29\%$ is achieved using linear density filtering). A difference in the level of discreteness between each design is present as a consequence of using the continuous formulation of the threshold filter (recall Figure 2.12).

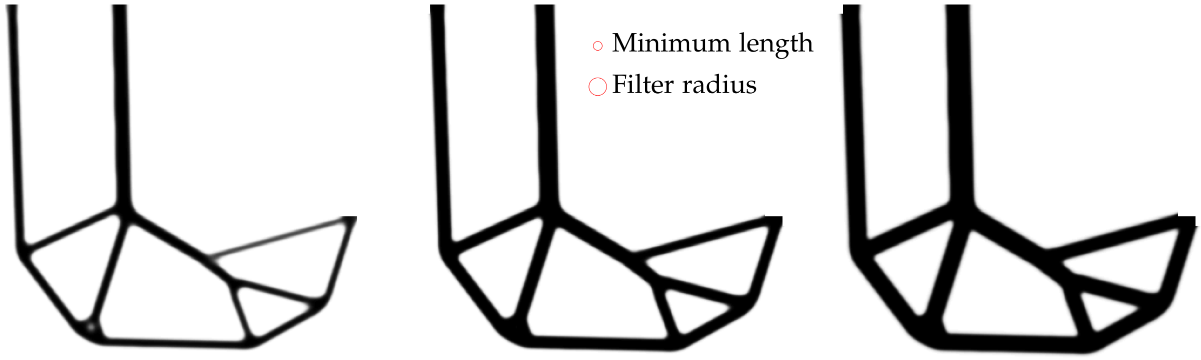

Design	Eroded	Intermediate	Dilated
Volume fraction	0.1625	0.2593	0.3517
M_{nd}	11.3%	8.7%	10.3%

Figure 5.8. Resulting density distribution for eroded (left), intermediate (middle) and dilated (right) designs.

The crisp representation of the structural members is a product of successful penalization, which is achieved by application of continuation of q. A pitfall of projection methods is observed if intermediate densities have not been penalized properly, as erroneous projection may happen which can cause gaps in the eroded design not present in the other or oppositely remove holes in the dilated. A precursor for ensuring minimum length scale on both phases is equivalent topology between the designs, which is violated in this case.

Considering the damage distribution, see Figure 5.9, it is observed that the intermediate and dilated designs have a high margin of safety. This is due to the high nonlinearity of the problem functions making it sensitive to small changes in imposed conditions. However, the problem is also local in nature, and it has been observed that the highest damage of the dilated design may exceed that of the intermediate.

The problem has also been solved without continuation of the weighting functions using

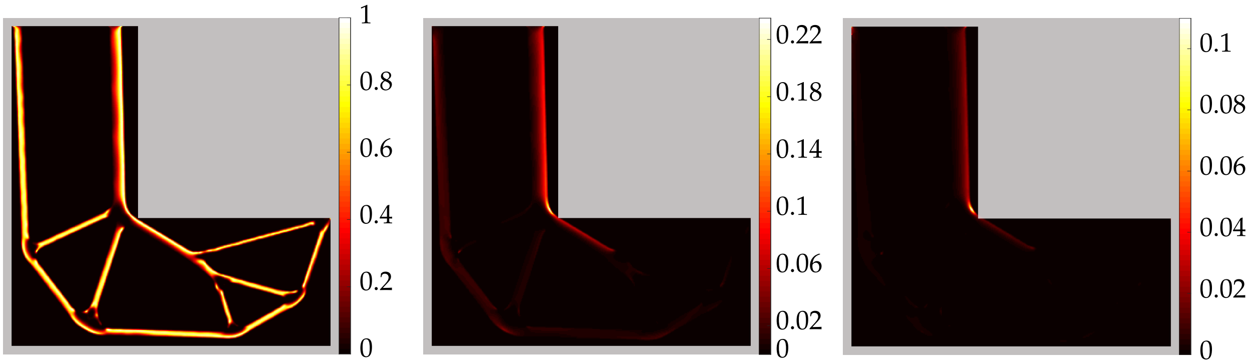

Figure 5.9. Resulting damage distribution for eroded (left), intermediate (middle) and dilated (right) designs. Highest element damages are 1.000, 0.2348 and 0.1099 respectively.

constant equal weighting i.e. $c_1 = c_2$. To illustrate the differences, the eroded design and damage of this problem is compared to that of the continuation example, see Figure 5.10.

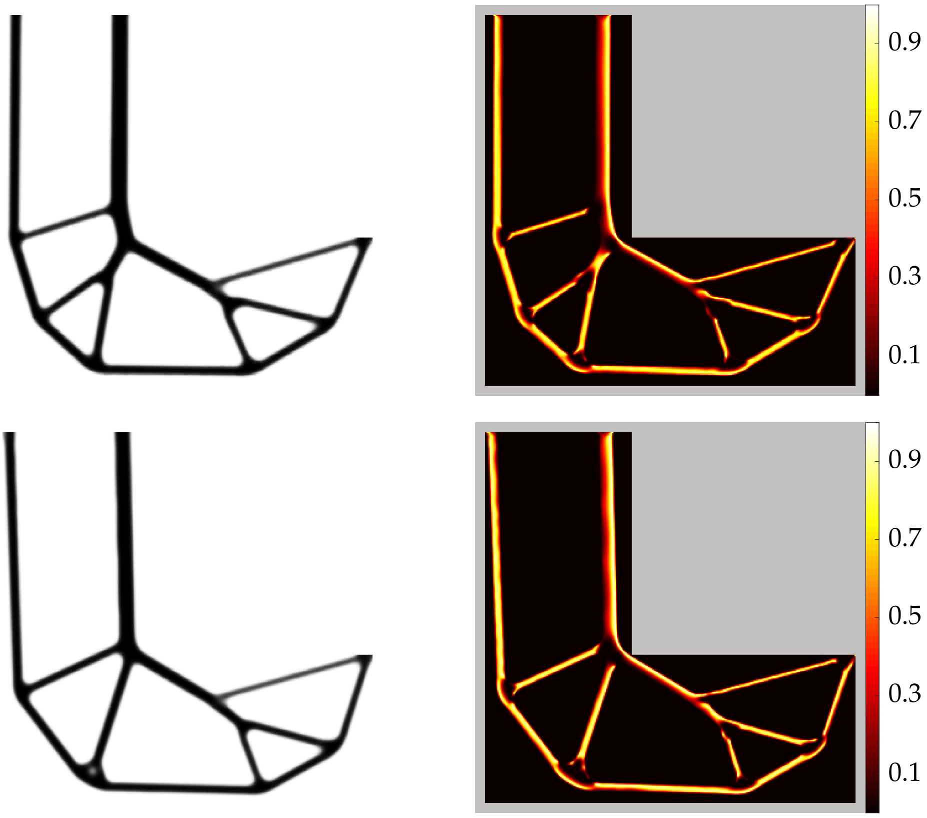

Figure 5.10. Eroded designs solved without continuation (top) and with continuation (bottom). Resulting volume fractions are 0.1748 and 0.1625 respectively - approximately 7% reduction in volume. Similar relative reductions were found for intermediate and dilated designs. Maximum damage is 0.9997 and 1.000 respectively. Damage is slightly higher for the non-continuation intermediate and dilated designs.

Both approaches are able to generate designs with good distribution of damage in the eroded design. The final volume fractions are however higher for the non-continuation designs, indicating that a no continuation approach has higher risk of being trapped in a poor local optimum.

Observing the convergence, see Figure 5.11, the purely linear formulation makes the problem more volatile for subsequent continuation of the discreteness parameter β. This is evident from the large peak in the eroded damage constraint at 1000 iterations. In this case the optimizer was able to return to a feasible design, but such a degree of infeasibilty may cause divergence in other cases. For increased robustness, a different continuation strategy may be preferable, e.g. by keeping the weight factor for the Basquin formulation nonzero.

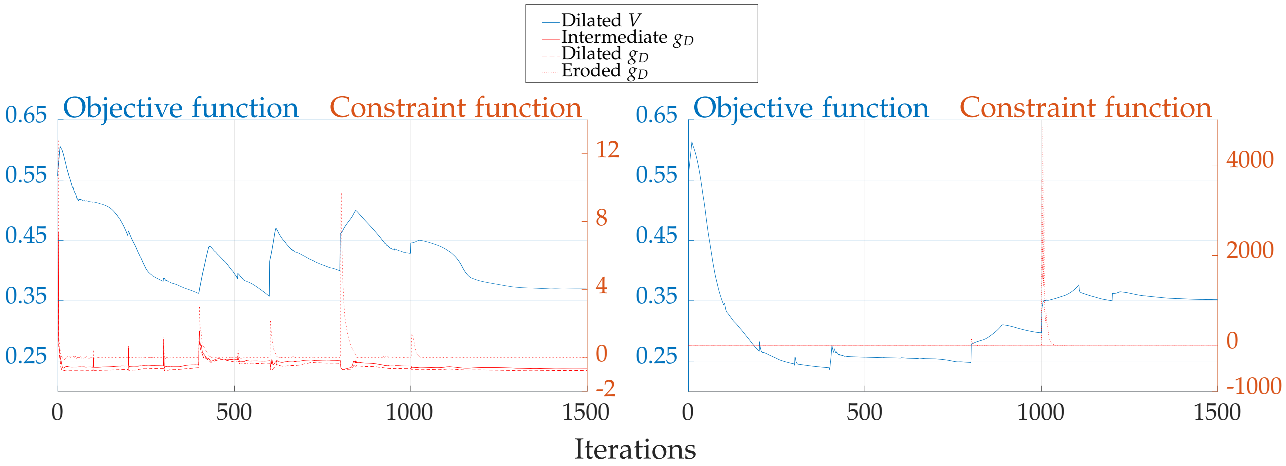

Figure 5.11. Convergence for the problem with no continuation of P-mean (left) and with continuation (right).

5.5 2D Optimization with Orientation of Print Plane

Three examples are used to illustrate the effects of the anisotropic criterion: first using no anisotropy (corresponding to signed von Mises), then with the anisotropic criterion and fixed print plane angle, and finally with both anisotropy and variable angle.

With outset in AISI 1020 (Table 2.1), a fictitious fatigue behavior is introduced, where the fatigue strength orthogonal to the print plane normal is double that of parallel, see Table 5.3. For these examples, influence from surface quality is assumed to be fully explained by the fatigue strengths of the fictitious material. The degree of anisotropy is large for illustration purposes, but not unreasonably so if compared to a real value as found in Equation (3.29). These values belong to a heat treated material, i.e. the defects and by extension fatigue properties should be improved over the as-built.

Fatigue strength $\sigma_{f\perp}$	1384	[MPa]
Fatigue strength $\sigma_{f\parallel}$	692	[MPa]
Basquin factor b	-0.156	

Table 5.3. Fictitious anisotropic fatigue properties of AISI 1020 in AM. Compare to Table 2.1.

Problems are solved using P-mean scaling with continuation of weighting parameters as described in Section 5.3.

5.5.1 Isotropic Fatigue

If material anisotropy cannot be modeled, the lowest fatigue strength must be used in combination with the isotropic fatigue constraint g_D (Equation (3.42)) to ensure that the design will not fail. In contrast to the design in Figure 5.7, this naturally means that more material is needed and that convergence is hindered by the additional restrictions to the design space, which is precisely what is seen in the solution for low fatigue strength, see Figure 5.12.

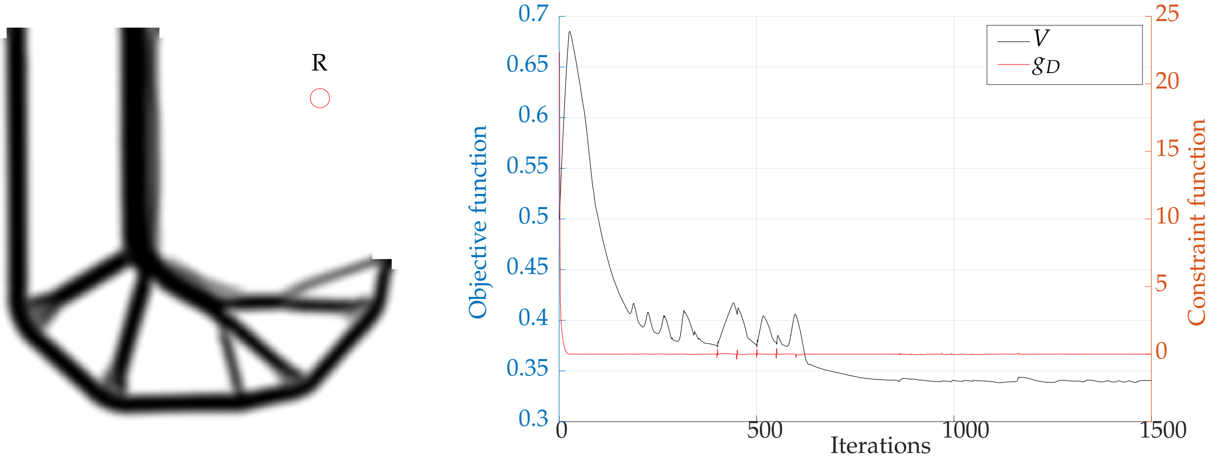

Figure 5.12. Density and convergence for isotropic solution of anisotropic material. Volume fraction is 0.3405.

Damage distribution is reasonable, see Figure 5.13, but the design suffers from poor penalization of intermediate densities particularly around the stress concentration, likely because the change toward linear damage scaling is applied too early, which also leads to a small concentration of damage in the reentrant corner. Stress distribution is even, similar to a stress constrained design, with slightly higher stresses for areas in compression. This distribution occurs due to the handling of compressive mean stresses, which are assumed to be beneficial as compared to tensile mean stresses.

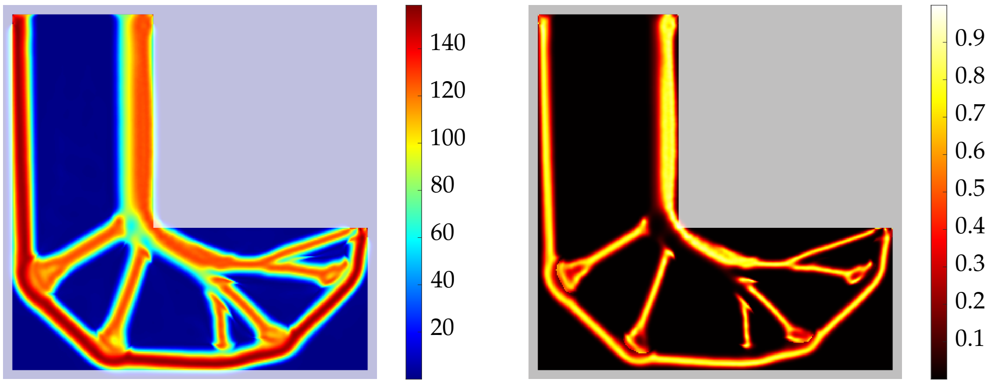

Figure 5.13. von Mises stress [MPa] (left) and damage (right) for worst case fatigue strength.

5.5.2 Anisotropic Fatigue with Fixed Print Plane Angle

Introducing anisotropic treatment of damage enables better use of material and better convergence, see Figure 5.14, as more of the available fatigue strength can be used. For this example, the print plane normal is arbitrarily selected to be parallel to the y-axis and damage is constrained by $g_{D\alpha\sigma_{VM}}(\boldsymbol{\rho})$, see Equation (3.46). Due to the direction of the print plane and principal stress direction in the reentrant corner (see also Figure 5.4), fatigue strength very close to $\sigma_{f\parallel}$ is observed here, whereby the local intermediate density is difficult to remove.

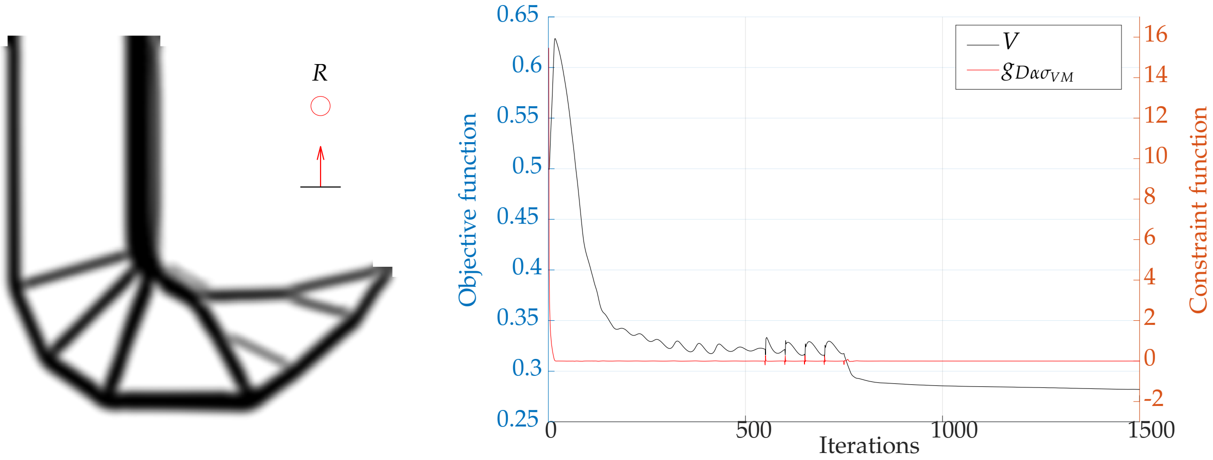

Figure 5.14. Density and convergence for anisotropic fatigue constraint $g_{D\alpha\sigma_{VM}}$ with fixed print plane normal. Volume fraction is 0.2819.

The stress distribution is clearly affected by anisotropy; knowing that the principal directions tend to align with the structural members, high stresses occur in near-horizontal structural members, corresponding to the $\sigma_{f\perp}$-case, and low stresses for $\sigma_{f\parallel}$, see Figure 5.15.

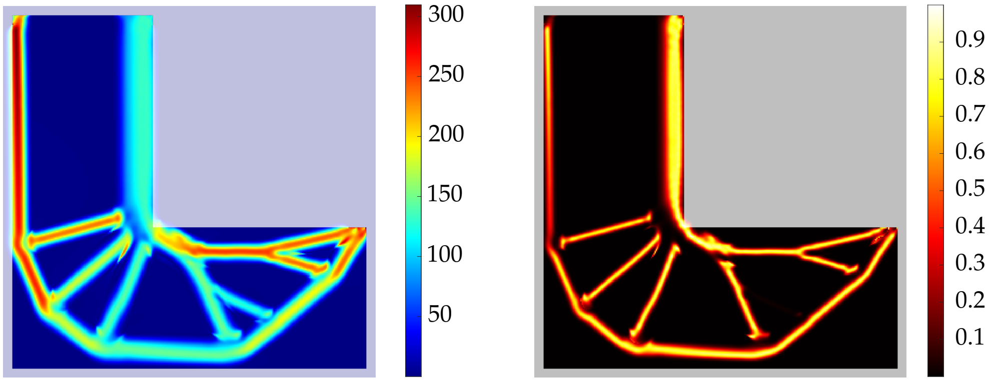

Figure 5.15. von Mises stress [MPa] (left) and damage (right) for anisotropic fatigue constraint $g_{D\alpha\sigma_{VM}}$ with fixed print plane normal.

An important observation here is the treatment of compressive stresses. Due to the α-parameter, equal damage is obtained for different stress combinations depending on the orientation; in areas where print plane normal and first principal direction align, the equivalent fatigue strength is reduced (see Figure 5.16) as intended. However, when using von Mises stress in the equivalent stress, compressive stresses are included - contrary to using the first principal stress and ignoring second/third principal. This means that the assumption that fatigue strength is only affected when defects are in tension no longer holds, as seen in Figure 5.15 where the stress in the compressed section is not constant. This results in varying thickness as seen in Figure 5.14, which is not intended.

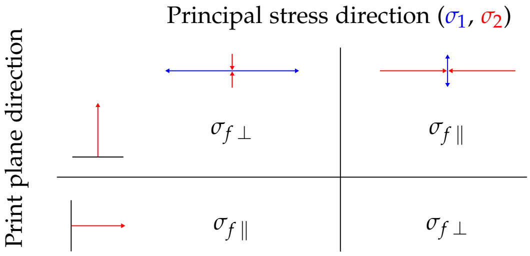

Figure 5.16. Combinations of print plane direction and principal stresses, and the fatigue strength for the given case. Note that the magnitude of stresses does not influence the fatigue strength.

A solution is to use the principal stress formulation (Equation (3.36)) with a second constraint g_σ (Equation (3.41)), such that compression is entirely ignored in fatigue computations, but still controlled by the stress constraint. The results of this are illustrated in Figure 5.17, where the stress limit is set to the yield stress, i.e. $\sigma_{VM} \leq S_y = 262\text{MPa}$. The most noticeable differences are those discussed, i.e. the compression side has a more consistent thickness and no damage is computed for the area in compression. Volume is also improved, since compressive stresses impose a less strict constraint for this formulation.

5.5.3 Anisotropic Fatigue with Variable Print Plane Angle

If the orientation of print plane is included as a variable, an optimized combination of material distribution and orientation is found simultaneously. The optimal print plane angle is trivial for the plane stress case: out-of-plane, such that all loads are orthogonal to the print plane normal (which is exactly what would be obtained for a similar geometry in three dimensions). Restricting the angle to be in-plane however admits clearer visualization of stress effects than the 3D case.

Initial guess of the print plane normal is vertical as in the previous example, i.e. $\theta_p = \frac{1}{2}\pi$. Due to the issues using the von Mises expression in equivalent stress, the first principal stress (i.e. $g_{D\alpha\sigma_1}$, Equation (3.43)) is also used here. On Figure 5.18 it is seen that the print plane normal aligns with the structure closest to the load, such that fatigue strength is lowest where the transferred moment is lowest, and vice versa. The same is seen from the stress distribution in Figure 5.19.

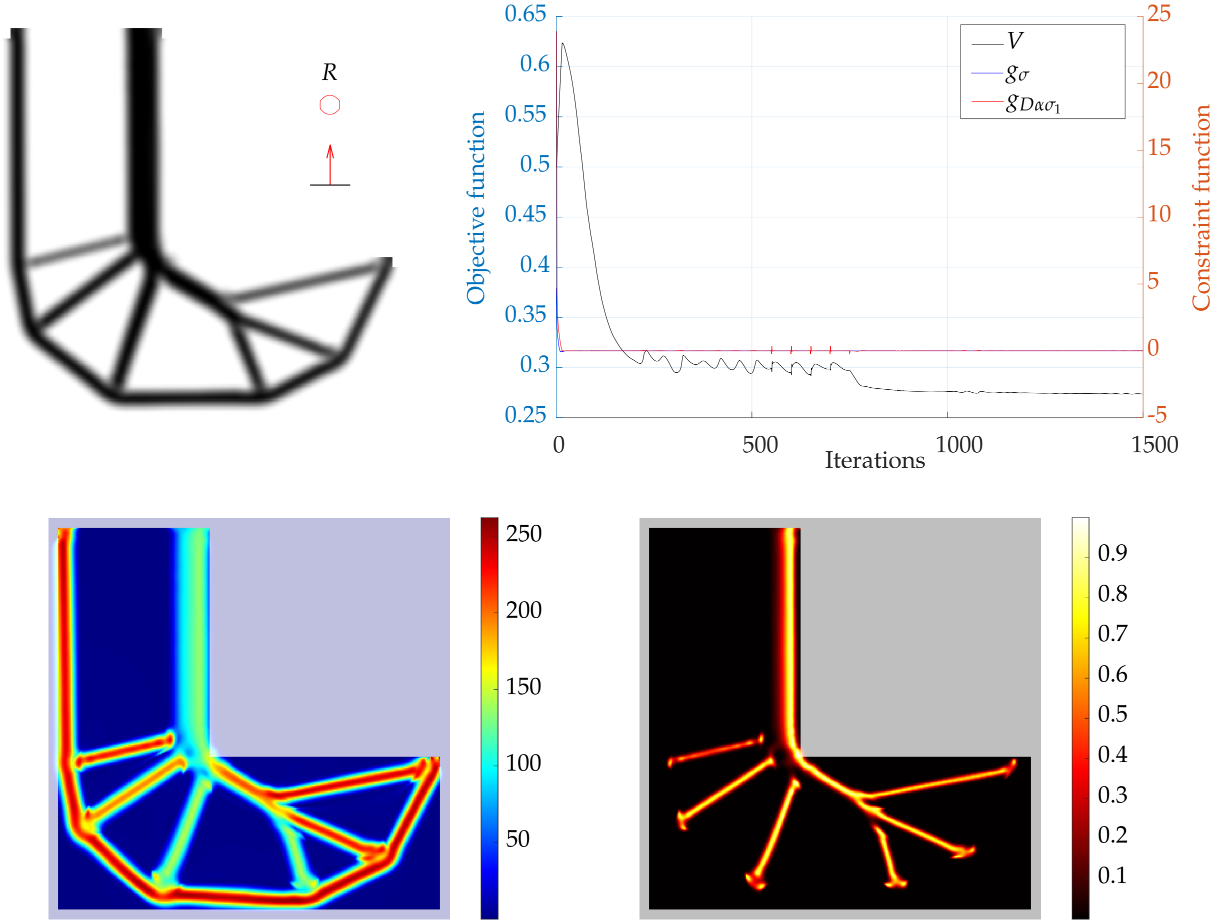

Figure 5.17. *Top*: Density and convergence for anisotropic fatigue constraint $g_{D\alpha\sigma_1}$ with fixed print plane normal and stress constraint $\sigma_{VM} \leq S_y = 262$ MPa. Volume fraction is 0.2736. *Bottom*: von Mises stress [MPa] (left) and damage (right) for the problem.

5.5.4 Body-fit Mesh Verification

To verify the implementation, results are compared to a body fitted mesh of an equivalent geometry in ANSYS. The design generated in Figure 5.18 is extracted using an isocurve for $\tilde{\rho} = 0.5$ and imported in ANSYS SpaceClaim, where a minor smoothing of the reentrant corner was performed to remove high stresses. The ANSYS model is meshed using 6586 second order quadrilateral elements, with an approximate side length of 5 mm and average aspect ratio of 0.98079.

In Figure 5.20 von Mises and first principal stresses are presented. Similar distributions are seen for both models, though some bending stress appears in the ANSYS models. Additionally, stress singularities occur at the fixed edges leading to the maximal high stresses, whereas the stress elsewhere in the model are always less than 220 MPa.

Comparison of damage is difficult as ANSYS does not allow implementation of the anisotropic fatigue model, but using the signed von Mises model (as in the isotropic example), see Figure 5.21, demonstrates some trends. In essence, the damage distribution is comparable to the distribution of von Mises stress, but affected by the sign of hydrostatic stress. Structural

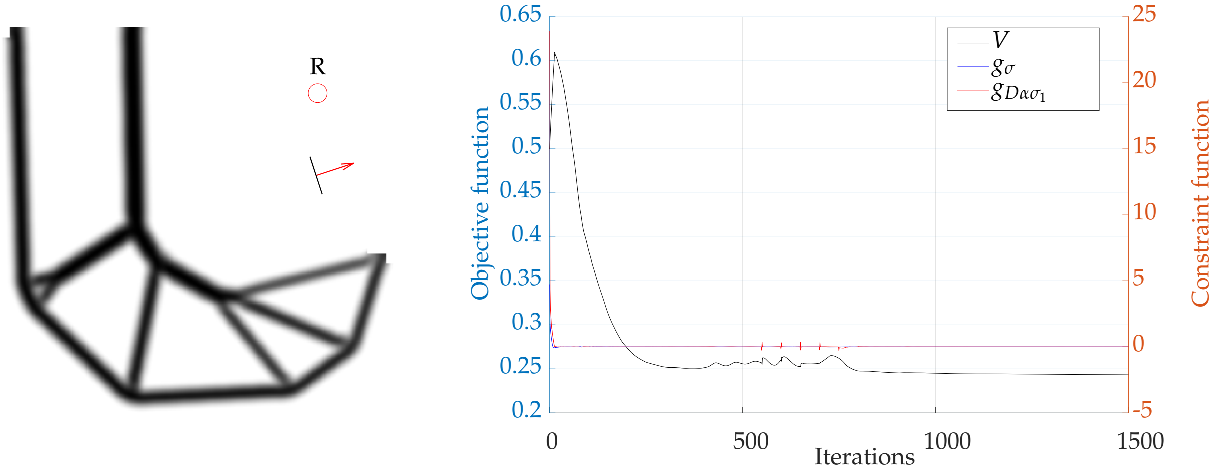

Figure 5.18. Density and convergence for anisotropic fatigue constraint $g_{D\alpha\sigma_1}$ with variable print plane normal. Volume fraction is 0.2433 and optimized print plane normal is angled 18.11° away from the x-axis ($\theta_p = 0.3160$).

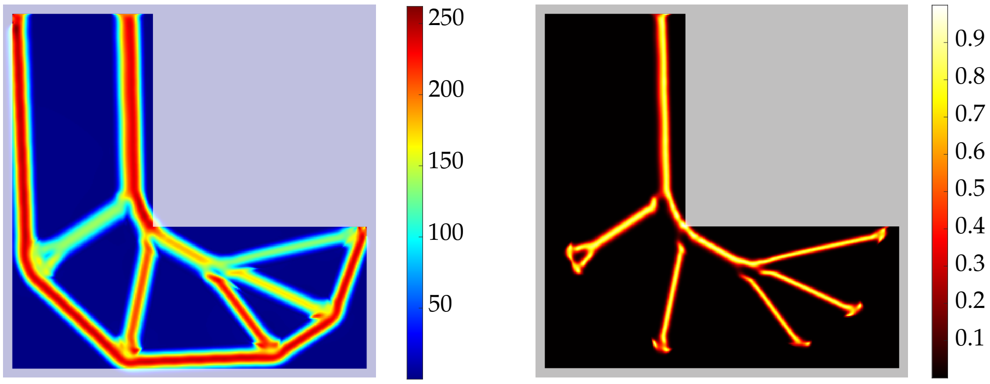

Figure 5.19. von Mises stress [MPa] (left) and damage (right) for anisotropic solution with variable print plane normal.

members parallel to the print plane normal have low damage, as these are dimensioned via the low fatigue strength, contrary to the members closer to orthogonal to the print plane normal.

The optimized volumes of the fatigue models are presented in Table 5.4. The introduction of anisotropic fatigue plainly means more efficient use of material, though only as far as allowed by the uncertainties of material data.

No anisotropy	0.3405
Anisotropy, $\theta_p = \frac{1}{2}\pi$	0.2736
Anisotropy, $\theta_p = 0.3160$	0.2433
ANSYS model	0.2450

Table 5.4. Final volume of the fatigue formulations.

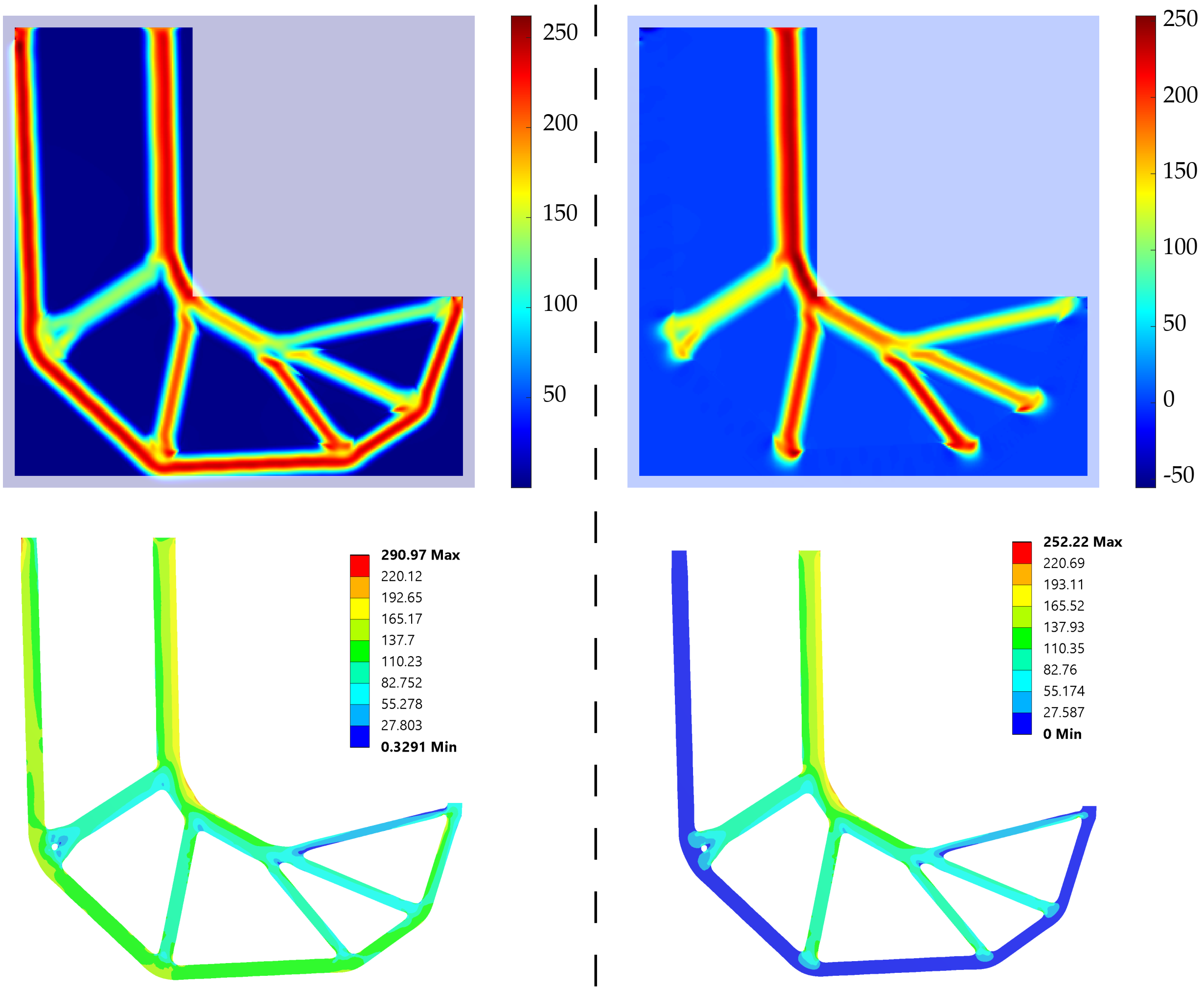

Figure 5.20. von Mises stress [MPa] (left) and first principal stress [MPa] (right), for anisotropic solution with variable print plane normal (top) and equivalent ANSYS model with body fitted mesh (bottom).

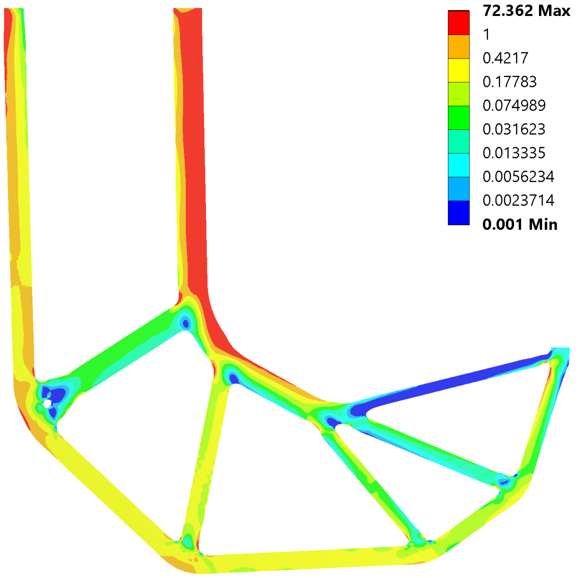

Figure 5.21. Damage computed using signed von Mises and low fatigue strength $\sigma_{f\parallel} = 692$ MPa.

5.6 3D Optimization with Orientation of Print Plane

To investigate the 3D implementation a modified L-beam problem is solved. Using the existing definition of the problem will result in the optimized orientation of print plane being placed exactly in the x-y plane. The problem is modified by adding a force component in the negative z-direction, see Figure 5.22, making the optimized orientation of the print plane non-trivial. Note the dimensions have also been changed, mainly to increase geometric resistance in the z-direction.

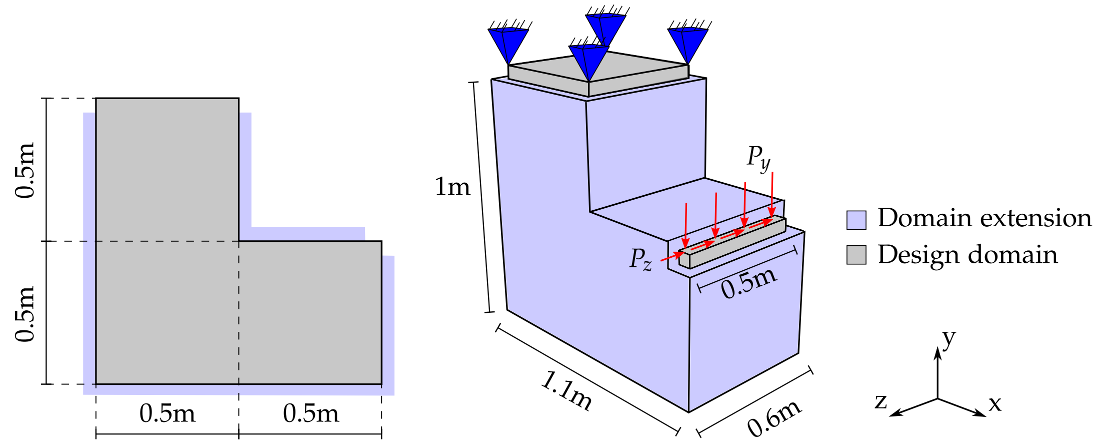

Figure **5.22.** The 3D problem. Domain extension adds 0.05 [mm] of thickness around the structure.

For the orientation variables, a starting guess of $\theta_x = \theta_y = -\pi/10$ is chosen.

The FE problem is discretized with 35 056 elements, 24 002 of them having design variables. The mesh is fully structured with element lengths of 0.025m. A load of 1 350 000 N is applied in both x and z, distributed over 18 nodes along z. Equivalent damage is computed using the maximum principal criterion, see equations (3.36) and (3.43).

A 3x3x3 density filter using $R = 0.045$ m is used to regularize the TO problem. The robust method is applied with the thresholds $[\eta_e, \eta_i, \eta_d] = [0.75, 0.5, 0.25]$. Continuation is used for the discreteness variable β, starting at 1, and then at 400 iterations it doubles for each 150 iteration, ending with $\beta_{lim} = 16$ at 850 iterations. q is kept constant at 0.75 for the first 100 iterations, then decreased to 0.5. Damage scaling is done using the P-mean scaling method with constant and equal weighting.

The resulting eroded, intermediate and dilated designs are illustrated in Figure 5.23. With this new load case, the position of the rounding changes location to the corner of the structure (the closest corner of the left view of Figure 5.23). A quite significant reduction in volume is achieved for every design due to the geometry being hollow. This very well illustrates the potential of TO for these three-dimensional designs, where placement of material is not at all intuitive. Using the robust method with threshold filtering, highly discrete designs are achieved as reflected by the measure of nondiscreteness.

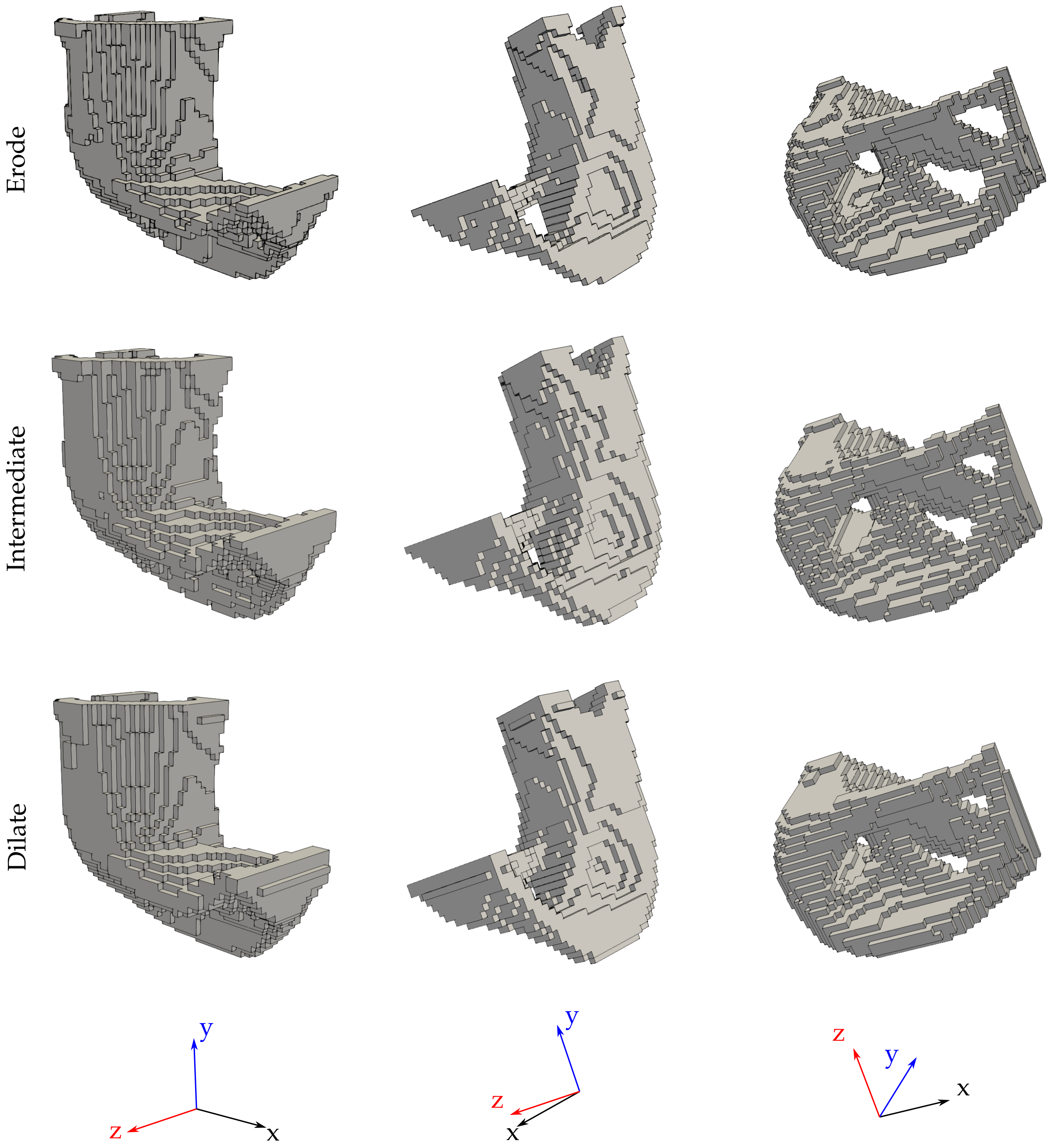

	Eroded	Intermediate	Dilated
Volume	0.0668	0.1076	0.1422
Volume fraction	0.1781	0.2869	0.3792
M_{nd} [%]	5.487	6.111	6.581

Figure 5.23. Resulting 3D design. The designs are illustrated using a density cutoff of $\rho \geq 0.5$. Percentage reduction is wrt. the starting design used in the optimization i.e. where densities are $\boldsymbol{\rho} = 0.5$.

The convergence of the problem is illustrated in Figure 5.24. In general the problem is sensitive, having more oscillatory behavior as a consequence of the continuation approach, yet still able to return to a feasible design in reasonable time and volume is stable when the iteration limit is reached. It is observed that changing q at 100 iterations may have been too early, as the objective function still had a steep slope of descent, and that a better minimum may have been achieved by delaying the decrease in q. Good penalization is however achieved by using this approach, indicated by similar topologies of the designs, see Figure 5.23.

The use of the relatively high (for problems involving stress) discreteness factor is arguably erroneous as the stress singularities become too dominant in the stress measure. Observing the degree of oscillation at the continuation points in the convergence curve of Figure 5.24, the most substantial increase in discreteness seems to occur when β is increased to 4. This is related to the effect of projection lessening as β is increased and not so much the stress singularities. Recall Figure 2.12, where projections are illustrated. Change in projection intensity is largest around $\beta = 5$ and so higher values of β have diminishing effects on the projected values.

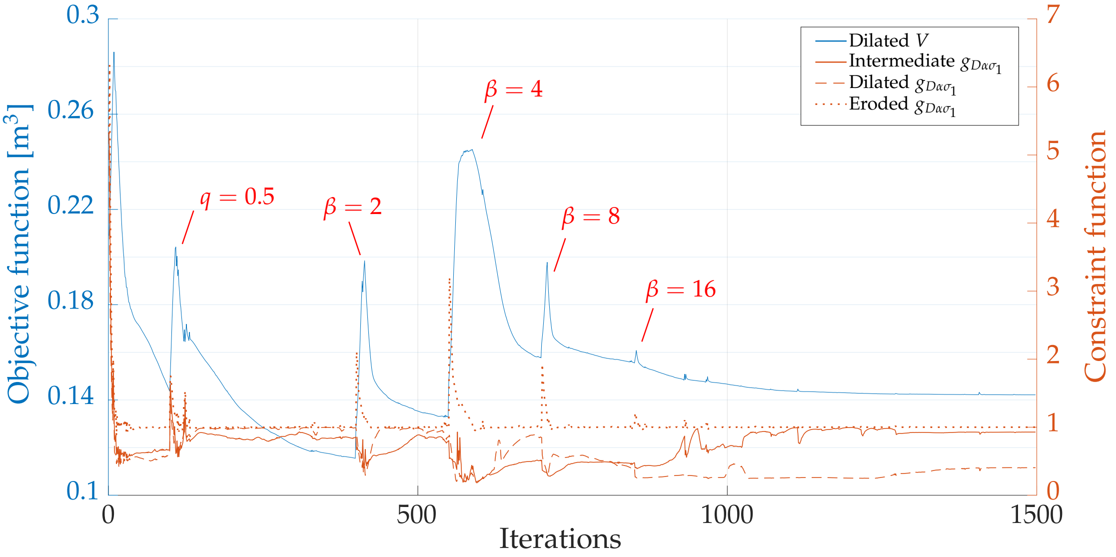

Figure 5.24. Convergence curve with highlighted points of continuation. Note, the constraint limit is defined as 1 for this problem, and that the objective function is measured in absolute volume.

The damage distributions of the designs are illustrated in Figure 5.25. Similar to the two-dimensional examples with the robust method, high damage is distributed to the entire geometry of the eroded design, whereas for the intermediate and dilated designs, the general damage level is significantly less. For this example, it is further observed that high damage is concentrated in a single element in both the intermediate and dilated designs. This is caused by the threshold filtering around these elements promoting the stress singularity problem. Because the relaxed version of the threshold filter is applied, the densities of each design are projected differently. Inspecting the element densities surrounding the highly damaged element of both intermediate and dilated designs reveal that while the entire density gradient is essentially projected to void in the intermediate design, some, albeit not much, intermediate density is still present in the dilated design, smoothing the sharp edge of the element. As a result, the local damage is higher in the intermediate design.

In Figure 5.24, the damage constraints for intermediate and dilated designs are approximately equal until $\beta = 16$, where they clearly separate. The dilated design contains more volume

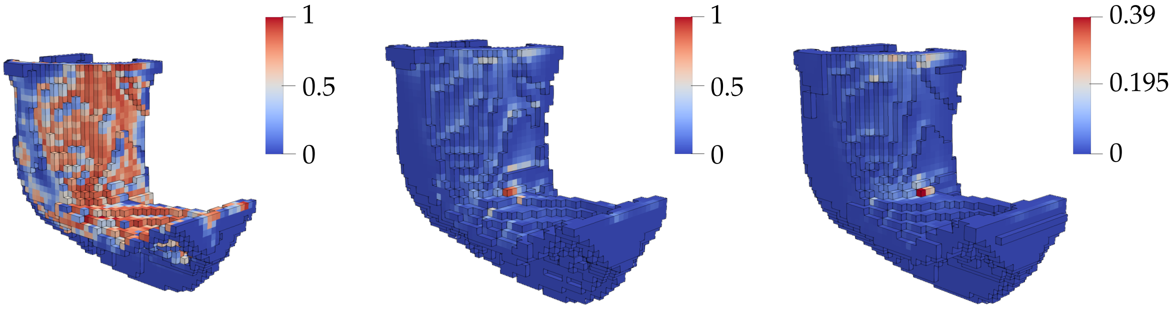

Figure 5.25. From left to right are the eroded, intermediate and dilated damage distributions. Highest damage of each design is 0.9999, 0.9011 and 0.3875 respectively.

and is therefore expected to be the geometrically most fatigue resistant design throughout the entire optimization. There are two contributions as to why this is not the case; the interference of the stress singularities already discussed, and the nonlinear local nature of the problem. The increase in thickness causes the radius of the rounding to be smaller, which increases the geometric stress concentration, and the damage may as a consequence be larger, locally, in the dilated design in the earlier stages of the optimization. When the design becomes highly discretized, the singularities instead become dominant causing the separation.

The highly nonlinear dependence of stress is apparent when comparing the damage distribution of Figure 5.25 with the principal stress distributions of Figure 5.26. Note that like the damage, the highest element maximum principal stress is concentrated in the same single distinct element of Figure 5.25.

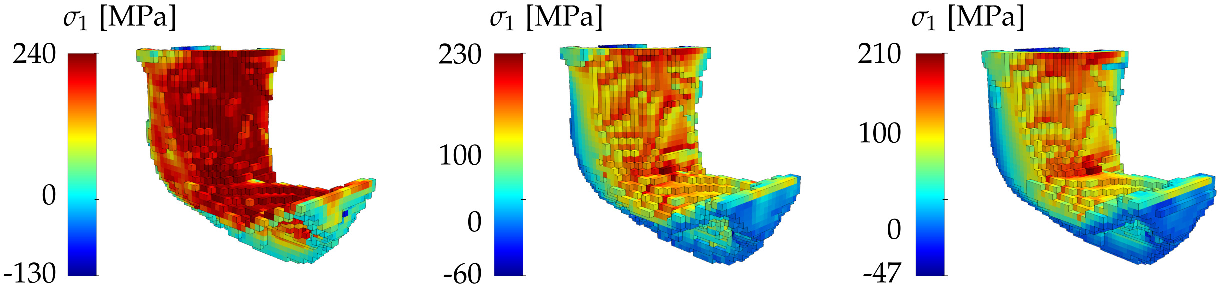

Figure 5.26. Stress distribution for the eroded (left), intermediate (middle) and dilated (right) designs. Maximum element damage is 237 [MPa], 233 [MPa] and 206 [MPa] respectively.

As only the tensile damages are accounted for in the maximum principal criterion, the damage is low in the lower part of the structure. This is observed in Figure 5.27, where the damage distribution of the eroded design is plotted from different views. The damage distribution attained corresponds to that achieved in the two-dimensional examples, see Figure 5.19. No information about compressive stresses is included in the criterion and these should therefore be contained by an accompanying stress constraint for realizing the design. This is not unique to the criterion, and will likewise be needed for e.g. the Sines criterion [Stephens et al., 2001].

The resulting optimized orientation of the print plane is found (in radians) as $[\theta_x, \theta_y]$ = [0.3313,

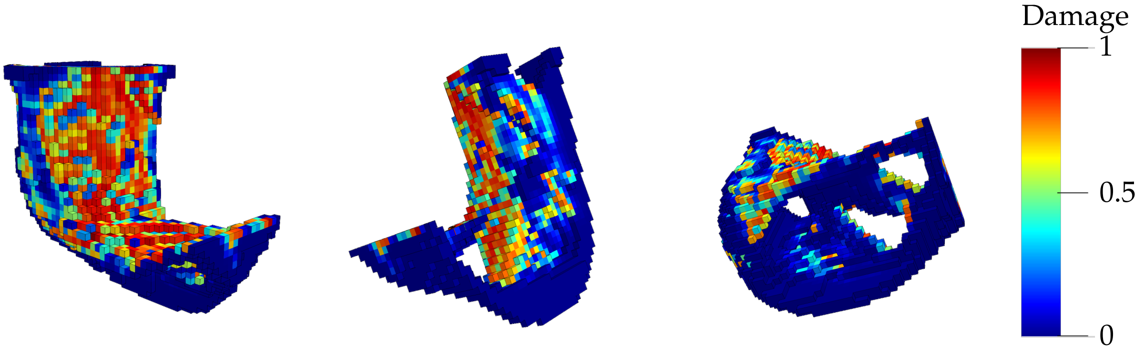

Figure 5.27. Damage distribution of the eroded design.

0.2935]. Its placement is illustrated on the geometry in Figure 5.28.

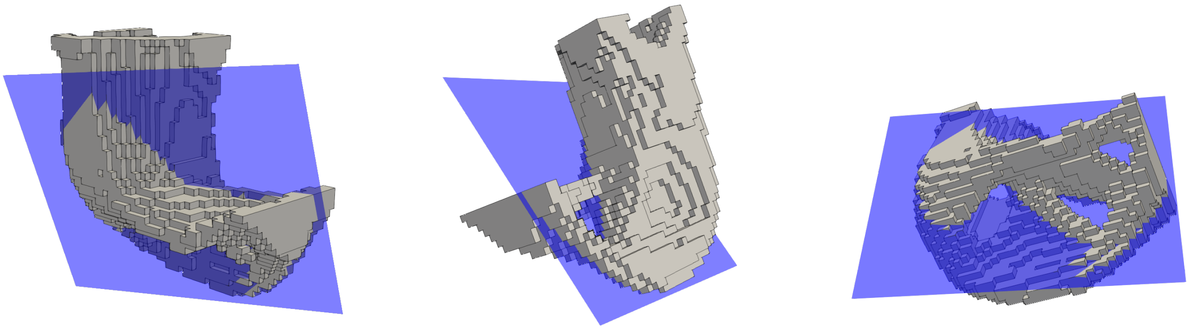

Figure 5.28. Illustration of the optimized orientation of the AM print plane in three-dimensional space.

Bodyfit Mesh Verification

Verification is performed to investigate the structural integrity of the TO design by performing a high quality FE analysis using the commercial program ANSYS. The verification takes offset in the intermediate design as this is the blueprint design. Focus will mainly be on comparing the stress distributions as the anisotropic fatigue model used is not implemented in commercial programs.

To facilitate the verification, consider the maximum principal stress plots in Figure 5.29, which are used for comparison.

As was done for the plane stress example, the geometry is interpolated (using the density interpolation described in Appendix A) and a mesh is fitted to the body in ANSYS. Only the intermediate density design is presented in these examples. 126 927 quadratic tetrahedral elements are used to model the geometry, with an average aspect ratio of 2.8785. No smoothing has been performed on the interpolated geometry to illustrate the quality of the extracted geometry.

Illustrations of the stress state in several orientations are presented in Figures 5.30 and 5.31 on

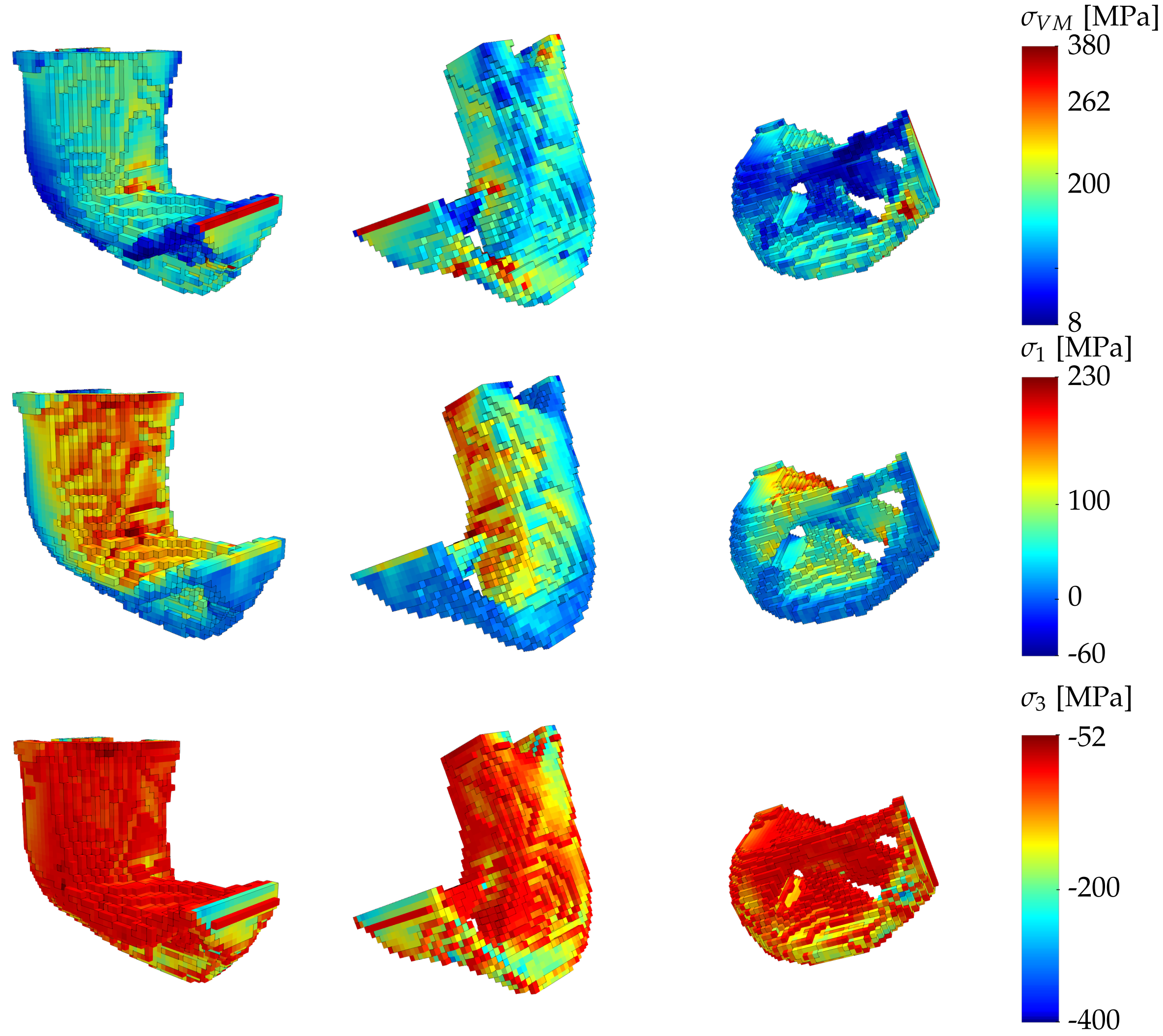

Figure 5.29. von Mises, maximum principal stress and minimum principal stress distributions in the intermediate design.

the following pages. Distributions are comparable to the TO model with somewhat larger stress level near concentrations. In particular note the load introduction area with high σ_1 caused by the increased FE discreteness enhancing the significance of boundary condition singularities. The design however shows a general tendency to distribute the local stress concentrations similar to the TO model. This indicates that the interpolated design is able to capture the stress of the TO model fairly well, and the difference between the two models is attributed to the comparatively poorly discretized FE model used in the TO and the difference in element order. Interestingly, the stress concentrations seem to occur as a result of the stress singularities of the TO model (see the left von Mises plot), locally affecting the density distribution. These local stresses may be alleviated by removing the effect of stress singularities from the optimization.

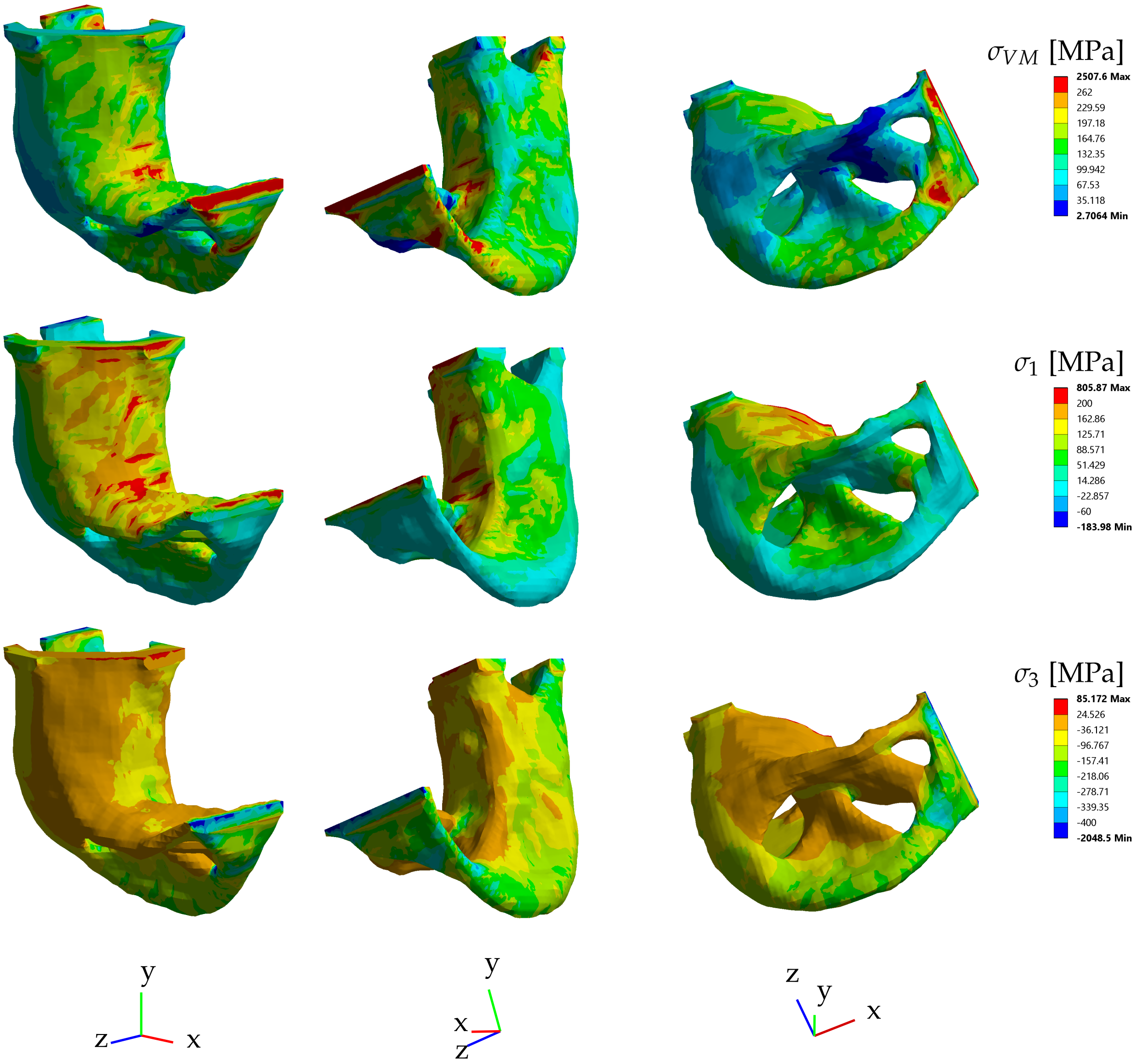

Figure 5.30. Stress distribution as computed in ANSYS. Note that values of the color scales differ between stress representations.

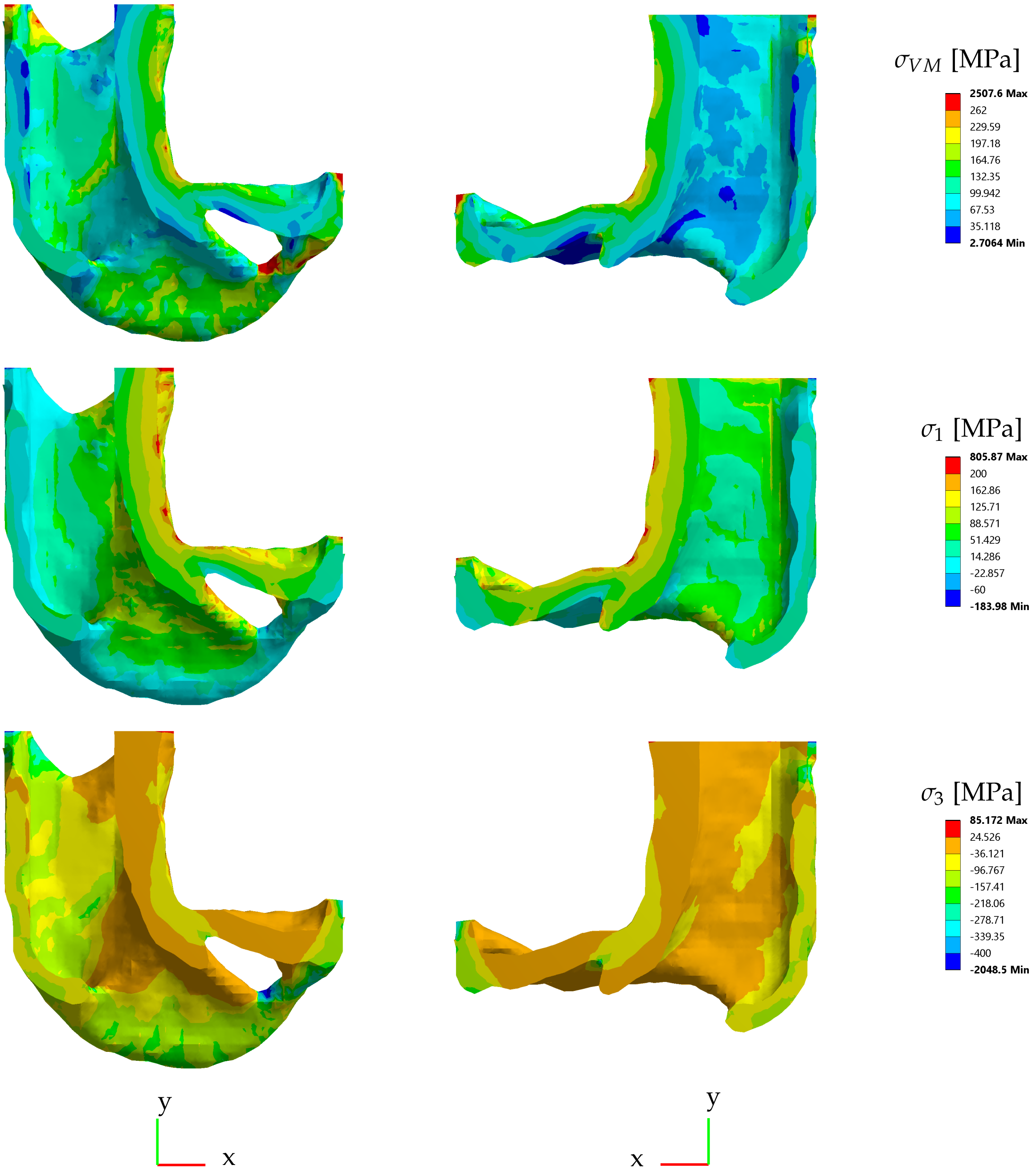

Figure 5.31. Stress distribution as computed in ANSYS, using a cross section in the x-y plane. Note that values of the color scales differ between stress representations.

5.7 "Finely" discretized 3D Example with Discussion

Another 3D problem is solved with results illustrating some important aspects regarding the interaction of the different methods used, and in particular the effect on post optimization smoothing.

The geometrical problem solved is that of Figure 5.22, however some changes have been made to the FE and TO formulations. For the FE problem, the amount of elements has been increased to 108 099, of which 73 169 have design variables, and the load has been decreased to 1 150 000, mainly to reduce thickness of the generated members (for reasons that will become evident in the following discussion). The mesh is still fully structured. The TO problem is formulated using the threshold filter of Equation (2.14). The same filter radius as the one used in the previous 3D example is reused here, such that the same width of the density filtered members should be guaranteed. The limit on the discreteness parameter is reduced to $\beta_{lim} = 8$ due to observations of the singularities influencing the previous result. Also, continuation on the P-mean scaling is applied for this example, see Table 5.5 for the entire continuation strategy. The resulting density, maximum principal stress and damage of the TO geometry is visualized in Figure 5.32.

Iteration	0	100	200	300	400	500	550	600	650	700	800	1000
β	1							2			4	8
c_1	1				0.81	0.62	0.43	0.24	0.05			
c_2	0				0.19	0.38	0.57	0.76	0.95			

Table 5.5. Continuation of parameters used in the 3D example. The P-mean constants are not pushed to the fully linear measure in the end, due to the high instability it imposes on the optimization.

5.7.1 Robustness of Surface Interpolation

The TO geometry is smoothed using the interpolation method of Appendix A. Similar conclusions can be drawn when performing verification of this smoothed design in ANSYS in respect to the stress and damage measures as the smoothed design of Section 5.6. This is however not the case for the smoothing itself. Due to the use of threshold filtering without the robust method, no minimum length scale is introduced and as such, the void and solid phases may become impossibly thin. While the surface interpolation generally performs well, it has one significant shortcoming. Due to how surfaces are generated, specifically using a single intra-element surface, features with a smallest dimension close to the element size are very difficult to capture accurately. In these cases, the surface interpolation may fail in one of two ways: either the geometry is entirely removed or non-manifold geometry is generated, illustrated in Figure 5.33.

The non-mainfold geometry occurs when more than two interpolated surfaces meet at an edge. As the filter radius is typically significantly larger than a single element, this failure mainly occurs in areas of exclusively intermediate density.

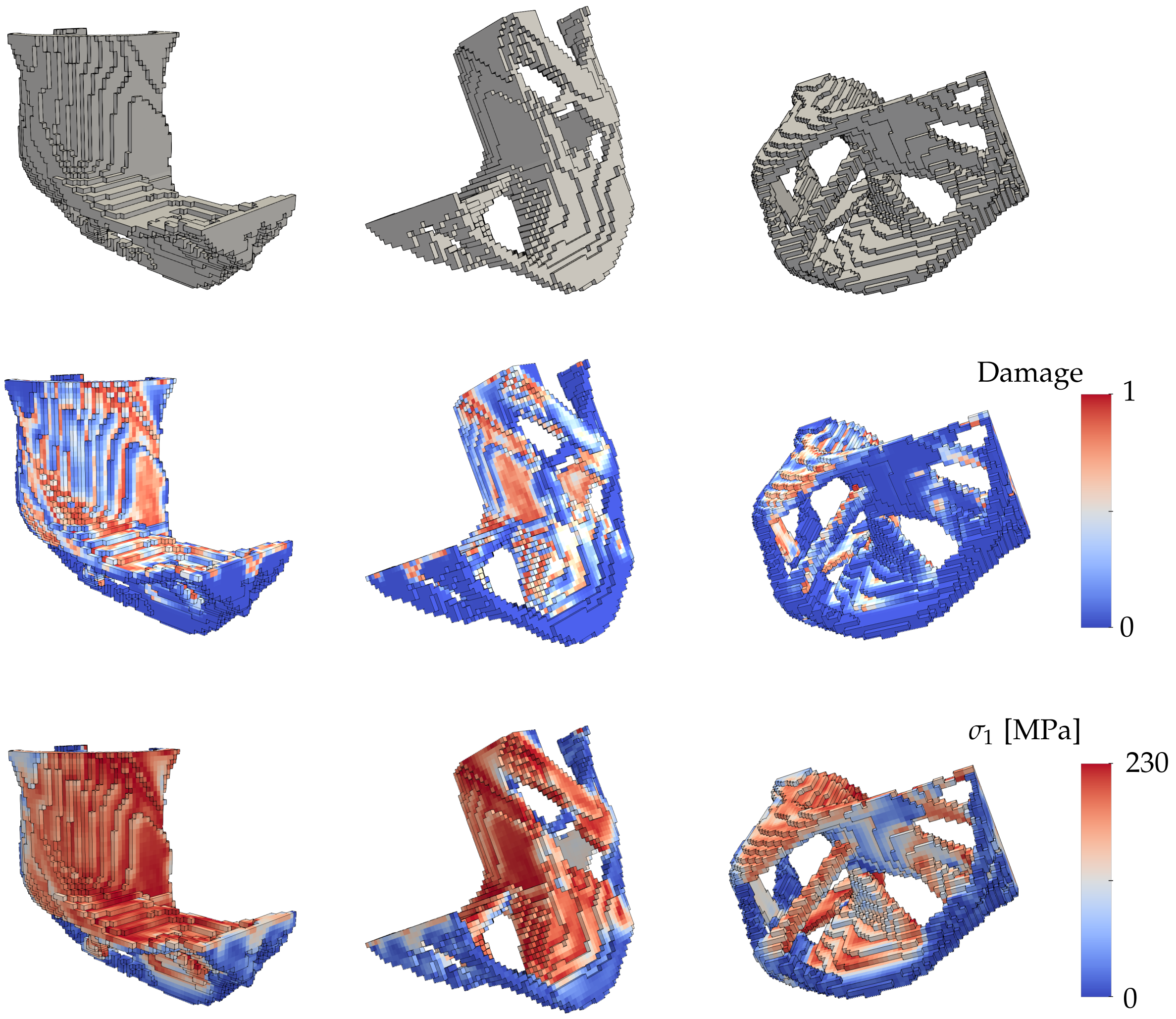

Figure 5.32. Results for the 3D example: density (top), damage distribution (mid) and maximum principal stress distribution (bottom).

The non-mainfold geometry can subsequently be repaired by something like a *shrink wrap* operation, where a new surface is generated from the most prominent features. This does however not affect the geometry that has been removed, which is only fixed by enforcing minimum length scale. This further increases the desire to have a clear definition of minimum length.

These problems are however consistent for other solid body extractions - a more conservative treatment of intermediate densities may instead assign more thickness, both in problematic areas, but also elsewhere, removing the design from the determined optimum. Further, in this specific example, the thin geometry arises due to improper handling of compressive stresses in the TO formulation and no defined minimum length scale, allowing extremely thin geometry. In general, thin geometry should be avoided already during optimization as it introduces issues not controlled for, such as buckling or increased effects of microstructure and surface

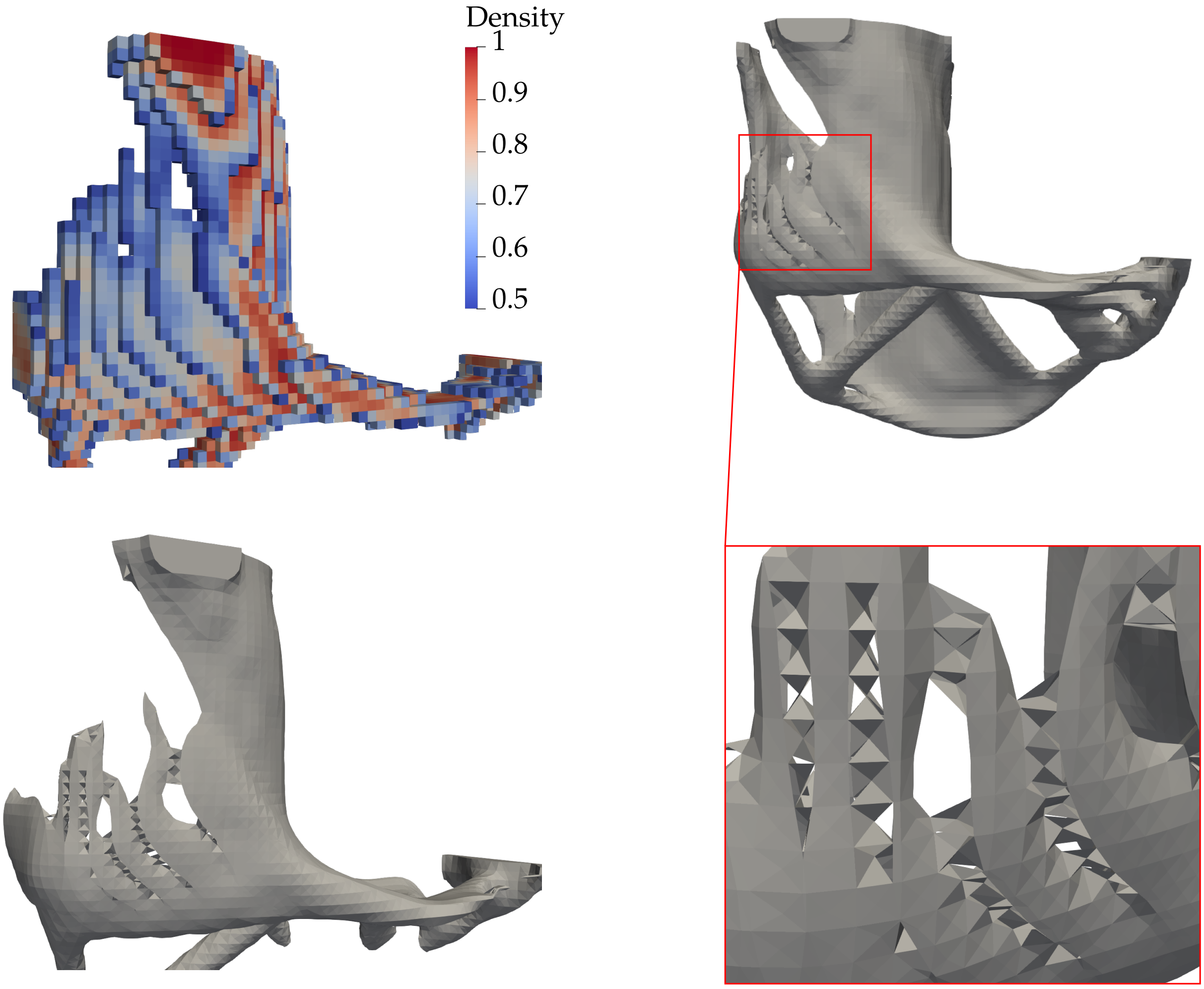

Figure 5.33. Interpolation of surface may fail when insufficient density is present, leading to removed or invalid geometry.

quality.

Returning to the example in Figure 5.30 and considering areas with adequate thickness in Figure 5.33, it is observed that the smoothing work quite well. It is also noteworthy that the despite the relatively crude discretization of the models that application of smoothing accomplish what is presently done by using mega-voxel discretization or higher, i.e. achieve smooth representation of the material boundaries.

6 Conclusion

This work has detailed modeling and implementational aspects regarding fatigue topology optimization (TO) of additive manufacturing (AM) metals. The approach is based on using the density-based method with Solid Isotropic Material with Penalization (SIMP) to interpolate stiffness properties of finite element (FE) discretized structures. Many regularization techniques have been presented and their impacts and shortcomings when applied to the model have been highlighted and discussed continuously throughout the report. The linear density filter is adopted as baseline and extensions in the form of projection filters are presented. These projections filters are also used in formulating the problem in a robust setting, which incorporates manufacturing uncertainties and imposes a minimum length scale on the structure. Boundary effects and their relation to filtering have until recently been consistently disregarded in literature. In this work the method of domain extension is used ensure consistency near these boundaries.

Including stress in TO has historically been a difficult challenge to overcome, due to complex issues inherent to the formulation, namely their local definition and the appearance of singular optima. To overcome these problems, the local stress is aggregated to a global measure using the P-norm scalarization function with adaptive constraint scaling and by introducing relaxation into the formulation respectively. Treatment of stress singularities imposed by jagged FE edges in the case of achieving highly discrete designs is also discussed.

A high cycle fatigue (HCF) stress-based fatigue model for metal materials has been presented with the purpose of determining the damage caused by an arbitrary load condition. Equivalent stress criteria are used to define a stress measure of the multiaxial stress state that is comparable to the material's fatigue strength at a given point in its load history described by the specific SN-curve. The HCF part of the SN-curve is approximated by Basquin's expression and the damage of all load combinations are accumulated using Palmgren-Miner's rule. Dealing with fatigue in a TO context is difficult as the function displays a highly unstable behavior due to the nonlinearity of its formulation. To solve this, the damage is scaled to reduce the degree of nonlinearity. The implications of this scaling approach is discussed and a new method for scaling, the P-mean scaling method, is proposed to more accurately characterize the actual fatigue damage measure. As the purpose of this work is to develop a model for AM fatigue optimization, a thorough literature study of the mechanical properties regarding fatigue of AM metals has been done. Based on this, a criterion is developed for including the anisotropy unavoidable with current AM methods in relation to orientation of the component wrt. a print plane.

It is desired to be able to solve the problem using first order sensitivity-based optimization methods. All expressions derived are therefore continuous such that analytical sensitivities can be derived. The sensitivities are derived using the adjoint design sensitivity analysis (DSA) method. The problems are solved using the Method of Moving Asymptotes (MMA).

Implementation has been discussed, herein the settings of the problems and how to make the problems easier to solve. Continuation is presented as a method to make arriving at a solution more tractable. Focus of the implementation is on investigating results generated by the developed anisotropic AM fatigue and to verify it. Both two- and three-dimensional problems are solved successfully. The P-mean scaling method successfully distributes the damage in the design as compared to previous methods. It may be combined with a continuation approach to also achieve good convergence characteristics.

The stress distributions of the TO models are compared to that of smoothed models in a commercial FE program, which shows good agreement on the distribution of stress in each. A full framework for performing this smoothing is also presented as part of this work, general for any mesh of linear elements. It is observed, that the smoothing interpolation struggles with very thin geometry, where it may create non-manifolds. This observation also enforces the importance of being able to properly define the optimized result in terms of introducing a minimum length scale.

7 Suggestions for Further Work

This chapter will discuss subjects relevant for further work. Emphasis is placed on approaches and methods to improve accuracy of the models, computational efficiency and generality of the methods implemented. Topics discussed are the FE model, TO routines, the fatigue model and AM related aspects.

7.1 Finite Element Model

The FE procedures implemented in this work has consistently been kept as simple as possible. Focus has been placed on TO and on the development of the anisotropic fatigue criterion. Modeling accurate to real-world physics is always essential and improving the FE model is desirable, particularly as TO is increasingly used in commercial design synthesis.

7.1.1 Improved Element Formulation

Linear elements are prone to exhibit shear locking behavior. Shear locking occurs when an element is not able to correctly model bending deformation. Instead, the element displays parasitic shear strains, which absorbs strain energy resulting in a significant underestimation of displacements [Belytschko et al., 2014]. The problem disappears as the solution converges, albeit slowly as no bending can be imposed on the individual elements. All presented examples are subject to bending deformation and a finely discretized mesh is necessary to accurately capture the deformation state, increasing computational effort.

Multiple solutions exist for the problem, e.g. reduced stiffness matrix integration with hourglass stabilization, B-bar method, QM6 element formulation or enhanced assumed strain, see Cook et al. [2002], Belytschko et al. [2014] and de Borst et al. [2012]. All these routines can be implemented as extensions of the existing element procedures as long as $\mathbf{k} = E\mathbf{k}_0$ which is required for SIMP.

Introduction of improved elements will remove the checkerboard problem allowing for investigation of other methods for regularization that may be more efficient than the filtering methods applied, e.g. by application of geometric constraints (discussed in Subsection 7.2.3) to govern minimum member size.

7.1.2 Density Boundary and Meshing

The approaches to mesh generation considered in this work are structured pixel/voxel-based and unstructured body-fitted. Most popular in TO is the former as the formulation is convenient for various TO procedures, especially filter calculation. Solely axis-parallel boundaries of the FE-domain are however poor approximations of most physical systems, as they are represented by jagged edges containing re-entrant corners, which causes artificial stress concentrations near the FE-boundaries. This is especially problematic as the stress in this area is often the cause of fatigue failure. Although a body-fitted mesh more accurately captures a given surface geometry, it will be subject to the same problem if used in a TO context and the problem may be more pronounced, since the mesh is likely to contain distorted elements and very sharp corners between elements.

The Interior Value Extrapolation (IVE) method by Svärd [2015b] is able to remedy this problem by extrapolation of stress from interior elements which are not exposed to singularities. Elements near the boundaries are identified by generating subsets of the mesh for each element. The position of the center of gravity is then computed for the subset, and a vector is made from the given element to the center of gravity. If the element is positioned at the boundary, the vector should point inward, approximately normal to the boundary. Boundary elements have then been identified and extrapolation from elements along the inward vector is performed.

Implementation of IVE allows for generation of highly discrete designs without being impaired by the artificial singularities, however the problem of poor representation of the actual geometry is not resolved. Here, an extension of FEM termed CutFEM [Burman et al., 2015] presents an interesting approach that may remove the discussed problems entirely. CutFEM is based on generating a background of structured mesh and then slicing the mesh at the geometry boundaries, forming new elements at the boundaries to produce a smooth FE surfaces, see Figure 7.1. CutFEM also possess advantages over traditional meshing algorithms that try to fit the entire geometry with elements as this often results in highly distorted elements for more coarse meshes. This can result in an inefficient mesh-layout that dampens computational efficiency.

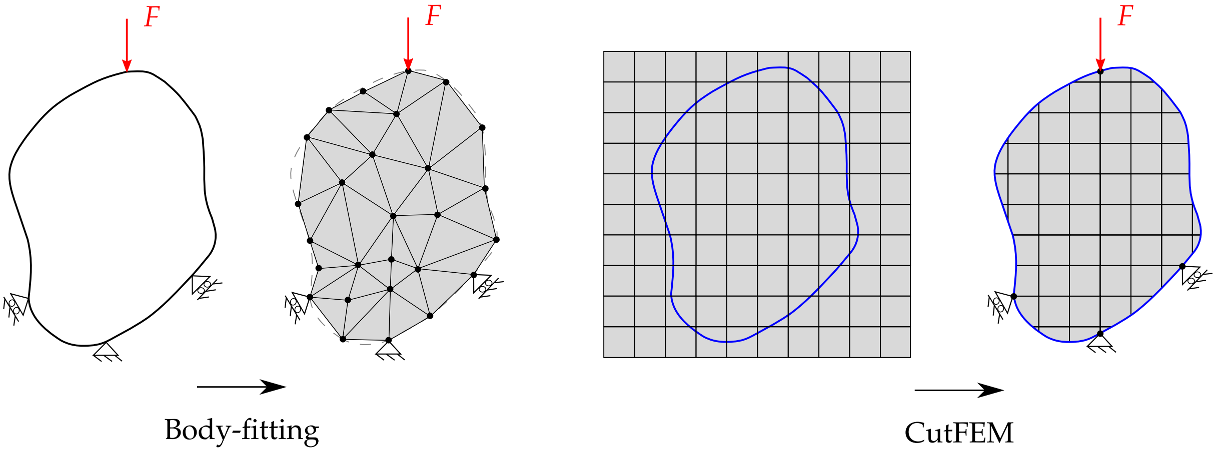

Figure 7.1. Conceptual mesh generation by body-fitting and CutFEM.

Recently, work has been published on applying CutFEM in a TO context, see e.g. Burman et al. [2019]. Also in Andreasen et al. [2020] a CutFEM inspired approach is taken to discretization and parameterization. In this work it is however emphasized that the method has significant drawbacks in relation to robustness, computational efficiency and ability to achieve the same quality of results as using classical FE density-based TO. They suggest the CutFEM approach as a postprocessing method, which can be applied on an optimized solution achieved from the regular density-based approach. Nevertheless it is believed by the authors that integration of the CutFEM approach is one of the most interesting subjects for further work as it is able to resolve the error of jagged geometry and poor boundary definition, which is a highly problematic subject in stress and fatigue problems. Further, being able to model the mesh of a general structure as a pixel- or voxel-based element mesh will increase mesh quality and reduce computational time needed to solve the problem.

7.2 Topology Optimization

Even though many procedures have been implemented for the TO, there are clear candidates for improving the implemented methods and designs achieved. Computational efficiency of TO should always be maximized, as it allows for larger and more accurate model solutions in reasonable time and inclusion of more accurate and costly criteria directly in the optimization to generate sufficient and close-to manufacturing ready designs.

7.2.1 Continuation of The Discreteness Parameter

To speed up convergence, it is of much interest to avoid continuation approaches, in particular of the discreteness variable β used in the projection filters. The objective of the projection filters is to make the designs more discrete and they should therefore not affect the topology of the final design.

A method for removing the continuation by tightly restricting the MMA asymptotes, proposed by Guest et al. [2011], was implemented and tested in this work. Because of the immediate and "hard" application of projection, all physical densities are forced to either fully solid or void essentially changing how the optimization problem is solved. The conclusion of the implementation (Subsection 5.1.2) is that using this approach likely results in a worse final design as compared to when using continuation.

A small adjustment to the approach of the method, that will emphasize the purpose of the projection filter, is to allow generation of an initial topology using only the linear density filter for regularization before the immediate application of the threshold filter and adjustment of asymptotes. This could be performed after sufficient penalization of intermediate densities is achieved. It is unclear whether this change will result in faster convergence, but is an interesting subject for further studies.

7.2.2 Filter Formulation as a Partial Differential Equation

Computation of the density filter in its conventional formulation, Equation (2.8), is tedious especially for larger models. For efficient computation, program parallelization should be performed, but is problematic and inconvenient with the conventional formulation [Lazarov and Sigmund, 2011]. Further, much memory must be allocated to store filter information.

To improve the formulation, the filter may be solved implicitly as a solution to the Helmholtz PDE. The method is introduced for linear density filtering in Lazarov and Sigmund [2011] and for including Heaviside projection filters in Kawamoto et al. [2011]. In a recent paper [Wallin et al., 2020] an alternative formulation for the PDE-filter is implemented which ensures consistency at the boundaries, eliminating the need for the domain extension approach.

7.2.3 Geometric Constraints

Using the geometric constraints by Zhou et al. [2015] for defining a minimum length scale will be highly beneficial in terms of computational efficiency. The present implementation is only able to ensure a minimum length scale through the robust TO approach, which is computationally expensive due to the additional two FE problems required. It is not entirely clear how robust the geometric constraints are in the general case, as artificial relaxation variables are introduced and must be tuned. Further studies and implementation would clarify this and what direction should be pursued in relation to defining a minimum length scale.

7.2.4 Uncertainty in Loading

Optimized structures are typically made with a specific load in mind and may as such be extremely sensitive to changes in the load case. Robustness towards this uncertainty is important if the design is to be used in realistic conditions and thus a control within the optimization procedures is advantageous. One approach is to solve the TO problem for several loads. This however has the same issues as non-proportional fatigue, where a sufficiently large set of loads leads to low computational efficiency.

In Holmberg et al. [2017] a game theory approach is presented as an alternative, using a so-called *non-cooperative game*. This involves finding an equilibrium between two or more competing objective functions, e.g. minimizing volume by choosing densities and maximizing volume by choosing worst case load. Once an equilibrium has been found, it is ensured that a change to the load (within the chosen load domain) does not invalidate the structure, since it is optimized wrt. the worst case.

7.2.5 Maximum Length Scale

This work presents a method for imposing a minimum length scale through the robust approach to TO (and suggests investigating geometric constraints for explicit definition), but a maximum length scale is not discussed. A maximum length scale may be relevant when using prefabricated substructures, e.g. beams, where an upper limit on length is desired. Nonetheless, it provides the designer with further control of the features in the final design.

Two approaches for introducing the maximum length scale are presented in Lazarov and Wang [2017]. The latter approach presented is based on morphological operators - which are also used in the robust approach. Using this method, the maximum length scale is imposed explicitly similarly to the geometric constraints. Results of a compliance optimization of the MBB-beam problem from the paper is shown in Figure 7.2.

Figure 7.2. Maximum and minimum length scale imposed on both solid and void (left) and on solid only (right). Figure from Lazarov and Wang [2017].

7.3 Fatigue Model

The present model employs rather simple fatigue modeling, which may be adequate in some cases, but if better accuracy in the estimations is desired, most of the expressions used in fatigue computation should be changed. In the following, the areas considered most significant are discussed.

7.3.1 Two-stage Fatigue Model

The fatigue model in this work is based on the stress-life approach for HCF. If the reversals till failure is placed in the LCF-regime, a strain-life approach is more appropriate and is in fact applicable for both LCF and HCF regions. This is therefore a method better suited for general cases.

An important benefit of strain-life is easier coupling to fracture mechanical fatigue models such as Linear Elastic Fracture Mechanical (LEFM) models or Elasto-Plastic Fracture Mechanical (EPFM) models [Stephens et al., 2001]. This is because a plastic zone is generated around a crack tip and the strain-life method is better at characterizing plastic behavior compared to the stress-life method. Introducing fracture mechanical methods in the fatigue formulation for AM materials is desirable due to the presence of defects that propagate similar to a mode I crack.

A starting point for implementation could be introducing LEFM to the formulation. However, care must be taken in regards to AM materials as LEFM is only valid for long cracks, i.e. cracks longer than 1-2 mm. For small cracks, LEFM will yield nonconservative estimations of the fatigue life. Fatemi et al. [2020] shows that some defects of AM materials may belong in the long cracks category for as-built specimens, although only very few. The size of the AM defects depends on the material considered and its ductility (materials with high ductility will typically not contain long cracks after manufacturing, as the material will yield locally instead). Furthermore, post-treatments such as HIP may remove large defects. This indicates that immediate application of LEFM to quantify fatigue life is erroneous for AM materials, but once a long crack is formed its application becomes desirable. Because AM materials skip the crack initiation stage the formation of long cracks is expected to happen earlier than in a wrought counterpart. Experimental evidence is however needed to gain information about when this occurs for each given component.

Another limitation of LEFM is that it is not viable for treating cracks with large crack tip plastic zones. Here, EPFM methods must be applied instead. Examples of such are the J-integral [Rice, 1968] or cohesive zone modeling [Alfano and Crisfield, 2001].

7.3.2 Microstructural Modeling

In Yadollahi and Shamsaei [2017] it is proposed to use microstructural sensitive mechanical models in determining the fatigue behavior. Microstructural models will introduce robustness in the design as the fatigue behavior of the given AM manufactured component is different as a result of differences in microstructure. Presently developed models requires a substantial amount of experimental work as they need to be calibrated for each case and this should be considered carefully before pursuing this direction.

7.3.3 Multi-axial Fatigue Criteria

Excluding the anisotropic criterion, this work has applied only a common and simple criterion for characterization of the multi-axial stress state: the signed von Mises criterion. The signed von Mises criterion is inadequate in evaluating mean stress effects due to the instantaneous signing of the mean stress in the expression [Papuga, 2012]. Furthermore using the signed von Mises also requires a mean stress correction method, which also affect the accuracy of the measure. The two mean stress corrections implemented in this work, modified Goodman and Morrow corrections, are widely used, but also conservative. An alternative correction method is the Smith-Watson-Topper, which shows much more promise in predicting mean stress effects [Papuga et al., 2018].

More accurate criteria have been developed and implementation of these for further work is therefore almost a given. A multi-axial criterion is either defined as a continuous expression or as a critical plane method and the choice of method should be chosen based not only on accuracy, but also on computational efficiency.

Continuous Expressions

A closely-related criterion to the well-known Sines criterion, the Crossland criterion, is an alternative. The criterion uses the maximum hydrostatic stress instead of the mean hydrostatic stress to incorporate mean stress effects. The criterion shows good agreement with experimental data but only applies to proportional loading and if extension to nonproportional loading is desired, other criteria should be investigated [Papuga, 2011].

Critical Plane Methods

Critical Plane Methods (CPM) are considered the most accurate approaches to quantifying multi-axial fatigue for both proportional and nonpropotional loading [Papuga, 2011]. Using CPM in conjunction with TO has not been investigated in this work as CPM are notorious for being computationally expensive, as they entail searching for the critical plane of loading in each element of the FE model.

To make applicability of CPM more realistic, much effort has to be put into making the implementation as computationally efficient as possible by e.g. vectorization and parallelization. One method to reduce the computational burden of CPM is proposed by Svärd [2015a], which entails finding the region of interest and then locally refining this region. The method is derived for the Findley criterion, but the concepts of the method applies to any CPM criterion.

Another problem with using CPM in an optimization context is the fact that it does not use continuous expressions. A semi-analytic DSA approach must therefore be adopted for gradient computation, where finite difference is used for the CPM gradient, in order to use sensitivity-based methods. Whether it is possible to implement these and solve the problem in a reasonable time frame is questionable and further research would clarify this.

7.4 Additive Manufacturing Aspects

For metal AM an important subject is generation of support structure. This has not been accounted for in the present work, but is a prudent and important topic for future work. Further, experimental studies are essential to validate the proposed methods.

7.4.1 Support Structure Design

In general, three approaches to generating support structure may be adopted. One is to intuitively build support in locations with overhang. This is not always a good solution, especially when using optimization to generate designs, as the material is sensitive to small changes in thermal history. Unnecessary material also increases build time and must be removed from the finished product, increasing post-processing costs. It is therefore a prime candidate for optimization. An "optimization" approach is presented in Calignano [2014], however this method is based on altering the design manually based on experimental data and should rather be termed an intuitive improvement approach.

A promising method is the overhang constraint by Langelaar [2016]. It entails enforcing a constraint on the amount of overhang allowed in the structure, such that support material is unnecessary. Excluding support entirely however severely limits the design space. In Langelaar [2019] a method for simultaneous optimization of component and support is presented. Which method to use will largely depend on the component and influence of overhanging details.

7.4.2 Experimental Studies

This project has been centered on developing computational models for optimizing metal structures for manufacturing using AM. No experimental validation of AM material modeling was performed. Due to how the AM process changes the properties for each material and each geometry, it is desired to test different designs and possibly different materials of varying ductility. In particular the complex relationship between geometry, thermal history and eventual local material properties should be investigated, as uniaxial test specimens do not necessarily capture all effects.

Testing the effect of the optimized print plane orientation is also highly relevant. Both destructive tests to investigate the fatigue strength but also microscopy tests to validate if the alignment of defects is as expected and provide the strength predicted. Further, the variation in fatigue strength between vertical and horizontal printed components is assumed to follow a cosinusoidal function, which also has to be validated.

Bibliography

Aage and Lazarov, 2013. Niels Aage and Boyan S. Lazarov. *Parallel framework for topology optimization using the method of moving asymptotes*. Structural and Multidisciplinary Optimization, 47, 493–505, 2013.

Aage et al., 2015. Niels Aage, Erik Andreassen and Boyan S. Lazarov. *Topology optimization using PETSc: An easy-to-use, fully parallel, open source topology optimization framework*. Structural and Multidisciplinary Optimization, 51, 565–572, 2015.

Aage et al., 2017. Niels Aage, Erik Andreassen, Boyan S. Lazarov and Ole Sigmund. *Giga-voxel computational morphogenesis for structural design*. Nature, 550, 84–94, 2017.

Alfano and Crisfield, 2001. G. Alfano and M. A. Crisfield. *Finite element interface models for the delamination analysis of laminated composites: mechanical and computational issues*. International Journal for Numerical Methods in Engineering, 50, 1701–1736, 2001.

Allaire et al., 2002. Grégoire Allaire, François Jouve and Anca-Maria Toader. *A level-set method for shape optimization*. Comptes Rendus Mathematique, 334(12), 1125–1130, 2002.

Allaire et al., 2004. Grégoire Allaire, François Jouve and Anca-Maria Toader. *Structural optimization using sensitivity analysis and a level-set method*. Journal of Computational Physics, 194, 363–393, 2004.

Andreasen et al., 2020. Casper Schousboe Andreasen, Martin Ohrt Elingaard and Niels Aage. *Level set topology and shape optimization by density methods using cut elements with length scale control*. Structural and Multidisciplinary Optimization, 44, 19–24, 2020.

Andreassen et al., 2011. Erik Andreassen, Anders Clausen, Mattias Schevenels, Boyan S. Lazarov and Ole Sigmund. *Efficient topology optimization in MATLAB using 88 lines of code*. Structural and Multidisciplinary Optimization, 43, 1–16, 2011.

Arora, 2016. Jasbir S. Arora. *Introduction to Optimum Design, 4th edition*. ISBN: 978-0-12-381375-6. Elsevier, 2016.

Bag et al., 2020. Amrita Bag, Dorian Delbergue, Jihane Ajaja, Philippe Bocher, Martin Lévesque and Myriam Brochu. *Effect of different shot peening conditions on the fatigue life of 300 M steel submitted to high stress amplitudes*. International Journal of Fatigue, 130, 2020.

Belytschko et al., 2014. Ted Belytschko, Wing Kam liu, Brian Moran and Khalil I. Elkhodary. *Nonlinear finite elements for continua and structures*. ISBN: 978-1-118-63270-3. John Wiley & Sons, 2nd edition, 2014.

Bendsøe, 1989. M. P. Bendsøe. *Optimal shape design as a material distribution problem*. Structural Optimization, 1, 193–202, 1989.

Bendsøe and Sigmund, 1999. M. P. Bendsøe and O. Sigmund. *Material interpolation schemes in topology optimization*. Archive of Applied Mechanics, 69, 635–654, 1999.

Bendsøe et al., 2005. Martin P. Bendsøe, Erik Lund, Niels Olhoff and Ole Sigmund. *Topology optimization – broadening the areas of application*. Control and Cybernetics, 34(1), 7–35, 2005.

Bendsøe and Kikuchi, 1988. Martin Phillip Bendsøe and Noboru Kikuchi. *Generating Optimal Topologies in Structural Design Using a Homogenization Method*. Computer Methods in Applied Mechanics and Engineering, 71, 197–224, 1988.

Bendsøe and Sigmund, 2003. M.P. Bendsøe and O. Sigmund. *Topology Optimization - Theory, Methods and Applications*. ISBN: 3-540-42992-1. Springer, 2003.

Bian et al., 2015. Linkan Bian, Scott M. Thompson and Nima Shamsaei. *Mechanical Properties and Microstructural Features of Direct Laser-Deposited Ti-6Al-4V*. The Journal of The Minerals, Metals & Materials Society (JOM), 67(3), 629–638, 2015.

Bourdin, 2001. Blaise Bourdin. *Filters in topology optimization*. International Journal for Numerical Methods in Engineering, 50, 2143–2158, 2001.

Bruggi, 2008. Matteo Bruggi. *On an alternative approach to stress constraints relaxation in topology optimization*. Structural and Multidisciplinary Optimization, 36, 125–141, 2008.

Bruns and Tortorelli, 2001. Tyler E. Bruns and Daniel A. Tortorelli. *Topology optimization of non-linear elastic structures and compliant mechanisms*. Computer Methods in Applied Mechanics and Engineering, 191, 3443–3459, 2001.

Bruns and Tortorelli, 2003. Tyler E. Bruns and Daniel A. Tortorelli. *An element removal and reintroduction strategy for the topology optimization of structures and compliant mechanisms*. International Journal For Numerical Methods In Engineering, 57, 1413–1430, 2003.

Burman et al., 2015. Erik Burman, Susanne Claus, Peter Hansbo, Mats G. Larson and André Massing. *CutFEM: Discretizing geometry and partial differential equations*. International Journal for Numerical Methods in Engineering, 107(7), 472–501, 2015.

Burman et al., 2019. Erik Burman, Daniel Elfverson, Peter Hansbo, Mats G. Larson and Karl Larsson. *Cut topology optimization for linear elasticity with coupling to parametric nondesign domain regions*. Computer Methods in Applied Mechanics and Engineering, 350(15), 462–479, 2019.

Calignano, 2014. F. Calignano. *Design optimization of supports for overhanging structures in aluminum and titanium alloys by selective laser melting*. Materials and Design, 64, 203–213, 2014.

Chen and Kikuchi, 2001. Bing-Chung Chen and Noburu Kikuchi. *Topology optimization with design-dependent loads*. Finite Elements in Analysis and Design, 37, 57–70, 2001.

Cheng and Guo, 1997. G. D. Cheng and X. Guo. *ε-relaxed approach in structural topology optimization*. Structural Optimization, 13, 258–266, 1997.

Cheng and Olhoff, 1981. Keng-Tung Cheng and Niels Olhoff. *An investigation concerning optimal design of solid elastic plates*. International Journal of Solids and Structures, 17(3), 305–323, 1981.

Christensen and Klarbring, 2009. Peter W. Christensen and Anders Klarbring. *An Introduction to Structural Optimization*. ISBN 978-1-4020-8665-6. Springer, 2009.

Clausen, 2016. Anders Clausen. *Topology Optimization for Additive Manufacturing*. Ph.d. Thesis, 2016.

Clausen and Andreassen, 2017. Anders Clausen and Erik Andreassen. *On filter boundary conditions in topology optimization*. Structural and Multidisciplinary Optimization, 56, 1147–1155, 2017.

Cook et al., 2002. Robert D. Cook, David S. Malkus, Michael E. Plesha and Robert J. Witt. *Concepts and Applications of Finite Element Analysis*. ISBN: 978-0-471-35605-9. John Wiley & Sons, 4th edition, 2002.

da Silva et al., 2019. Gustavo Assis da Silva, André Teóflo Beck and Ole Sigmund. *Stress-constrained topology optimization considering uniform manufacturing uncertainties*. Computer Methods in Applied Mechanics and Engineering, 344, 512–537, 2019.

de Borst et al., 2012. René de Borst, Mike A. Crisfield, Joris J.C. Remmers and Clemens V. Verhoosel. *Non-linear finite element analysis of solids and structures*. ISBN: 978-0-470-66644-9. John Wiley & Sons, 2nd edition, 2012.

Duysinx and Bendsøe, 1998. P. Duysinx and M. P. Bendsøe. *Topology Optimization of Continuum Structures with Local Stress Constraints*. International Journal for Numerical Methods in Engineering, 43, 1453–1478, 1998.

Duysinx and Sigmund, 1998. P. Duysinx and O. Sigmund. *New developments in handling stress constraints in optimal material distribution*. American Institute of Aeronautics and Astronautics, 98(4906), 1–9, 1998.

Díaz and Sigmund, 1995. A. Díaz and O. Sigmund. *Checkerboard patterns in layout optimization*. Structural Optimization, 10, 40–45, 1995.

Eschenauer and Olhoff, 2001. Hans A. Eschenauer and Niels Olhoff. *Topology optimization of continuum structures: A review*. Applied Mechanics Review, 54(4), 331–390, 2001.

Fatemi and Socie, 1988. Ali Fatemi and Darrell F. Socie. *A Critical Plane Approach to Multiaxial Fatigue Damage Including Out-of-phase Loading*. Fatigue & Fracture of Engineering Materials and Structures, 11(3), 149–165, 1988.

Fatemi et al., 2019. Ali Fatemi, Reza Molaei and Nam Phan. *Multiaxial Fatigue of Additive Manufactured Metals*. MATEC Web of Conferences, 300, 2019. doi: 10.1051/matecconf/201930001003.

Fatemi et al., 2020. Ali Fatemi, Reza Molaei and Nam Phan. *Multiaxial fatigue of additive manufactured metals: Performance, analysis, and applications*. International Journal of Fatigue, 134, 1911–1919, 2020.

Gibson et al., 2016. Ian Gibson, David Rosen and Brent Stucker. *Additive Manufacturing Technologies: 3D Printing, Rapid Prototyping, and Direct Digital Manufacturing*. ISBN: 978-1-4939-2112-6. Springer, 2nd edition, 2016.

Guest et al., 2004. J. K. Guest, J. H. Prévost and T. Belytschko. *Achieving minimum length scale in topology optimization using nodal design variables and projection functions*. International Journal for Numerical Methods in Engineering, 61, 238–254, 2004.

Guest et al., 2011. James K. Guest, Alireza Asadpoure and Seung-Hyun Ha. *Eliminating beta-continuation from Heaviside projection and density filter algorithms*. Structural and Multidisciplinary Optimization, 44, 443–453, 2011.

Hackel et al., 2018. Lloyd Hackel, Jon R. Rankin, Alexander Rubenchik, Wayne E. King and Manyalibo Matthews. *Laser peening: A tool for additive manufacturing post-processing*. Additive Manufacturing, 24, 67–75, 2018.

Haftka and Grandhi, 1986. Raphael T. Haftka and Ramana V. Grandhi. *Structural shape optimization - a survey*. Computer Methods in Applied Mechanics and Engineering, 57, 91–106, 1986.

Holmberg et al., 2013. Erik Holmberg, Bo Torstenfelt and Anders Klarbring. *Stress constrained topology optimization*. Structural and Multidisciplinary Optimization, 48, 33–47, 2013.

Holmberg et al., 2014. Erik Holmberg, Bo Torstenfelt and Anders Klarbring. *Fatigue constrained topology optimization*. Structural and Multidisciplinary Optimization, 50, 207–219, 2014.

Holmberg et al., 2017. Erik Holmberg, Carl-Johan Thore and Anders Klarbring. *Game theory approach to robust topology optimization with uncertain loading*. Structural and Multidisciplinary Optimization, 55, 1383–1397, 2017.

Kawamoto et al., 2011. Atsushi Kawamoto, Tadayoshi Matsumori, Shintaro Yamasaki, Tsuyoshi Nomura, Tsuguo Kondoh and Shinji Nishiwaki. *Heaviside projection based topology optimization by a PDE-filtered scalar function*. Structural and Multidisciplinary Optimization, 44, 19–24, 2011.

Kirsch, 1990. U. Kirsch. *On singular topologies in optimum structural design*. Structural Optimization, 2, 133–142, 1990.

Langelaar, 2016. Matthijs Langelaar. *Topology optimization of 3D self-supporting structures for additive manufacturing*. Additive Manufacturing, 12, 60–70, 2016.

Langelaar, 2019. Matthijs Langelaar. *Integrated component-support topology optimization for additive manufacturing with post-machining*. Rapid Prototyping Journal, 25(2), 255–265, 2019.

Lazarov and Sigmund, 2011. B. S. Lazarov and O. Sigmund. *Filters in topology optimization based on Helmholtz-type differential equations*. Computer Methods in Applied Mechanics and Engineering, 86, 765–781, 2011.

Lazarov and Wang, 2017. Boyan S. Lazarov and Fengwen Wang. *Maximum length scale in density based topology optimization*. Computer Methods in Applied Mechanics and Engineering, 318, 826–844, 2017.

Le et al., 2010. Chau Le, Julian Norato, Tyler Bruns, Christopher Ha and Daniel Tortorelli. *Stress-based topology optimization for continua*. Structural and Multidisciplinary Optimization, 41, 605–620, 2010.

Leuders et al., 2014. Stefan Leuders, Tobias Lieneke, Stefan Lammers, Thomas Tröster and Thomas Niendorf. *On the fatigue properties of metals manufactured by selective laser melting – The role of ductility*. Journal of Materials Research, 29(17), 1911–1919, 2014.

Lund, 1994. Erik Lund. *Finite Element Based Design Sensitivity Analysis and Optimization*. Ph.d. Dissertation, 1994.

Lund, 2018. Erik Lund. *Discrete Material and Thickness Optimization of laminated composite structures including failure criteria*. Structural and Multidisciplinary Optimization, 57, 2357–2375, 2018.

Maamoun et al., 2018. Ahmed H. Maamoun, Mohamed A. Elbestawi and Stephen C. Veldhuis. *Influence of Shot Peening on AlSi10Mg Parts Fabricated by Additive Manufacturing*. Manufacturing and Materials Processing, 2(40), 2018.

Martins and Poon, 2005. Joaquim R. R. A. Martins and Nicholas M. K. Poon. *On Structural Optimization Using Constraint Aggregation*. 6th World Congress on Structural and Multidisciplinary Optimization, 2005.

Nelson, 1976. Richard B. Nelson. *Simplified Calculation of Eigenvector Derivatives*. AIAA Journal, 14(9), 1201–1205, 1976.

Norton, 2014. Robert L. Norton. *Machine Design, 5th edition*. ISBN: 978-0-13-335671-7, Hardback. Pearson Education Inc., 2014.

Oest and Lund, 2017. Jacob Oest and Erik Lund. *Topology optimization with finite-life fatigue constraints*. Structural and Multidisciplinary Optimization, 56(5), 1045–1059, 2017.

Olesen and Hermansen, 2019. Asbjørn M. Olesen and Sebastian M. Hermansen. *Structural Topology Optimization with Fatigue Constraints*. Aalborg University project library: `https://projekter.aau.dk`, 2019. 9^{th} semester student project.

Papuga, 2011. Jan Papuga. *A survey on evaluating the fatigue limit under multiaxial loading*. International Journal of Fatigue, 33, 153–165, 2011.

Papuga, 2012. Jan Papuga. *Evaluation of uniaxial fatigue criteria applied to multiaxially loaded unnotched samples*. Engineering Mechanics, 19, 99–111, 2012.

Papuga et al., 2018. Jan Papuga, Ivona Vízková, Maxim Lutovinov and Martin Nesládek. *Mean stress effect in stress-life fatigue prediction re-evaluated*. MATEC Web of Conferences, 165, 2018.

París et al., 2010. J. París, F. Navarrina and M. Casteleiro I. Colominas and. *Block aggregation of stress constraints in topology optimization of structures*. Advances in Engineering Software, 41, 433–441, 2010.

Qian and Sigmund, 2013. Xiaoping Qian and Ole Sigmund. *Topological design of electromechanical actuators with robustness toward over- and under-etching*. Computer Methods in Applied Mechanics and Engineering, 253, 237–251, 2013.

Rice, 1968. J. R. Rice. *A Path Independent Integral and the Approximate Analysis of Strain Concentration by Notches and Cracks*. Journal of Applied Mechanics, 35, 379–386, 1968.

Sigmund and Petersson, 1998. O. Sigmund and J. Petersson. *Numerical instabilities in topology optimization: A survey on procedures dealing with checkerboards, mesh-dependencies and local minima*. Structural Optimization, 16, 68–75, 1998.

Sigmund, 1994. Ole Sigmund. *Design of Material Structures using Topology Optimization*. Ph.d. Thesis, 1994.

Sigmund, 2001. Ole Sigmund. *A 99 line topology optimization code written in Matlab*. Structural and Multidisciplinary Optimization, 21, 120–127, 2001.

Sigmund, 2007. Ole Sigmund. *Morphology-based black and white filters for topology optimization*. Structural and Multidisciplinary Optimization, 33, 401–424, 2007.

Sigmund, 2009. Ole Sigmund. *Manufacturing tolerant topology optimization*. Acta Mechanica Sinica, 25, 227–239, 2009.

Sigmund, 2011. Ole Sigmund. *On the usefulness of non-gradient approaches in topology optimization*. Structural and Multidisciplinary Optimization, 43, 589–596, 2011.

Sigmund and Maute, 2013. Ole Sigmund and Kurt Maute. *Topology Optimization Approaches*. Structural and Multidisciplinary Optimization, 48, 1031–1055, 2013.

Sistiaga et al., 2016. M. L. Montero Sistiaga, S. Nardone, C. Hautfenne and J. Van Humbeeck. *Effect of heat treatment of 316L stainless steel produced by Selective Laser Melting (SLM)*. Solid Freedom Fabrication, Proceedings of the 26th Annual International Solid Freeform Fabrication Symposium – An Additive Manufacturing Conference, 367–377, 2016.

Smith et al., 1970. K. N. Smith, P. Watson and T. H. Topper. *A Stress-Strain Function for the Fatigue of Metals*. Journal of Materials, 5(4), 767–778, 1970.

Spierings et al., 2011. A.B. Spierings, N. Herres and G. Levy. *Influence of the particle size distribution on surface quality and mechanical properties in AM steel parts*. Rapid Prototyping Journal, 17(3), 195–202, 2011.

Spierings et al., 2013. A.B. Spierings, T. L. Starr and K. Wegener. *Fatigue performance of additive manufactured metallic parts*. Rapid Prototyping Journal, 19(2), 88–94, 2013.

Stephens et al., 2001. Ralph I. Stephens, Ali Fatemi, Robert R. Stephens and Henry O. Fuchs. *Metal Fatigue in Engineering*. Wiley Interscience, 2nd edition, 2001.

Stolpe and Svanberg, 2001a. M. Stolpe and K. Svanberg. *An alternative interpolation scheme for minimum compliance topology optimization*. Structural and Multidisciplinary Optimization, 22, 116–124, 2001.

Stolpe and Svanberg, 2001b. M. Stolpe and K. Svanberg. *On the trajectories of penalization methods for topology optimization*. Structural and Multidisciplinary Optimization, 21, 128–139, 2001.

Svanberg, 1987. Krister Svanberg. *The Method of Moving Asymptotes - A New Method for Structural Optimization*. International Journal for Numerical Methods in Engineering, 24, 359–373, 1987.

Svanberg, 2007. Krister Svanberg. *MMA and GCMMA, versions September 2007*. Technical Report, 2007.

Sved and Ginos, 1968. G. Sved and Z. Ginos. *Structural Optimization Under Multiple Loading*. International Journal of Mechanical Sciences, 10, 803–805, 1968.

Svärd, 2015a. Henrik Svärd. *A branch and bound algorithm for evaluation of the Findley fatigue criterion*. International Journal of Fatigue, 73, 27–38, 2015.

Svärd, 2015b. Henrik Svärd. *Interior value extrapolation: a new method for stress evaluation during topology optimization*. Structural and Multidisciplinary Optimization, 51, 613–629, 2015.

Tolosa et al., 2010. Itziar Tolosa, Fermín Garciandía, Fidel Zubiri, Fidel Zapirain and Aritz Esnaola. *Study of mechanical properties of AISI 316 stainless steel processed by "selective laser melting", following different manufacturing strategies*. The International Journal of Advanced Manufacturing Technology, 51, 639–647, 2010.

Wallin et al., 2020. Mathias Wallin, Niklas Ivarsson, Oded Amir and Daniel Tortorelli. *Consistent boundary conditions for PDE filter regularization in topology optimization*. Structural and Multidisciplinary Optimization, 2020.

Wang et al., 2011. Fengwen Wang, Boyan Stefanov Lazarov and Ole Sigmund. *On projection methods, convergence and robust formulations in topology optimization*. Structural and Multidisciplinary Optimization, 43, 767–784, 2011.

Wang et al., 2003. Michael Yu Wang, Xiaoming Wang and Dongming Guo. *A level set method for structural topology optimization*. Computer Methods in Applied Mechanics and Engineering, 192, 227–246, 2003.

Xu et al., 2010. Shengli Xu, Yuanwu Cai and Gengdong Cheng. *Volume preserving nonlinear density filter based on heaviside functions*. Structural and Multidisciplinary Optimization, 41, 495–505, 2010.

Yadollahi and Shamsaei, 2017. Aref Yadollahi and Nima Shamsaei. *Additive manufacturing of fatigue resistant materials: Challenges and opportunities*. International Journal of Fatigue, 98, 14–31, 2017.

Yadollahi et al., 2015. Aref Yadollahi, Nima Shamsaei, Scott M. Thompson and Denver W. Seely. *Effects of process time interval and heat treatment on the mechanical and microstructural properties of direct laser deposited 316L stainless steel*. Materials Science & Engineering A, 644, 171–183, 2015.

Yadollahi et al., 2017. Aref Yadollahi, Nima Shamsaei, Scott M. Thompson, Alaa Elwany and Linkan Bian. *Effects of building orientation and heat treatment on fatigue behavior of selective laser melted 17-4 PH stainless steel*. International Journal of Fatigue, 94, 218–235, 2017.

Zhang et al., 2019. Shanglong Zhang, Chau Le, Arun L. Gain and Julián A. Norato. *Fatigue-based topology optimization with non-proportional loads*. Comput. Methods Appl. Mech. Engrg., 345, 805–825, 2019.

Zhou et al., 2015. Mingdong Zhou, Boyan S. Lazarov, Fengweng Wang and Ole Sigmund. *Minimum length scale in topology optimization by geometric constraints*. International Journal for Numerical Methods in Engineering, 293, 266–282, 2015.

A Post Optimization Density Interpolation

This appendix covers the reasoning for developing a new method for post-processing geometry and describes the technicalities of interpolating density in a finite element context.

The use of element densities to describe geometry in the optimization setting means that the geometry cannot be directly exported as a physically meaningful model. To allow for subsequent post-processing and analysis in other programs, a full density model must somehow be extracted. In two dimensions this may be done by interpolating an isoline for some density level, but the problem becomes less tractable in three dimensions.

The simplest method is discrete threshold filtering, selecting some density cutoff value and removing all elements with densities below, see Figure A.1. This method however creates a staircase-effect, where lines not parallel to element sides are poorly approximated, leading to many stress concentrations.

To alleviate the problem of stress concentrations, a smoothing operation may be performed, see Figure A.2. The filter used is the standard surface smoothing filter in ParaView.

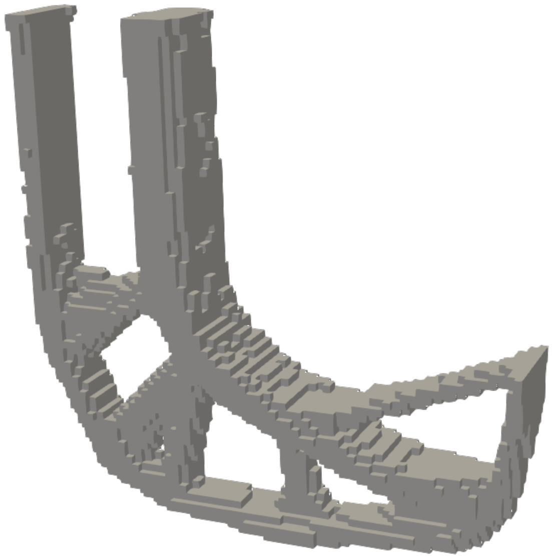

Figure A.1. Elements filtered for $\rho \geq 0.5$.

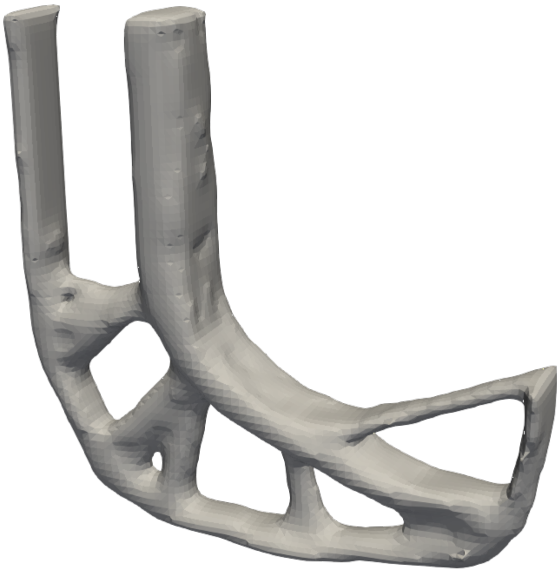

Figure A.2. Smoothed geometry of Figure A.1.

This introduces a number of issues; the most obvious being that no information about boundary conditions is preserved, i.e. areas with fixture and load application are smoothed and lose definition. Similarly, all information about density gradient is lost in the threshold filter and the smoothed geometry is not guaranteed to follow the specified density cutoff - this is exemplified by consecutive smoothing operations changing the thickness of the geometry. In other words, filtering is not volume-conservative and minimum length scale may be violated for aggressive smoothing. A separate issue of threshold filtering and smoothing is non-manifold or zero-thickness geometry leading to poorly smoothed geometry. This is however related to the fact that the surface is not re-meshed during smoothing, which would remove this type of artefact.

These issues can be avoided entirely by smoothly interpolating the density field rather than using a threshold filter. On Figure A.3 an interpolated geometry is shown. The interpolation makes use of the density gradient to create smooth surfaces and the benefit is seen by the overlaid geometries - boundary conditions are preserved and more material is present for concave geometry.

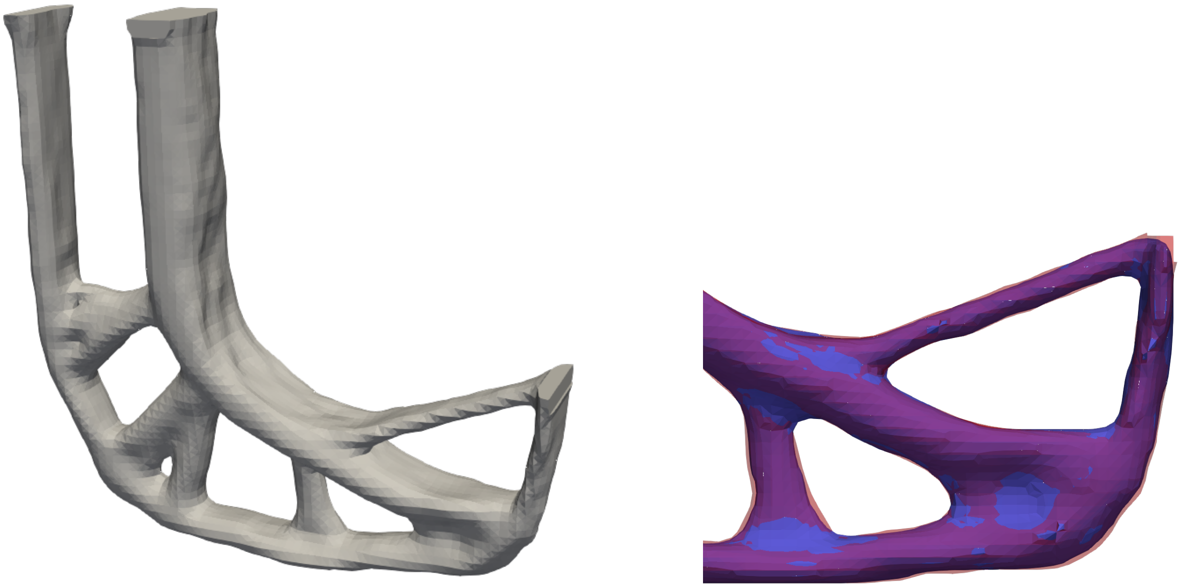

Figure A.3. *Left*: interpolated surface geometry for $\rho = 0.5$. *Right*: detail of interpolated surface (red) overlayed on the smoothed surface (blue).

The example geometry is based on a relatively finely discretized structured mesh, which is the best case scenario for smoothing operations. If a coarse non-structured mesh is used instead, elements with large distortions are likely to reduce the quality of the smoothed surface - this again is largely avoided by interpolating the gradient.

The smooth geometry interpolation scheme is described in the following.

A.1 Method Overview

The interpolation scheme revolves around finding the surface of the entire structure on a per-element basis and is split into three steps (elaborated in the next sections):

1. **Global operations**
   Data of neighboring elements is collected, such that computations with a single element also considers surrounding element data - specifically this is finding nodal density values and element faces that lie on the outside of the design domain (these would be the

outermost faces visible, including domain extension).

2. **Element interpolation**
   Using the above data, the density is interpolated and points are found which will eventually describe the surface. A density gradient vector is also determined.
3. **Surface description**
   Using the density gradient as an approximate surface normal, the points are sorted and used to generate a surface.

The end result of this procedure is an .STL file, which is a common format and easily imported in commercial programs. An illustrated overview of element interpolation and surface description is presented in Figure A.12 at the end of this appendix.

A.2 Global Operations

The interpolation is done on a per-element basis, simplifying the required computations, although some information must be found on a global scale first, namely nodal density and outer element faces. All elements are investigated, including those generated for domain extension.

Nodal density is found by simple nodal averaging:

$$\rho_n^{(n)} = \frac{1}{N^{(n)}} \sum_{e \in S^{(n)}} \rho^{(e)} \tag{A.1}$$

where $\rho_n^{(n)}$ and $\rho^{(e)}$ are nodal and element densities, respectively, $N^{(n)}$ is the total number of elements connected to node n and $S^{(n)}$ is the set of elements connected to the node. Note that no calculations for the density interpolation use element density. More accurate schemes can be implemented if higher accuracy is required, particularly in the case of coarse meshing.

Outer faces, see Figure A.4, are found by comparison of global node numbers - if faces of different elements share all nodes, then neither is an outer face. In explicit terms, this is done by a series of loops, see the pseudo code of Algorithm 2. This is a rather cumbersome computation as it involves N_{elem}^2 comparisons. It is however constant for a given mesh and the data can be reused for subsequent interpolations.

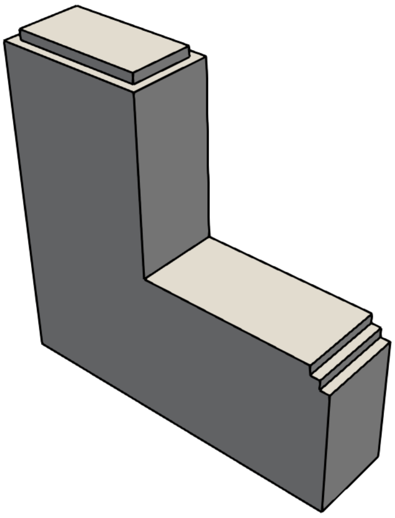

Figure A.4. Outer faces of the design domain, including domain extension. This is the domain used to generate designs in Figures A.1, A.2, and A.3.

Algorithm 2: Determination of outer faces.

```
Data: Nodal numbers $n$, element numbers $e$, local node numbers belonging to face $f$
Result: Boolean matrix $\mathbf{O}$ containing state of all element faces, with True for outer faces,
        False for inner.
Initialization;
$\mathbf{O} = False$;
for $e_1 \leftarrow 1$ to $N_{elem}$ do
    for $e_2 \leftarrow 1$ to $N_{elem}$ do
        if $e_1 \neq e_2$ then
            for $f \in e_1$ do
                if $n(f) \notin n(e_2)$ then
                    $\mathbf{O}(e_1, f) = True$
                end if
            end for
        end if
    end for
end for
```

A.3 Element Interpolation

The isoparametric finite element expressions in this section are inspired by Cook et al. [2002].

Once nodal densities and outer element faces are found, individual elements are considered. Three things must be found to determine a surface:

- points $\mathbf{v}_i$ along element edges
- a center point $\mathbf{v}_0$
- an approximate normal $\mathbf{n}$ to the surface, pointing away from the inferred solid

A surface constructed from these is illustrated in Figure A.5.

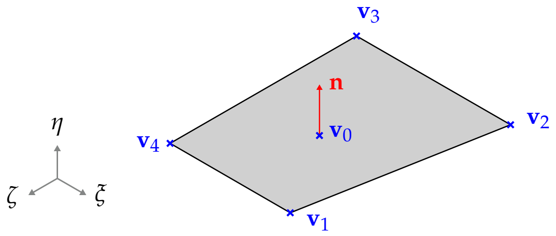

Figure A.5. Information required to describe a surface: center point $\mathbf{v}_0$, corner points $\mathbf{v}_i$, and a surface normal $\mathbf{n}$.

The element is considered in its natural coordinates, rather than global Cartesian coordinates, such that a point $\mathbf{v}$ is given by:

$$\mathbf{v} = \begin{bmatrix} \xi & \eta & \zeta \end{bmatrix} \qquad \text{where} \qquad -1 \leq \{\xi,\ \eta,\ \zeta\} \leq 1 \tag{A.2}$$

By doing this, elements can be considered as voxels and then generalized to an arbitrary distortion - or even collapsed into a tetrahedral element, if some additional bookkeeping is done. This means that the method is general for any linear solid element mesh.

The interpolated surface is found by locating points corresponding to a cutoff density value. To simplify consistency with neighboring elements, corner points $\mathbf{v}_i$ are found exclusively along the edges of an element, such that only the nodal densities which are shared between elements are needed. The points that do not coincide with an element node are found by interpolating along the element edge:

$$\mathbf{v}_i = \begin{bmatrix} \frac{\rho_{nb}-\rho_{cut}}{\rho_{nb}-\rho_{na}} & \frac{\rho_{cut}-\rho_{na}}{\rho_{nb}-\rho_{na}} \end{bmatrix} \begin{bmatrix} \mathbf{c}_a \\ \mathbf{c}_b \end{bmatrix}, \qquad \rho_{na} < \rho_{cut} < \rho_{nb} \tag{A.3}$$

where ρ_{na} and ρ_{nb} are nodal densities and $\mathbf{c}_a$ and $\mathbf{c}_b$ are nodal coordinates, with subscripts a and b indicating the node at either end of the edge. The center point is found as a mean coordinate of $\mathbf{v}_i$:

$$\mathbf{v}_0 = \frac{1}{N_v} \sum_{i=1}^{N_v} \mathbf{v}_i \tag{A.4}$$

where N_v is the number of corner points.

The entire element is not considered at once, but as element faces first, followed by the element interior. Program-wise, this means considering 7 potential surfaces: 6 element faces and an interior intersection. By treating the element faces separately, it is possible to describe flat surfaces as required near boundary conditions, one of the things lost by filtering. This also involves differences in computation of $\mathbf{v}_i$ and $\mathbf{n}$, elaborated in the following.

A.3.1 Outer Faces

A surface must be generated on the element face, if two conditions are fulfilled: it is an outer face and at least one node has a nodal density $\rho_n^{(n)}$ higher than or equal to a chosen cutoff value ρ_{cut}. The number of nodes where $\rho_n^{(n)} \geq \rho_{cut}$ decides how the surface is made. If all

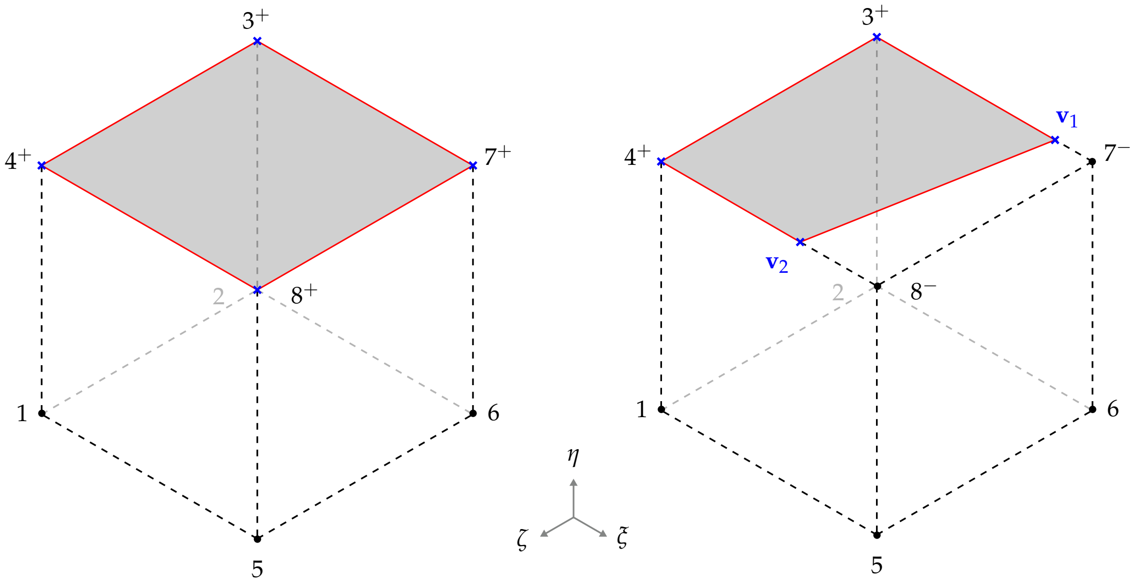

Figure A.6. An element where an outer face contains node numbers $\{3;4;7;8\}$. If all relevant nodal densities are above a cutoff, a full surface is generated (left). If only some are above cutoff, a partial surface is generated (right). Blue crosses indicate corners of the surface, which are the points that must determined. The superscript sign indicates whether the node density is above the cutoff (+) or below (-).

nodes making up the given face are above the cutoff, the full face is the surface - otherwise, it is a partial surface, see Figure A.6.

Given that the isoparametric element is axis parallel in natural coordinates, the normal vector can be described as a positive or negative basis vector, e.g. for the surface in Figure A.6 the normal would be:

$$\mathbf{n} = \hat{\eta} = \begin{bmatrix} 0 & 1 & 0 \end{bmatrix}^T \tag{A.5}$$

where $\hat{\eta}$ is a coordinate basis vector.

A.3.2 Element Interior

The element interior is then considered. The element is intersected if nodal densities are to both sides of the cutoff value, i.e. if

$$\rho_{cut} \begin{cases} < \rho_n^{(n_1)} \\ > \rho_n^{(n_2)} \end{cases}, \qquad n_1 \cup n_2 = n \tag{A.6}$$

where n is the set of node numbers. Again, corner points are only found on element edges according to Equation (A.3), however they are not restricted to a single element face, see Figure A.7.

The approximate normal is taken as the negative density gradient, such that the normal points away from the solid, as required:

$$\mathbf{n} = -\nabla\rho = -\mathbf{B}\ \rho_n \tag{A.7}$$

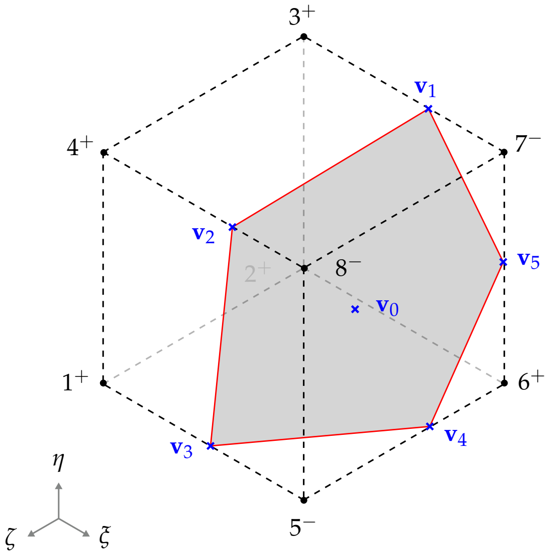

Figure A.7. Isoparametric element intersection.

where $\nabla\rho$ is the linear gradient vector, $\mathbf{B}$ is the first derivative of shape functions evaluated at the element center, and $\boldsymbol{\rho}_n$ is a vector containing all nodal densities.

Improvement of Center Point

If using the mean coordinate is not accurate enough for the center point, the density gradient can be used to improve the evaluation:

$$\mathbf{v}_0^* = \mathbf{v}_0 + d\ \nabla\rho \tag{A.8}$$

where $\mathbf{v}_0^*$ is the improved center point and d is a step along the gradient vector, such that density coincides with the cutoff. To find d, the intercept between the cutoff density and a linear function $\rho(d)$ is considered (see also Figure A.8):

$$\rho_{cut} = \rho(d) \tag{A.9}$$

The function is expressed as:

$$\rho(d) = \rho_{\mathbf{v}_0} + d\ |\nabla\rho| \tag{A.10}$$

where $\rho_{\mathbf{v}_0}$ is the density evaluated at $\mathbf{v}_0$ via shape functions $\mathbf{N}_{\mathbf{v}_0}$:

$$\rho_{\mathbf{v}_0} = \mathbf{N}_{\mathbf{v}_0}\ \boldsymbol{\rho}_{nodes} \qquad \text{where} \qquad \mathbf{N}_{\mathbf{v}_0} = \frac{1}{8}\left[(1 \pm v_{0,\xi})(1 \pm v_{0,\eta})(1 \pm v_{0,\zeta}) \quad \cdots\right] \tag{A.11}$$

Inserting Equation (A.11) into Equation (A.10) and solving for d:

$$d = \frac{p_{cut} - \mathbf{N}_{\mathbf{v}_0}\ \boldsymbol{\rho}_n}{|\nabla\rho|} \tag{A.12}$$

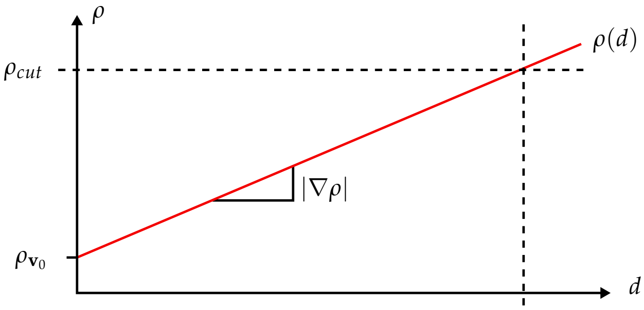

Figure A.8. Determining intercept for the specified cutoff density ρ_{cut}.

A.4 Surface Description

As previously described, the end result of the interpolation scheme is an .STL file, which provides a convenient way of describing a surface geometry. The surface is described as a set of triangular facets, each consisting of three vertices and a normal vector, see Figure A.9. The description of the individual facet must follow certain conventions:

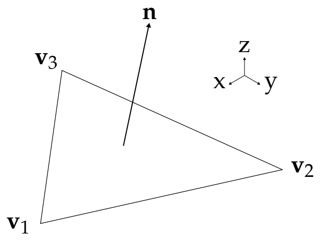

```
solid
    ...
    facet normal nx ny nz
        outer loop
            vertex v1x v1y v1z
            vertex v2x v2y v2z
            vertex v3x v3y v3z
        endloop
    endfacet
    ...
endsolid
```

Figure A.9. An .STL facet and the equivalent plaintext in the file itself. The .STL file begins with the keyword `solid` (optionally followed by a space and a name) on the first line, then the description of each facet and finally ends with keyword `endsolid` on the last line.

- The normal must point outwards, away from the model.
- The normal must be unit length.
- All vertex coordinates must be positive.
- Vertex numbering must follow right hand rotation wrt. the normal.

The information needed for the .STL file is determined from that found in the previous section. Specifically, a group of points must be found to describe a surface of facets, with no overlaps. The local point coordinates are then transformed to global Cartesian coordinates and an exact normal is determined for each facet.

The grouping of points is done by considering the surface as a set of triangles/facets, all connected at the center point, see Figure A.10. The points needed to make each facet is found by a sorting algorithm, using the angles between vectors from $\mathbf{v}_0$ to $\mathbf{v}_i$.

Because the points are rarely perfectly in a common plane, inconsistencies can occur in the angle calculation. The angle calculation and sorting are therefore done wrt. the approximate

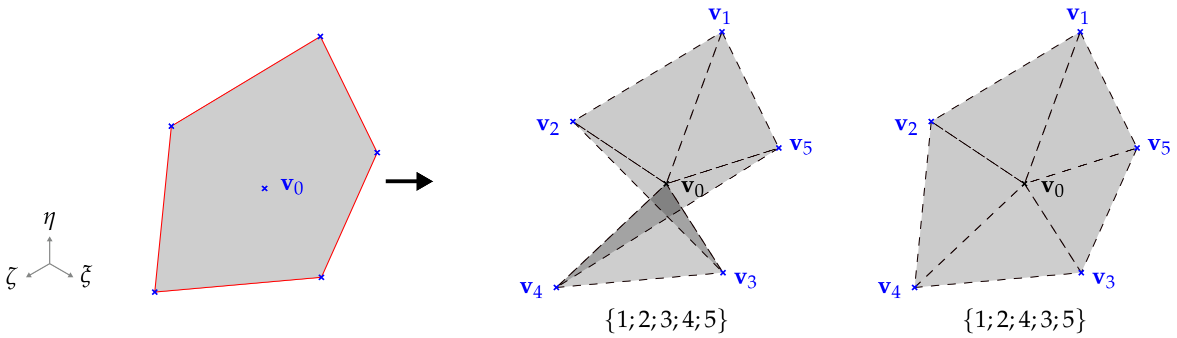

Figure A.10. Order of corner points must be correct for facets to represent the surface completely and with no overlaps.

normal **n**. First, vectors $\mathbf{r}_i$, lying in the plane to which **n** is normal, are found as the rejection from **n**. The rejection vector is the complement to the vector $(\mathbf{v}_i - \mathbf{v}_0)$ projected onto **n**, see Figure A.11, and is found as vector subtracted by projection:

$$\mathbf{r}_i = (\mathbf{v}_i - \mathbf{v}_0) - \frac{(\mathbf{v}_i - \mathbf{v}_0) \cdot \mathbf{n}}{\mathbf{n} \cdot \mathbf{n}} \mathbf{n} \tag{A.13}$$

As $\mathbf{r}_i$ are all in the same plane, the sum of angles between vectors is exactly 2π for a non-overlapping surface. A right-hand convention is then introduced when calculating the angles, see Figure A.11.

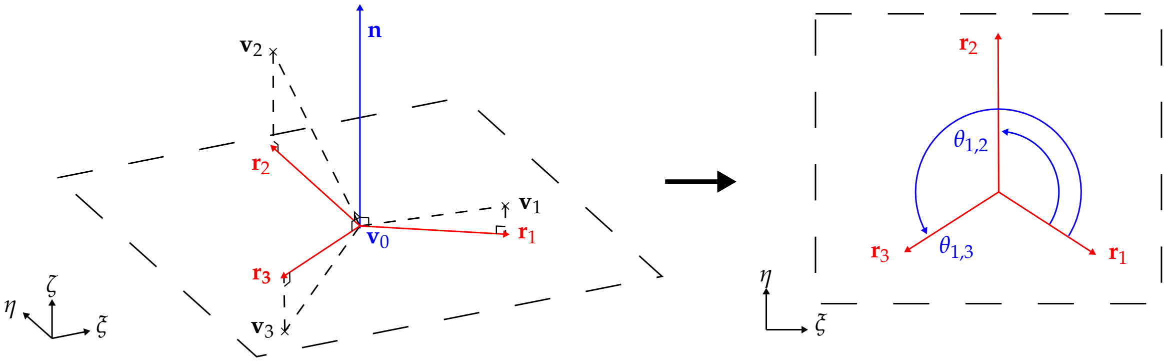

Figure A.11. Left: rejection vectors $\mathbf{r}_i$ all lie in a plane normal to **n**. *Right*: Angles between vectors are calculated by right-hand rule wrt. **n**, which is pointing outwards here.

The sorting is then done as follows:

- Select a vector $\mathbf{r}_i$.
- Calculate angle $\theta_{i,k} = \mathbf{r}_i \angle \mathbf{r}_k$ to all other $\mathbf{r}_k$.
- Select the vector that satisfies $(\mathbf{r}_i \times \mathbf{r}_k) \angle \mathbf{n} = 0$ and minimizes $\theta_{i,k}$
- Save the index k in a list and add angle $\theta_{k,i}$ and restart from vector $\mathbf{r}_k$, unless $\sum \theta = 2\pi$, then stop

When the sorting is complete, the list of indices is used to select and group the original points $\mathbf{v}_i$, such that a facet is always made up of vertices $\mathbf{v}_0$, $\mathbf{v}_{I(k)}$, and $\mathbf{v}_{I(k+1)}$, in that order as required by the .STL format.

The points are converted to Cartesian coordinates as:

$$\begin{bmatrix} x & y & z \end{bmatrix} = \mathbf{N}_{\mathbf{v}_i} \begin{bmatrix} \mathbf{x} & \mathbf{y} & \mathbf{z} \end{bmatrix} - \begin{bmatrix} x_{min} & y_{min} & z_{min} \end{bmatrix} \tag{A.14}$$

The vector of minimum values is subtracted to ensure that all coordinates are positive, again required in the STL format. Finally, the actual unit normal vector is found for each facet:

$$\mathbf{n} = \frac{\mathbf{v}_{I(k)} \times \mathbf{v}_{I(k+1)}}{|\mathbf{v}_{I(k)} \times \mathbf{v}_{I(k+1)}|} \tag{A.15}$$

Note that due to the sorting using a strict right-hand rule, the direction of the normal is preserved, i.e. it points away from the solid material.

On Figure A.12 the element surface computation is illustrated.

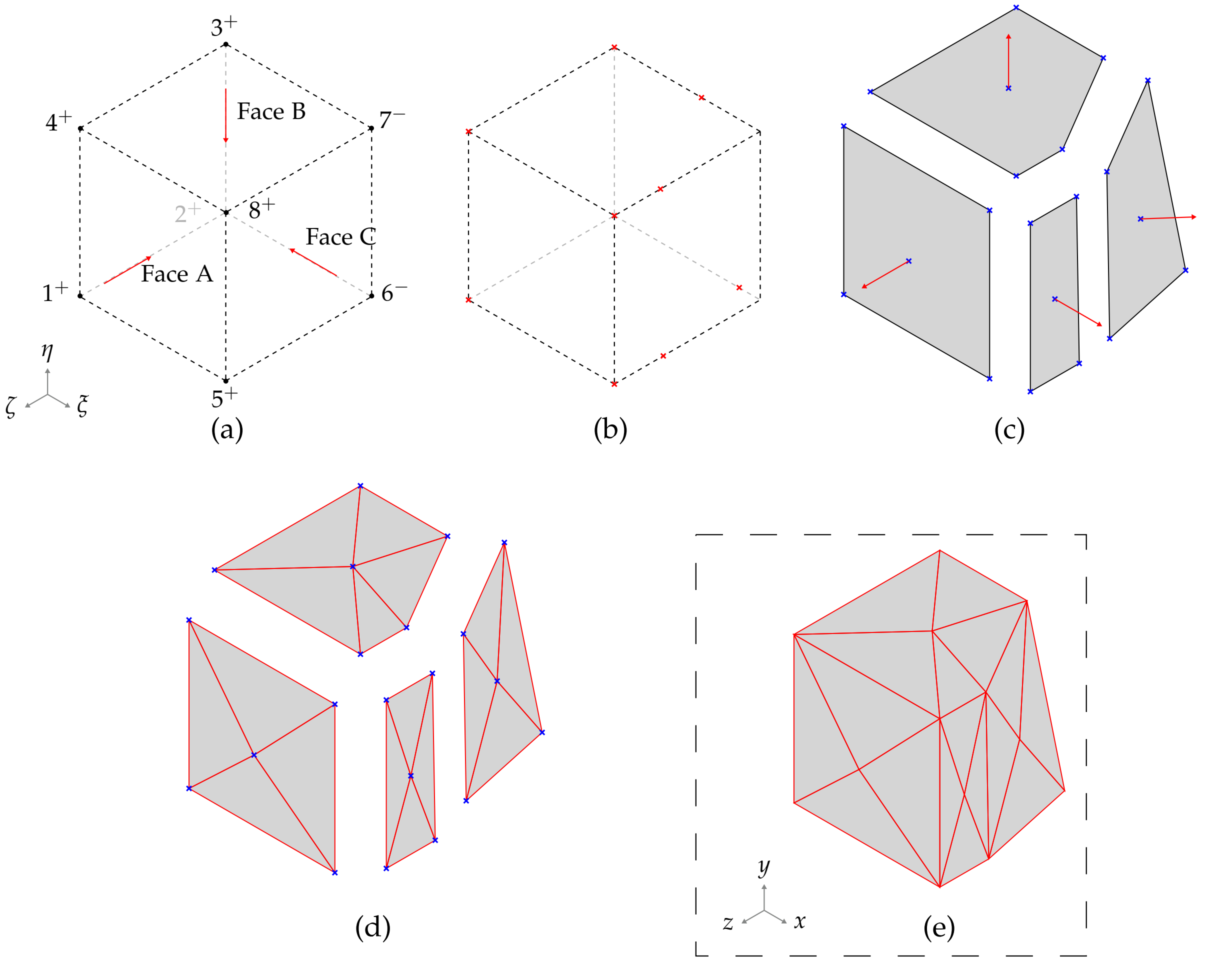

(a) (b) (c)

(d) (e)

Figure A.12. Overview of element interpolation and surface description. (a): For an element it is found that all nodal densities are above the cutoff value except 6 and 7, and that faces A (nodes 1,5,8,4), B (nodes 3,4,8,7) and C (nodes 5,6,7,8) are outside faces. (b): It is determined that the surface consists of nodes 1,3,4,5,8 and interpolated points on edges between nodes (3,7), (6,8), (7,8), and (5,6). (c): Individual faces and the element intersection are considered; center points and approximate normals are calculated. (d): Using the center point and normals, non-overlapping triangular facets are found. (e): The facets are transformed from natural to Cartesian coordinates, normals are recalculated and the data is written to an .STL file. Process is repeated for all elements.